THE GEOCHEMISTRY OF THE MT. LYELL COPPER DEPOSITS

by

J.L. WALSHE, B.Sc. (Hons.)

I agree that, if this thesis is accepted
for a degree of the University of
Tasmania, it may then be available for
loan and copying.

(signed) ....

date ....

Submitted in partial fulfilment of the requirements
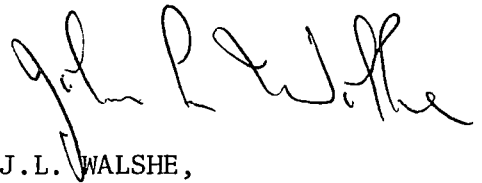
for the degree of Doctor of Philosophy.

UNIVERSITY OF TASMANIA

HOBART

1977
1978

This thesis contains no material which has been accepted for
the award of any other degree or diploma in any University and,
to the best of my knowledge and belief, contains no copy or
paraphrase of material previously published or written by another
person, except where due reference is made in the text of this thesis.

J.L. WALSHE,

University of Tasmania,

May, 1977.

" . . . be warned that writing books involves
endless hard work, and that much study wearies
the body."

ECCLESIASTES, ch. 11, v. 12.

ABSTRACT

The Mt. Lyell copper field is located near Queenstown on the
west coast of Tasmania. It occurs within Cambrian felsic lavas
and pyroclastics which are part of the central lava belt of the
Mt. Read Volcanics. The mineralization is probably of Cambrian
age and is associated with an extensive zone of hydrothermal
alteration. Sulphide deformation and minor remobilisation of
silicates and sulphides occurred during subsequent deformation,
mainly in the Tabberabberan Orogeny (Devonian).

The mineral deposits on the field may be grouped as:

(1) Disseminated pyrite-chalcopyrite type

      Prince Lyell, "A" Lens, Royal Tharsis, Cape Horn,

      Crown Lyell No. 1 and 3, Lyell Tharsis (in part),

      and Western Tharsis.

(2) Bornite-chalcopyrite type

      North Lyell, Crown Lyell No.2, 12 West, Lyell Tharsis

      (in part) and Lyell Comstock (in part).

(3) Massive pyrite-chalcopyrite type

      The Blow (Mt. Lyell orebody)

(4) Massive pyrite-galena-sphalerite-chalcopyrite type

      Tasman and Crown Lyell Extended and Lyell Comstock

      (open cut).

Prince Lyell consists of a central core of fragmental felsic
volcanics which have been altered to an assemblage of quartz-sericite-
chlorite-pyrite-chalcopyrite. Minor phases include siderite, apatite,
hematite, and some magnetite and barite. Inclusions of pyrrhotite,
pyrrhotite-chalcopyrite, bornite and bornite-chalcopyrite occur in
the pyrite. The hangingwall of the orebody consists of chloritised
intermediate-mafic volcanics, the footwall of massive or fragmental

pink rhyolites which have an alteration assemblage of quartz-sericite-minor hematite, chlorite, sulphide, siderite and barite. A quartz-sericite-pyrite-minor chalcopyrite alteration assemblage occurs on the northern end of Prince Lyell.

Minor lenses of massive magnetite and chlorite occur in the central core and a quartz-chlorite-minor sericite-hematite-magnetite-sulphide assemblage in the footwall adjacent to the central core.

The suggested reconstruction of hydrothermal alteration and mineralization is:

(1) An early, essentially non-sulphide, alteration forming the assemblage:

quartz-sericite-minor chlorite-hematite-barite-carbonate - possibly clays(?).

(2) Initial sulphide deposition, which began with pyrrhotite-magnetite-chlorite-siderite formation in reduced conditions and/or at a higher temperature relative to:

(3) The mainstage sulphide deposition, which probably began in the quartz-sericite-pyrite stable conditions at 250-300°C (?). Increasing pH and decreasing fO_2, as reaction with the host rock proceeded, lead to chlorite formation and subsequently to chalcopyrite formation.

(4) A late-stage phase of quartz-sericite-pyrite-chalcopyrite mineralization and alteration.

Hematite was produced during later metamorphism by the oxidation of magnetite, pyrrhotite(?), and pyrite(?). All phases except pyrite appear to have been completely recrystallised and quartz, siderite, chalcopyrite and chlorite have been locally remobilised.

Crown Lyell - North Lyell ores consist of:

(1) Disseminated pyrite-chalcopyrite mineralization in chert and
     silicified volcanics with minor sericite-barite-carbonate
     (Crown Lyell No. 3).

(2) Bornite-chalcopyrite mineralization in chert or chert-breccia
     with minor sericite and pyrophyllite (North Lyell, Crown Lyell
     No. 2, 12 West).

(3) Disseminated pyrite-chalcopyrite mineralization in chloritised
     felsic volcanics; the common assemblage is quartz-chlorite-
     minor sericite-hematite-magnetite-pyrite-chalcopyrite-barite
     (Crown Lyell No. 3 footwall, Lyell Tharsis, Crown Lyell No.1).

Bornite-chalcopyrite mineralization suggests a probable lower
temperature of deposition relative to Prince Lyell (assuming a
similar copper content to the ore fluids of Prince Lyell); the quartz-
chlorite-oxide-barite assemblage suggests higher oxidation conditions
relative to Prince Lyell.

The Cape Horn orebody consists of the assemblages:

(1) quartz-sericite-chlorite-pyrite-chalcopyrite-minor barite

(2) quartz-chlorite-minor sericite-hematite-magnetite-pyrite
     -chalcopyrite-barite

(3) quartz-sericite-pyrite-chalcopyrite-minor barite.

The combination of assemblages common to Prince Lyell and Crown
Lyell - North Lyell is consistent with fO_2-T conditions intermediate
between the conditions of deposition of Prince Lyell and Crown Lyell-
North Lyell.

Western Tharsis consists of disseminated pyrite-minor chalcopyrite
mineralization in altered felsic volcanics; the common assemblage is
quartz-sericite-pyrite-chalcopyrite-minor carbonate and chlorite.
Relative to Prince Lyell the mineralization and alteration occurred
at lower temperatures(?) or the ore fluid contained a higher initial

sulphur content.

The δS^{34}_{py} and ΔS^{34} py-ccp values for the various deposits are:

	δS^{34}_{py}, ‰	ΔS^{34}py-ccp, ‰
Prince Lyell	+10.0 to +5.2	+1.2 to -0.6
Cape Horn	+ 6.4 to -0.4	-1.3 to -1.5
Crown Lyell-North Lyell	+ 0.8 to -5.3	+0.3 to +1.2
Western Tharsis	+ 4.8 to +6.4	+1.6 to +1.8

The variation in δS^{34}_{py} values from Prince Lyell to Cape Horn to Crown Lyell-North Lyell is consistent with a progressive increase in the oxidation conditions of deposition. Mass transfer calculations indicate the variation in ΔS^{34}py-ccp is consistent with the oxidation trend; with chalcopyrite precipitating at a higher pH and lower oxidation conditions relative to pyrite, and/or precipitating from a solution enriched in S^{34} by the precipitation of a significant amount of the sulphur in solution as pyrite. The estimated initial value of $\delta S^{34}_{\Sigma S}$ for the Prince Lyell, Cape Horn and Crown Lyell-North Lyell ore solutions is +7 per mil. If the Western Tharsis ΔS^{34}py-ccp data approximates equilibrium partitioning, the initial $\delta S^{34}_{\Sigma S}$ value for the Western Tharsis solutions must be less than +7 per mil.

Cobalt contents of pyrite from the chlorite assemblages of Prince Lyell, Cape Horn, and Crown Lyell No.3 footwall, average 1600, 1050 and 1800 ppm respectively with values up to 4000 ppm. In contrast, cobalt contents of pyrite from quartz-sericite-pyrite assemblages are less than 1000 ppm, although pyrite from the Western Tharsis quartz-sericite-pyrite-chalcopyrite assemblage averages 1400 ppm. Nickel contents are also higher in pyrite from chlorite assemblages, particularly Cape Horn (av. 700ppm) and Crown Lyell No.3 footwall.

Increasing Co/Fe and Ni/Fe ratios in solution, due to the precipitation of chlorite, and chalcopyrite replacing pyrite, are

the likely reasons for cobalt and nickel enrichment in pyrite from chlorite-rich and chalcopyrite-rich assemblages. Mass transfer calculations suggest depletion of Co and Ni in solution is also an important factor controlling the cobalt and nickel content of pyrite.

ACKNOWLEDGEMENTS

CONTENTS

ACKNOWLEDGEMENTS   i

1. INTRODUCTION TO THE MT. LYELL FIELD   1

    1.1 The Mt. Read Volcanics   1

    1.2 Cambrian/Ordovician Relationships   2

    1.3 The Tabberabberan Orogeny   4

    1.4 The Lyell Schists   5

    1.5 Mineralization   6

    1.6 Previous Research on the Lyell Ores   8

    1.7 The Genesis of Mt. Lyell   9

    1.8 Background to the present study   10

    1.9 The Lake Selina Prospect   11

2. DESCRIPTION OF THE MT. LYELL MINERALIZATION   12

    2.1 Introduction   12

    2.2 Prince Lyell   14

        2.2.1 Introduction   14

        2.2.2 Quartz-Sericite-Chlorite-Pyrite-
               Chalcopyrite Alteration   15

        2.2.3 Quartz-Sericite-Pyrite-
               Chalcopyrite Alteration   20

        2.2.4 Footwall Alteration   21

        2.2.5 Intermediate Tuffs and Intrusives   25

        2.2.6 Massive Magnetite   27

    2.3 Western Tharsis   28

    2.4 Cape Horn   31

        2.4.1 Introduction   31

        2.4.2 Pink Felsic Pyroclastics and Lavas   32

        2.4.3 Intermediates   33

        2.4.4 Ore Horizon: Chloritic Felsic Lavas
               and Grey Felsic Lavas   33

FIGURES.

1. INTRODUCTION TO THE MT. LYELL FIELD

The Mt. Lyell copper field is located near Queenstown in Western Tasmania and is one of a group of "volcanic" massive sulphide deposits occurring within the Mt. Read Volcanics. The field was discovered in 1883 when gold found in the Linda Valley led to the discovery of the Blow in 1884. By 1898 some 42 companies had been formed to explore and exploit the field. The Mt. Lyell Mining and Railway Company Limited began mining the Blow deposit in 1896. In 1903 the company merged with its major rival the North Lyell Company and by 1933 it had become the sole operator on the field.

1.1 The Mt. Read Volcanics

The Mt. Read Volcanics are of calc-alkaline type, predominantly rhyolitic and dacitic but with minor andesites and basalts (Spry, 1962; Solomon and Griffiths, 1974; White, 1976). The volcanics form the eastern part of a zone of Cambrian rocks bounded by the Precambrian rocks of the Tyennan Nucleus on the east and the Rocky Cape Region on the west (fig. 1.1). The western part of the trough is a sedimentary sequence of mudstones, greywacke and conglomerates.

In the Queenstown area the volcanics have been subdivided (Corbett *et al.*, 1974; fig. 1.2 and fig. 1.3) into (i) a central belt of lavas, (ii) a flanking belt of pyroclastics, the Queenstown Pyroclastics, and (iii) a late Cambrian sequence of volcanic and sedimentary rocks, the Tyndall Group, which unconformably overlies the central lavas and the Queenstown Pyroclastics. The central lava unit consists of massive pink potassic (Darwin) rhyolite, massive or flow banded feldspar and quartz porphyry lavas and minor pyroclastic
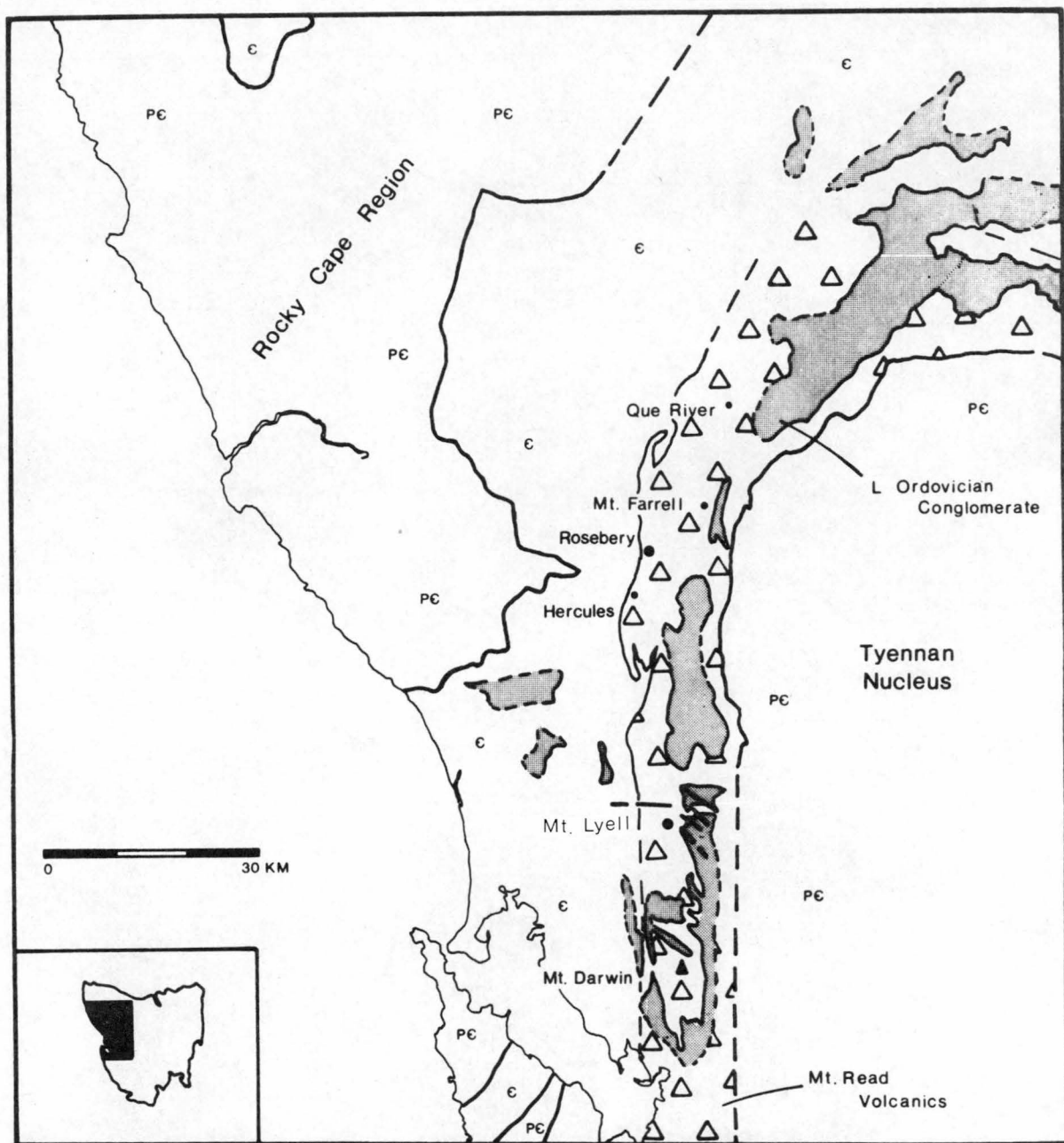
Fig. 1.1:   Generalised geological map of western Tasmania
showing the distribution of the Mt. Read Volcanics and the
locations of the major "volcanic" massive sulphide deposits.
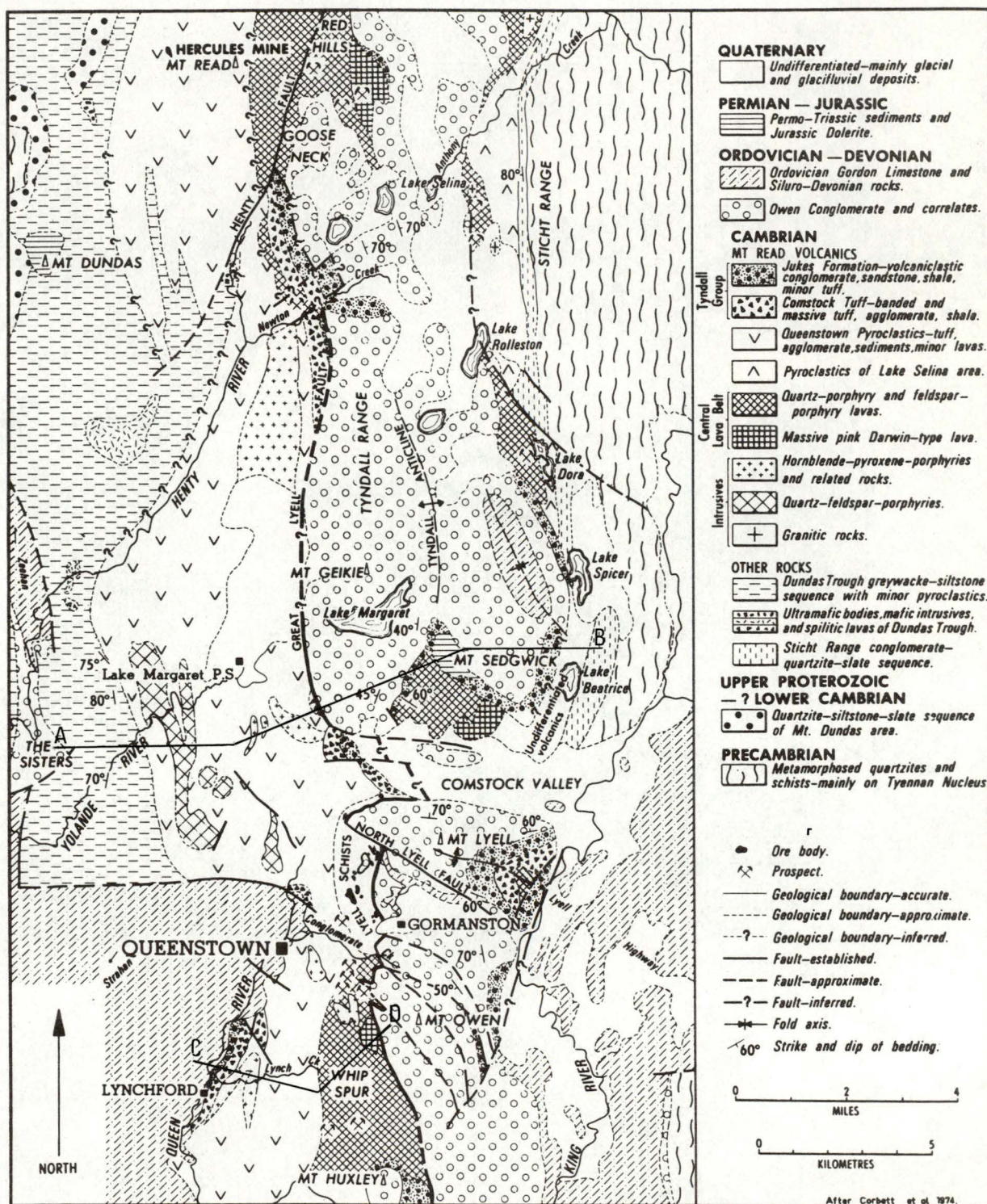
Fig. 1.2:   Geological map of the Queenstown-Red Hills
area showing the distribution of the main units of the
Mt. Read Volcanics (after Corbett et al., 1974; Reid, 1976).

WEST
A
The Sisters   YOLANDE RIVER   Crown Hill   GREAT LYELL FAULT   MT SEDGWICK   Lake Beatrice   EAST B

0   1   2 Kilometres
0   1 Miles
V = H

PRECAMBRIAN

CROSS SECTION A - B THROUGH MT SEDGWICK

Legend:

PERMO–TRIAS sediments, JURASSIC Dolerite.
SILURO–DEVONIAN Eldon Group.

ORDOVICIAN

Gordon Limestone
Owen Conglomerate.

CAMBRIAN

Jukes Formation. ⎫
Comstock Tuff. ⎬ Tyndall Group
Queenstown Pyroclastics.
Quartz–porphyry lavas
Feldspar–porphyry lavas.
Massive pink Darwin–type lava
Quartz–feldspar–porphyry intrusives
Hornblende–pyroxene–porphyry intrusives.
Lynch Creek "Basalts"
Sedimentary sequences of Yolande River and Lake Beatrice area

C
QUEEN RIVER   Miners Ridge   Whip Spur   MT OWEN   D

0   1   2 Kilometres
0   1 Mile
V = H

Sandstone

CROSS SECTION C - D THROUGH WHIP SPUR

Fig. 1.3:   Provisional E-W cross-sections through
Mt. Sedgwick and Whip Spur (after Corbett et al., 1974).
See Fig. 1.2 for locations of cross sections.

and sedimentary rocks. The unit extends south of Queenstown to the Jukes - Darwin area, where it has been called the Intercolonial Volcanics by White (1976). The Queenstown Pyroclastics consist of a variable sequence of felsic ashfall and ashflow pyroclastics, lavas and sedimentary units. Their relationship to the central lava unit is problematical.

The Tyndall Group consists of a basal unit of banded felsic tuffs, breccias and siltstones, the Comstock Tuff, and a conformable upper unit of volcanoclastic conglomerate and sandstone. A fossili-ferous limestone at the base of the Comstock Tuff at Comstock unconformably overlies mineralized volcanics. Marine fossils in the limestones provide a minimum Late Middle or Early Upper Cambrian age for the Mt. Lyell mineralization (Jago *et al.*, 1972). To the west the volcanics grade into a marine sequence of greywackes and siltstones. Quartz-feldspar porphyrys and hornblende - pyroxene porphyrys (basaltic andesites) intrude the Queenstown pyroclastics.

The identification of ignimbrites in the volcanic units studied in detail suggest a predominantly subaerial environment for the bulk of the Mt. Read volcanics (Solomon *et al.*, 1976; White, 1976). Sedimentary units within the volcanics lack features indicative of strong currents and suggest most sediments formed in shallow ephemeral lakes and lagoons (Solomon *et al.*, 1969; Corbett *et al.*, 1974).

1.2 Cambrian/Ordovician Relationships

Although the central lava belt appears to have formed a structural high throughout the Cambrian (Corbett *et al.*, 1974; White, 1976), active subsidence had begun east of the Great Lyell fault (The Lyell Shear) by the Late Cambrian. Owen Conglomerate, a siliceous conglomerate and quartz sandstone, deposited in an

WEST

QUEENSTOWN

WESTERN
COMSTOCK VALLEY

EASTERN
COMSTOCK VALLEY

EAST

Drill holes

COMSTOCK UNCONFORMITY

LYNCHFORD UNCONFORMITY

HAULAGE
UNCONFORMITY

GREAT LYELL FAULT

JUKESIAN
UNCONFORMITY

ORDOVICIAN

Gordon Limestone

OWEN CONGLOMERATE

Pioneer Beds

Main part of Owen

CAMBRIAN

TYNDALL GROUP

Jukes Formation

Comstock Tuff

Older volcanics
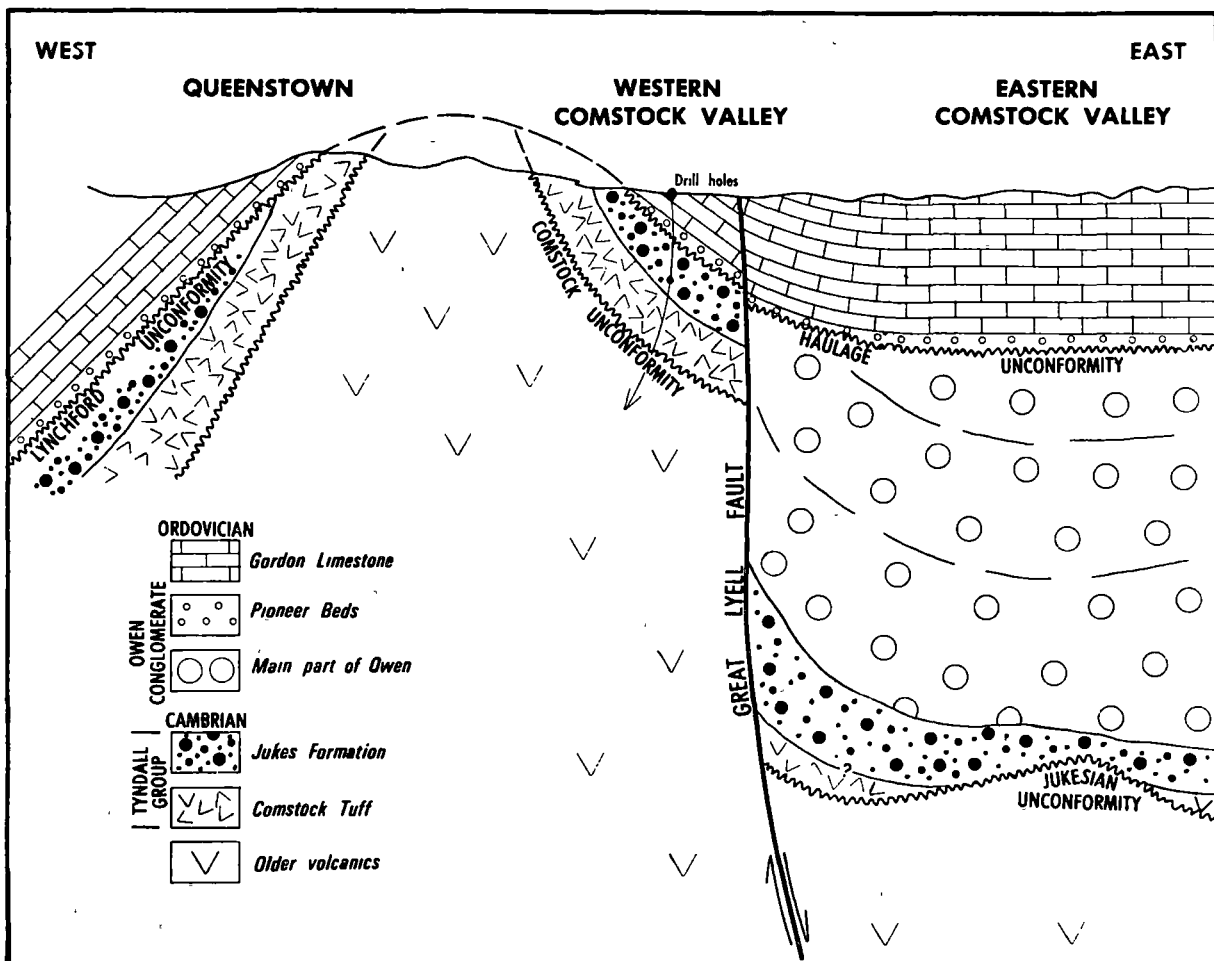
Fig. 1.4: Diagrammatic cross-section through Queenstown and the Comstock Valley showing relationships between various unconformities, Great Lyell Fault and Owen Conglomerate (after Corbett et al., 1974).

elongate basin bounded by the Great Lyell fault and the Tyennan

nucleus. The conglomerate consists almost entirely of Precambrian

detritus except near the fault where local detritus was shed off

the fault scarp.

In the Queenstown area the lower part of the Owen Conglomerate

and the Jukes Formation is either unconformable on the older

volcanics, representing the Jukesian Movement of Carey and Banks

(1954), or is conformable with the Comstock Tuff which is uncon-

formable on the older volcanics, the Comstock Unconformity (Corbett

et al., 1974).

The maximum thickness in the Owen Conglomerate (1200 m) was

developed in the mine area against the Great Lyell fault and this

possibly reflects early movement on E-W graben structures, the

Linda Disturbance, that developed in the Devonian (Solomon *et al.*,

1976; Solomon, 1976). Deposition of the Owen was restricted to

east of the Great Lyell fault until after the Haulage movement, a

local disturbance in the Queenstown area (Solomon, 1964; Solomon,

1969). Following the Haulage movement, marine sediments (the Pioneer

Beds, a characteristic unit of interbedded sandstones and mudstones

with abundant chromite at the base) transgressed the volcanics west

of the Great Lyell fault. West of the fault the Pioneer Beds uncon-

formably overlie both a reduced Tyndall Group sequence and in the

mine area mineralized volcanics (Corbett *et al.*, 1974; Reid, 1976).

The late Cambrian - early Ordovician relationships are summarised

in fig. 1.4.

The Pioneer Beds are conformably overlain by the Ordovician

Gordon Limestone which is succeeded conformably by Siluro-Devonian

interbedded sandstones and mudstones, the Eldon Group. The sediments

are shallow marine deposits reflecting an unstable shelf environment

that persisted from the Upper Ordovician through to the Lower Devonian.

1.3 The Tabberabberan Orogeny

A phase of Devonian deformation, the Tabberabberan Orogeny, is
recorded throughout Tasmania. In western Tasmania it involved an
early phase of N-S trending folds developed by E-W compression
against the stable Tyennan nucleus and a later phase of N-W trending
folds and associated faulting (Carey, 1953; Solomon, 1962; Williams
et al., 1976).

The effect of the Tabberabberan movement on the Mt. Lyell area
has been discussed on numerous occasions (Wade and Solomon, 1958;
Solomon and Elms, 1965; Solomon, 1964; Reid, 1976). The principal
structure is an overturned, east facing, N-S trending anticlinorium.
The eastern limb of the structure is defined by the steeply west
dipping and faulted Owen Conglomerate contact, the reactivated
Great Lyell fault. The complexity of the fault surface in the mine
area results in part from the imposition of E-W crossfolding and
faulting visible in the Owen Conglomerate (figs. 1.2 and 1.5) on
the N-S structure. The E-W faulting, the Linda Disturbance, produced
small-scale horst and graben structures, the Linda and Comstock
valleys forming the principal grabens. Cleavage development is
pronounced in the mineralized and altered volcanics. Cleavage trends
tend to be parallel or sub-parallel to the Owen Conglomerate contact
and dip steeply southwest. West of the contact zone a northwest
trend is predominant. The obvious folding and faulting in the
competent Owen Conglomerate is less evident in the volcanics and the
movement appears to be largely dissipated in movement on the cleavage
and in faulting. The dominant fault trend is north-northwest with
variable dips to the southwest and northeast.

The Tharsis Schist Trough, a trough of volcanics extending from
the North Lyell - Crown Lyell area in the north to the Blow in the

south and bounded on the west in the North Lyell - Lyell Tharsis

area by an outlier of Owen Conglomerate, the Tharsis Ridge, is thought

to have had its origins in Haulage Unconformity times. Solomon

(1964, 1969) has suggested that slumping off the Great Lyell fault

scarp resulted in a wedge of volcanics locally overlying the Lower

Owen Conglomerate. Thrusting along the Great Lyell fault during the

Tabberabberan Orogeny upturned the Lower Owen Conglomerate against

the fault completing the formation of the trough structure (fig. 1.6).

1.4 The Lyell Schists

Although the volcanics in the mine area have been extensively

altered and cleaved producing the "Lyell Schists" (Wade and Solomon,

1958; fig. 1.2) recent work (Corbett *et al.*, 1974; Reid, 1976; White,

1976) suggest the major units of the volcanic stratigraphy in the

Queenstown area can be traced through the schist zone.

The host unit for the mineralization, a sequence of felsic lavas

and pyroclastics (fig. 1.5), including flowbanded and auto-brecciated

lavas, lappilli tuffs and ignimbrites, form part of the central laval

belt.   The Queenstown Pyroclastics in the mine area are represented

by a sequence of coarse pyroclastics of intermediate to felsic

composition. They include volcanic breccias, lappilli and ignimbritic

tuffs. In the western part of the field the pyroclastics interfinger

with a sequence of siltstones, crystal lithic tuffs and subaqueous

tuffs (fig. 1.5). The contact between the pyroclastics and the

mineralized felsic volcanics is well defined north of the West Lyell

opencut (Prince Lyell, A lens, Royal Tharsis) through to the hanging

wall of the Cape Horn orebody. The situation is less clear west of

the Prince Lyell orebody, the difficulties being compounded by the

West Lyell dumps. Intermediate and felsic pyroclastics occur in the

hanging wall of Prince Lyell.
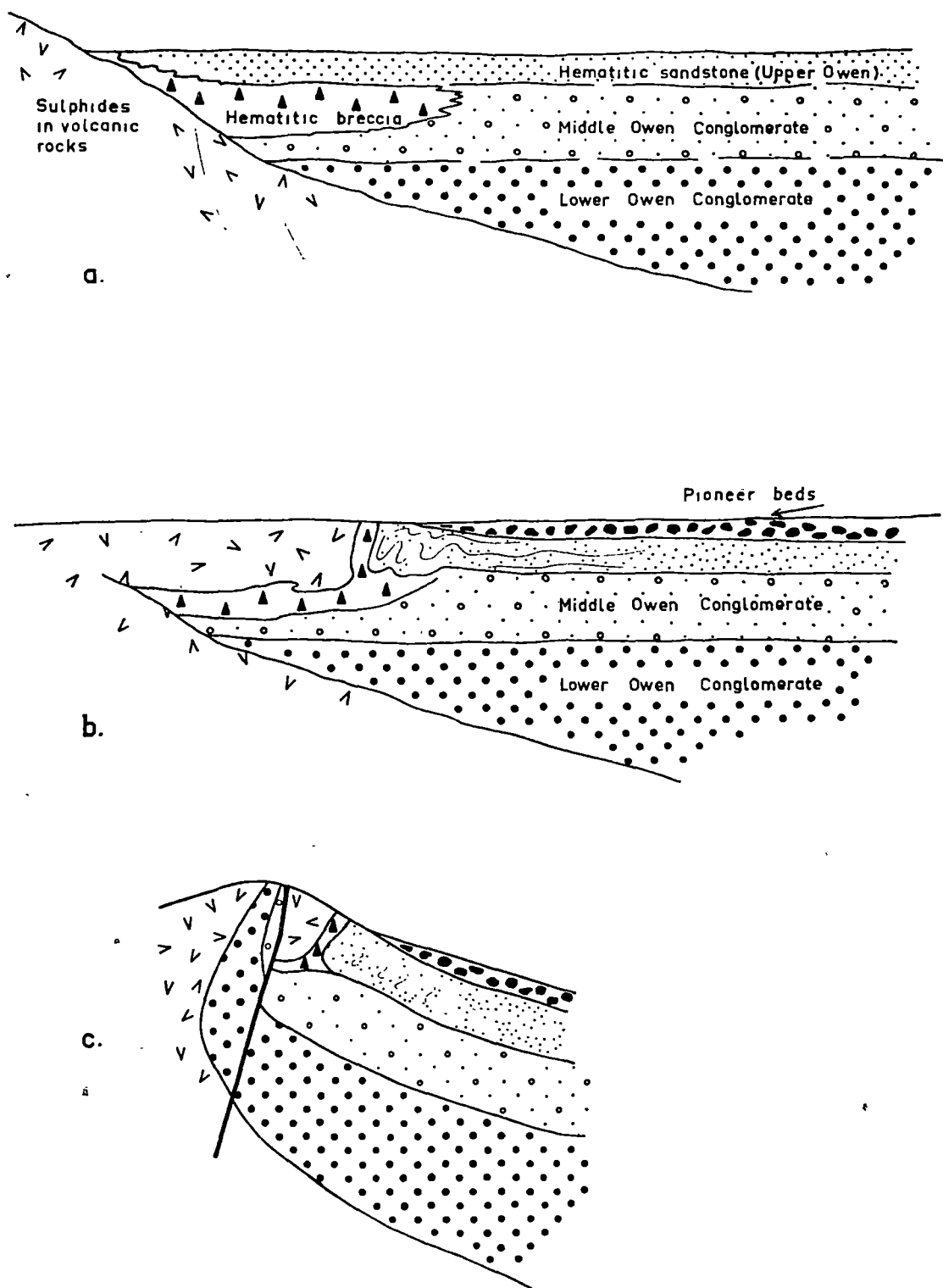
Fig. 1.6:   Suggested sequence of events leading to the
formation of the Tharsis Schist Trough (E-W cross-sections).
(a)   During Upper Owen deposition.
(b)   During deposition of the Pioneer Beds.
(c)   Following the Tabberabberan Orogeny.

(after Solomon, 1969)

Intermediate intrusives and lavas (?) are volumetrically important in the pyroclastic sequence (fig. 1.5). Mafic dykes, probably with an extrusive component, intrude the felsic lava sequence south of the West Lyell open cut and one unit has been mapped in the hanging wall of Prince Lyell.

The hydrothermal alteration and Tabberabberan deformation of the "Lyell Schists" has reduced most of the rocks to a greenschist assemblage of quartz-sericite-chlorite-siderite-hematite-magnetite-pyrite. Macroscopic features, such as flow banding, brecciation, fiamme structures, may be observed on suitably weathered outcrop surfaces but most microscopic textures of the original rock have been obliterated. Feldspar and ferromagnesian phenocrysts are sericitised and chloritised respectively and commonly occur as sericite and chlorite flecks in the cleavage. In thin section the rocks generally consist of fine quartz aggregrates in a quartz-sericite-chlorite matrix. The felsic rocks commonly contain relict partially resorbed quartz phenocrysts. Feldspar phenocrysts occur rarely.

A comparative study of the chemistry of the Lyell Schists and the Mt. Read Volcanics (Solomon, pers. comm.) indicated the principal changes during alteration involved loss of aluminium, alkalies, particularly sodium and calcium, and addition of water and some carbon dioxide. The silica content and the stable trace elements, particularly the vanadium/scandium ratio, are generally consistent indicators of the general classification of the original rock, i.e. basalt-andesite, dacite or rhyolite.

1.5 Mineralization

Mineralization in the Mt. Read Volcanics conveniently divides into two districts; a Zn-Pb-Cu district centred on the massive sulphide

deposits of Rosebery, Hercules, Mt. Farrell(?) and the newly dis-
covered Que River deposit, and a Cu district centred on Mt. Lyell
(fig. 1.1).

The Mt. Lyell field consists of 15 deposits, principally of
disseminated pyrite-chalcopyrite mineralization in altered felsic
volcanics but also including bornite-chalcopyrite mineralization
in silicified volcanics and cherts, massive pyrite-chalcopyrite,
and minor massive pyrite-sphalerite-galena-chalcopyrite mineraliza-
tion. The field also includes a number of zones of disseminated
pyrite mineralization with minor chalcopyrite.

Production figures and reserves up until June 1974 for the
copper ore bodies are given by Reid (1976). Current production is
principally from disseminated pyrite-chalcopyrite deposits, the
Prince Lyell mine being the largest and most important of this group.

Although Mt. Lyell is the only operating copper mine in the
district there are numerous copper prospects particularly in the
20 km south of Mt. Lyell. All of the deposits occur within the
Intercolonial volcanics, a correlate of the Central Lava Belt (White,
1976). They have a N-S linear distribution which includes Mt. Lyell
as the northernmost deposit. Some of the prospects are similar to
parts of the Mt. Lyell mineralization consisting of disseminated
pyrite-minor chalcopyrite mineralization, but most prospects consist
of oxide, oxide-copper sulphide and oxide-silicate assemblages (White,
1976).

A number of prospects occur to the north of Mt. Lyell and these
are also dominantly sulphide-oxide (Lake Selina) or oxide (Red Hills)
assemblages. Both Red Hills and Lake Selina prospects occur within
the Central Lava Belt.

1.6 Previous Research on the Lyell Ores

Comprehension of the Mt. Lyell ores has evolved over many years through the efforts of a large number of workers. Gregory (1905) considered the Mt. Lyell ores to be hydrothermal replacement deposits of Devonian age and this concept was maintained by later workers, Hills (1927); Nye *et al.* (1934); Edwards (1939); Conolly (1947); Carey (1953); Bradley (1954, 1956, 1957); Solomon (1957) and Solomon and Wade (1958). A Cambrian component to the mineralization was first suggested by Hall and Solomon (1962) and amplified by Solomon (1964) and Solomon and Elms (1965). A full transition to a Cambrian age for the mineralization has been made in the last 10 years. Work by Solomon (1967, 1969); Markham (1968); Jago *et al.* (1972); Green (1971); Walshe (1971); Corbett *et al.* (1974); Reid (1976); White (1976); Bryant (1976) has tended to link the mineralization to the volcanism.

Markham's comprehensive study emphasised the deformed nature of the ores and he gives a full account of deformation, recrystallisation and remobilisation phenomena. He considered the depositional locations of the disseminated ores were lithologically controlled, with certain units such as brecciated lavas and fragmental tuffs providing favourable sites. A similar view has been adopted by MacDonald (1968) and later mine geologists, Reid (1976).

The ore mineralogy and textures have been described by Edwards (1939), Markham (1963, 1968) with additional work by Green (1971) and Bryant (1976).

Principal geochemical studies have been whole rock analysis of altered volcanics and silicate mineral analysis (Solomon, 1964), trace element analysis of the Prince Lyell and 12 West ores (Hendry, 1972), trace cobalt, nickel and selenium analysis of sulphides

(Loftus-Hills and Solomon, 1967; Loftus-Hills, 1968; Walshe, 1971) and sulphur and oxygen isotope studies (Solomon *et al.*, 1969).

1.7 The Genesis of Mt. Lyell ores

Recent workers, e.g. Solomon (1967, 1976), Markham (1968), Green (1971), Walshe (1971), Reid (1976) have favoured a combined epi-genetic and syngenetic volcanic exhalative origin for the Mt. Lyell ores. A reconstruction by Solomon (1976) and fig. 1.7 suggests a partially subaerial environment, consistent with the regional environment. The disseminated py-ccp deposits form by replacement of the volcanics as solutions disperse along permeable horizons, massive lenses deposit where solutions flow onto the seafloor and the bn-ccp deposits form in a terrestrial environment associated with sinter deposits around a volcanic fumarole.

The Mt. Lyell ore deposits occur at the intersection of prominent N-S and E-W faults. If, as inferred by Solomon, the faults in the mine area predate the deposition of the Owen Conglomerate then they may well have been active during the time of the formation of the Mt. Lyell ore deposits. It seems likely they would have acted as channels for solution movement, thereby controlling the regional location of the field.

Solomon (1976) has suggested the mineralizing solutions were generated by circulating seawater leaching the volcanic pile (the geothermal or convection model). Hence the base metal content of the solutions would reflect the overall composition of the volcanic pile and the conditions of leaching. The sulphur content of the solutions would be a combination of residual reduced seawater sulphate and igneous sulphur (Solomon, 1972, 1976; Walshe, 1971).

If the discharge rates for the convecting cell are low or if the
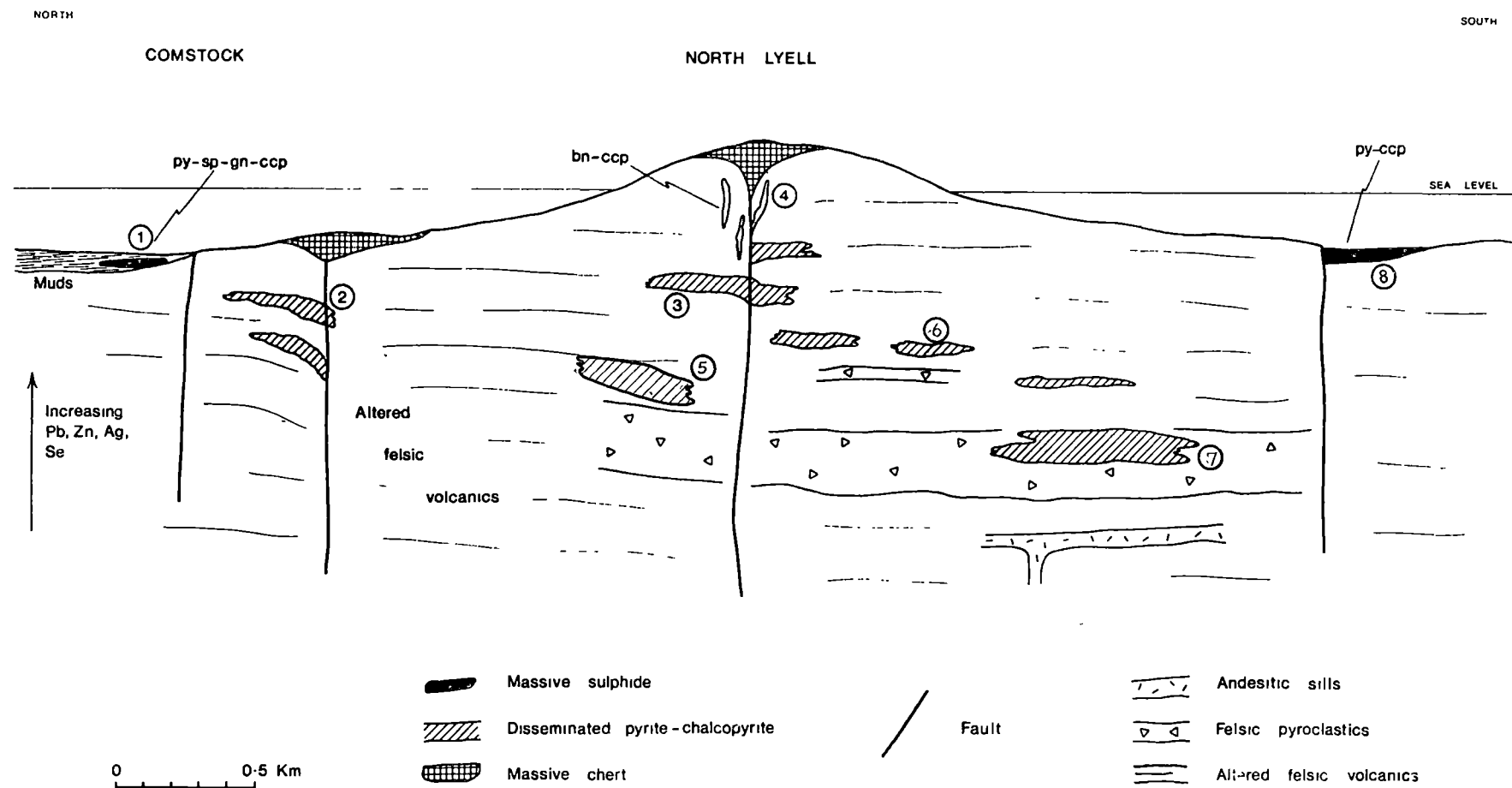
Fig. 1.7:   Speculative N-S cross-section of the Mt. Lyell
field at the time of mineralisation, allowing for 25% shortening.
Numbers refer to the following ore bodies: 1 = Tasman and Crown
Lyell; 2 = Comstock; 3 = Crown Lyell; 4 = North Lyell; 5 = Cape
Horn, 6 = Royal Tharsis; 7 = Prince Lyell; 8 = Blow (or Mt. Lyell).
Diagram from Solomon (1976).

rising solutions meet an impermeable layer (e.g. the ground/air interface) then the column of solution will mushroom out giving rise to secondary convection cells.   Solomon (1976) suggests that such secondary circulation cells might have given rise to the cluster of deposits and the wide alteration zone observed at Mt. Lyell.

1.8 Background to the present study

The present study is an attempt to develop some understanding of the chemical constraints active during the formation of the Mt. Lyell deposits and if possible to draw some conclusions about the initial chemistry of the mineralizing solutions.   Because of the deformation, direct information about the mineralizing fluids normally available from fluids inclusions (e.g. the salinity and temperature of the solutions) has been lost.   Even so, since the ores have undergone only lower greenschist metamorphism and most of the initial assemblages remain, much can be done to define the initial conditions of deposition.   An important background point is the recognition that the Mt. Lyell deposits belong to the massive sulphide or volcanogenic sulphide group of depositions, albeit of a somewhat different style.   If this is correct, it means useful analogies may be drawn from other massive sulphides in volcanic terrains, e.g. the Kuroko Deposits.

Because Mt. Lyell has been much studied it is impossible to avoid overlap with previous work and this is particularly true of the descriptive work.   However, as the mineralogy forms the basis for later geochemical discussion it has been described in some detail. However, the focus of the descriptive work has been altered so as to emphasise the types of mineral assemblages associated with the sulphides.   Interest in the geochemistry has centred on extending the

trace element and sulphur isotope studies of earlier workers.

1.9 The Lake Selina Prospect

In addition to the work at Mt. Lyell, a parallel study of the
Lake Selina prospect, 20 km north of Queenstown, was undertaken.
The aim of the study was to establish some understanding of the
genesis of the prospect by evaluating the similarities and
differences with the Mt. Lyell mineralization. Details of the
work are given in appendix D.

2. DESCRIPTION OF THE MT. LYELL MINERALIZATION

2.1 Introduction

The mineralization types are generally subdivided as follows:

(1) Disseminated pyrite-chalcopyrite.

Prince Lyell, "A" Lens, Royal Tharsis, Cape Horn, Crown

Lyell No. 1 and 3, Lyell Tharsis (in part) and Western Tharsis.

(2) Bornite - chalcopyrite.

North Lyell, Crown Lyell No. 2, 12 West, Lyell Tharsis (in

part), Lyell Comstock (in part).

(3) Massive pyrite-chalcopyrite.

The Blow (Mt. Lyell orebody).

(4) Massive pyrite-galena-sphalerite-chalcopyrite.

Tasman and Crown Lyell Extended and Lyell Comstock (open cut).

The ores have been described on numerous occasions; Edwards (1939),

MacDonald (1968), Markham (1968), Green (1971), Hendry (1972), Reid

(1976). MacDonald and Markham gave detailed attention to the mapping

and description of the mineral assemblages of the Prince Lyell-"A" Lens

mineralized zone. The present study is essentially concerned with the

disseminated pyrite-chalcopyrite mineralization. It is an extension

of the work of Markham and MacDonald and was undertaken in collaboration

with the Mt. Lyell mine geologists.

The ore outlines of the disseminated pyrite-chalcopyrite mineraliza-

tion are lenticular and generally concordant with the cleavage and the

general layering of the volcanic rocks. The host rocks are principally

felsic but some intermediate/mafic rocks are present in the Prince Lyell

and Cape Horn orebodies.

In this study the rocks have been classified on the basis of

original host-rock composition and the alteration assemblage. The

alteration assemblage types have been grouped on the basis of the relative abundance of the sulphides, oxides, and silicates. This grouping is purely descriptive and does not indicate whether the assemblage originated from Cambrian mineralization and hydrothermal alteration and/or later metamorphism.

The mineralization of Prince Lyell-"A" Lens, Cape Horn, and Western Tharsis may be subdivided into four common assemblage types:

(i)   Quartz - sericite - pyrite ± chalcopyrite alteration of a felsic host with minor bornite, carbonate and barite (e.g. Western Tharsis).

(ii)   Quartz-sericite-chlorite-pyrite-chalcopyrite alteration of a felsic host. Minor carbonate and hematite is usually present. Hematite and magnetite may be locally dominant (e.g. Prince Lyell).

(iii)   Quartz-chlorite-sericite-hematite-magnetite-pyrite alteration of an intermediate host.

(iv)   Quartz-sericite-pyrite-hematite-minor chlorite-carbonate alteration of a felsic host (e.g. footwall of Prince Lyell).

The Crown Lyell-North Lyell Ores (the chert ores) are generally much more siliceous, with a lower silicate content, the exceptions being the chlorite rich assemblage beneath and on the footwall of Crown Lyell No. 3, Crown Lyell No. 1, and Lyell Tharsis.
The assemblage types are:

(i)   Quartz-pyrite-chalcopyrite-minor sericite and bornite. Crown Lyell No. 3.

(ii)   Quartz-bornite-chalcopyrite-pyrite-sericite-minor pyrophyllite. North Lyell, Crown Lyell No. 2, 12 West.

(iii)   Quartz-chlorite-minor sericite-pyrite-chalcopyrite-magnetite-hematite-barite.   Beneath and on the footwall of Crown Lyell No. 3, Crown Lyell No. 1, Lyell Tharsis.
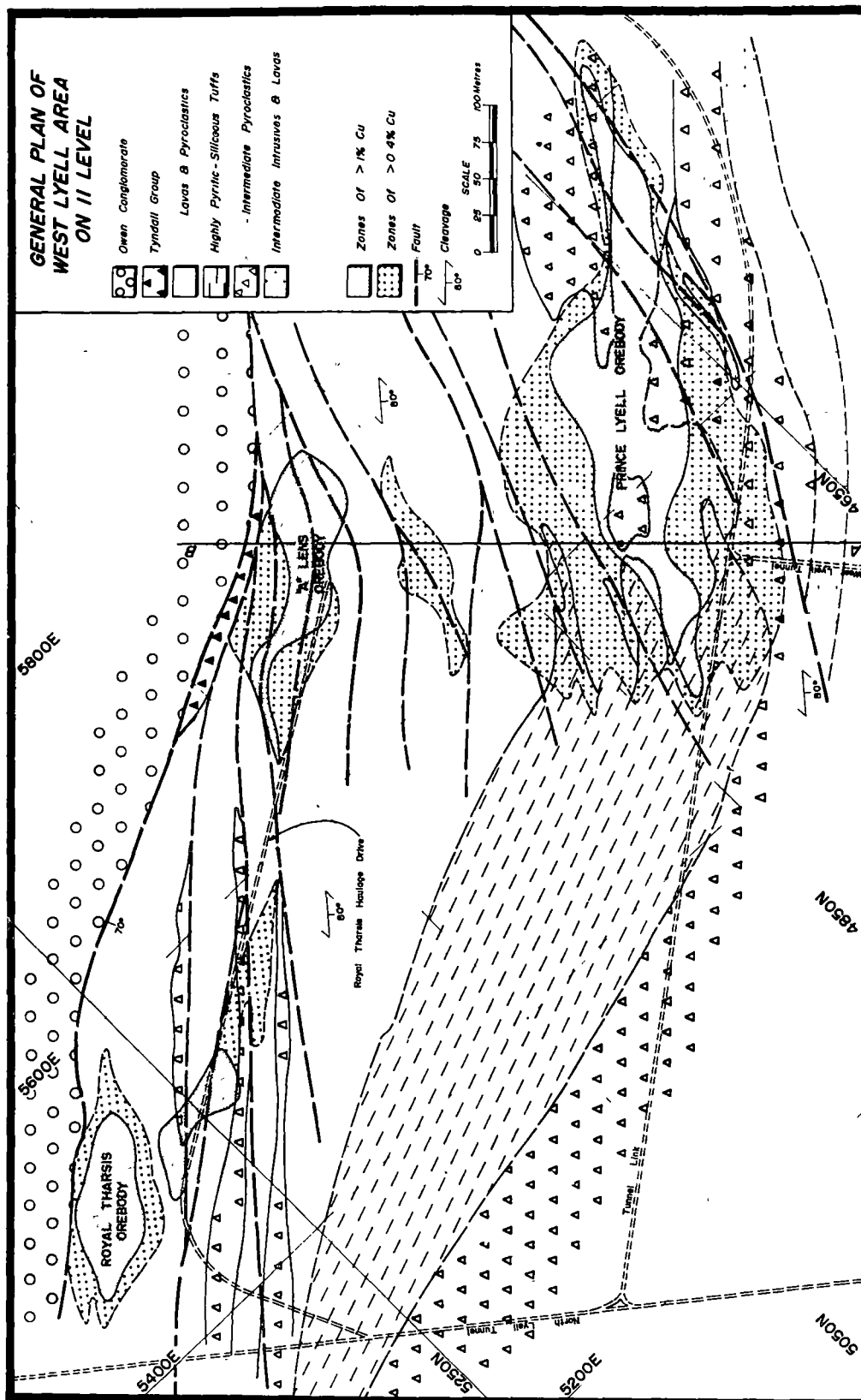
Fig. 2.1: Generalised plan of the West Lyell area, showing the Prince Lyell, "A" Lens and Royal Tharsis orebodies on 11 Lyell (after Reid, 1976).
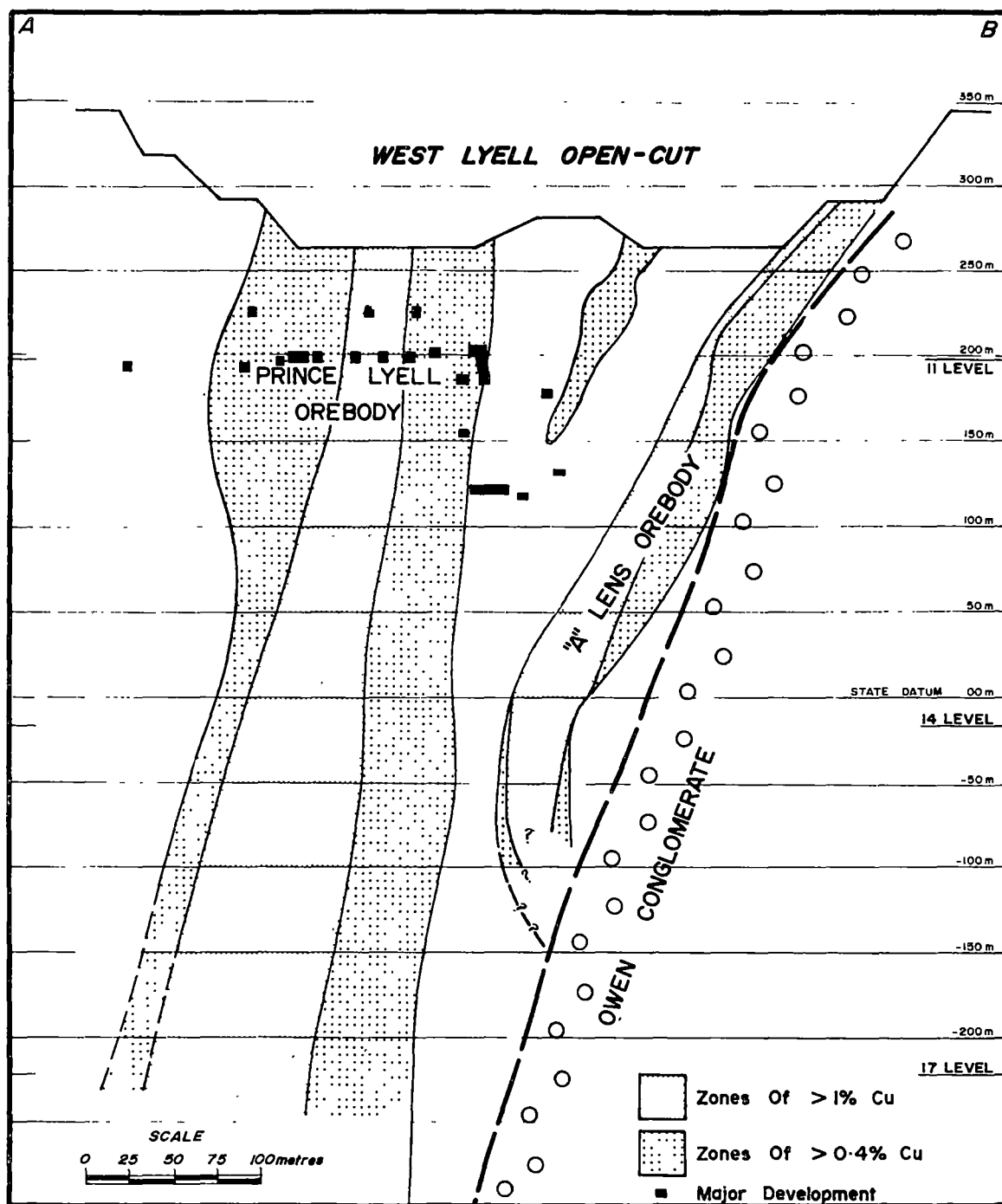
Fig. 2.2: Cross-section through the Prince Lyell and "A" Lens orebodies, looking north (after Reid, 1976).

For the purposes of description each zone of mineralization will

be considered separately. Subdivisions within each zone will be on

the basis of the classification given above. Changes in alteration

assemblages may coincide with the footwall or hanging wall limits

of an orebody (defined by a certain cut-off grade of copper). In

such circumstances a particular assemblage may be simply referred to

by its structural position relative to the orebody, i.e. the footwall

assemblage or the hanging wall assemblage.

2.2 Prince Lyell

2.2.1 Introduction

Prince Lyell is part of the West Lyell group of deposits

(Prince Lyell, "A" Lens, Royal Tharsis and Razorback) and is

the largest deposit on the field. The dimensions, defined by

0.4 percent copper cut off, are 400 metres strike length and

variable width of 50 to 180 metres. A central core (fig. 2.1,

2.2) of higher grade copper, better than 0.8 percent and up

to 3-4 percent, 360 metres long and 10 to 95 metres wide

essentially defines the Prince Lyell orebody (Reid, 1976).

The central core of the orebody consists of fragmental felsic

volcanics which have been altered to a characteristic assemblage

of quartz-sericite-chlorite-pyrite-chalcopyrite. However, in

part the orebody overlaps into the hanging wall intermediates

and the footwall massive pink rhyolites (figs. 2.3, 2.4). To

the north the orebody gives way to highly pyritic and quartz-

sericite altered felsic tuffs and lavas. The quartz-sericite-

pyrite assemblage has only weak chalcopyrite mineralization

although grades remain high in the transition zone between it

and the quartz-sericite-chlorite-pyrite-chalcopyrite assemblage

Fig. 2.3   Geological plan of Prince Lyell.

830' level plan.
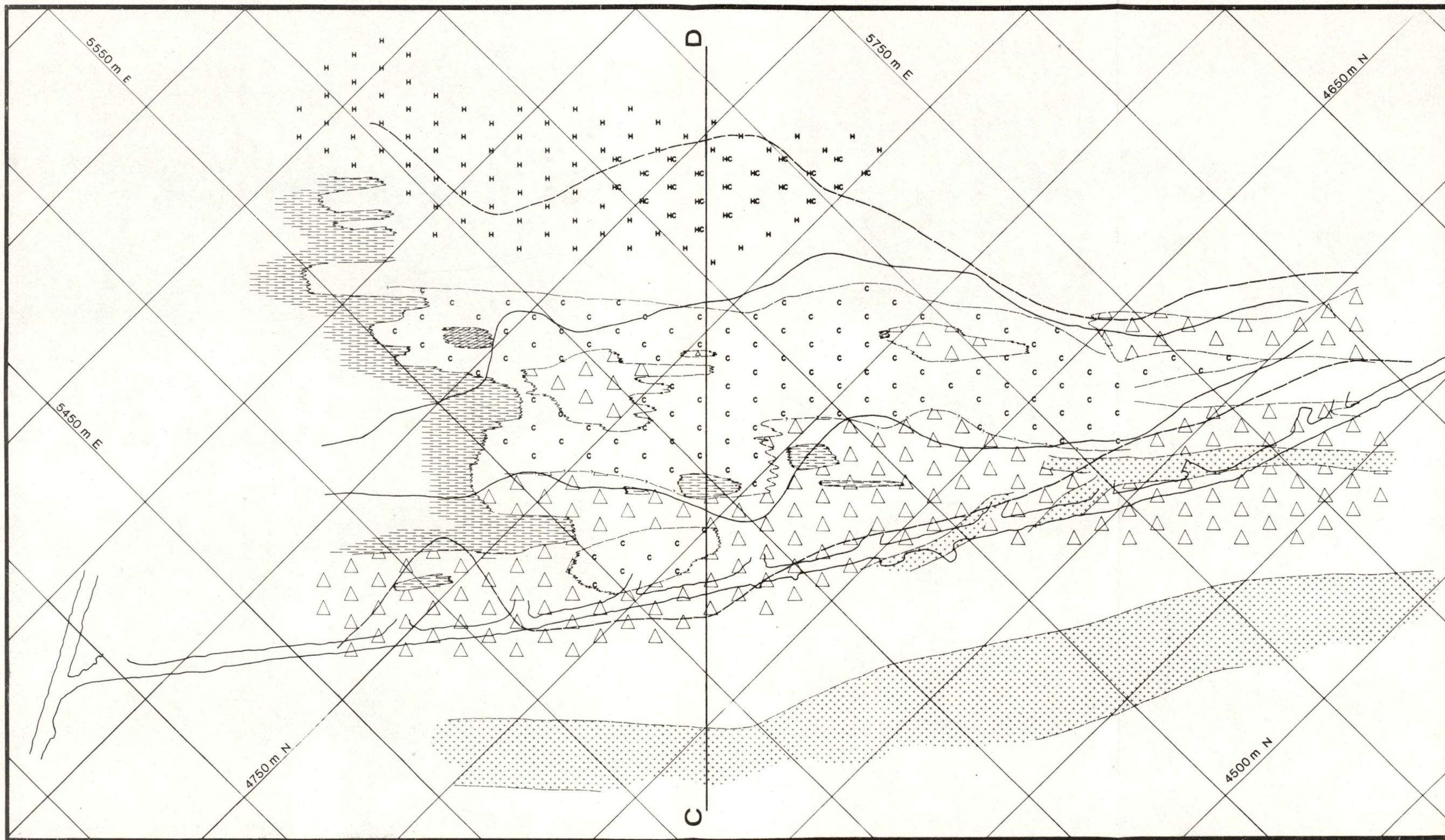
Fig. 2.4 Geological cross-section through Prince
Lyell and "A" lens orebodies.

D

C

830' Level

11 Level

Massive pink rhyolite

Massive pink rhyolite

Massive grey rhyolite

0   100'   200'
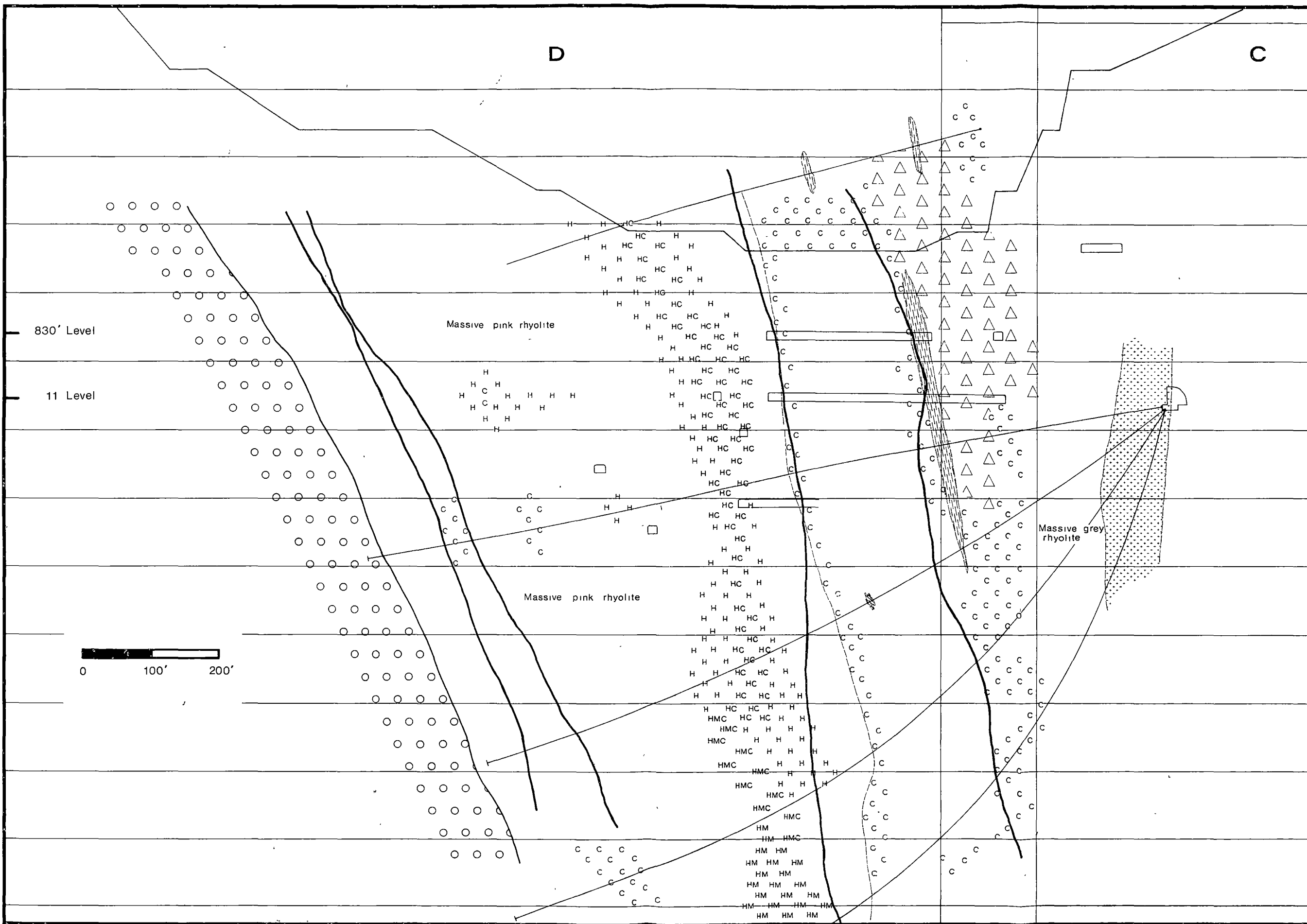
KEY TO FIGURES 2.3 and 2.4.
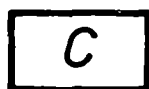
| C | Felsic volcanics. Quartz-chlorite-sericite-pyrite-chalcopyrite alteration. |

| HC | Felsic volcanics. Hematite-chlorite alteration. |

| HMC | Felsic volcanics. Hematite-magnetite-chlorite alteration. |

| HM | Felsic volcanics. Hematite-magnetite alteration. |
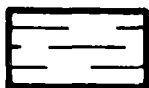
Felsic volcanics. Quartz-sericite-pyrite-chalcopyrite alteration.

Intermediate and mafic volcanics. Quartz-sericite-chlorite-hematite/magnetite-pyrite-chalcopyrite alteration.
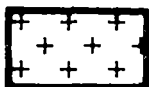
Mafic intrusive.
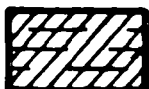
Massive magnetite with chlorite.

Owen Conglomerate.

of the central core of Prince Lyell.

2.2.2 Quartz-Sericite-Chlorite-Pyrite-Chalcopyrite Alteration

This assemblage forms the central core of Prince Lyell mineralization and is also the main type for "A" Lens and Royal Tharsis. For Prince Lyell chlorite averages 15 to 18 weight percent, pyrite 10 and chalcopyrite 3. [1] The proportion of sericite varies from 17 to 28 weight percent. Minor amounts of carbonate, generally less than 1 weight percent, and hematite are present. The averaged compositions of sericite, chlorite and carbonate are given below: [2]

	No. of samples
Sericite $K_{1.81} Fe_{0.37}Mg_{0.3}Ti_{0.04}Al_{5.09}Si_{6.36}O_{20} (OH)_4$	16
Chlorite $Mg_{2.91}Fe_{6.41}Mn_{0.05}Al_{5.68}Si_{5.02}O_{20} (OH)_6$	34
Siderite $Ca_{0.02}Fe_{1.42}Mg_{0.35}Mn_{0.14}(CO_3)_2$	18

Sericite has a $2M_1$ structure (Solomon, 1964). Texturally the rocks are highly variable but the common type is a "fragmental" rock (MacDonald, 1968) consisting of grey or pink siliceous fragments in a green, chlorite-sericite matrix (samples 45728, 45747, 45763, plates 2.1, 2.2, 2.3). Fragments are irregular in shape and size but are generally rounded with a mean size range of 10-25 mm. Coarse fragmentals may contain fragments up to 70 mm in size. Fine-grained fragmentals containing 1-2 mm sized quartz granules grade into chloritic tuffs. The amount of matrix is variable. It may be present as

1   For details see fig. 6.9 and footnote in chapter 6.

2   Based on probe data obtained from the School of Earth Sciences, Canberra.

only minor clots of chlorite and sulphides or it may be

locally dominant. The fragmental texture probably reflects

an original brecciated rhyolite or coarse pyroclastic host,

the texture being accentuated by later deformation. In some

cases the matrix forms planar structures suggestive of fiamme

(sample 45742, plate 2.4) which would indicate some ash-flow

component in the host rocks. Some minor units of undoubted

tuff or reworked tuff material are present (samples 45730,

45755, plate 2.5).

Sulphides occur as disseminations in the matrix (plate 2.2,

2.3) or less commonly as bands of massive pyrite and chalco-

pyrite (plate 2.6) or as minor veinlets (plate 2.1). The

massive bands are generally conformable with the cleavage and

the broad stratification in the volcanics. The cleavage intersects

the veinlets at a variable but commonly high angles. Sulphides

and silicates show classic deformation textures particularly

in sections cut parallel to the cleavage. Pyrite is commonly

fractured and drawn out along the cleavage, quartz and chalco-

pyrite are recrystallised in pressure shadows against the

fractured pyrite grains and the chalcopyrite smeared out along

the cleavage (sample 45735, plate 2.7). In thin section the

siliceous fragments consist of a fine-grained mozaic of quartz

with minor sericite. A characteristic granular texture is

present (sections 45739, 45751, 45763, plate 2.8, 2.9). White

(1976) has described the development of micropoikilitic or

"snow flake" textures in the Intercolonial Volcanics and by

analogy it is suggested the granular texture represents a

recrystallised "snowflake" texture. In part the granular

structure may be more open allowing a higher sericite matrix

plate 2.1: Siliceous fragmental texture with chloritic matrix and disseminated pyrite and chalcopyrite. Chalcopyrite occurs in the pressure shadows against the fractured pyrite grains. specimen 45728.

plate 2.2: Siliceous fragmental texture with chloritic matrix
and disseminated pyrite and chalcopyrite.
specimen 45747.

plate 2.3: Coarse grained siliceous fragmental with chloritic
matrix and disseminated pyrite and chalcopyrite.
specimen 45763.

plate 2.4: The chloritic matrix forming planar structures
within a siliceous fragmental.
specimen 45742.

VELOS 18

VELOS 18

plate 2.5: A tuffaceous lens within a siliceous,

chloritic fragmental. specimen 45755.

plate 2.6: Massive band of pyrite and chalcopyrite within
a siliceous, chloritic fragmental.
specimen 45753.

plate 2.7: Sulphide lenses, in a chlorite rich matrix,
showing typical deformation textures.
Fractured pyrite porphyroblasts, recrystallised
pyrite, and fine smears of chalcopyrite in the
cleavage. specimen 45735.
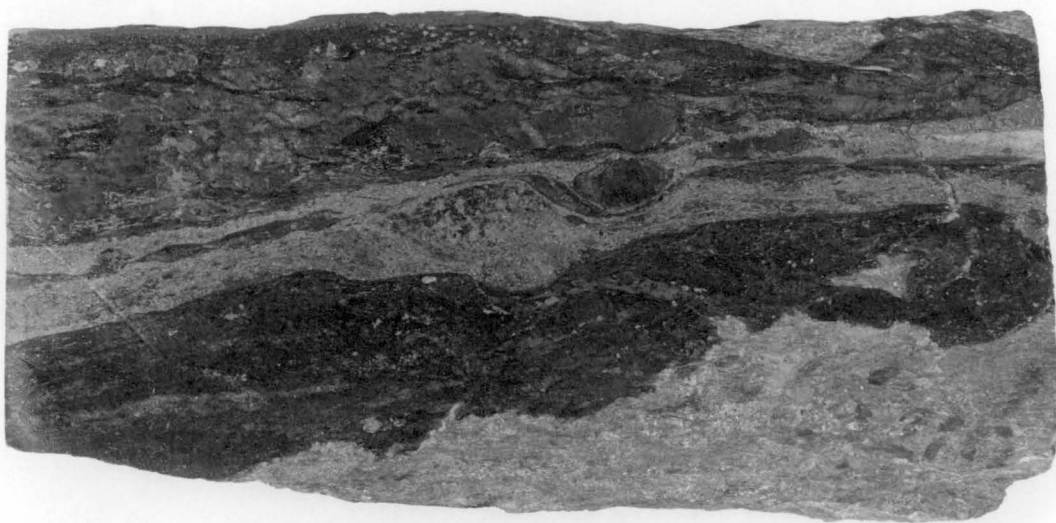
plate 2.8: The fine-grained granular texture present in the
groundmass of the siliceous fragments. The
texture probably represents recrystallised
"snowflake texture".
specimen 45739; magnification x30.

plate 2.9: As for 2.8.
specimen 45739; magnification x30.
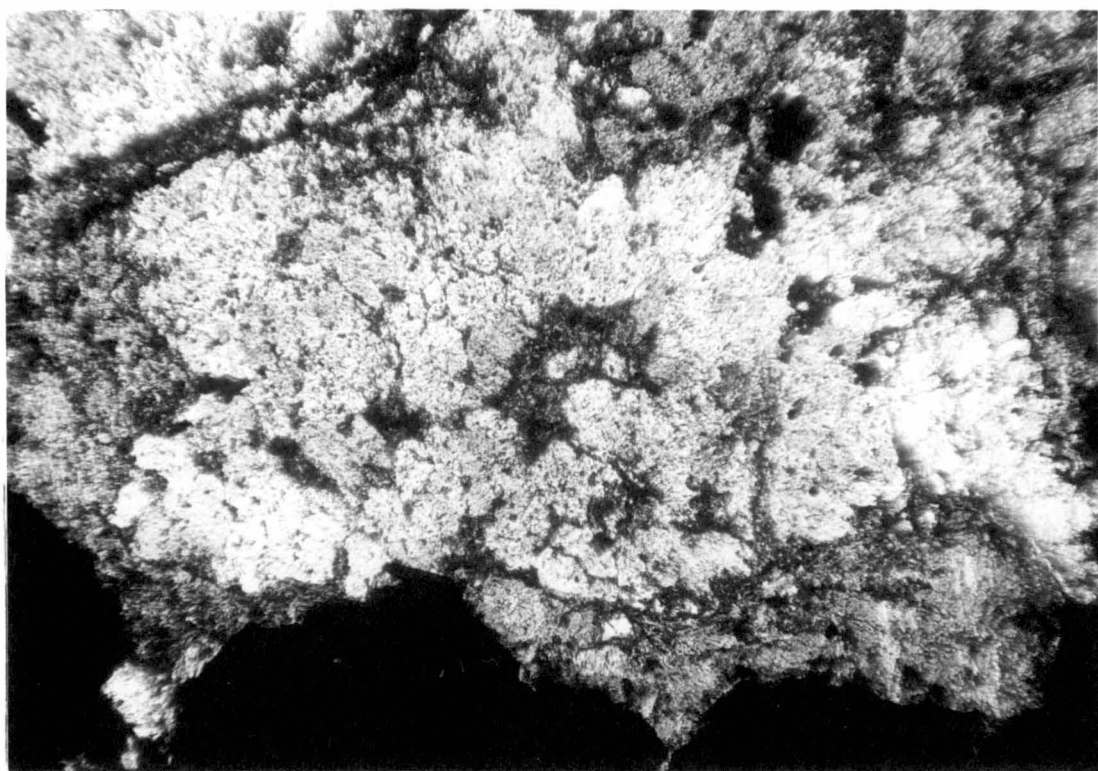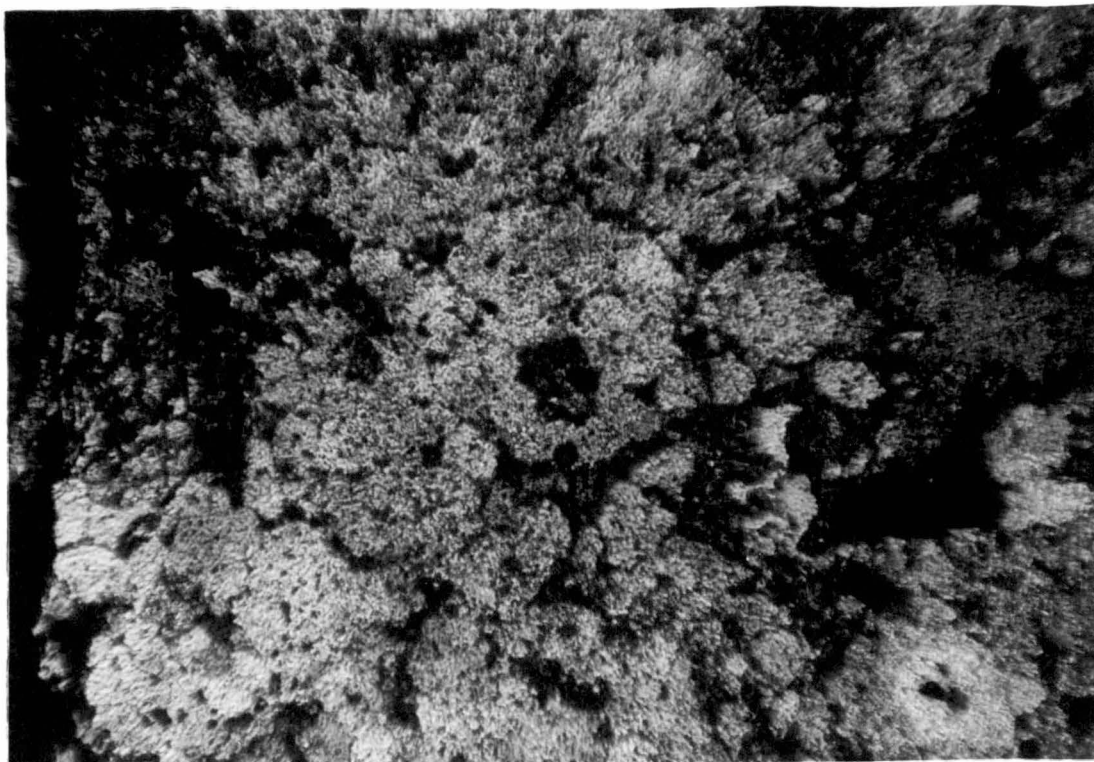
component (section 45754). Relict resorbed quartz phenocrysts occur, commonly with overgrowths, and are taken to imply an original rhyolite or possibly dacite composition for the host rocks (Markham, 1968). Sericite clots, although deformed, give the impression of altered feldspars. Siderite is common occurring as discrete rhombs or small clusters of rhombs. Minor chlorite and sulphide may be present. The matrix in thin section is composed essentially of sericite and chlorite with chlorite tending to form clots or lenses within a sericite framework. There is a marked tendency for pyrite and chalcopyrite to be associated with the chloritic clots (sections 45755, 45767). The clots, although irregular in shape, appear to be flattened in the cleavage (section 45766). Apatite, zircon, rutile, monazite and rare barite occur as accessary minerals (Markham, 1968). Apatite may locally constitute 25 percent of the matrix. The grains are generally rectangular in outline, ranging from 0.02 to 0.4 mm in size. They have a characteristic low birefringence which Hendry (1972) suggests indicates a high carbonate content. Typically, apatites contain large numbers of inclusions of chlorite, carbonate, zircon, hematite, opaque minerals and fluids. Carbonate appears to partly replace the apatite grains (sections 45762, 45770). Many apatite grains have severely corroded margins (sections 45747, 45752, 45762, 45763). Corroded apatites are associated with both the chlorite and the sericite portions of the groundmass (section 45752).

Pyrite and chalcopyrite are the dominant opaque phases. They show clear evidence of deformation, the pyrite commonly brecciated with chalcopyrite infilling the fractures in the pyrite or occurring in the pressure shadows of pyrite grains. Accessory opaque phases are rutile and hematite with minor molybdenite, gold,

galena,sphalerite, magnetite, and tennantite. Hematite occurs
both in the groundmass and in fractures across pyrite grains
where it is commonly associated with chalcopyrite.

Large number of inclusions occur within the pyrites, the most
common being phases that occur in the groundmass, hematite,
rutile, and chalcopyrite. Phases which occur as pyrite
inclusions but are not found in the groundmass can be grouped
as follows:

A   (i)   chalcopyrite + bornite

      (ii) bornite

    (iii) bornite + digenite

     (iv) digenite (very rarely)

B   (i)   pyrrhotite + chalcopyrite

      (ii) pyrrhotite

Members of group A commonly occur together as small clusters
within the pyrite. Those of group B are not usually found
with group A although an instance is noted below of bornite/
chalcopyrite and chalcopyrite/pyrrhotite inclusions occurring
in the same thin section.

Clearly, there are a number of equilibrium inconsistencies
in the assemblages outlined. Taken overall, three mutually in-
compatible groups occur:[1]

      (i)   pyrite, chalcopyrite with hematite (both a ground-
          mass condition as well as an inclusion type).
          Minor magnetite may occur.

      (ii) pyrite and pyrrhotite or pyrite, pyrrhotite and
          chalcopyrite (as pyrite inclusions only).

    (iii) pyrite, chalcopyrite and bornite (as pyrite
          inclusions only). Digenite probably replaces bornite.

[1] The assemblage bornite-chalcopyrite-pyrite-hematite is stable only
at geologically unreasonable pH conditions.

These groups indicate a complex history of sulphide formation, particularly for pyrite. Obviously the pyrite - hematite relationship must be the final event and may well be metamorphic in origin. This is consistent with the hematite after magnetite relationship observed in the intermediates and mafic rocks and the specular hematite, quartz, carbonate veining observed in the massive magnetite (see below). Much of the hematite found included in the pyrite probably originated during metamorphic recrystallisation.

It should be noted that the formation of hematite during metamorphism does not exclude the possibility of hematite having formed at an earlier stage. It is also important to note that the disequilibrium assemblages, whatever their origin, clearly indicate that the pyrite has not fully equilibrated during the metamorphism.

The most obvious metamorphic feature of the ore host is the quartz-sulphide (mostly chalcopyrite)-siderite-chlorite veining (plate 2.10). It occurs on all scales. In underground mapping and in hand specimen the veins are most noted as tension gash features. Solomon *et al.* (1969) note from observations made in the open-cut that the veins mostly occur at the nodes of large-scale cleavage boudins. In thin section typical remobilisation features are microveins, crosscutting the cleavage, and irregular splashes of clear quartz and coarse grained siderite with sulphide and minor chlorite. This latter feature is restricted to the matrix component of the rock (sections 45768, 45746). Both quartz and siderite grains may be elongate and strained (sections 45736, 45766). Section 45750 illustrates incipient vein development both within and cross-cutting the cleavage. Fine, elongate and strained quartz grains are often intergrown with chlorite

plate 2.10: Remobilised quartz-siderite-minor chlorite and
coarse grained remobilised chalcopyrite.
specimen 45765.

plate 2.11: Coarse siliceous fragmental with quartz-sericite-
minor chlorite alteration and disseminated pyrite-
minor chalcopyrite mineralization.
specimen 45724.
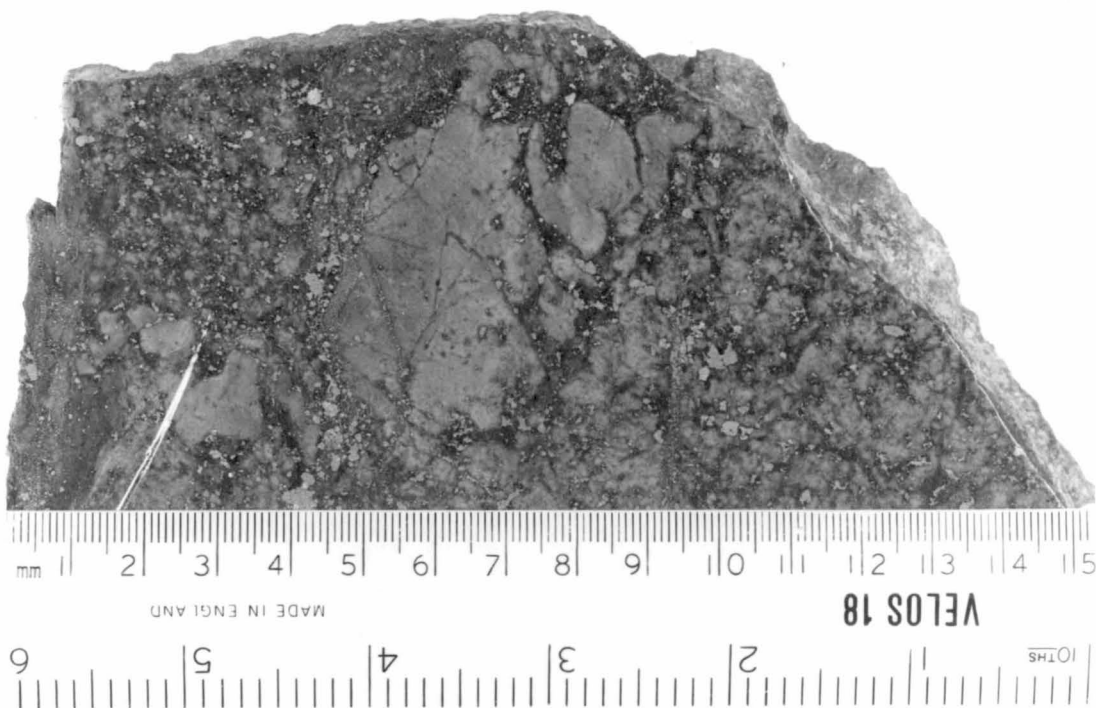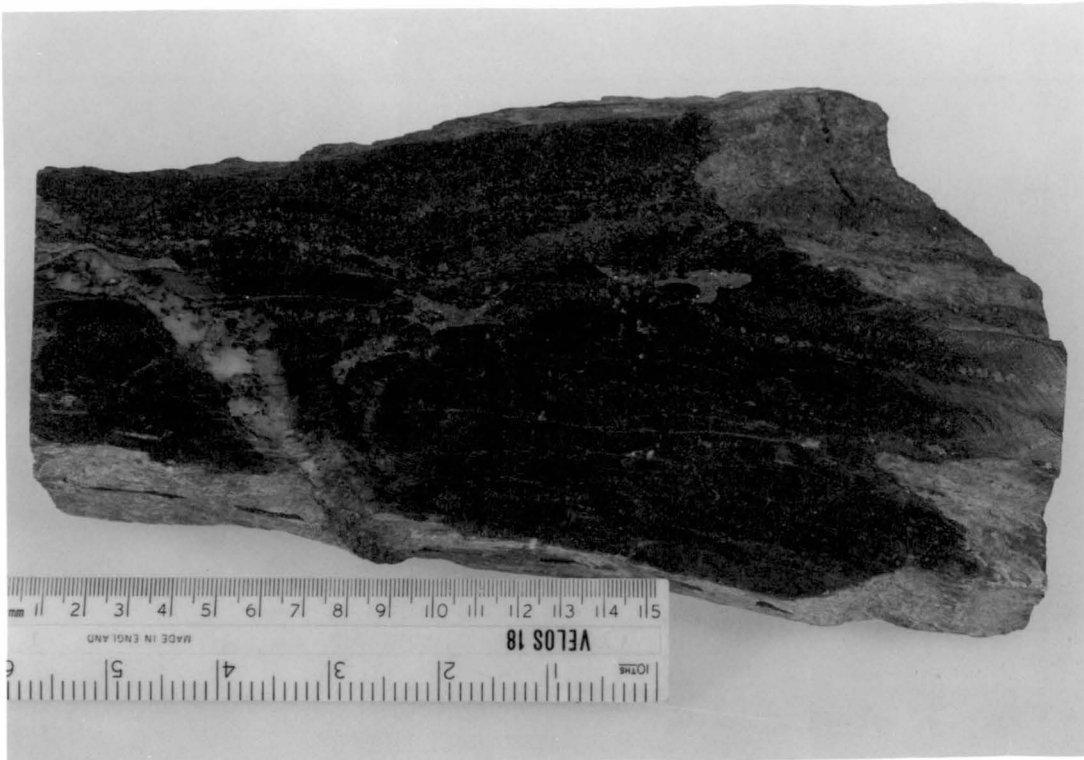
plate 2.12: Massive pyrite-minor chalcopyrite band in
the quartz-sericite fragmentals.
specimen 45723.
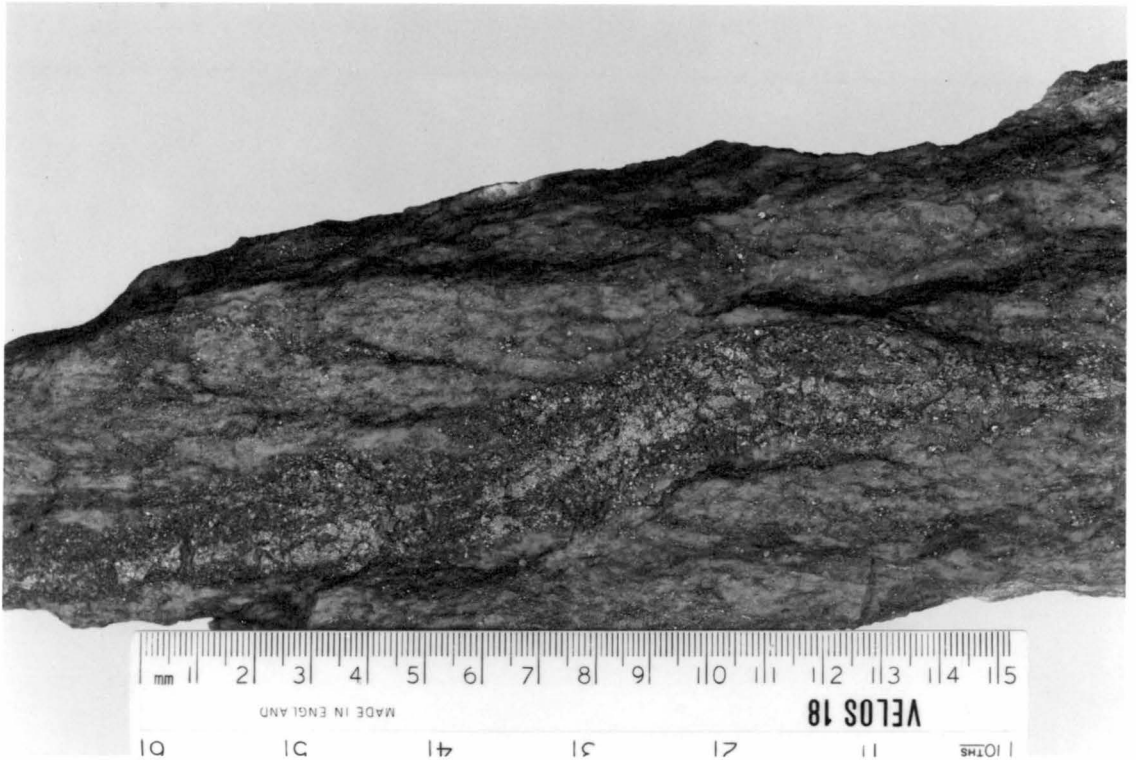
laths around the margins of remobilised zones. Clear quartz grains, intergrown with pyrite, occur to a limited extent around the edges of siliceous fragments and within siliceous fragments.

2.2.3 Quartz-Sericite-Pyrite-Chalcopyrite Alteration

The quartz-sericite-pyrite assemblage interfingers with the chloritic assemblage at the northern end of Prince Lyell (fig. 2.3) and extends discontinuously through to the Western Tharsis area. The pyrite content of the northern end of Prince Lyell averages 18-20 percent (fig. 6.9, sections Decline, WL 315 and 1-2 cross-cut) compared to 10 percent for the central-core chloritic zone. This increase in pyrite content reflects the absence of chlorite rather than any substantial change in the total iron of the rocks (fig. 6.9). The sericite in the quartz-sericite assemblage has a lower phengite component than the sericite in the quartz-sericite-chlorite-assemblage.

$K_{1.71}Na_{0.09}Fe_{0.07}Mg_{0.10}Al_{5.65}Si_{6.23}O_{20}(OH)$ (av. of 3 analyses)

The rocks are white-grey or grey-pink in colour. Texturally they are massive with disseminations of coarsely crystalline pyrite grains (45721), coarsely fragmental (45724, plate 2.11) or finely fragmental (45726). Massive bands of pyrite and minor chalcopyrite are present, up to 50cm in width but more commonly of 1-5cm (45723, 45725, plate 2.12). MacDonald (1968) noted from the open cut mapping that pyrite bands may be continuous over a number of metres. He also noted that although the banding coincided with the cleavage these cleavage directions showed appreciable departure (up to 40°) from the general cleavage direction in surrounding rocks. He concluded this was probably due to cleavage refraction by original banding. Clear quartz is a common component within the pyrite banding.

Some massive pyrite bands, with parallel quartz-sericite
zones, occur within the chloritic alteration.   These bleached
zones are usually limited to 30-50 cm in overall width with
the sericite alteration appearing to over-print the chlorite
alteration.   In one hand specimen situation (sample 45741) pink
apatite grains 1-2 mm in size are associated with the pyrite
bands.   Small-scale laminations occur within some of the bands
(MacDonald, 1968).

In thin section the rocks are texturally similar to those of
the central core described above.   Chlorite may be locally
present (section 45722) and minor apatite, monazite, barite
and siderite occur.   Pyrite dominates the opaque assemblages.
Pyrite overgrowths (section 45722) and arrowhead style pyrite/
chalcopyrite intergrowths, particularly in the massive-sulphide
sections are recrystallisation features.   Minor rutile, tennantite
and rare bornite, hematite and galena occur in the groundmass.

Types of inclusions found in the pyrites are:

(i)   pyrrhotite, pyrrhotite + chalcopyrite

(ii)   bornite + chalcopyrite, bornite, bornite + digenite

(iii)   mawsonite (section 45726);

as well as chalcopyrite, tennantite and rutile.   The bornite +
chalcopyrite and pyrrhotite + chalcopyrite inclusions commonly
occur in the same thin section (45723, 45725, 45726).

2.2.4   Footwall Alteration

The footwall of Prince Lyell consists of a unit of
massive, partly fragmental, pink rhyolites (sample 45757,
plate 2.13) continuous from the footwall of the central core
of Prince Lyell through to "A" lens or the conglomerate contact.
Minor tuff units appear in the sequence and these become more

common near the conglomerate contact. The unit grades into
highly pyritic, quartz-sericite altered tuffs and lavas to the
north (figs. 2.1, 2.4).

The unit is characterised by its texture, colour, the overall
lack of chlorite and the presence of hematite. The dominant
assemblage is quartz, sericite, minor hematite, pyrite, siderite
with minor chlorite, barite and rutile. Minor lenses of
chalcopyrite occur between Prince Lyell and "A" lens (fig. 2.1).
Hematite commonly occurs as fine grained disseminations and
where concentrated gives the rock a purple colour (plate 2.14).
The purple hematite zones appear in part, particularly along
fractures, to be replaced by the more common pink colouration.
Pyrite is often associated with the latter and appears to
replace hematite (samples 45787, 45793, 45794). Hematite also
occurs as massive bands (DDH 308/387, 416), as concentrations
along fractures, or associated with siderite and barite veining
(samples 45795, 45796) and as a minor component is some sulphide
veins.

In thin section the pink rhyolite is characterised by fine
grained intergrowths of quartz and sericite. Where fragmental,
the fragments are separated by an irregular and discontinuous
framework of sericite. Regular-shaped sericite laths are
possibly pseudomorphs of feldspar. Minor but persistent relict,
resorbed quartz phenocrysts are present. Minor siderite occurs as
dispersed rhombs or coarse grained recrystallisations. Quartz-
siderite-minor barite occurs recrystallised in the pressure
shadows of pyrite grains.

Hematite is present either as dispersed lamellae or, particu-
larly in the purple hematitic zones, as regular shaped inter-
growths of lamellae and as single equidimensional hematite grains

up to 2 mm in size. It is commonly associated with siderite and appears in part to be replacing siderite. Pyrite veins in the strongly hematitised zones (45791) typically have margins free from hematite but this feature may also occur to some extent around small hematite-pyrite veins (45792). In some instances pyrite completely rims hematite grains (plate 2.15). Hematite inclusions in pyrite commonly occur around the margins of grains probably associated with pyrite regrowth (plate 2.16). Chalcopyrite, chalcopyrite-bornite, bornite-digenite inclusions also occur. Other inclusions are rutile, minor magnetite, hematite-chalcopyrite, hematite-magnetite and rare pyrrhotite-chalcopyrite (45788). Magnetite appears to be present only as an inclusion phase in pyrite.

Although minor hematite is widely distributed throughout the pink rhyolite unit its predominate concentration occurs adjacent to the footwall contact with the chlorite alteration zone of the central core (figs. 2.3, 2.4). Here it occurs either as the disseminated type described above or as a matrix component with chlorite and minor chalcopyrite and pyrite in a chloritic fragmental pink rhyolite (45789, 45790, 45797, plate 2.17). From thin section it is apparent the hematite is in part replacing magnetite. In what appears to be a continuation of this hematite-chlorite alteration at depth (fig. 2.4) magnetite is observed in hand specimen. The magnetite is either veined or disseminated with chlorite, siderite and sulphide (samples 45778, 45780). Some veins have pyrite cores which are rimmed with magnetite (45777, 45778). In thin section the chlorite-oxide-siderite assemblage commonly occurs interstitial to siliceous fragments or as a discrete assemblage within the

sericite matrix (a similar relationship was described between the sericite and chlorite in Section 2.2.2). The oxide is predominately hematite. Magnetite is principally found in sections from the deeper levels (45778, 45785). All stages of alteration of magnetite to hematite have been observed (45779, 45782, 45785, 45797) and it seems reasonable to assume that the oxide was initially magnetite which has been oxidised during the metamorphism. This is consistent with the evidence given elsewhere (2.2.2 and 2.2.6).

Common inclusions in pyrite are hematite, chalcopyrite and magnetite and less commonly chalcopyrite-bornite, bornite-digenite and digenite. Pyrrhotite and pyrrhotite-chalcopyrite occurs in section 45785. In this section magnetite is the groundmass oxide phase and there is only limited alteration to hematite. Magnetite inclusions in pyrite are common in sections where there is only hematite in the groundmass.

If the groundmass oxide prior to metamorphism is assumed to be magnetite, magnetite inclusions in pyrite must result from a premetamorphic event involving pyrite and magnetite. Hematite inclusions must then result from metamorphic recrystallisation. The fact that magnetite inclusions in pyrite remain after the magnetite in the groundmass has completely altered is consistent with the other inclusion assemblages still present in pyrite but not in equilibrium with the groundmass conditions (see 2.2.2 for discussion). In section 45781 magnetite inclusions persist even though the groundmass phases hematite, chalcopyrite, sericite and minor chlorite are completely recrystallised and mutually-bounded pyrite grains show equilibrium triple points.

In section 45786 the oxide (hematite) has regular skeletal

plate 2.13: Massive pink rhyolite. Quartz-sericite-minor
chlorite-minor hematite alteration and minor
pyrite - chalcopyrite mineralization.
specimen 45757.

plate 2.14: Massive rhyolite. Disseminated hematite gives
the rock a distinct purple colour. Pyrite is
associated with the pink colouration and
appears to replace the hematite.
specimen 45793.

plate 2.15: Pyrite replacing hematite.
            specimen 45788; magnification x100.

plate 2.16: Hematite inclusions occurring within pyrite
            overgrowths.   specimen 45758;
            magnification x160, oil immersion.
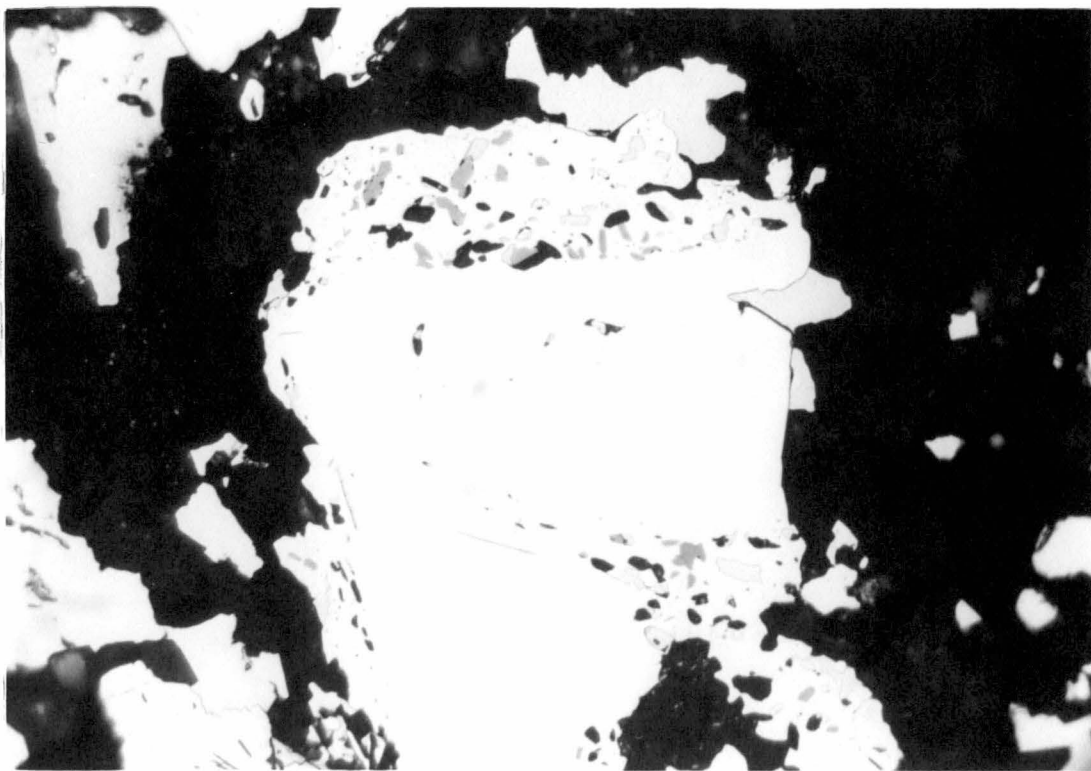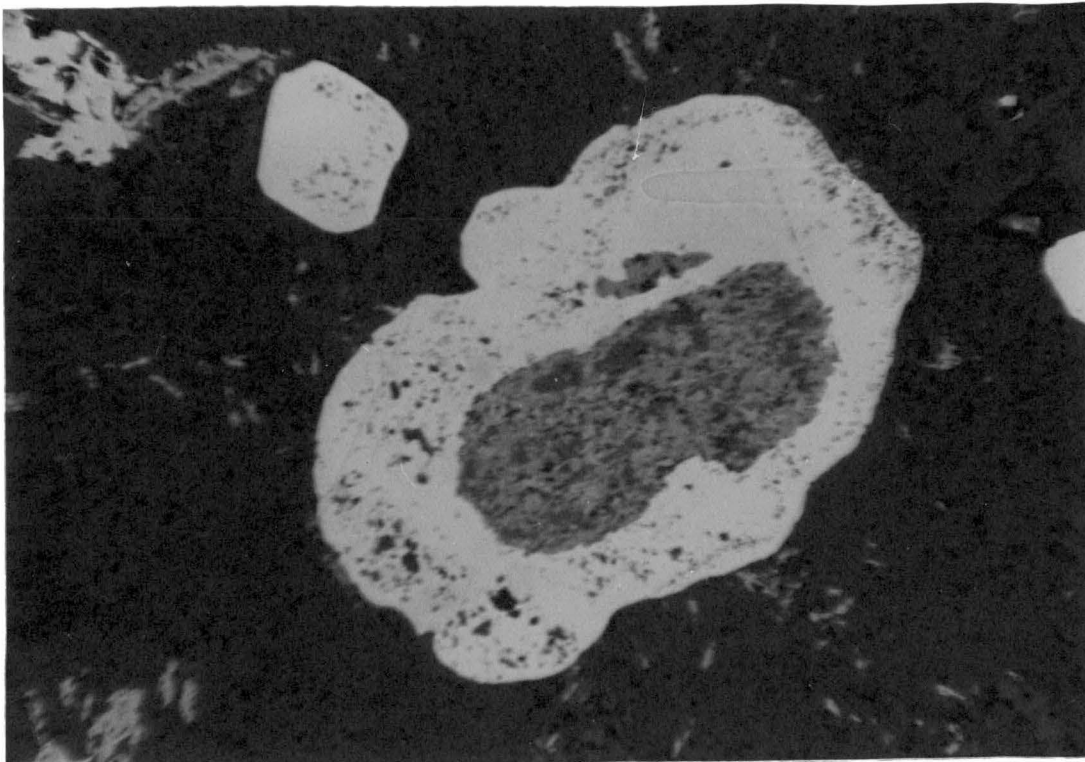
plate 2.17:   Fragmental pink rhyolite with a matrix component
              of quartz-chlorite-minor sericite-hematite/
              magnetite-minor sulphide and siderite.
              specimen 45797.

VELOS 18

plate 2.18: Siderite rhombs rimmed and partially replaced
by hematite.
specimen 45786; magnification x30.
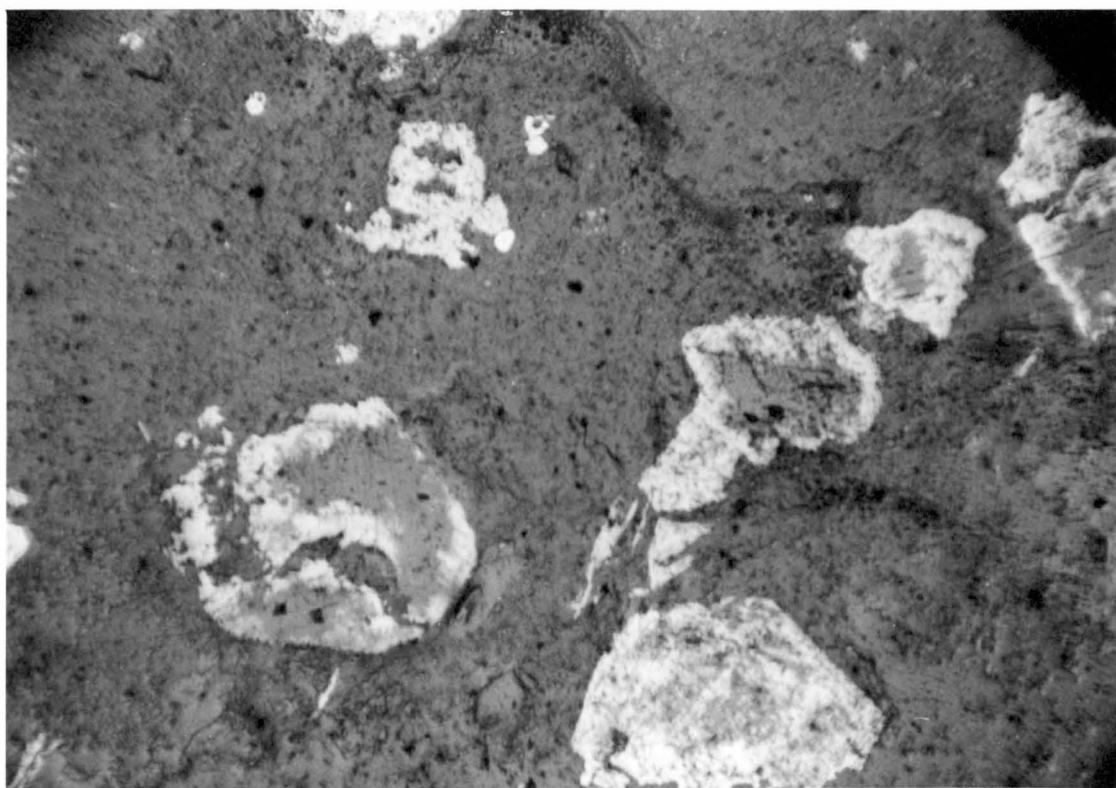
outlines which enclose chlorite and siderite. In some instances an impression is given of replacement of siderite rhombs by the oxide (plate 2.18). Hendry (1972) suggested these textures could be oxide siderite pseudomorphing a third phase. In the examples he referred to, magnetite and hematite rimmed siderite and all stages of magnetite alteration to hematite were observed.

2.2.5 Intermediate Tuffs and Intrusives

Rocks of dominantly intermediate to mafic composition and of probable pyroclastic origin occur on the hanging wall of Prince Lyell and as discontinuous lenses within the chloritic siliceous fragmentals of the central core of Prince Lyell (figs. 2.3, 2.4). Two rocks types are distinguished:

(i) Intermediate tuffs and lavas (?)

These are a loose grouping of rocks generally fine-grained and grey-green with chlorite flecks (samples 45738, 45740, plates 2.19, 2.20). Fine-grained siliceous fragmentals may be present (samples 45775, 45784). The boundary with the chloritic siliceous fragmentals of the central core is not well defined but is marked by an overall decrease in grainsize and fragmentation. The mineralogy is generally quartz, sericite, chlorite, pyrite and minor chalcopyrite. Hematite and magnetite are common throughout the unit as veins and disseminations. Pyrite has a tendency to occur in veins and bands (45733, 45743, 45731) although disseminations occur within fine-grained fragmentals (45775, 45784). The unit includes a number of minor felsic tuffs (45759) with some textures suggestive of fiamme (45760).

In thin section (samples from units within the central-core siliceous fragmentals) there is a notable absence of relict, volcanic, quartz phenocrysts. Chlorites tend to have purple-maroon interference colours (sections 45772, 45731) in contrast to the 'normal' grey-blue colours. These colours appear to be absent when magnetite is present.

Obvious fragmentation in thin section is lacking but discrete quartz aggregates (up to 1 mm) or granules (less than 0.2 mm) are dispersed in a chlorite and sericite matrix (sections 45737, 45740). Chlorite and/or sericite clots are common and some chlorite clots also include magnetite (sections 45764, 45769, 45771). Hematite replaces magnetite. The sericite, chlorite clots appear to be replacements of feldspar and ferromagnesian phenocrysts respectively.

Apatite is a common accessory, generally associated with the chlorite clots and commonly corroded (45744) but it may occur as prismatic grains within the groundmass (45732). Siderite content appears to be higher than for the siliceous fragmentals and is dispersed throughout the groundmass (45769, 45773). Regular skeletal outlines of fine-grained anatase (?), usually formed within the chloritic clots (45732, 45734, 45740), are probably alteration products of ilmenite or sphene in the original host.

Quartz-siderite-minor hematite veining is common. Sample 45774 contains a folded quartz-siderite-pyrite-chalcopyrite vein.

plate 2.19: Fine-grained, chloritic intermediate tuff.
specimen 45738.

plate 2.20: Fine-grained, chlorite flecked intermediate
tuff with disseminated hematite/magnetite.
specimen 45771.
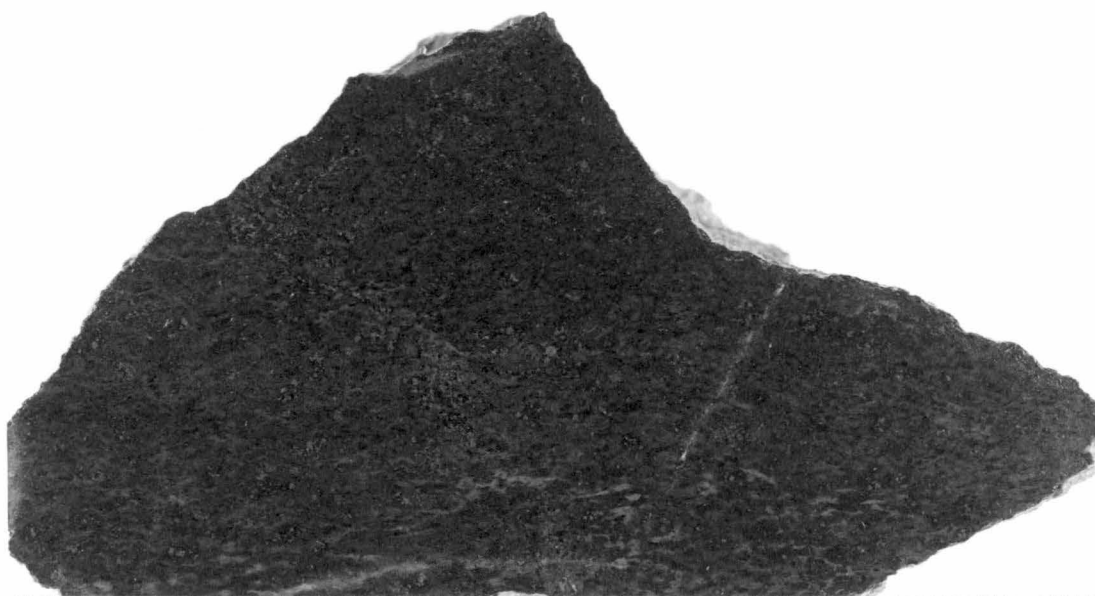
plate 2.21: Massive magnetite with chlorite and pyrite.
The chlorite and pyrite has replaced or
partially replaced apatite crystals.
A partially replaced apatite crystal is
visible at centre-top of the specimen.
specimen 45800.
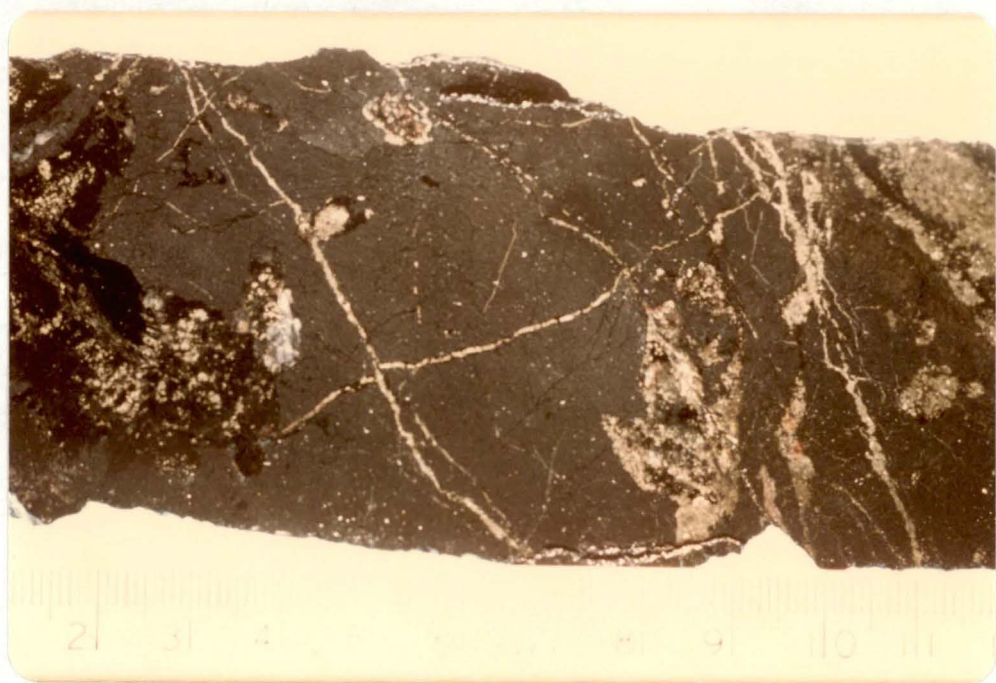
(ii)   Mafic intrusives

The intrusive units appear to be a continuation of the
chloritic units mapped south of the open cut (fig. 1.5).
The dominant unit has an average thickness of 20 metres
and dips 75-80°W. (D.D.H. logging on section 13).

It is characteristically very fine grained, dark green
with chlorite flecks (sample 45776).   The rocks have a
silica content consistent with a basalt composition
(Solomon, 1964; Walshe, 1971).

Sulphide veining and banding and quartz-siderite veining
may be present.   Hematite flecks are common in the
groundmass.   Specimen 45783 appears to contain siderite
amygdales and these are partially or wholly replaced by
sulphides.

2.2.6   Massive Magnetite

Small discontinuous lenses of massive magnetite, chlorite
and apatite occur within the central-core chloritic zone.   The
lenses tend to be located on the footwall side of the zone
(5-6/250' and 2-3/320', 830' level and D.D.H. 227/520' and 384/602m).
The exposure on the 830' level at 2-3/320 (fig. 2.3) measured 2.5
metres across and consisted of coarse-grained massive magnetite,
chlorite, minor apatite and veinlets of pyrite.   The lens was
fault bounded and crosscut by post-cleavage quartz-siderite
veining containing well developed specular hematite.   This
feature is evidence for a magnetite to hematite metamorphic
reaction.

Some large apatite fragments, up to 15 cm. in size and commonly
veined with sulphide, hematite and siderite (sample 45782) occur

with the magnetite.

In places chlorite and pyrite replace small apatite crystals (plate 2.21).   Pseudomorphing of apatite by pyrite and chlorite probably accounts for the regular shapes of many chlorite/pyrite intergrowths (samples 45756, 45800).   The magnetite has undergone varying degrees of alteration to hematite along fractures and pyrite veins.

A possible genetic sequence is:

(i)   magnetite and apatite

(ii)   pyrite and chlorite (siderite?)

(iii)   hematite (metamorphic).

2.3 Western Tharsis

Western Tharsis is a large zone (approximately 600 metres in strike length) of disseminated and banded pyrite (average 10 percent) and low grade chalcopyrite (average 0.5 percent copper) lying midway between Prince Lyell and Cape Horn.   Its western margin is marked by the felsic lava/intermediate pyroclastics boundary (fig. 1.5).

Surface mapping[1] and diamond drill hole logging[2] has indicated a series of felsic lavas and pyroclastics with minor intermediate intrusives.   Diamond drill hole 374 indicated a number of repeated units of coarse and fine grained pyroclastics.

The alteration is essentially quartz-sericite-pyrite.   The sericite commonly occurs as discrete layers between siliceous bands and fragments (45823) and possibly reflects original tuff or flow banding.   X-ray diffraction of a number of specimens indicated that

1 By J. Knight, former student geologist, Mt. Lyell.

2 By B. Smyth, former mine geologist, Mt. Lyell.

sericite is the only white mica present.   Chlorite is not spatially
well developed although it may occur in limited zones.   However the
chlorite that is present does not appear to be associated with
chalcopyrite as at Prince Lyell.   Minor carbonate is present.

The mineralization is dominantly pyrite with minor chalcopyrite
(samples 45818, 45821, 45828).   Some bornite with pyrite and
chalcopyrite has been recorded (WL 257/1040-1135', WL 409, sample
45815).   A one metre interval of massive magnetite, minor pyrite
and quartz-carbonate veining occurs at WL 374/238.   Some magnetite
appears to be dispersed with pyrite and chlorite in the host around
the contacts.

The footwall of the mineralized zone (as seen in WL 317/1450- E.H.)
consists of a sequence of altered lavas and tuffs.   The alteration assemb-
lage is quartz-sericite-minor chlorite, carbonate and hematite.   Pyrite-
hematite veining and massive pyrite banding occurs.   These characteristics
suggest an overall similarity with the footwall of Prince Lyell.

In thin section the rocks consist of siliceous fragments in a
sericite matrix.   Fragments usually contain wisps of sericite, relict
quartz phenocrysts and minor carbonate.   The matrix is generally
quartz and sericite.   Chlorite may occur as a minor component
associated with the sulphides (45814, 45829).   Interference colours
are brown/red or maroon.   Carbonate is locally well developed (45829).
Minor phases include zircon, monazite (?) and fine-grained barite.
Deformation textures, sericite beards between fragments and quartz
grains recrystallised in the pressure shadows of pyrite grains are
common.

Pyrite is either disseminated or massive.   Massive pyrite
commonly shows growth zones outlined by fluid inclusion pits (?).
Apart from chalcopyrite, rutile, rare hematite and tennantite are
associates.   Hematite is much more common in the footwall zone (45825).

Pyrite commonly contains inclusions with chalcopyrite, chalcopyrite-bornite, bornite, bornite-digenite and rutile the most common.   The inclusions usually appear to be randomly distributed but some occur in linear zones within cores and around the perimeters of grains along with gangue and fluid inclusion pits.   Etching in one instance (45826) indicated zoning in the pyrite which corresponded with inclusion zones.   In sample 45820 an inclusion zone is broken by fracturing of the pyrite and this together with the absence of bornite in the groundmass of any of the samples suggests a pretectonic, premetamorphic origin for the bornite.   The instances of inclusions in specific zones within the pyrite strongly suggests that at some stage during the growth of the pyrites conditions were at or close to the bornite-chalcopyrite-pyrite boundary.   However, lack of bornite in the groundmass suggests that this situation was short lived. The exception to this would be WL 257/1040-1135' and WL 409.

Hematite, hematite-chalcopyrite, magnetite-hematite inclusions in pyrite, although rare are also present.   Sample 45819 has well developed magnetite, hematite, magnetite-chalcopyrite, hematite-chalcopyrite, hematite-magnetite-chalcopyrite and rare hematite-magnetite inclusions.   In general these tend to occur within the cores of grains.   No bornite-chalcopyrite inclusions occurred in this section.   This sample, which is a section across a sulphide band, shows a distinct gradation in sulphide grainsize across the band.   Pyrrhotite inclusions in pyrite occur very rarely and with chalcopyrite.   They were found in sections 45826, 45817 and 45829.   Samples 45826 and 45817 also contained bornite-chalcopyrite inclusions in the pyrite.   Sample 45829 contained a pyrrhotite - chalcopyrite inclusion and hematite inclusion in the same pyrite grain.
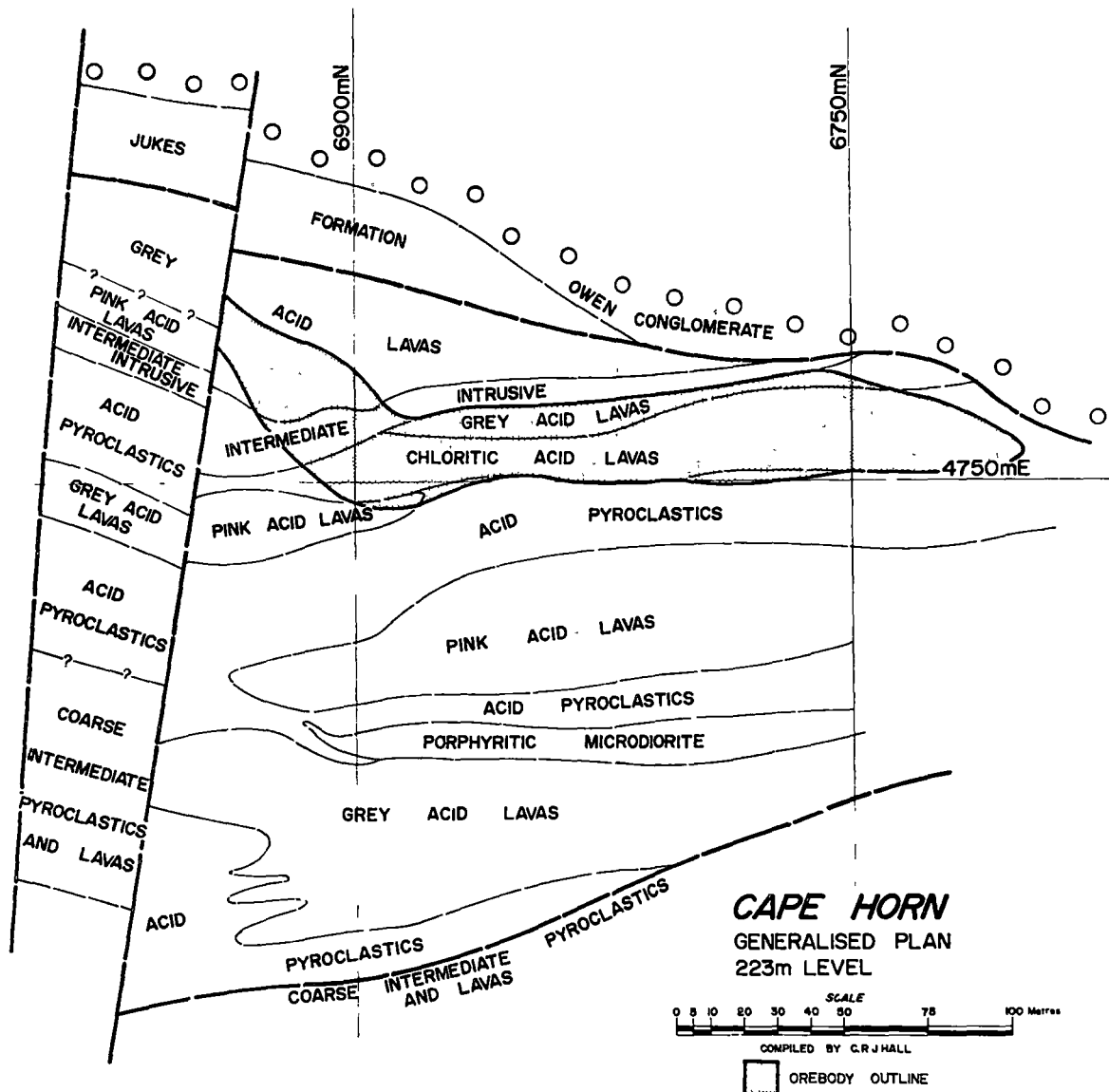
Fig. 2.5:   Generalised geological plan of the Cape Horn
orebody on the 233m. level (after Reid, 1976).
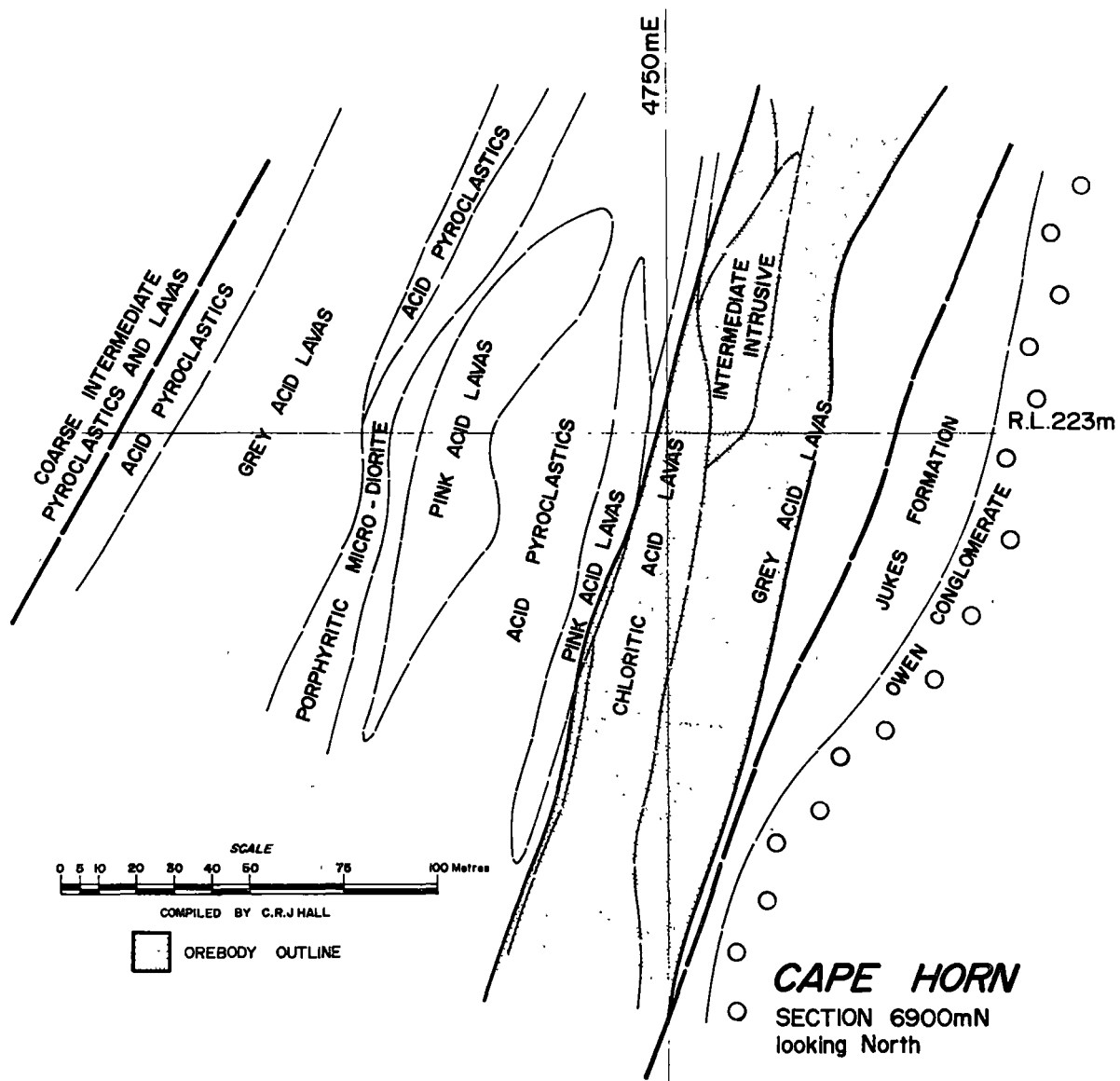
Fig. 2.6: Cross-section through the Cape Horn orebody on
Section 6900mN., looking north (after Reid, 1976).

This section also contained magnetite-hematite, magnetite-
chalcopyrite, magnetite and magnetite-hematite-chalcopyrite
inclusions in pyrite. No hematite was identified in the ground-
mass. Minor chlorite occurred in 45829 and probably in 45826
and 45817.

2.4 Cape Horn

2.4.1 Introduction

A recent summary of the geological setting of Cape
Horn is given by Reid (1976).

"The Cape Horn orebody is contained within a series of pyritic
altered acid lavas and pyroclastics and intermediate intrusives
which dip steeply west, subparallel to the faulted contact with
the Jukes Formation and Owen Conglomerate (fig. 2.5 and 2.6).
The host rocks and orebody are truncated by this contact to the
south and by a series of E.-W. trending faults to the north.
On the western side they are faulted against barren intermediate
pyroclastics and lavas. The orebody reaches maximum dimensions
of about 250 metres strike length, 45 metres wide and extends to
a depth of about 420 metres, although weak chalcopyrite
mineralization persists to at least 640 metres."

Green (1971) listed the Cape Horn mineralogy as quartz, chlorite,
sericite, pyrite, chalcopyrite with minor apatite, monazite,
zircon, rutile, tennantite, hematite, and magnetite with rare
molybdenite, galena, sphalerite, and gold.

C. Hall[1] and D. Greenway[2] (fig. 2.5) have subdivided the
mineralized horizon into three units:

(i)   Pink felsic pyroclastics and lavas (hanging wall),

(ii) Chloritic felsic lavas and grey felsic lavas (orebody horizon),

(iii) Intermediate intrusive.

2.4.2 Pink Felsic Pyroclastics and Lavas

The hanging wall rocks are pink and massive in hand
specimen (45801) but in detail commonly contain fine granular
quartz structures. Minor but locally important rhyolite frag-
ments, varying in size from 1 to 20 mm, and irregular grey-green
sericitic wisps and clots, 10-20 mm in length, are characteristic.
Larger tabular sericitic structures (e.g. 45805; dimensions 50 x
20 x 50-80 cm) are suggestive of fiamme.

In thin section the rocks are typically quartzose with abundant
sericite, minor carbonate and some chlorite. Relict, partially
resorbed, quartz phenocrysts are common.

Hematite is characteristic, occurring as rather regularly
shaped blebs suggesting pseudomorphing. Locally, concentrations
of disseminated hematite may be as high as 10-15% (45804). Thin
section indicates quartz, chlorite, carbonate and minor sericite
associated with the hematite blebs. In many instances the
hematite blebs are rimmed or partially replaced by pyrite. In
polished section hematite lamellae included in pyrite are
observed to have similar orientations to hematite lamellae in
the groundmass, confirming hematite replacement by pyrite.

1 Formerly of the Mt. Lyell geological staff.

2 Former senior mine geologist, Mt. Lyell.

plate 2.22:   Displacement of hematite lamellae against pyrite
during the deformation.
specimen 45804; magnification x160, oil immersion.
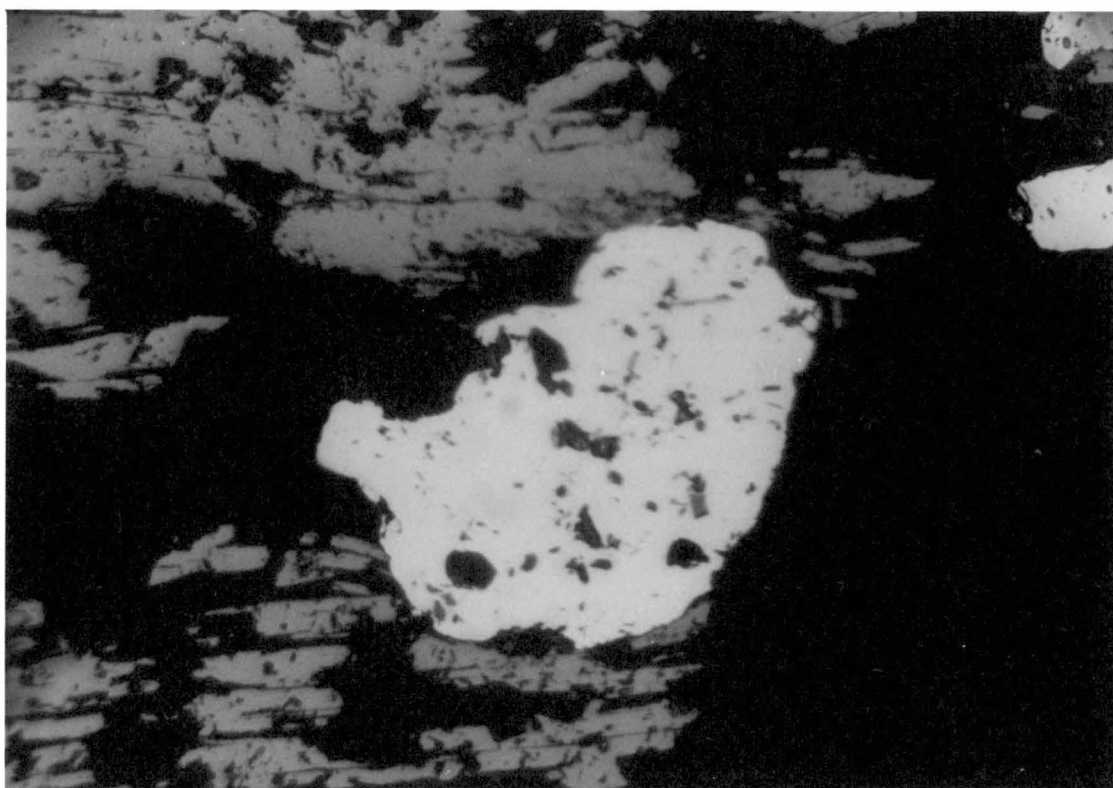
Displacement of hematite lamellae against the pyrite grains

indicates replacement prior to deformation (plate 2.22).

Minor magnetite inclusions are present in the pyrite, commonly

associated with hematite inclusions and more rarely with

chalcopyrite inclusions.   A possible source of the magnetite

in this situation is as a reaction intermediary between hematite

and pyrite although it could also be argued that any magnetite

associated with hematite prior to sulphide introduction and not

being included into the pyrite was oxidized during the meta-

morphism.   However, although the magnetite to hematite reaction

has been observed in the groundmass elsewhere, no magnetite was

observed in the groundmass of the hanging wall rocks.

Minor rutile occurs with the hematite.

2.4.3 Intermediates

The intermediate is a fine grained dark grey-green;

chlorite flecked rock (sample 45802) which intrudes the

mineralized horizon.   It contains only nominal amounts of

copper (0.1 - 0.2 percent copper) and pyrite (1 - 1.5 percent).

2.4.4 Ore Horizon : Chloritic Felsic Lavas and Grey Felsic Lavas

The ore horizon consists of grey-green, chlorite-sericite

altered,felsic volcanics and grey, sericite altered,felsic

volcanics.   The latter is generally confined to the footwall

of the orebody.

The mineralogy of the chlorite-sericite altered host rocks is

similar to that of Prince Lyell although there are important

differences.   Texturally the rocks are finer grained than the

Prince Lyell counterparts, generally lacking the coarse fragmental

appearance that characterises much of the Prince Lyell ore.

Granular quartz structures, 1-2 mm in dimension, as noted for the

hanging wall rocks may be present.

Chlorite occurs either as a fine disseminated matrix around quartz granules and fragments or as wisps or streaks similar to textures described in the hangingwall rocks. Again some textures suggest fiamme (45808). The chlorite/sericite ratio is very variable but there are a few highly chloritic zones (e.g. D.D.H. 71/560-615, D.D.H. 76/55-132 m). Coarse grained barite crystals (20-30 mm dimensions) occur in a part of the chlorite-rich zone (45812). Chalcopyrite may occur either as disseminations associated with chlorite in less deformed specimens or as noted by Reid (1976) as coarse veinlets and as smears on cleavage and fracture planes (45810). Carbonate veining is common.

In thin section sericite generally dominates chlorite. Chlorite shows both normal and maroon interference colours. Minor carbonate is common occurring as discrete rhombs, as small 1-2 mm aggregates, or as post- and syn-cleavage veining. Apatite is an important accessory, euhedral grains occurring up to 4 x 2 mm in size. Local bands of apatite may comprise 10 percent of the rock. Grains may be both brecciated and corroded. Apatite may locally show an association with chlorite and chalcopyrite (45808). Minor disseminated barite is a feature in many thin sections. Relict volcanic quartz phenocrysts commonly occur. The important opaque phases are chalcopyrite and pyrite with minor hematite and rutile. Hematite is well developed in sections from heavily chloritised zones (45811, 45807). In 45811 hematite in part replaced magnetite. Sericite is still significant in these chlorite rich sections. However, the oxides tend to be associated with the chlorite and the sulphides. In 45806 clots of hematite with associated chalcopyrite and minor pyrite show a similar relationship to the hematite/pyrite relationship
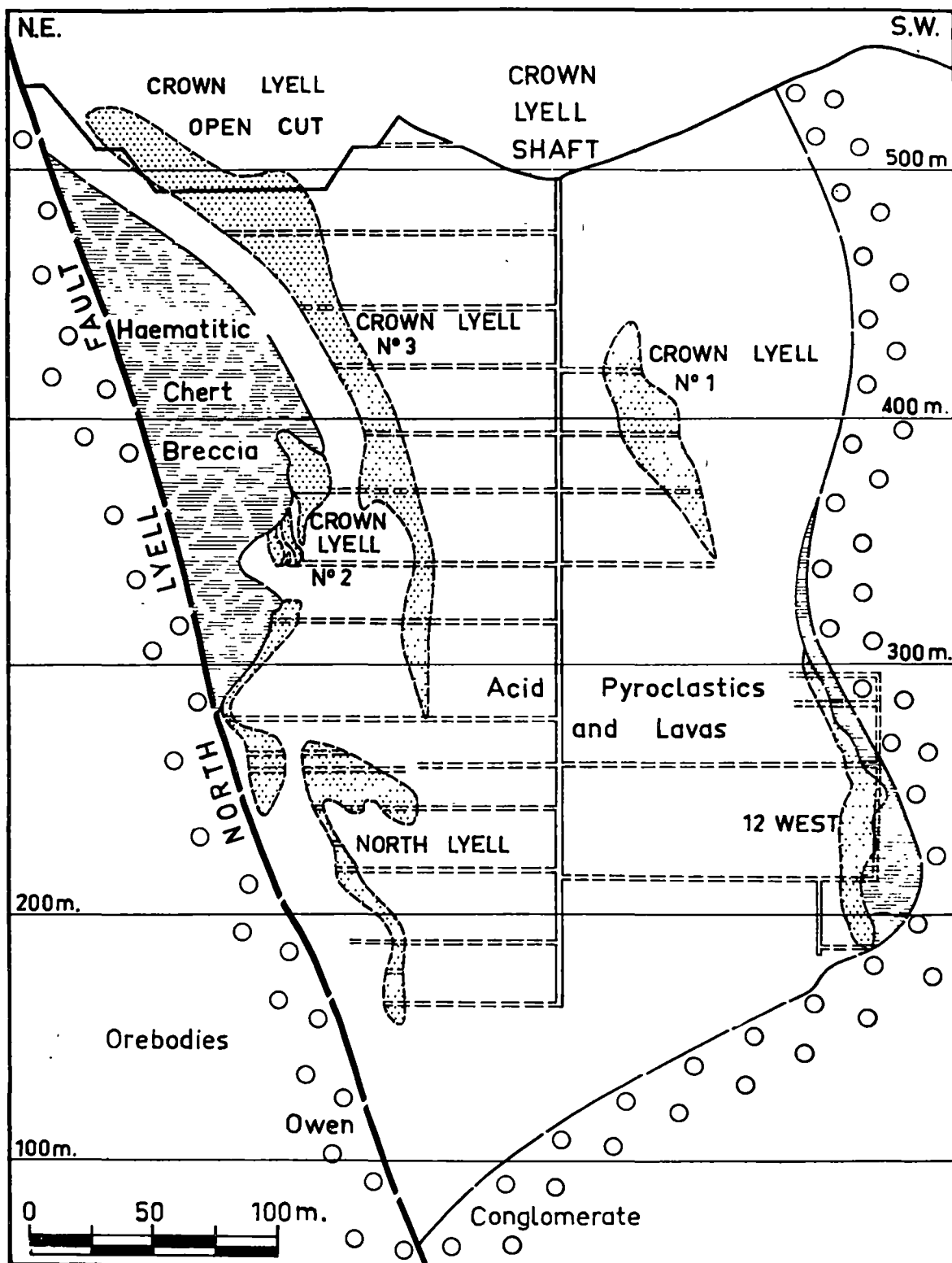
Fig. 2.7:   Projected section through the Crown Lyell area,
looking south-east.

described from the hanging wall rocks. Common inclusions in pyrite are magnetite, hematite, hematite/magnetite, hematite/magnetite/chalcopyrite. Only one specimen with pyrrhotite and pyrrhotite/chalcopyrite inclusions in pyrite was found (45809).

The grey sericitic volcanics are massive or fragmental (45803). Quartz-sericite-pyrite-chalcopyrite alteration with minor bornite is characteristic. Accessory minerals include rutile, tennantite and chalcocite (45813).

2.5 North Lyell, 12 West and the Crown Lyell ores

2.5.1 Introduction

The author's work has predominately concerned the geology/geochemistry of the pyrite and chalcopyrite mineralization of Prince Lyell, Cape Horn and Western Tharsis. Some trace element in pyrite analyses were done on samples from two Crown Lyell No. 3 D.D.H.s (nos NL1044 and NL1062). These holes intersected partly Crown Lyell No.3 mineralization and partly the chloritic sulphide assemblage of the Crown Lyell No.3 footwall. Also previous sulphur isotope analyses on samples from Crown Lyell No.2, North Lyell and 12 West ores (Solomon *et al.*, 1969) are referred to in later discussion. Hence for completeness a brief description of these ores is given.

The descriptions are based on the work of Markham (1968), Bryant (1976) and Reid (1976). The ore bodies group conveniently into three types.

(i)   The Crown Lyell No.3 siliceous pyritic ore.

(ii) The chloritic ores of Crown Lyell No.1, beneath and on the footwall of Crown Lyell No.3 and Lyell Tharsis

(iii)   The siliceous bornite-chalcopyrite ore of North Lyell,

Crown Lyell No.2 and 12 West.

Ore body locations are shown on figures 1.5 and 2.7.

2.5.2 Crown Lyell No.3

Crown Lyell No.3 is contained within a massive or brecciated, fine-grained chert with minor carbonate, barite and sericite.   Sulphides are typically disseminated and commonly outline breccia fragments (45830).   Sulphides also occur in crosscutting carbonate veins with minor barite.   Carbonate, principally dolomite and siderite with occasional calcite, is most common on the northern end of the orebody.

The dominant sulphides are pyrite (up to 20 percent) and chalcopyrite with minor galena, sphalerite, hematite and rutile and occasional bornite, tennantite, hexastannite, mawsonite (45831, 45832, 45833, 45834) and molybdenite.   Secondary covellite, chalcocite and native copper have been noted in the upper levels of the orebody.

2.5.3 Chloritic Assemblages on the footwall of Crown Lyell
No.3 and Crown Lyell No.1 and Lyell Tharsis

These ores are characterised by an assemblage of quartz, chlorite, minor sericite, pyrite, chalcopyrite, carbonate and barite.   In D.D.H. NL Nos. 1044 and 1062 (Crown Lyell Mine, 7 and 9 level) the host rock is a variable, massive or fragmented, siliceous volcanic (45837, 45838, 45844).   Chlorite and sulphides typically form the matrix around siliceous fragments. Pyrite is present as disseminated grains (45837).   Chalcopyrite occurs as splashes and smears, intimately intergrown with chlorite (45847, (45836).

Magnetite is present as banding (45846) or as disseminations in the matrix (45845). It is partially replaced by hematite and generally occurs with the chlorite (45840, 45847) but not uniquely (45839).

Some thin sections contain only minor hematite (45841, 45842).

Barite is present principally as veins (45835, 45836) but may also occur as a minor disseminated component (45839). Fluid inclusions occur in the barite veins. Carbonate is a common component in thin section (45839, 45840). Apatite is common in some sections (45840, 45847) and most grains have corroded margins. Minor monazite is also present plus minor rutile, galena and sphalerite (45843, 45847).

Descriptions by Reid (1976) and Bryant (1976) indicate Crown Lyell No.1 and Lyell Tharsis assemblages to be of similar type to that described above. However Reid (1976) notes that the northern end of Lyell Tharsis contained high-grade bornite ore which was worked between 1899 and 1901. He suggests Lyell Tharsis is a transitional zone between the bornite-rich ores and the disseminated pyrite, chalcopyrite ores. No pyrrhotite inclusions were observed in the pyrite.

2.5.4 North Lyell, Crown Lyell No.2 and 12 West

The North Lyell ores consisted of coarse-grained masses of bornite with minor chalcopyrite and pyrite in a grey fine-grained chert or chert breccia or a sericite-quartz schist. Chalcopyrite, pyrite rich ore tended to be associated with less silicified rocks. Accessory minerals included galena, chalcocite, digenite, betechtinite, tennantite, enargite, mawsonite, linnaeite, sphalerite, stromeyerite, magnetite, hematite, gold, rutile and barite (Reid, 1976; summary of Markham, 1968; Markham and Otteman,

1968; Markham and Lawrence, 1965; Wade and Solomon, 1965; and Edwards, 1939). The orebody is generally separated from the Owen Conglomerate by irregular masses of brecciated and fractured hematitic chert.

Crown Lyell No.2 forms part of the North Lyell orebody. 12 West is similar to the North Lyell ore, bornite with subordinate chalcopyrite and minor pyrite occurring as massive pods, irregular fracture fillings and coarse disseminations in a siliceous quartz-sericite schist (Reid, 1976). The minor phases described for 12 West are similar to those given above (Bryant, 1976).

Minor pyrophyllite occurs with the bornite ores (Solomon, 1964; Bryant, 1976). It generally occurs on shear and cleavage planes but Bryant (1976) also reports muscovite and pyrophyllite intimately associated with the sulphides. Some pyrophyllite occurs adjacent to the northern end of Crown Lyell No.3 (Bryant, 1976) and with the bornite in NL1044/30-50.

3. DISCUSSION OF ALTERATION ASSEMBLAGES

3.1 Phase Diagram Representation

The $\log fO_2$-pH diagram is the main diagram used in this discussion to illustrate the relationships between alteration assemblages and to facilitate discussion of the genesis of the assemblages. A detailed discussion of the construction of the diagram is given in Appendix B and relevant thermodynamic data in Appendix A.

The copper sulphide phases have been plotted by fixing the concentration of copper in solution (fig. B2). This allows discussion of the relationship between pyrite and chalcopyrite. However the positioning of phase boundaries involving copper sulphides depends on ΣCu (ΣCu taken to be equivalent to m_T Cu as given by Helgeson, 1969) as well as ΣS. The Fe silicate to non-Fe silicate reactions have been written by conserving Al between the silicates and Fe between the Fe silicate and an Fe oxide, an Fe sulphide, or a Cu-Fe sulphide (fig. B5). This leads to reactions dependent on fO_2, pH and ΣS for Fe sulphides, and reactions dependent on fO_2, pH, ΣS and ΣCu for Cu-Fe sulphides. The free energy of Fe chlorite ($Fe_{4.5} Al_{3.0} Si_{2.5} O_{10} (OH)_8$) has been estimated using the method of Tardy and Garrels (1974). Available information allows discussion of possible hydrothermal and metamorphic conditions up to $300°C$ and 500 bars. Pressure dependence under these conditions is negligible (Helgeson 1969, 1967).

3.2   Phase Relationships of Sulphides, Oxides, Silicates and

Carbonates Under Possible Metamorphic and Hydrothermal Conditions

3.2.1   Temperature and Pressure Conditions

Difficulty arises in discussing possible hydrothermal and

metamorphic conditions because of a lack of knowledge of

pressure-temperature conditions.   Initially the hydrothermal

temperature will be taken to be 250°C.   This is partly because

of the Western Tharsis sulphur isotope partitioning data but

also because it is consistent with the fluid inclusion and

isotopic temperature data from the siliceous ore and the yellow

ore parts of the Kuroko deposits (Tokunaga and Honma, 1974;

Sasaki, 1974).   The Kuroko deposits are the best known of the

massive sulphide class of deposits with which Mt. Lyell has been

grouped.   A maximum confining pressure of 30-40 bars will be

assumed for the hydrothermal model.

The metamorphic pressure-temperature conditions are also

poorly defined.   Solomon (1967) estimated the overburden

deposited between the early Ordovician and Devonian orogenies

as 3000m.   This would give a maximum lithostatic pressure of 1Kb

or allowing for tectonic overpressure a minimum pressure estimate

of 1 Kb.

The occurrence of pyrophyllite suggests a maximum and minimum

temperature of approximately 400°C and 325°C respectively

assuming 1Kb pressure (Miyashiro, 1973, p. 199; Thompson,

1970).   However the possibility also exists that pyrophyllite

formed in association with silica gel as part of the hydrothermal

process.   Experimental work by Fournier and Hemley (reported by

Fournier, 1967) indicates that under conditions of high-silica

activity kaolinite may convert to pyrophyllite at temperatures

log fO_2

-28

Hematite

-30

-32

Pyrite

-34

-36

Magnetite

-38

Sericite

Fe Chlorite

-40

-42

-44

Pyrrhotite

-46

-8   -6   -4   -2   0   2   log aH_2S

0 0001   0 01 0 1   1 0   ΣS if H_2S is the dominant
                                sulphur species   I = 1.

0 03
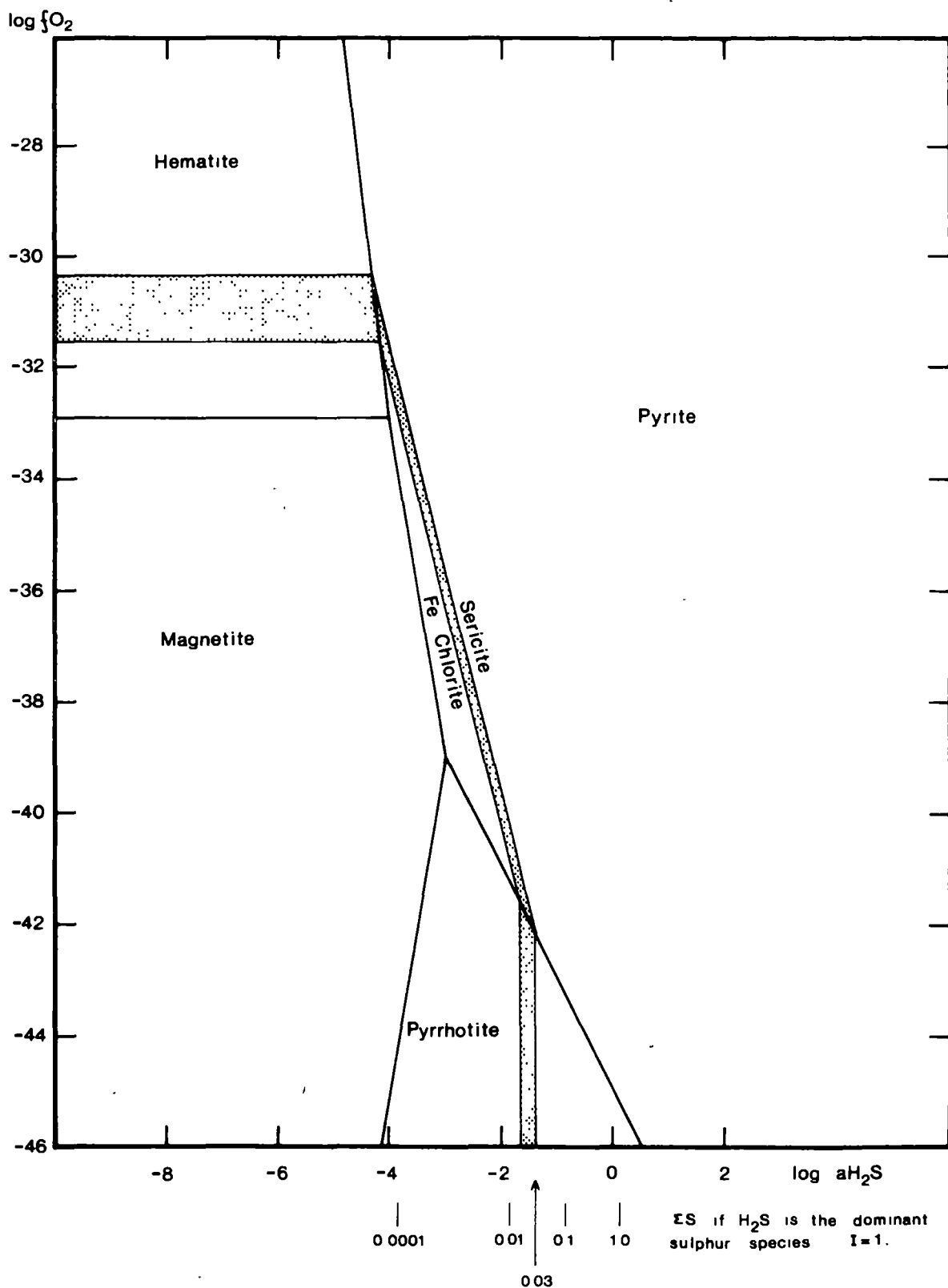
Fig. 3.1:   Log fO_2-log aH_2S diagram for 250°C at
1 atmos. Kaol./Ser. < log aK^+/aH^+< Ser./K-Feld. Activity
of H_2O is taken as unity. Quartz is present in excess.
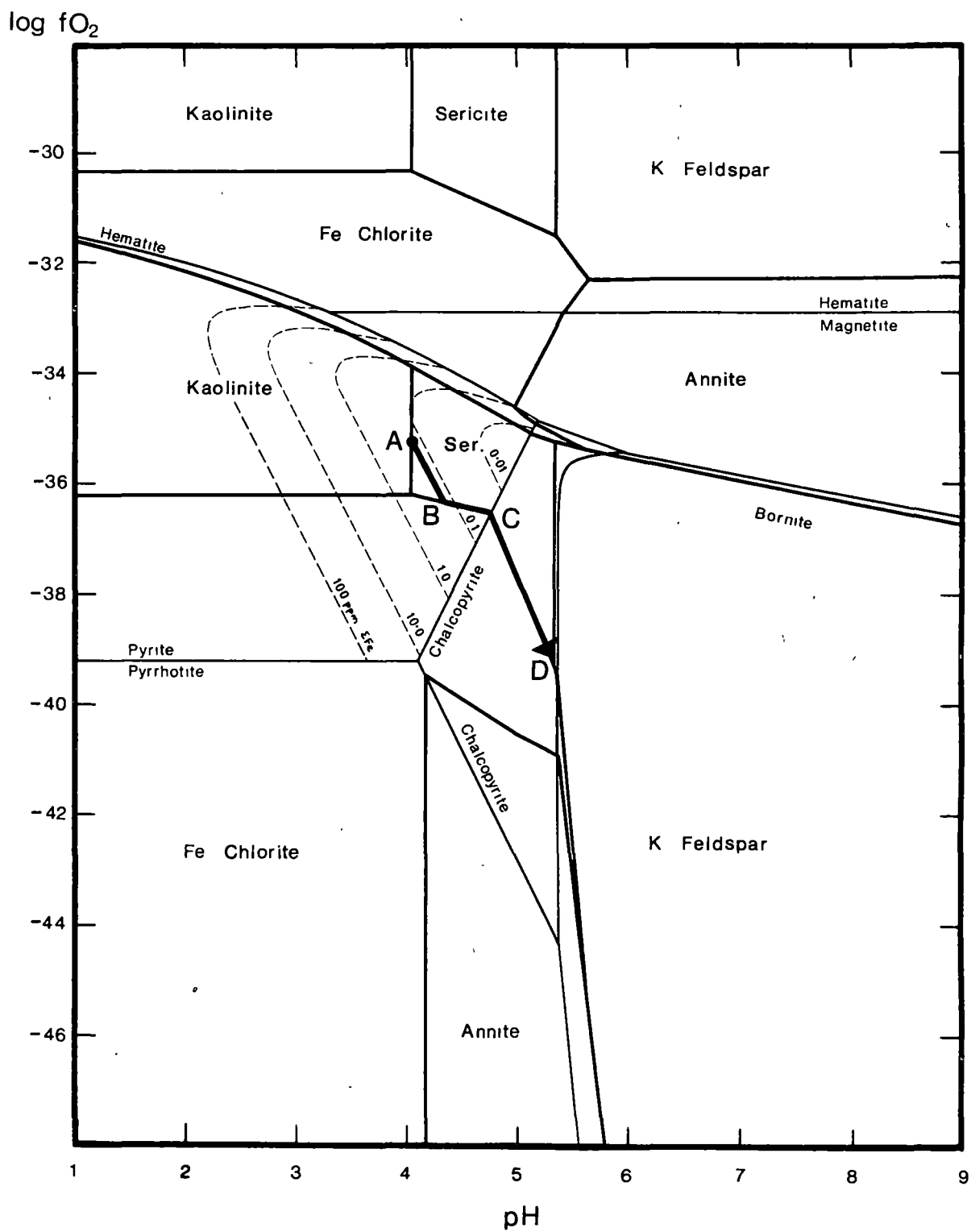
Fig. 3.2: Log fO_2-pH diagram drawn for 250°C and
1 atmos. ΣS = 0.001 and ΣCu = 0.00002 moles/kg H_2O.
Ionic strength = 1. K/Na = 0.1. Activity of H_2O is taken
as unity. Quartz is present in excess.
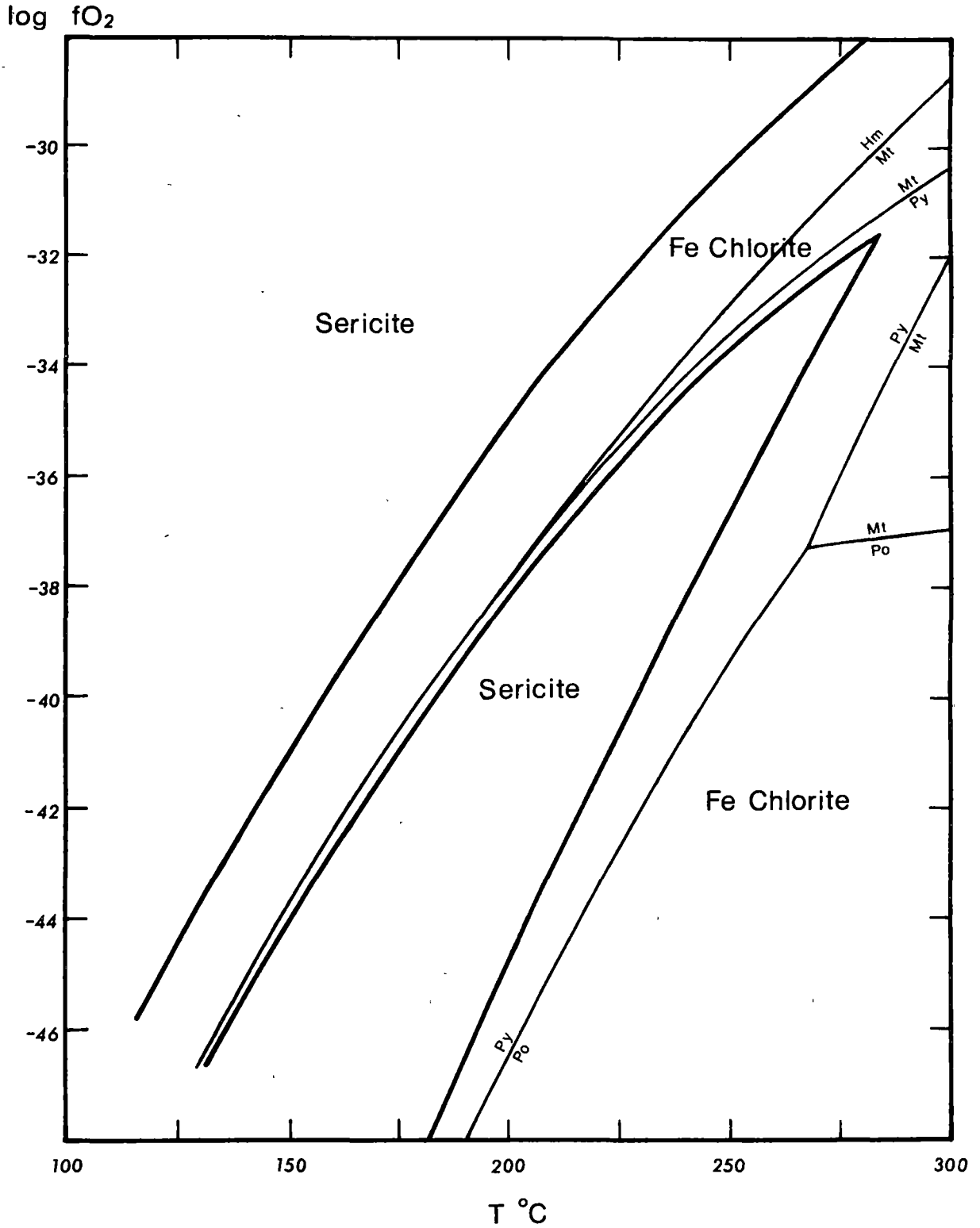
Fig. 3.3: Log fO_2-T diagram for 1 atmos. pH is
buffered at the kaolinite/sericite boundary. ΣS = 0.001
moles/kg H_2O. Ionic strength = 3. K/Na = 0.1. Activity
of H_2O is taken as unity. Quartz is present in excess.

less than 200°C.

Homogenisation temperatures from inclusions in recrystallised fluorite (specimen from a quartz-chlorite-chalcopyrite vein, Western Tharsis D.D.H. 371/229.5) ranged from 130 to 150°C. Applying an approximate pressure correction of 1 Kb gives a temperature of 200 to 225°C (Klevtsov and Lemmlein, 1959).

It is assumed that the metamorphic P-T conditions were probably in the range of 250 to 300°C and 1 Kb. The pyrophyllite may be a hydrothermal phase consistent with the formation of chert from amorphous silica-saturated solutions.

3.2.2 Stability of the Quartz-Sericite-Chlorite-Sulphide-Oxide Assemblage

Although it is clear from figure 3.1 that the assemblage quartz-sericite-chlorite-pyrite-hematite may be a stable assemblage it is clear from figure 3.2 (and fig. B5) that this assemblage will not coexist at reasonable pH values (i.e. within 2 or 3 units of neutrality) for ΣS values in the acceptable ore solution range of 0.1 to 0.001 moles/kg H_2O as given by Ohmoto (1972) for temperatures less than 300°C. A similar relationship will hold over the temperature range of 150-300°C (fig. 3.3). To stabilise the quartz-sericite-chlorite-pyrite-hematite assemblage at 250°C and pH values of not more than 3 units acid it is necessary for ΣS to approximate 50 moles/kg H_2O, which is well above acceptable ore-solution levels. Hence it is unlikely that the quartz-sericite-chlorite-pyrite-hematite assemblage will be a stable hydrothermal assemblage associated with ore deposition. This assemblage may possibly stabilise under metamorphic conditions. A ΣS of approximately 50 moles/kg H_2O represents a mole fraction of S of 0.5 and generating this fluid composition

requires a closed system reaction of limited pore fluids with the sulphides. It should also be noted that to stabilise the assemblage quartz-sericite-chlorite-magnetite and hence quartz-sericite-chlorite-pyrite-magnetite requires a temperature greater than 400°C (fig. B4).

It thus appears that quartz-sericite-chlorite-pyrite (and also chalcopyrite for the appropriate ΣCu value) will not coexist in equilibrium with hematite and magnetite under likely conditions of hydrothermal alteration and also will not coexist in equilibrium with magnetite at likely metamorphic conditions (assuming 1 Kb pressure does not significantly effect the diagrams). Possible equilibrium assemblages for the hydrothermal situation are therefore limited to:

   quartz - sericite - sulphide,

   quartz - sericite - chlorite - sulphide (except coexisting
                                          pyrite and bornite),

   quartz - chlorite - sulphide,

   quartz - chlorite - sulphide - oxide,

   quartz - chlorite - oxide,

   quartz - sericite - chlorite - hematite,

(see fig. 3.2). The assemblage quartz - sericite - chlorite - sulphide - hematite is a possible metamorphic assemblage. Kaolinite may occur with all of the assemblages noted. However, even though certain assemblages are precluded as equilibrium assemblages, they may occur as disequilibrium assemblages, e.g. rapid changes in fO_2 may lead to a partial replacement sequence of quartz - sericite - pyrite to quartz - sericite - chlorite - pyrite to quartz - chlorite - pyrite to quartz - chlorite - magnetite (fig. 3.2). Such replacement
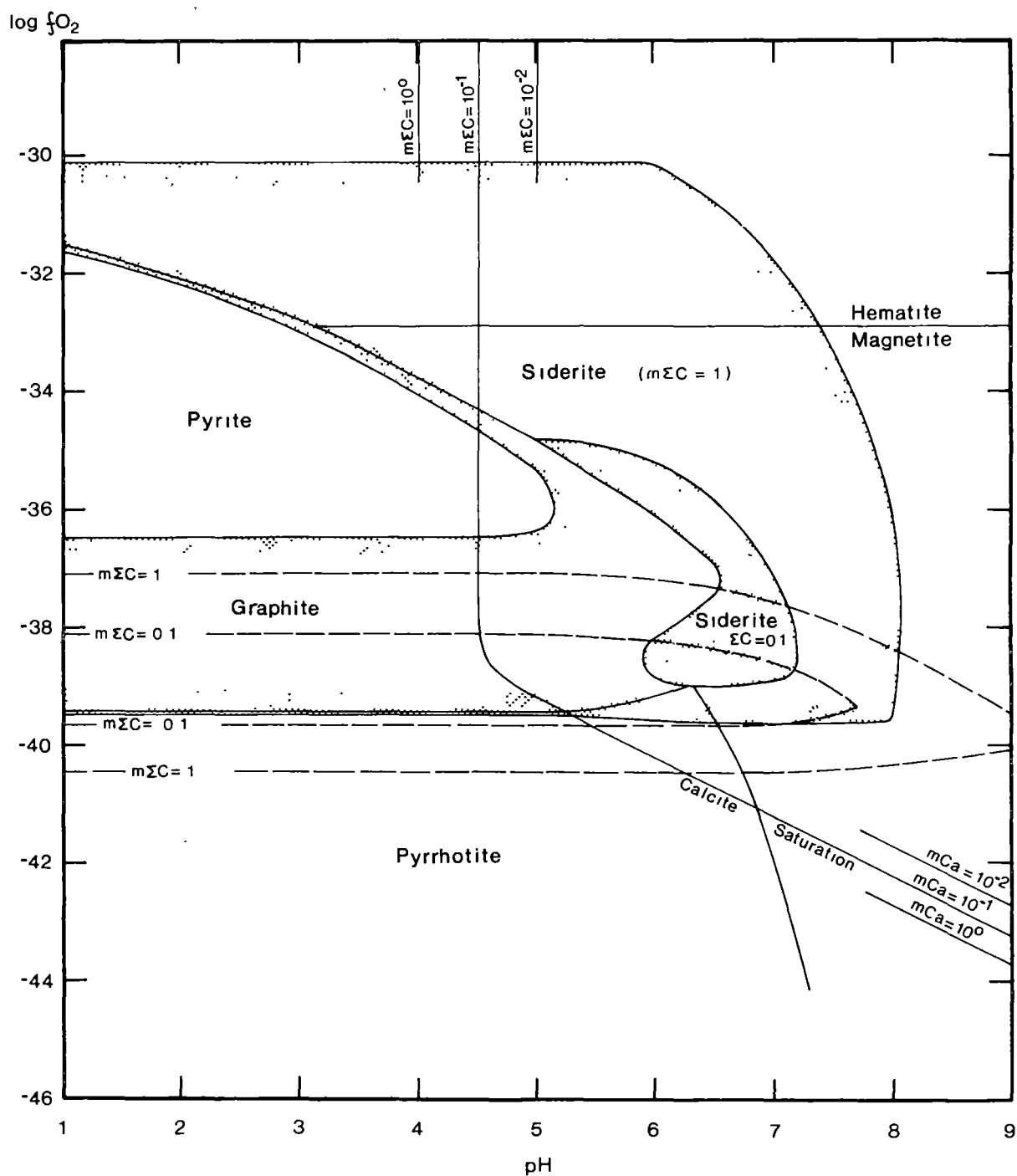
Fig. 3.4:   Log fO_2-pH diagram for 250°C and 1 atmos.
ΣS = 0.001 moles/kg H_2O.   Ionic strength = 3.   Activity of
H_2O is taken as unity.

sequences will be controlled by changes in the fluid phase and pressure, temperature conditions. They are more likely to represent hydrothermal reactions where the alteration products are mainly controlled by the behaviour of the fluid phase and temperature rather than metamorphic reactions where the fluid phase is more likely to be buffered by the host mineralogy and pressure-temperature conditions.

3.2.3 Siderite

The relationship between siderite and the sulphides and oxides is dependent on the relative values of ΣS and ΣC. At low ΣC siderite is restricted to the high pH field and is unstable relative to calcite (fig. 3.4). Increasing ΣC stabilises siderite relative to the oxides and sulphides. Siderite is particularly likely to form equilibrium assemblages with pyrite and hematite-magnetite. Pyrite siderite assemblages at lower fO_2 conditions are likely to be precluded by the graphite saturation line (fig. 3.4). Pyrite is destabilised relative to siderite with increasing temperature (fig. 3.5), although the degree to which this occurs depends on the $\Sigma C/\Sigma S$ ratio.

3.3 Hydrothermal Models

The Mt. Lyell ores consist of a number of discrete mineralized zones, in most cases linked by poorly defined areas of weak mineralization. The spatial relationships between the mineralized zones are poorly understood and it is not possible to tell, from the geology, whether the ores were derived from a single phase, or multiple phases, of hydrothermal activity. Zoning within each unit may have assisted in this problem, but it is limited. The most notable example is the transition from the chlorite assemblage to the sericite assemblage on
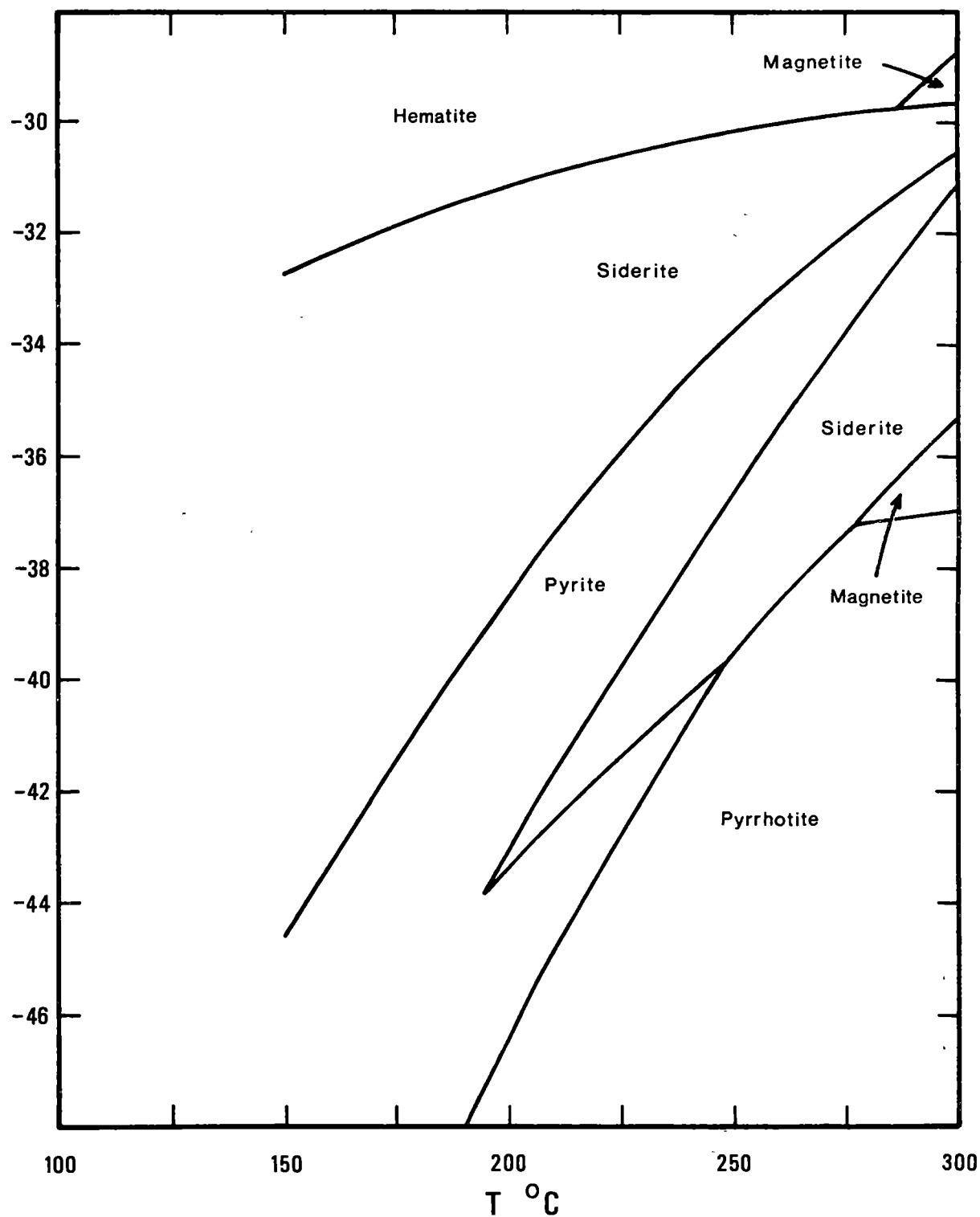
Fig. 3.5: Log fO_2-T diagram for 1 atmos. pH is buffered at the kaolinite/sericite boundary. $\Sigma S = 0.001$ and $\Sigma C = 1.0$ moles/kg H_2O. Ionic strength = 3. K/Na = 0.1. Activity of H_2O is taken as unity.

the northern end of Prince Lyell.

Given these difficulties, the approach adopted has been to test the thesis that each unit is the result of continuous introduction of solution into a given unit of rock until it is completely altered. This will produce a succession of assemblages which will represent neither complete equilibration of the rock with the solution nor complete equilibration of the solution with the rock, but some intermediate stage. In developing models in this manner any assumptions about stratigraphical or structural relationships are avoided. Ultimately it may be possible to use the analysis of the assemblages to assist in interpreting these relationships.

Three basic models are proposed to account for the mineralization and alteration:

1 The alteration and mineralization is controlled by pH changes induced by reaction between the ore solution and the host rock at constant temperature. This is the simplest possible model that could be used to explain the disseminated sulphide mineralization.

2 Reaction of the solution and the host rock occurs with some decrease in the temperature.

3 Reaction of the solution and the host rock occurs with a decrease in the temperature and an increase in the oxidation conditions. This situation would reflect a near surface environment relative to 1 and 2.

Because there is always the potential for interference between the three basic models, they need to be viewed as convenient end-member models, each of which appears to have been the dominant mechanism in a particular situation.

3.4 Discussion of the Prince Lyell Alteration Assemblages.

3.4.1 Summary of the Salient Features of the Prince Lyell Alteration Assemblages.

Prince Lyell has been subdivided into a number of alteration assemblages.

A. Altered felsic volcanic rocks.

(i) Quartz-sericite-chlorite-pyrite-chalcopyrite alteration in the Central Core of Prince Lyell. Minor carbonate (siderite), rutile, hematite, apatite and more rarely magnetite and barite are present. Numerous inclusions occur in the pyrite, most commonly chalcopyrite, hematite and rutile. Groups of inclusions occurring in pyrite but not in the groundmass are:- (a) chalcopyrite-bornite, bornite, bornite-digenite; (b) pyrrhotite-chalcopyrite, pyrrhotite.

(ii) Quartz-sericite-pyrite±chalcopyrite alteration. Minor carbonate (siderite), rutile and barite are present. Hematite is rare and bornite was found in one specimen. Inclusions occurring in the pyrite but not found in the groundmass are: (a) pyrrhotite, pyrrhotite-chalcopyrite; (b) mawsonite (rarely); (c) bornite-chalcopyrite, bornite and bornite-digenite.

(iii) Footwall alteration. The common assemblage is quartz-sericite-pyrite with minor hematite, siderite, chlorite and barite. Of note is the quartz-chlorite-sericite-hematite-magnetite-pyrite-chalcopyrite-siderite assemblage occurring adjacent to the central core chlorite alteration; hematite replaces magnetite.

Massive-pyrite banding occurs, particularly in the quartz-sericite-pyrite assemblage. Minor massive magnetite with chlorite and apatite occurs. Apatite is partially replaced.

B. Altered intermediate/mafic volcanic hosts.

The common assemblage is quartz-chlorite-sericite-magnetite-hematite-pyrite.

3.4.2 Discussion and Interpretation of the Prince Lyell Central Core Quartz-Sericite-Chlorite-Pyrite-Chalcopyrite Assemblage.

All of the major phases in this assemblage may coexist under the P-T conditions considered reasonable for the initial hydrothermal alteration and the metamorphism. It is most likely they were initially hydrothermal phases that have subsequently been recrystallised. Some minor changes in the silicate compositions may be anticipated but significant sulphide/silicate reactions are unlikely at this low metamorphic grade. The study of Bachinski (1976) gives an indication of the metamorphic sulphide/silicate reactions possible at higher temperatures.

This central core assemblage commonly contains minor hematite, siderite and more rarely magnetite in the groundmass. As noted in 3.2.2 the assemblage quartz-sericite-chlorite-sulphide-hematite cannot be considered an equilibrium hydrothermal assemblage although it may be possible as a metamorphic assemblage, or as a high oxidation disequilibrium assemblage. This latter possibility is unlikely as the oxides and barite would become major phases. The simplest explanation is to assign the minor hematite to a metamorphic product. This is consistent with the observations and conclusions from 2.2. Obviously from the discussion in 3.2.2 attainment of sulphide-hematite equilibrium requires local dissolution of sulphide. The minor amounts of hematite present

suggest that if this reaction occurred the sulphur loss would have been minimal. The sulphur in the fluid phase, if not lost from the system, might rereact with hematite to give retrograde pyrite. This would account for hematite inclusions in the pyrite. Alternatively pyrite-hematite equilibrium may not have been established during the metamorphism. The hematite may have been derived from oxidation of minor amounts of magnetite or pyrrhotite, now only found as an inclusion phase in pyrite.

Although the overall hydrothermal reaction was from a felsic volcanic rock to a quartz-sericite-chlorite-pyrite-chalcopyrite assemblage it is clear from the inclusion assemblages found in the pyrites that the reaction was more complex than simply quartz,sericite, chlorite,pyrite and chalcopyrite forming in equilibrium. The sulphur isotope and trace element date (see chapters 4 and 5 respectively) support this conclusion.

As noted above, the simplest reaction mechanism is the reaction of the felsic host with the ore solution at constant temperature, and confining pressure sufficient to prevent boiling of the solutions. In the following discussion of this possible mechanism it will be assumed the solution was an acid, chloride-rich solution[1] with the pH initially buffered close to the kaolinite/sericite boundary. The host rock can be approximated to quartz, K-feldspar, albite and minor anorthite.

If the reaction of a limited amount of solution with the host rock is considered, initially sericite will be produced at the expense of the feldspar and the pH increase.

1   The likely ionic strength and K/Na ratio of solution are 0.5-1.0 m NaCl and 0.1 respectively, consistent with the data from Kuroko, Tokunaga and Honma (1974), the experimental work of Dickson and Ellis (1976) on seawater/rhyolite reaction, and the K/Na vs temperature plot of natural waters of White (1968). The diagrams have been constructed for a range of ionic strengths.

e.g. $3 \ Na \ Al \ Si_3 \ O_8 + K^+ + 2 \ H^+ \ \rightleftarrows$

$$K \ Al_3 \ Si_3 \ O_{10} \ (OH)_2 + 3 \ Na^+ + 6 \ SiO_2 \qquad (3.1)$$
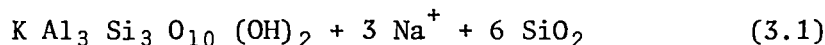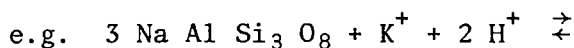
The initial increase in pH will lead to the saturation of

pyrite at position A in figure 3.2 if it is not already

saturated.

$$FeS_2 + H_2O + 2H^+ \ \rightleftarrows \ Fe^{2+} + 2H_2S + \tfrac{1}{2}O_2 \qquad (3.2)$$
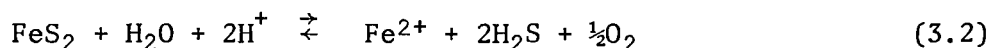
Continued increase in pH as reaction proceeds will lead to a

decrease in fO_2 of 4 units per unit change of pH:

$$\log fO_2 = 2 \log K_{3.2} + 4 \log \gamma H^+ - 2 \log aFe^{2+}$$

$$- 4 \log aH_2S - 4 \ pH \qquad (3.3)$$

assuming aFe^{2+} and aH_2S remain approximately constant.

Decreases in aFe^{2+} and aH_2S would lessen the decrease in fO_2

per unit increase in pH (ΣFe contours for the pyrite field

are shown in fig. 3.2).

Continuing decrease in fO_2 causes Fe chlorite to saturate at B

(fig. 3.2) probably at the expense of some pyrite already

precipitated.   The fO_2/pH path is now constrained by the reaction

$$K \ Al_3 \ Si_3 \ O_{10} \ (OH)_2 + 4.5 \ FeS_2 + H^+ + 11.5 \ H_2O$$

$$\rightleftarrows \ Fe_{4.5} \ Al_{3.0} \ Si_{2.5} \ O_{10} \ (OH)_8 + 0.5 \ SiO_2 + K^+$$

$$+ 9 \ H_2S + 2.25 \ O_2 \qquad (3.4)$$
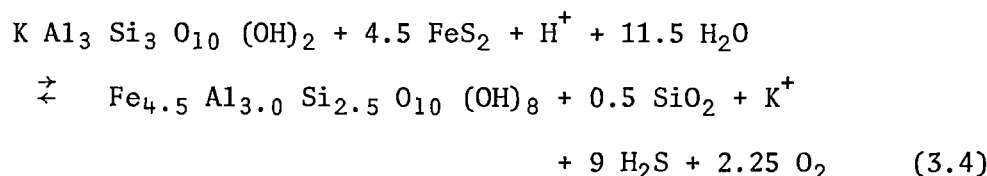
for which

$$\log fO_2 = 0.44 \log K_{3.4} - 4 \log aH_2S + 0.44 \log \gamma H^+$$

$$- 0.44 \log aK^+ - 0.44 \ pH \qquad (3.5)$$

This leads to an increase in the rate of change in pH relative

to fO_2 and causes a marked decrease in ΣFe in solution (fig. 3.2).

Any decrease in aH_2S will further increase the pH change relative

to the fO_2 change.   Continued reaction leads to chalcopyrite

precipitation at C at the expense of pyrite.

$$FeS_2 + Cu^+ + \tfrac{1}{2}H_2O \ \rightleftarrows \ Cu \ FeS_2 + H^+ + \tfrac{1}{4} \ O_2 \qquad (3.6)$$
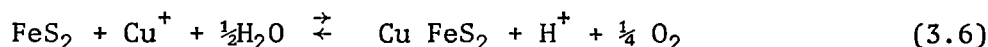
Reaction will continue at C until all the pyrite has been

replaced. The solution will then be buffered by the reaction

$$K\ Al_3\ Si_3\ O_{10}\ (OH)_2\ +\ 4.5\ Cu\ FeS_2\ +\ 9.25\ H_2O\ +\ 5.5\ H^+$$

$$\overrightarrow{\leftarrow}\quad Fe_{4.5}\ Al_3\ Si_{2.5}O_{10}\ (OH)_8\ +\ 0.5\ SiO_2\ +\ K^+$$

$$+\ 4.5\ Cu^+\ +\ 9\ H_2S\ +\ 1.125\ O_2 \qquad (3.7)$$
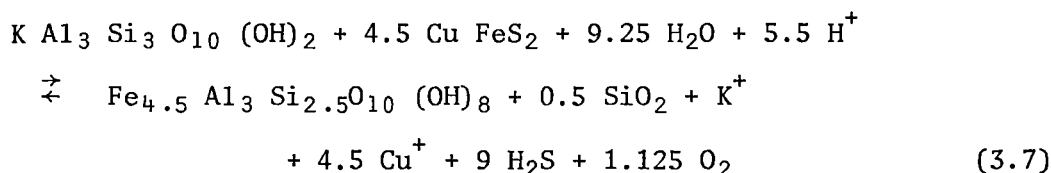
for which

$$\log\ fO_2\ =\ 0.89\ \log\ K_{3.7}\ -\ 0.89\ \log\ K^+\ -\ 4\ \log\ aCu^+$$

$$-\ 8\ \log\ aH_2S\ +\ 4.89\ \log\ \gamma H^+\ -\ 4.89\ pH \qquad (3.8)$$

Continued reaction leads to further increase in pH and decrease

in fO_2 along CD until at D K-Feldspar equilibrates with the

solution. No further pH change will occur and therefore no

further reaction between the sulphides is possible. Further

reaction will be limited to K^+ exchange with Na^+ and Ca^{2+}.

A summary of the reaction sequence is:

1. quartz - sericite

2. quartz - sericite - pyrite

3. quartz - sericite - chlorite - pyrite

4. quartz - sericite - chlorite - pyrite - chalcopyrite

5. quartz - sericite - chlorite - chalcopyrite

6. quartz - sericite - K Feldspar - chlorite - chalcopyrite

Depending on the initial mK^+/mCu^{1+} ratio it is possible that

before K-Feldspar equilibrates and the reaction stops, bornite

will replace chalcopyrite.

The reaction paths in fig. 3.2 have been plotted assuming

that from A to B, ΣFe and ΣS are effectively constant, from B to

C ΣS is effectively constant and that from C to D and E ΣS and ΣCu

are constant. These assumptions may be examined by calculating

the decrease in concentration in solution of these species as

reaction proceeds (see chapter 6).

Within the framework of this model the quartz-sericite-chlorite-pyrite-chalcopyrite assemblage of the central core must represent the reaction of just sufficient solution (of condition A) with the host rock (effectively represented by some point in the quartz, K-feldspar field) to completely alter the rock and produce the assemblage at C.   A higher total-solution/total-altered-rock ratio would have produced some assemblage along AC, a lower total-solution/total-rock ratio would have produced some assemblage along CD.   The assemblage at D effectively represents the reaction of a limited amount of solution at condition A with the rock, the assemblage at A represents the reaction of a large volume of solution with rock and the phases produced are in equilibrium with the initial solution.

Given the inhomogeneous nature of the host rocks, it is likely the solution/rock ratio varied considerably, at least locally, throughout the period of alteration. Hence, although the mean total-solution-introduced/total-rock-altered ratio produced an assemblage at C there was probably a significant deviation from the mean which produced a significant variation in the total amount of sulphide produced, the sericite/chlorite ratio and the pyrite/chalcopyrite ratio. It is possible that in local environments and for short periods the assemblage at D was stable and this could include bornite if the ΣCu in solution was sufficient. Because a quartz-sericite-chlorite-chalcopyrite-bornite assemblage represents a large deviation from the mean it would be inherently unstable and likely to be replaced. This is consistent with the bornite and bornite/chalcopyrite inclusions observed in the pyrite. Given this interpretation, and within the temperature and solution conditions already specified, a lower

limit can be placed on the ΣCu in solution. However, within this pH controlled model there is not a ready explanation for the pyrrhotite inclusions or the magnetite. This suggests some modification of the mechanism is necessary to fully account for the observed assemblages. A suitable modification would be to allow for some cooling (and possibly some oxidation?) during initial reaction. This would permit an initial assemblage of quartz-chlorite-magnetite (fig. 3.3) or of quartz-chlorite-magnetite-pyrrhotite, given an initial ΣS of approximately 0.01 moles/kg H_2O.

Cooling would lead first to a quartz-chlorite-pyrite assemblage and then to a quartz-sericite-chlorite-pyrite assemblage. If further cooling continued this would lead to a quartz-sericite-pyrite assemblage. However, if the temperature is maintained and given that the host-rock reaction will tend to buffer the solution at the quartz-sericite-chlorite-pyrite boundary, the reaction is then likely to proceed as outlined earlier.

This alternative mechanism, which allows for the formation of magnetite and pyrrhotite (now only found as an inclusion phase in the pyrite), also provides for the formation of siderite. Comparison of figures 3.2 and 3.4 indicates that siderite is an unlikely phase in the constant temperature, pH controlled reaction path. However, because the lower oxidation field of siderite expands relative to pyrite with increasing temperature, (fig. 3.5) there is a greater probability of forming siderite at an initially higher temperature. (The ΣC of 1.0 moles/kg is given as an example and not as the envisaged ΣC content of the system).

In summary, the following reaction sequence is proposed for the formation of the Prince Lyell central-core chloritic assemblage:-

(a)   quartz-chlorite-pyrrhotite/magnetite-siderite

(b)   quartz-chlorite-pyrite

(c)   quartz-sericite-chlorite-pyrite

(d)   quartz-sericite-chlorite-pyrite-chalcopyrite

(e)   quartz-sericite-chlorite-chalcopyrite-bornite.

It would be reasonable to include the massive magnetite and the apatite as part of phase (a). The commonly corroded nature of apatite in the chlorite assemblages suggests this might be an early phase but this is not always the case.

3.4.3   The Footwall Alteration Assemblages

It has been concluded that the initial assemblage of the central-core alteration may have been of the type

quartz-chlorite-pyrrhotite/magnetite-siderite and

quartz-chlorite-pyrite.

This proposed early assemblage is similar, given that pyrrhotite is now only stable as remnant inclusions in pyrite and that all the oxide was initially magnetite, to the quartz-chlorite-oxide-pyrite-chalcopyrite-siderite assemblage which is developed as a diffuse zone on the footwall side of the central core (figs. 2.3 and 2.4). It is suggested that this zone is a remnant of the early stages of alteration and mineralization.

The relationship of the predominant quartz, sericite, pyrite, minor hematite, chlorite, siderite, barite assemblage of the pink rhyolite to the central-core chloritic zone is not clear. There is no evidence to suggest alteration of magnetite to hematite. Generally sulphide appears to be replacing hematite and the sulphur isotope data (chapter 4) gives no indication of pyrite-hematite equilibrium. It is therefore suggested that the altered pink rhyolite represents a pre-sulphide or pre-mainstage sulphide

alteration. This would be an oxidising alteration producing

an assemblage quartz-sericite-hematite-carbonate-barite and

possibly including clay minerals. A similar style of alteration

occurs in the hanging wall of Cape Horn and in parts of Western

Tharsis and suggests an early stage of non-sulphide alteration

was developed over much of the field.

3.4.4 Quartz-Sericite-Pyrite-Alteration

Within the framework of the constant-temperature, pH-

controlled model the quartz-sericite-pyrite assemblage of Prince

Lyell could be considered an initial alteration assemblage with a

probable prograde relationship to the chloritic assemblage.

However, given the above conclusion that this model is inadequate

to fully account for the chloritic assemblage, this interpretation

is no longer tenable. An alternative is to consider the

assemblage a late-stage alteration event, forming at a lower

temperature and possibly higher oxidation conditions.

The occurrence of rare bornite in the groundmass might suggest

some proximity to the chalcopyrite-bornite-pyrite triple point.

The occurrence of pyrrhotite inclusions would be consistent with

the assemblage being prograde, in part, over an existing pyrite-

chlorite assemblage.

Pyrite commonly occurs as massive bands which Reid (1976)

has suggested may be of exhalative origin.

3.4.5 A Summary of the Proposed Sequence of Events

Alteration in the Prince Lyell area probably commenced with

a nonsulphide quartz-sericite-hematite-siderite-barite alteration.

Mainstage sulphide deposition and alteration probably began

with a pyrrhotite (?), magnetite, chlorite and siderite assemblage

being superposed on the partially altered volcanics. The
magnetite-chlorite-hematite-siderite and magnetite-hematite
assemblage on the footwall is interpreted as representing
this early assemblage (assuming the hematite is after magnetite).

Cooling of the solutions led to the formation of pyrite and sericite, and
increasing pH, as reaction with the host rock proceeded, led to the forma-
tion of chalcopyrite. If pyrite was at any stage completely
replaced (or nearly so, such that its buffering capacity
diminished) then the pH could increase further to produce
bornite. The overall reaction sequence gave rise to a quartz-
sericite-chlorite-pyrite-chalcopyrite assemblage. Initial
highest temperature phases pyrrhotite and magnetite and the high
pH phase bornite were generally short lived.

The location of the ore deposit was probably controlled by the
fragmental nature of the volcanics (MacDonald, 1968). A late-
stage phase of mineralization and alteration superposed a quartz-
sericite-pyrite-chalcopyrite assemblage onto the northern end of
Prince Lyell.

Metamorphism produced hematite by the oxidation of magnetite,
pyrrhotite (?) and pyrite (?). All phases except pyrite appear
to have been completely recrystallised. Quartz, siderite,
chalcopyrite and chlorite have been locally remobilised.

Hendry (1972) has suggested that the formation of Prince Lyell
involved two phases of mineralization; an early phase of pyrite,
magnetite, siderite and apatite, and a later phase of chalcopyrite,
hematite, barite, apatite and rare-earths. There is some
similarity between this two phase proposal and the sequence of
events proposed above, for mainstage sulphide deposition and
alteration. However, Hendry (pers. comm.) has suggested the
two phases of mineralization are quite separate events rather than

the one sequence of events as proposed here.   Also, it is

argued here that hematite is an early alteration phase and/or a

metamorphic phase and that barite is an early alteration phase.

Hendry's work has demonstrated a marked rare-earth enrichment

associated with the Prince Lyell mineralization.

3.5   Discussion of Western Tharsis

Western Tharsis is essentially a large zone of quartz-sericite-

pyrite-minor chalcopyrite alteration of felsic volcanics.   Minor

chlorite may occur and also some bornite.   Bornite is also a common

inclusion phase in pyrite with chalcopyrite and digenite.   Pyrrhotite

inclusions are rare.

The quartz-sericite-pyrite assemblage stablises relative to the

quartz-sericite-chlorite-pyrite assemblage with increasing ΣS.   Hence,

reaction of a solution of high initial ΣS and low pH with the host

rock, at constant temperature, would produce the following reaction

sequence:-

1. quartz - sericite

2. quartz - sericite - pyrite

3. quartz - sericite - pyrite - chalcopyrite

4. quartz - sericite - chalcopyrite

5. quartz - sericite - chlorite - chalcopyrite

6. quartz - sericite - K feldspar - chlorite - chalcopyrite

If the ΣS was sufficiently high no chlorite will precipitate at any stage.

As indicated by fig. 3.3, the quartz - sericite - pyrite field expands

as the temperature decreases.   This allows an alternate mechanism of a

lower temperature to account for the formation of the quartz-sericite-

sulphide assemblages.   A high ΣCu will also favour the formation of

this assemblage.   A low ΣCu and high ΣS will allow the formation of a

pyrrhotite assemblage.

The common occurrence of bornite and bornite-chalcopyrite

inclusions, locally found in regular growth zones, and also the

occurrence of bornite as a groundmass phase, suggests some

proximity to the bornite-chalcopyrite-pyrite triple point.

Chlorite may still occur as a minor component in some sections

as does rare magnetite, magnetite inclusions in pyrite and very

rare pyrrhotite inclusions. These features suggest minor influences

of the conditions envisaged for the Prince Lyell chlorite assemblage.

There is a basic similarity between the quartz-sericite-pyrite

assemblages of Western Tharsis and Prince Lyell, and suggests an

overall similarity of depositional conditions. Also, as noted in

2.3, the footwall of the Western Tharsis mineralization has a similar

mineralogy to the footwall of Prince Lyell. A similar origin to

that suggested for the Prince Lyell footwall is implied.

3.6   Discussion of the North Lyell and Crown Lyell Ores

3.6.1   Summary of the North Lyell and Crown Lyell Ores

The ores consist of three types:

1. Siliceous pyrite-chalcopyrite mineralization.

    e.g. Crown Lyell No. 3 which consists of mineralized

    massive or brecciated chert and/or silicified volcanics(?).

    Minor bornite, carbonate, barite and sericite are present.

2. Chloritic pyrite-chalcopyrite mineralization.

    e.g. Lyell Tharsis, Crown Lyell No.1, footwall of

    Crown Lyell No.3.   The deposits have a typical

    alteration assemblage of quartz-chlorite-minor sericite-

    pyrite-chalcopyrite-magnetite-hematite-barite and

    minor carbonate.

Fig.3.6: Log fO_2-T diagram indicating probable fO_2-T conditions of deposition for the Mt. Lyell mineralization.

1. Possible early phase of Prince Lyell mineralization:- qtz-chl-mt-po-sid (mt and sid not shown).

2. Main-stage Prince Lyell mineralization:- qtz-ser-chl-py-ccp, and late-stage qtz-ser-py-minor ccp.

3. Crown Lyell No.3 mineralization:- qtz-minor ser-py-ccp-minor barite.

4. North Lyell, Crown Lyell No.2 and 12 West mineralization:- qtz-minor ser-minor pyrophyllite-bn-ccp-minor py.

5. Crown Lyell No.3 footwall, Crown Lyell No.1 and Lyell Tharsis (in part) mineralization:- qtz-minor ser-chl-py-ccp-hematite/magnetite-barite.

Diagram conditions: log $\Sigma KCl/\Sigma HCl$ = 3.0, log ΣS = -2 and log ΣCu = -4.5. mNa = 1.0, mK = 0.1 and mBa = 0.001 moles/kg H_2O.   Quartz is present in excess.

The diagram was constructed using a modified program from Pennsylvania State University (courtesy of M E. Ripley, 1976) and the pyrite and chalcopyrite solubility data of Crerar and Barnes (1976).
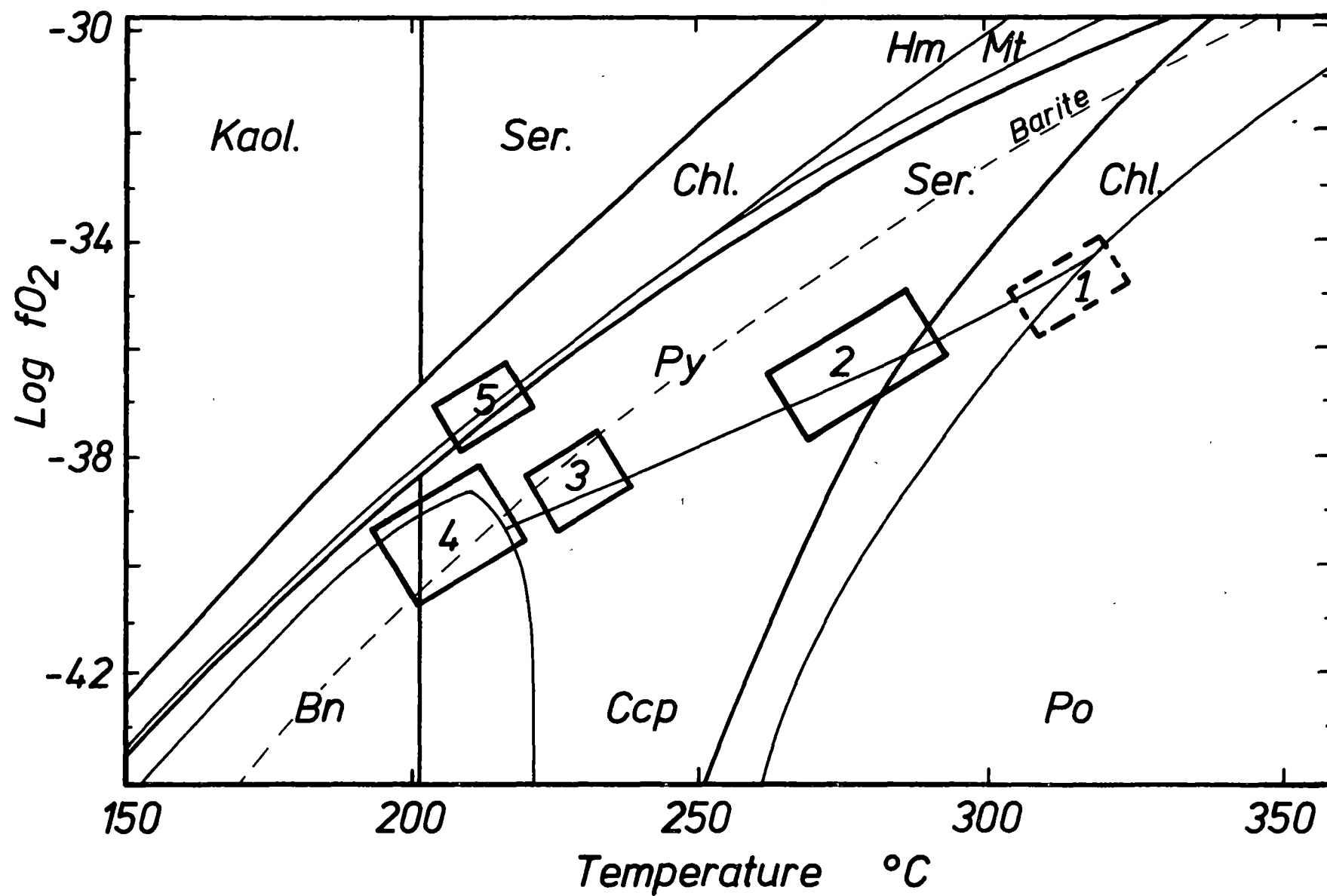
3. Siliceous bornite-chalcopyrite mineralization.

   e.g. North Lyell, Crown Lyell No. 2, 12 West. The
   deposits consist of disseminated bornite and
   chalcopyrite in fine-grained massive or brecciated
   chert or quartz-sericite schists. Minor sericite
   and pyrophyllite are present.

3.6.2 The Bornite Ores

In comparison with the pyrite-chalcopyrite assemblages,
which constitute the bulk of the Mt. Lyell mineralization, the
bornite ores represent a markedly different style of mineraliza-
tion. Previous workers (Solomon, 1964; Markam, 1968; Green,
1971) have suggested the chert bodies occurring at North Lyell
and Comstock formed as sinter deposits around volcanic fumaroles
and the bornite ores have been linked to this environment.
To saturate bornite, rather than pyrite or chalcopyrite,
in the presence of kaolinite or pyrophyllite, given the same
                    ionic strength and temperature as assumed in the
discussion of Prince Lyell and Western Tharsis, requires a higher
ΣCu in solution. Hence to produce the bornite ores, maintaining
the same temperature of formation as Prince Lyell, would require
either a different, Cu-enriched, solution or some local enrichment
of Cu in solution, possibly by boiling. However, as the solutions
would need to be enriched in Cu by at least an order of magnitude
the latter is an unlikely mechanism. Bornite stablises relative to
pyrite and chalcopyrite with decreasing temperature (fig. 3.6) and
therefore the simplest method of forming the bornite ores is to
assume a solution of similar ΣCu to that suggested for the
formation of Prince Lyell and to quench the solution through
the pyrite field into the bornite field. This mechanism would
probably require a near surface environment resulting in oxidising

conditions.   The light sulphur isotope values of the North Lyell
ores (chapter 4) are consistent with this suggestion.   Quenching
could also saturate amorphous silica and produce pyrophyllite.
The conditions envisaged are consistent with the fumarolic
environment suggested by earlier workers.   Boiling, although not
directly controlling the precipitation of bornite, is probably
the main cause of heat loss and the temperature decrease in the
system.

3.6.3   The Chloritic Pyrite-Chalcopyrite Mineralization

This chlorite assemblage differs from the Prince Lyell
chloritic assemblage in that it contains significant amounts of
hematite/magnetite and barite and no pyrrhotite inclusions in the
pyrite.   The barite and lack of pyrrhotite inclusions dis-
tinguishes the assemblage from the chlorite-oxide assemblage of
the Prince Lyell footwall.   The combination of chlorite-oxide-
barite suggests the chlorite represents the high-oxidation
chlorite stability field (figs. 3.2, 3.3 and 3.6) rather than the
low-oxidation chlorite stability field which Prince Lyell chlorites
represent.   The high-oxidation conditions required by this
assemblage type are consistent with the proximity of these ores
to the bornite ores.   The temperature of formation was probably
similar to temperature of formation of the bornite ores.   The
mineralization possibly represents the reaction of dispersed
fluids around the fumarolic centres with the volcanics.

Increasing fO_2, decreasing the temperature, and increasing the
pH through reaction with the volcanics could produce the following
assemblages:-

quartz - sericite - pyrite ± chalcopyrite ± barite

quartz - sericite - chlorite - pyrite ± chalcopyrite ± barite.

For further changes in the pH and the temperature the solution would remain buffered at the quartz-sericite-chlorite-sulphide boundary. Further increases in fO_2 (probably caused by reaction with oxygenated groundwaters) would lead to:-

quartz - chlorite - pyrite ± chalcopyrite ± barite

quartz - chlorite - pyrite - magnetite (hematite) ± barite

quartz - chlorite - magnetite (hematite) ± barite

3.6.4 The Siliceous Pyrite-Chalcopyrite Mineralization

The siliceous nature of this ore and its proximity to the bornite ores suggests a similar environment of deposition for this deposit. It is likely (fig. 3.6) the pyrite-chalcopyrite ore formed at a higher temperature than the bornite ore and at lower oxidation conditions relative to the chlorite, disseminated pyrite-chalcopyrite ores.

Crown Lyell No. 3 has the highest total sulphide content of the disseminated pyrite-chalcopyrite ores. It averages 20% compared to Prince Lyell 13% and Cape Horn 10%. The higher total sulphide content may reflect sulphide deposition essentially controlled by decreasing temperature rather than by increasing pH through reaction with the host rock.

3.6.5 Summary

The North Lyell-Crown Lyell ores represent a different style of mineralization. It is argued that this reflects different conditions of deposition rather than requiring a different solution composition. The bornite ores contain a wide variety of accessory phases not observed in the other deposits (e.g. mawsonite, betechtinite, stromeyerite) and it is probable

they also reflect the different conditions of deposition.

Sphalerite and galena occur as accessories. Given the reaction

path in figure 3.6, if significant Pb and Zn were present in

solution galena and sphalerite could be expected to occur as

major phases. At higher temperatures significant Pb and Zn

could be present in solution and galena and sphalerite not

saturate. The minimum amounts of galena and sphalerite present

therefore suggests high Cu/Zn and Cu/Pb ratios in the solutions

responsible for much of the Mt. Lyell mineralization.

The Lyell Comstock mineralization is similar to North Lyell-

Crown Lyell (Green, 1971; Reid, 1976) probably reflecting a

similar environment of deposition.

3.7 Cape Horn

Cape Horn has assemblages similar to Prince Lyell, Western

Tharsis and North Lyell-Crown Lyell. The ore body horizon contains

the following assemblages:-

    quartz-sericite-chlorite-pyrite-chalcopyrite.

    quartz-sericite-chlorite-pyrite-chalcopyrite-barite.

    quartz ± sericite-chlorite-magnetite-hematite-pyrite-

                            chalcopyrite-barite.

    quartz-sericite-pyrite-chalcopyrite ± bornite.

Magnetite-hematite and magnetite-hematite-chalcopyrite inclusions

are common in the pyrite. Pyrrhotite-chalcopyrite inclusions were

observed in one section. The ore body has a total sulphide content

of 10% with pyrite and chalcopyrite present in approximately equal

proportions. The average chlorite content of the orebody is

approximately 8%.

The combination of assemblages common to Prince Lyell and North

Lyell-Crown Lyell suggests fO_2-T conditions intermediate between the conditions envisaged for these deposits. The occurrence of chlorite assemblages consistent with the high and low oxidation quartz-sericite-chlorite-pyrite boundary suggests proximity to the point of convergence of the two boundaries. If the temperature of formation lies between the likely temperatures of formation of Prince Lyell and North Lyell this implies a low ΣS content for the solution.

The hangingwall assemblage is similar to the footwall assemblage of Prince Lyell. Textural evidence suggests the pyrite replaces the hematite.

4. SULPHUR ISOTOPES

4.1 Introduction

Solomon, Rafter and Jensen (1969) published data on the δS^{34} values of sulphides and sulphates from Mt. Lyell in a general sulphur and oxygen isotope report on the Mt. Lyell, Rosebery and Mt. Farrell ores. For Mt. Lyell they found the sulphide ratios formed two groups:

1) The pyrite-chalcopyrite ores from the Blow, West Lyell, Lyell Comstock (massive sulphide lens) and Tasman and Crown Lyell which gave a range of +10.0 to +5.2 $^0/_{00}$, and average of +7.00 $^0/_{00}$ and a standard deviation of 1.2 $^0/_{00}$.

2) The bornite-chalcopyrite-pyrite ores from North Lyell, Crown Lyell No.2 and 12 West which gave a range of +0.8 to -7.7 $^0/_{00}$ with an average of -2.6 $^0/_{00}$.

Data on coexisting samples were limited to four pyrite-chalcopyrite pairs from Crown Lyell No. 2(2) and 12 West (2). These gave $\Delta S^{34} py-ccp$ results of +1.0 and +1.2, and +0.3 and +0.6 respectively. Later additional analyses (7) were made on the chert ores of Lyell Comstock by Dr. Rafter. These showed a similar range (+3.5 to -10.5) to the group 2 ores (samples collected by G.R. Green). Solomon *et al.* *(op. cit.)* were unable to suggest a satisfactory explanation for the two groups. However in the light of the work of Sakai (1968) and Ohmoto (1972), Solomon and Green (pers. comm.) have suggested higher oxidation and probable lower temperature conditions of formation to account for the lower δS^{34} values of group (2).

The current work was intended to investigate δS^{34} partitioning between pyrite and chalcopyrite. Most of the samples (28) were analysed by Dr. B. Robinson of the D.S.I.R. for Dr. M. Solomon. An

additional 20 samples were analysed by J.W. Smith of the C.S.I.R.O.
The 48 additional analyses included 17 pyrite-chalcopyrite pairs,
two of which were duplicates.

4.2 Sample Preparation and Data

The samples used in this additional work were a selection of
those prepared by the author for the study of trace element dis-
tribution in pyrite and chalcopyrite.   They were separated from bulk
ore samples using flotation and where necessary magnetic separation
for further cleaning.   A detailed description of sampling method,
separation technique and purity is given in Appendix C.   One sample (4-5/
228) had an unusual texture of 1-2 cm sized augens or kernels of
pyrite in a very chalcopyrite-rich matrix. This permitted separation
(by M. Solomon using a small drill) of chalcopyrite and adjacent
pyrite in a small area approximately 2 cm by 1 cm.   The new data is
given in table 4.1 with the analysing laboratory indicated.   Inter-
laboratory checks between C.S.I.R.O. and D.S.I.R. suggests a difference
of no greater than 0.3 $^0/_{00}$ is likely between results from the
C.S.I.R.O. and the D.S.I.R.

Histogram plots of all available pyrite and chalcopyrite data
for each orebody are shown in figures 4.1.1 and 4.1.2.   Histogram
plots of the spread of ΔS^{34}py-ccp values for each orebody are shown in
table 4.2 and figure 4.2.

4.3 Discussion of Data

4.3.1 Comparison of Cape Horn and Western Tharsis with West
Lyell (Prince Lyell) and the Chert Ores

The new data has tended to merge the initial groups dis-
tinguished by Solomon *et al.* (1969).   Cape Horn samples have a range
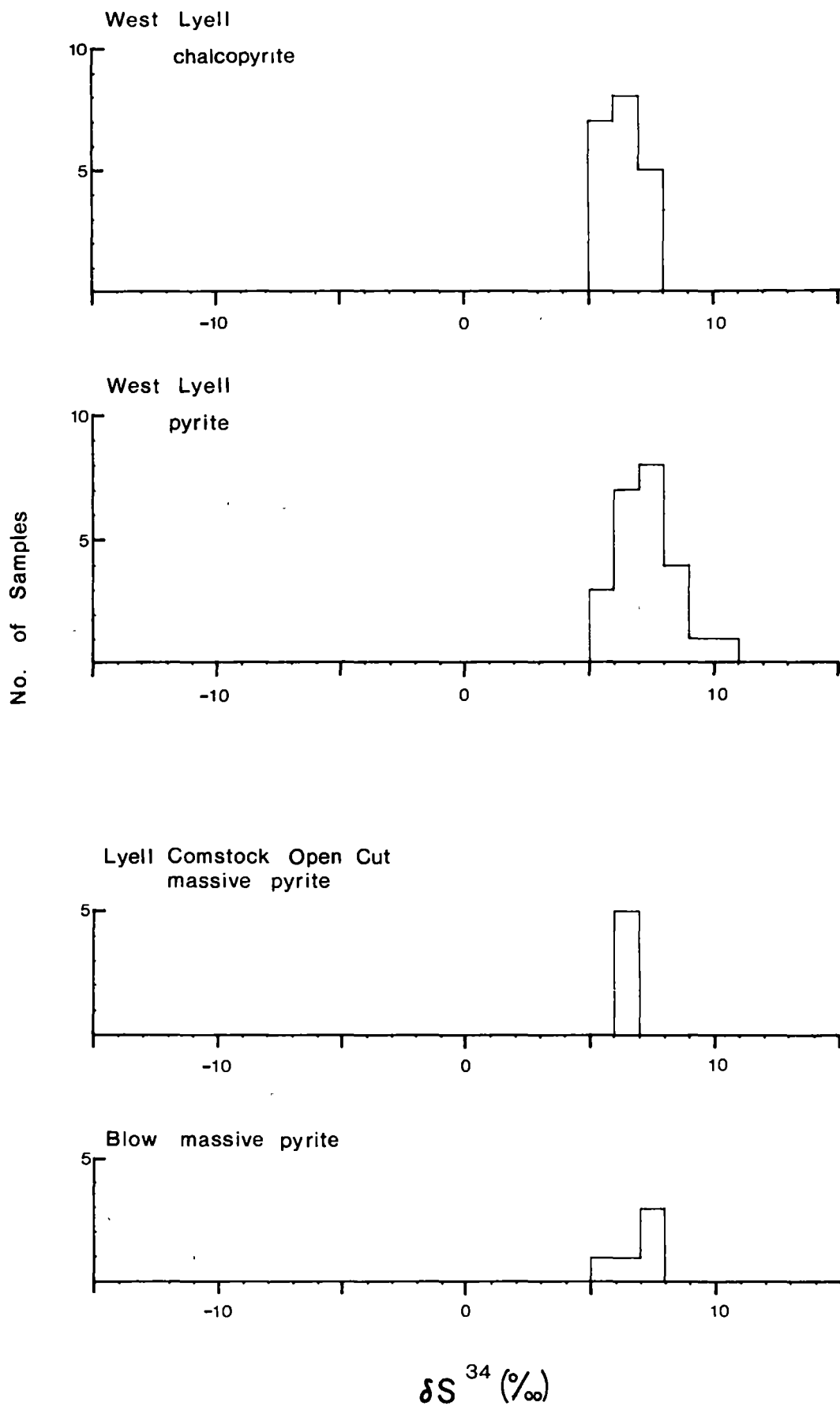
Fig. 4.1.1: Sulfur Isotope Data for West Lyell(Prince Lyell,"A" Lens, Royal Tharsis),Lyell Comstock Open Cut and the Blow.
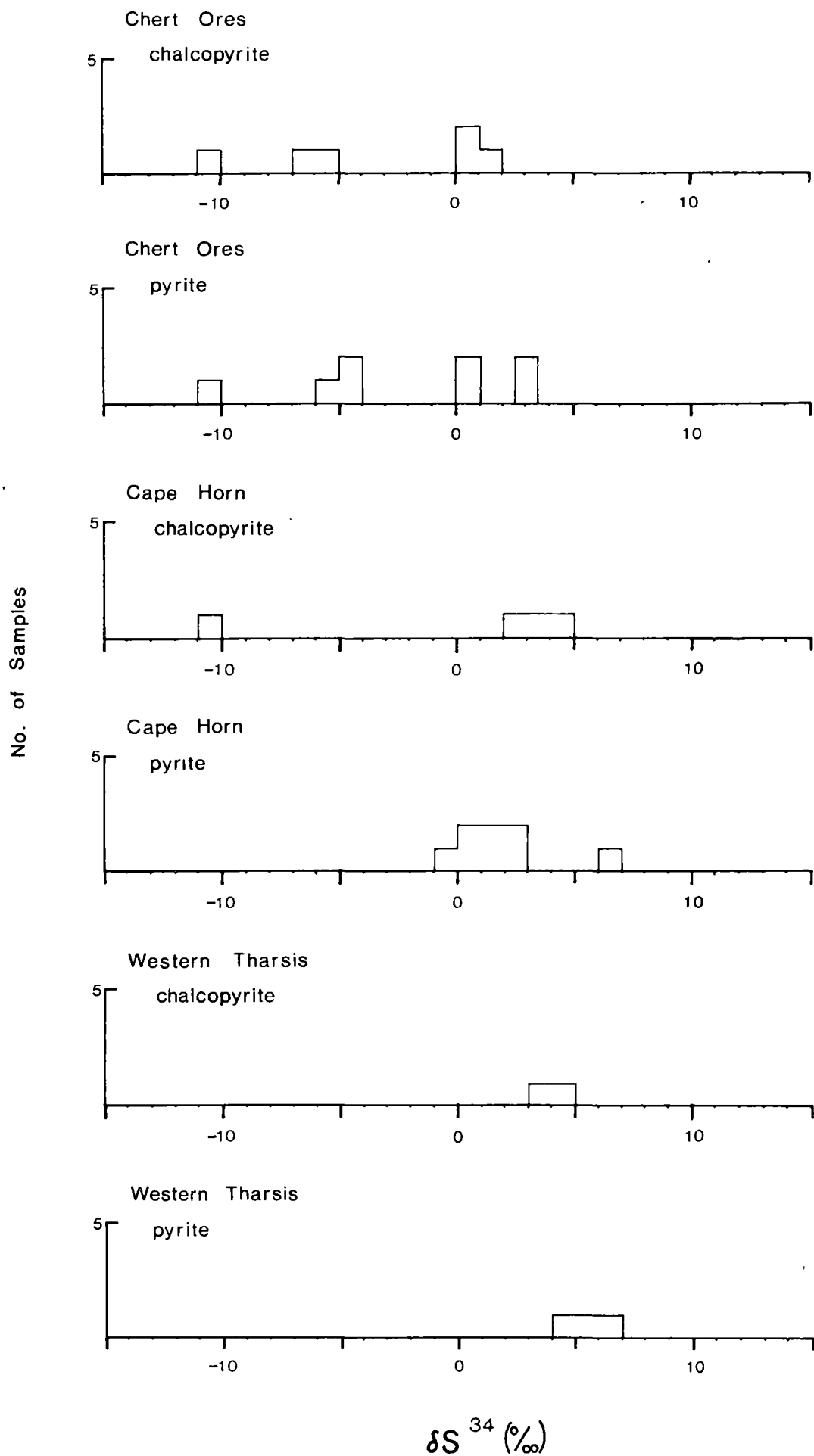
Fig. 4.1.2: Sulfur Isotope Data for the Chert Ores(North Lyell,Crown Lyell No.2,12 West,Lyell Comstock),Cape Horn and Western Tharsis.

Crown Lyell No.2 , 12 West

Cape Horn

Prince Lyell

Western Tharsis

No. of samples

$\Delta S^{34}_{pyrite - chalcopyrite}$ $\left(^o/_{oo}\right)$
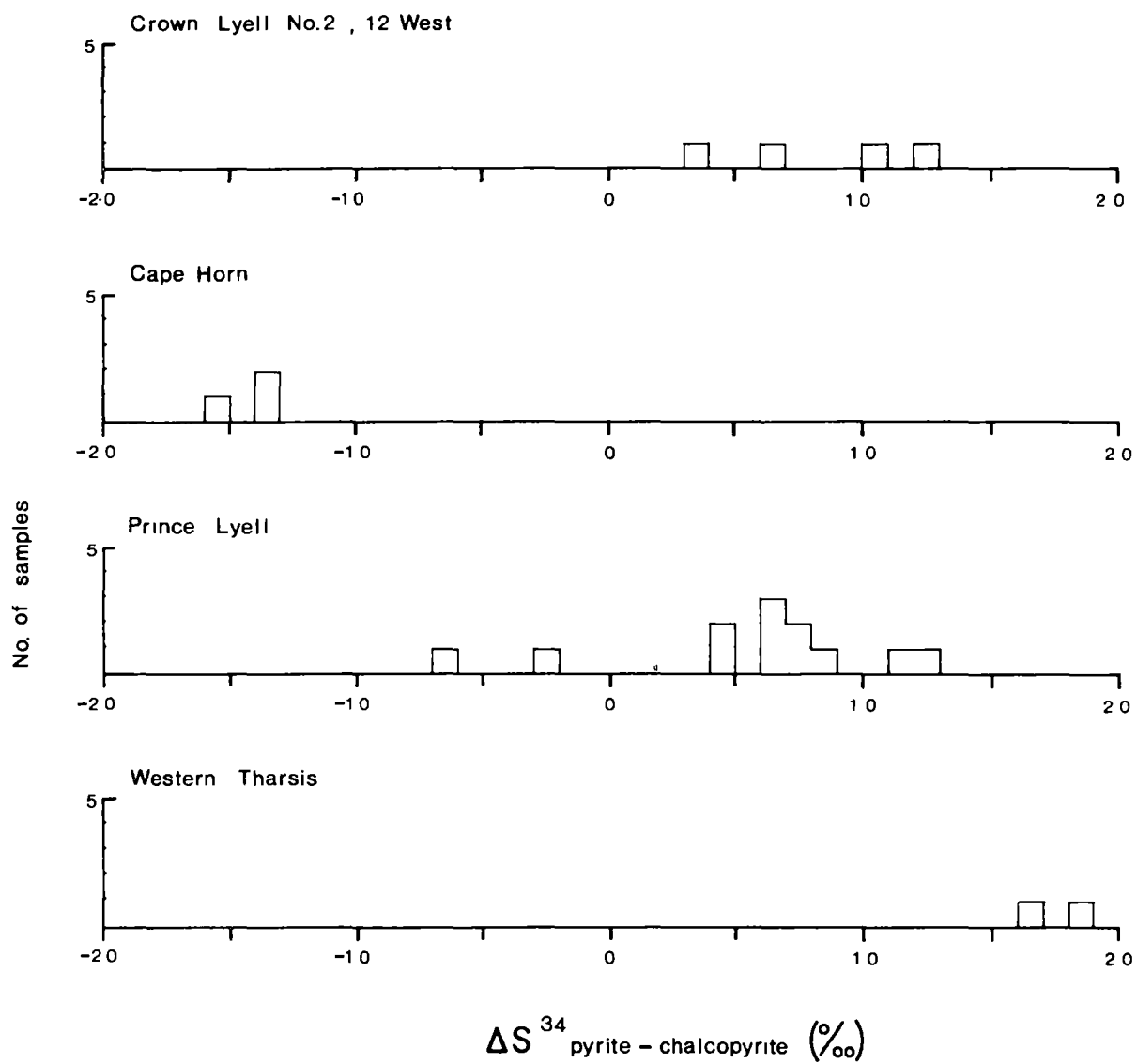
Fig. 4.2

from +6.4 to -10 with a mean of +1.3 and standard deviation of 4 (12 samples). As such they lie in the upper range of the sulphides associated with the chert ores apart from sample 290m (δS^{34} of -10). This sample and 71/765 (δS^{34} of -0.4), the two lightest values, came from the grey sericite lava unit (see Section 1.4). Sample 71/765 contained minor bornite. The limited Western Tharsis data, with a range of +3.0 to +6.4, are much closer to the West Lyell data, although they appear to be slightly less enriched in S^{34}.

4.3.2 Partitioning between Pyrite and Chalcopyrite

Figure 4.2 indicates pyrite-chalcopyrite partitioning at Mt. Lyell is not a straight forward problem! The temperature-dependence diagram of pyrite-chalcopyrite partitioning, figure 4.3, is taken from Kajiwara and Krouse (1971). If the temperature of the Mt. Lyell ores is assumed to have not exceeded 350°C at any stage (hydrothermal alteration or metamorphism) then the smallest ΔS^{34}py-ccp values to be expected would be about 1.2. Only the two Western Tharsis points exceed a value of 1.2, and at 1.6 and 1.8 these correspond to 260 and 225°C respectively. The other data for Prince Lyell, Cape Horn, Crown Lyell No.2 and 12 West, spreading from ΔS^{34}py-ccp of +1.2 to -1.5 obviously represents a lack of isotopic equilibrium. This raises the possibility that the Western Tharsis data represents apparent rather than real isotopic equilibrium.

The situation is further complicated by the two duplicate analyses, 2-3/270 and 4-5/220. The variation in analysis for each sample is shown below.
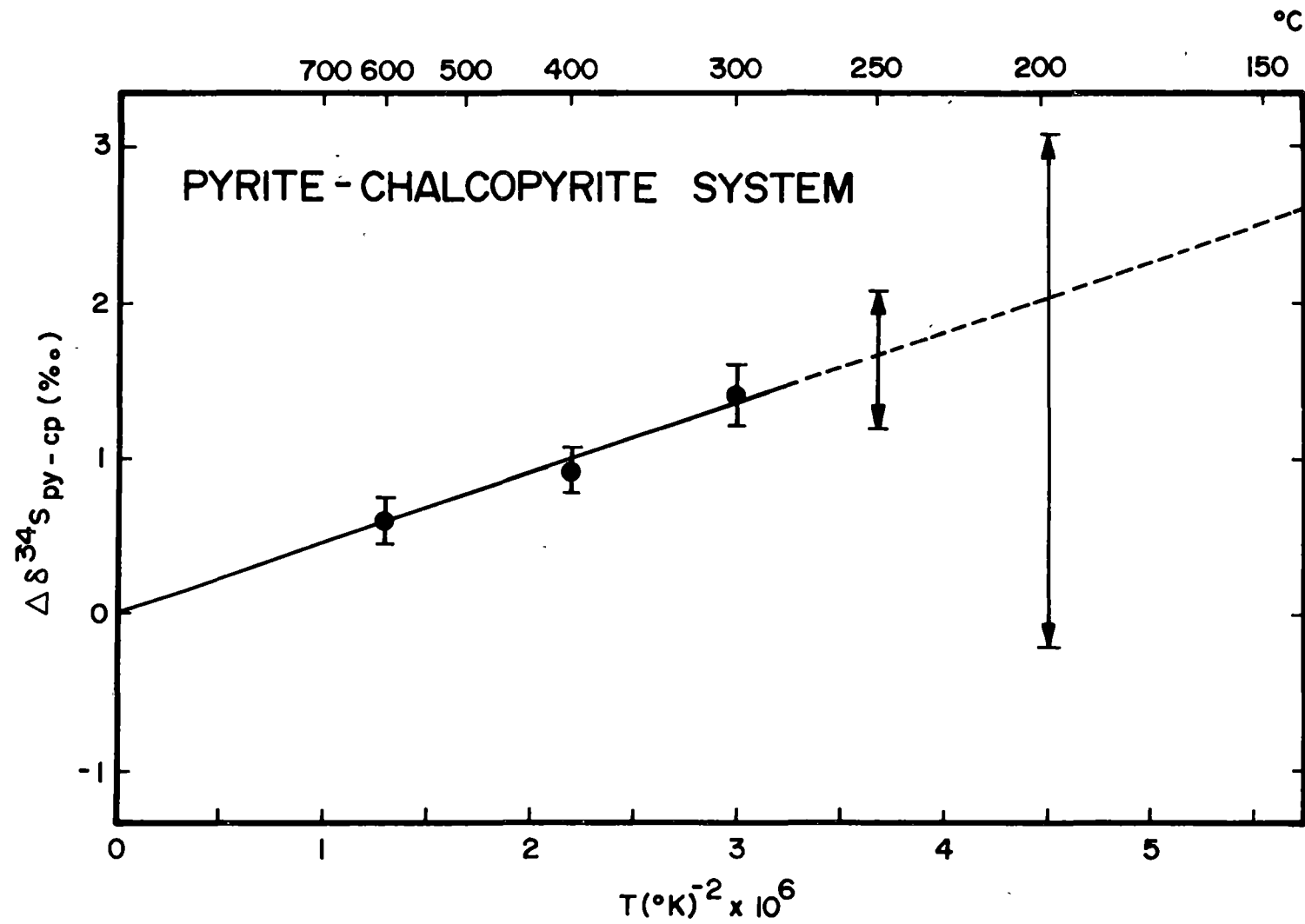
Fig. 4.3: The Temperature Dependence of the Isotope Partitioning in the Pyrite-Chalcopyrite System(from Kajiwara and Krouse,1971).

		C.S.I.R.O.	D.S.I.R.	Variation
2-3/270	Pyrite	5.6	7.0	1.4
	Chalcopyrite	5.2	6.6	1.4
4-5/220	Pyrite	6.7	7.5	0.8
	Chalcopyrite	5.9	6.4	0.5

This internal inconsistency means that the ΔS^{34}py-ccp value

for any pair, at least for Prince Lyell, is very unreliable.

Although with only two duplicates it is difficult to be certain,

there is probably as much variation within samples and between

sample pairs as there appears to be for the whole orebody.

Data from small scale samples of coexisting pyrite and

chalcopyrite (sample 4-5/228 and the chip samples used by

Solomon et $al.$ (1969) for the Crown Lyell No. 2 and 12 West

data) are similar to the bulk sample data.

4.4 A Tentative Interpretation

4.4.1 The Effect of Metamorphism

For metamorphism up to upper greenschist or lower

amphibolite facies, Rye and Ohmoto (1974) suggest two

principles of sulphur isotope distribution, viz

(i)   Large-scale pre-metamorphic variations are generally

preserved.

(ii)   Small-scale sulphur isotopic changes are superimposed.

In the light of this it would seem reasonable that the

gross variation of δS^{34} observed by Solomon et $al.$ (1969) is

an original, pre-metamorphic feature.

That isotopic disequilibrium might be preserved necessarily

implies that the sulphides do not isotopically re-equilibrate

with changing solution conditions, temperature or pressure.

Pyrite is very sluggish in its solid state reaction (Barton
et al., 1963; Barton, 1970). Salomons (1971) experienced
experimental difficulty in studying the isotopic fractionation
between pyrite and galena because pyrite was sluggish in its
isotopic readjustment, and Rye and Ohmoto (1974) have referred
to the difficulty of using pyrite for equilibrium studies.
Conversely, solid-state reaction in chalcopyrite is relatively
rapid and this may lead to homogenisation of internal zoning
(Barton 1970).

If the pyrite-chalcopyrite pair previously coexisted either in
isotopic equilibrium and/or disequilibrium, prolonged heating
during the metamorphism would tend to cause readjustment towards
equilibration with the heating temperature. However, since
pyrite is slow to readjust and the metamorphic temperatures at
Mt. Lyell are low to moderate, readjustment is only likely to
occur around the grain margins of the pyrite (Salomons, 1971).
Adjustment of the chalcopyrite to the metamorphic conditions,
which are oxidising relative to the initial conditions of deposi-
tion, would lead to a depletion of S^{34} in chalcopyrite relative to
its equilibrium value with pyrite. The observed situation is the
reverse, chalcopyrite is enriched in S^{34} relative to its equilibrium
value with pyrite and indicates that the pyrite-chalcopyrite dis-
equilibrium cannot be generated by sulphide reaction with metamorphic
fluids. Hence it seems likely that the disequilibrium relates to
the initial formation of the pyrite and chalcopyrite.

4.4.2   The Significance of the Pyrite-Chalcopyrite Partitioning Data

The pyrite-chalcopyrite partition values, except for
Western Tharsis, are smaller than the values suggested from
reasonable temperature estimates. Assuming equilibrium isotopic

fractionation this situation may arise in the following ways:

(1) Chalcopyrite precipitates under more reducing conditions relative to pyrite, providing the change in conditions results in changes in the reduced/oxidised sulfur ratio at or near the $SO_4^=/H_2S$ boundary at constant $\delta S_{\Sigma S}^{34}$ value

(2) The precipitation of significant amounts of pyrite prior to the precipitation of chalcopyrite at conditions such that the solution is enriched in S^{34}

(3) Chalcopyrite and pyrite precipitate from different solutions, the solution from which chalcopyrite precipitates being enriched in S^{34} relative to the solution from which pyrite precipitates.

For the pH controlled alteration of a felsic host to the assemblages quartz-sericite-pyrite, quartz-sericite-chlorite-pyrite and quartz-sericite-chlorite-pyrite-chalcopyrite, pyrite progressively forms in a more reducing environment and chalcopyrite forms in a more reducing environment than pyrite (fig. 4.4). That is, inherent within the reaction sequence is the potential to generate the observed isotopic disequilibrium between pyrite and chalcopyrite, given the oxidation range over which pyrite and chalcopyrite precipitate is such that variation in $\delta S^{34}py$ may occur.

If precipitation is limited to the very reducing areas of figure 4.4, where no variation of $\delta S^{34}py$ is permissible, then equilibrium isotopic partitioning would occur. Further it would seem likely that the more oxidising the conditions the greater the probability of producing large variations in $\delta S^{34}py$ (and possibly $\delta S^{34}ccp$) and hence more extreme disequilibrium partitioning values. Conversely, if disequilibrium is small, then the oxidation
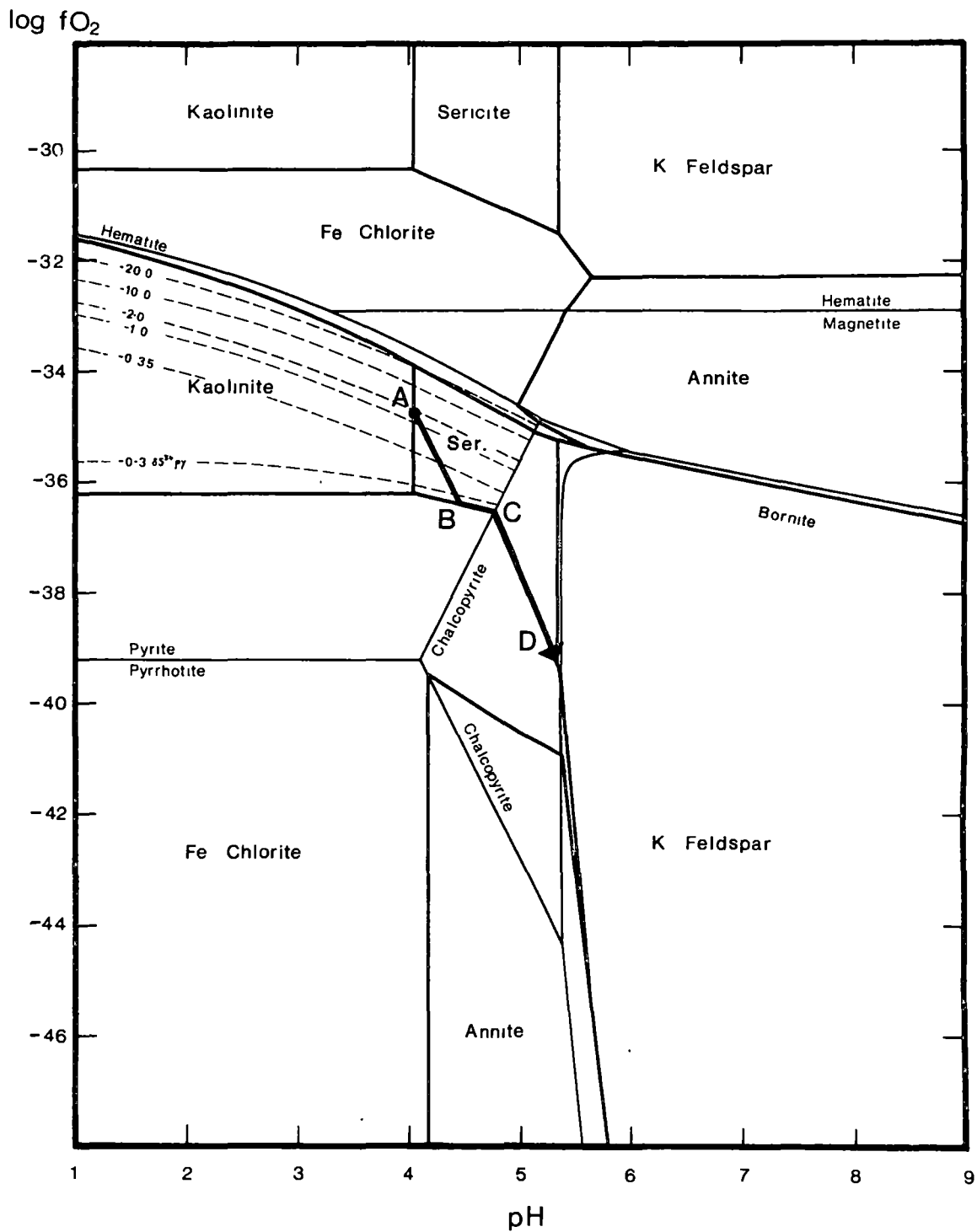
Fig. 4.4:   Log fO_2-pH diagram drawn for 250°C and
1 atmos. ΣS = 0.001 and ΣCu = 0.00002 moles/kg H_2O.
Ionic strength = 1.   K/Na = 0.1. $\delta S_{\Sigma S}^{34}$ = 0.   Activity of
H_2O is taken as unity.   Quartz is present in excess.

range over which precipitation occurred was probably restricted
to areas where little variation of $\delta S^{34}py$ and $\delta S^{34}ccp$ was permissible.
This would have the necessary implication that the observed
$\delta S^{34}py$ values would be close, within a few permil, of the $\delta S^{34}_{\Sigma S}$
value of the solution.

In addition to the reduction mechanism the value of $\delta S^{34}_{\Sigma S}$ may
increase as reaction proceeds. This will occur if the value of
$\delta S^{34}py$ is less than $\delta S^{34}_{\Sigma S}$ and a significant proportion of the ΣS
is precipitated. Since the value of $\delta S^{34}py$ - $\delta S^{34}_{H_2S}$ is always
positive (Ohmoto and Rye, in press), precipitation of a signifi-
cant proportion of the ΣS, in the reduced sulphur field, leads to
a depletion of S^{34} in solution rather than enrichment. This
indicates, that given the equilibrium thermodynamic interpretation,
it is not possible to account for the direction of the pyrite-
chalcopyrite disequilibrium using the reaction sequence described
in 3.4.2 for the Prince Lyell central-core chloritic assemblage;
i.e. commencing precipitation in the quartz-chlorite-magnetite/
pyrrhotite field and by cooling and increasing the pH reacting
through to quartz-sericite-chlorite-pyrite and quartz-sericite-
chlorite-pyrite-chalcopyrite. It suggests a need to consider a
change; or an evolution, in the initial chemical state of the
hydrothermal fluids. Early fluids may have been hottest and
most reduced, producing the quartz-chlorite-magnetite/pyrrhotite
assemblage; later fluids were possibly cooler, more oxidised and
produced the dominant quartz-sericite-chlorite-pyrite-chalco-
pyrite assemblage.

Another alternative is to postulate two differing source
solutions of differing $\delta S^{34}_{\Sigma S}$ to account for the disequilibrium

between the pyrite and the chalcopyrite.   In view of the nearness
to equilibrium of the Western Tharsis data and that the Prince
Lyell data is generally only 1 or 2 $^0/_{00}$ from equilibrium this
seems unnecessary.

An important conclusion concerning equilibrium partitioning
temperature estimates is that, given the model, the Western
Tharsis "temperature" should be treated as a maximum hydrothermal
temperature.   This of course assumes limited metamorphic
readjustment (see above discussion) which, if true for the
disequilibrium pairs, will be true for equilibrium or near
equilibrium pairs.

4.4.3   Interpretation of the S^{34} Isotope Distribution for the Mt. Lyell Ores

Solomon and Green (pers. comm.) have proposed a model of
increasing oxidation and decreasing temperature to account for
the spread of isotopic data from West Lyell, +10 to +5, to North
Lyell, Crown Lyell 2 and 12 West, +0.8 to -7.7 at a constant $\delta S_{\Sigma S}^{34}$
value.   In this model Prince Lyell has been inter-
preted as being deposited at the most reduced conditions (the sulphur
in solution was assumed to be 90% reduced) and subsequent oxidation
led to the formation of the bornite ores with low δS^{34} pyrite values.
The interpretation of the mineral assemblages supports their
isotope model. The $\delta S^{34}py$ and $\delta S^{34}ccp$ values for Cape Horn, assuming
a similar range of $\delta S_{\Sigma S}^{34}$ as that suggested for Prince Lyell, suggest
an oxidation environment intermediate between Prince Lyell, Western
Tharsis and the North Lyell, Crown Lyell, 12 West ores.

4.5 Summary

Values of δS^{34} in pyrite and chalcopyrite range from +10.0‰ to -10.0‰. Pyrite chalcopyrite partition values for paired samples range from +1.8 to -1.5. There is difficulty in interpreting the partition data because of sampling problems. In particular the large variations in the duplicate analyses suggests any one determination of Δ py-ccp is neither reliable nor meaningful. The spread of isotope data from West Lyell, +10 to +5, to the North Lyell-Crown Lyell ores, +0.8 to -7.7, is consistent with a change in the environment of deposition from a high temperature and reduced conditions to a lower temperature and oxidised conditions. The disequilibrium observed between pyrite and chalcopyrite is consistent with chalcopyrite forming in a reduced environment relative to pyrite and/or from a solution enriched in S^{34}. Such conditions arise by the reaction of a slightly oxidised and acid solution with the felsic host rock. The initial value of $\delta S^{34}_{\Sigma S}$ was within the range of the Prince Lyell data and probably close to the mean of +7.

Table 4.1 : ADDITIONAL SULPHUR ISOTOPE DATA

	$\delta^{34}py$	$\delta S^{34}ccp$	$\delta S^{34}bar.$	$\delta O^{18}bar.$
Prince Lyell				
DAO	+ 6.3			
315/150[1]	+ 6.7	+ 6.0		
359/102[1]	+ 6.8	+ 6.1		
352/250[1]	+ 5.2			
2-3/270[1]	+ 5.6	+ 5.2		
2-3/270	+ 7.0	+ 6.6		
3-4/20	+ 7.6	+ 6.4		
4-5/70	+ 8.1	+ 7.5		
4-5/220[1]	+ 6.7	+ 5.9		
4-5/220	+ 7.5	+ 6.4		
4-5/228	+ 7.3	+ 7.5		
4-5/232	+ 7.6	+ 7.0		
5-6/192	+ 7.9	+ 7.3		
7-8/95S[1]	+ 7.1	+ 7.7		
150 m level (footwall drive)	+ 8.6		+28.5	+7.3, +7.1
960' level (1020W/42605)	+ 8.7		+19.0	+6.8
Cape Horn				
2-3/0 m	+ 2.9			
2-3/14 m	+ 6.4			
2-3/110	+ 1.0			
4/70	+ 0.3			
4-5/80	+ 1.3	+ 2.6		
71/580[1]	+ 2.0	+ 3.5		
71/600	+ 2.5	+ 3.8		
71/765[1]	- 0.4			
290 m level (2800N/4000W)	- 10.0			

Table 4.1 (contd.)

	$\delta^{34}py$	$\delta S^{34}ccp$	$\delta S^{34}bar.$	$\delta O^{18}bar.$
Western Tharsis				
371/267.2[1]	+ 4.8	+ 3.0		
374/212[1]	+ 6.4			
374/224[1]	+ 5.9	+ 4.3		
Lyell Comstock				
102102	- 4.3			
102103		- 10.5		
102104	- 10.4			
102097 A	+ 3.5			
102097 B		- 2.0 (bn)		
102098	+ 1.6			
102099	+ 3.1			

[1] Analysed by J.W. Smith of the C.S.I.R.O.   All other samples
   analysed by Dr. B.W. Robinson and Dr. T.A. Rafter of the D.S.I.R.

Table 4.2 : ΔS py-ccp DATA FOR CROWN LYELL NO.2, 12 WEST, CAPE HORN, PRINCE LYELL AND WESTERN THARSIS.

Samples	$\delta S^{34}py$	$\delta S^{34}ccp$	$\Delta S^{34}py\text{-}ccp$
Crown Lyell No. 2			
(Solomon *et al.*, 1969)			
10738 A	- 5.3	- 6.3	+ 1.0
10738 B	- 4.2	- 5.4	+ 1.2
12 West			
(Solomon *et al.*, 1969)			
10739 A	+ 0.6	+ 0.3	+ 0.3
10739 B	+ 0.8	+ 0.2	+ 0.6
Cape Horn			
CH 4-5/80	+ 1.3	+ 2.6	- 1.3
CH 71/580	+ 2.0	+ 3.5	- 1.5
CH 71/600	+ 2.5	+ 3.8	- 1.3
Prince Lyell			
2-3/270 (C.S.I.R.O)	+ 5.6	+ 5.2	+ 0.4
4-5/220 (C.S.I.R.O)	+ 6.7	+ 5.9	+ 0.8
315/150	+ 6.7	+ 6.0	+ 0.7
359/102	+ 6.8	+ 6.1	+ 0.7
2-3/270 (D.S.I.R.)	+ 7.0	+ 6.6	+ 0.4
7-8/95 S	+ 7.1	+ 7.7	- 0.6
4-5/228	+ 7.3	+ 7.5	- 0.2
4-5/220 (D.S.I.R.)	+ 7.5	+ 6.4	+ 1.1
3-4/20	+ 7.6	+ 6.4	+ 1.2
4-5/232	+ 7.6	+ 7.0	+ 0.6
5-6/192	+ 7.9	+ 7.3	+ 0.6
4-5/70	+ 8.1	+ 7.5	+ 0.6
Western Tharsis			
371/267.2	+ 4.8	+ 3.0	+ 1.8
374/224	+ 5.9	+ 4.3	+ 1.6

5.   TRACE COBALT AND NICKEL DISTRIBUTION PATTERNS

IN PYRITE AND CHALCOPYRITE

5.1   Review of Trace Element Studies in Sulphides

5.1.1   Main Themes of Field Studies

The approach to the study of trace element content and distribution in a particular sulphide has been essentially empirical, attempting to define metallogenic provinces and sub-provinces (e.g. Burnham, 1959) or to identify genetic links between deposits and/or environments of deposition.   For a full review see Loftus-Hills and Solomon (1967) and Loftus-Hills (1968).   Using cobalt and nickel content of pyrite and the Co/Ni ratio as indicators, Loftus-Hills (1968) investigated several types of mineralization in the southern part of the Tasman Orogenic Zone, and concluded that:

(i)   Sedimentary pyrites commonly contain Co/Ni <0.5, as observed for many sedimentary pyrites.

(ii)   Pyrites in the Cambrian volcanic rocks have Co/Ni ratios ranging from 1 - 150 and containing up to 0.8 wt. % cobalt. The trends for Rosebery and Mt. Lyell deposits were found to be consistent with this, implying a genetic link. Loftus-Hills (op. cit.) also noted a tendency for greater cobalt and nickel concentrations to occur with copper rather than with lead-zinc ores both within and between deposits.   In the Mt. Lyell group of deposits there was a strong tendency for cobalt to be associated with the chalcopyrite mineralization.

(iii)   Pyrites from Devonian hypogene replacement and vein deposits show two main trends:

(a)   0 - 1500 ppm nickel with Co/Ni <1

and (b)   0 - 400 ppm cobalt with nickel ranging from

10 - 100 ppm.

He considered the differences between groups was fundamentally

due to differences in availability of the elements while smaller

scale variations within groups resulted from differing depositional

processes and conditions.

Rose (1970, 1967) in a study on the Central and Bingham mining

district came to similar conclusions. He distinguished groups

of orebodies on trace element contents of sphalerite and chalco-

pyrite. In his analysis he suggested three possible origins

for the differences:

(i)   Differences in ore-fluid composition.

(ii)   Differences in temperatures of deposition.

(iii)   Differences in host rock composition.

Because of lack of any geological correlation with (ii) and (iii),

Rose preferred (i) as the reason for the observed differences.

He explained zonation patterns within groups of deposits (with

reference to McIntire's work, see below) as resulting from a

combination of the depletion of the trace in solution and the

changing nature of ion complexing in solution.

Detailed studies of the distribution of trace elements

between sulphides are limited, the most notable being that of

Gosh-Dastidar *et al.* (1970). They demonstrated considerable

departure from Henry's law in many instances but were able to

account for some of the departure by considering 'interaction' and

'concentration' effects. They also considered in some detail

the problem of demonstrating equilibrium.

Attention in recent years has also been focused on zonation of

trace elements within sulphide grains. With respect to cobalt in pyrite Brown and Barthlome (1972) suggested that heterogenous nonconcentric zoning in pyrite in the Chibuluma copper-cobalt deposit, Zambia, is probably a primary feature which has been partially or completely removed by metamorphism.

In a study of the cupriferous-pyrite deposits of Japan, Itoh (1973) also found heterogenous distribution of cobalt in pyrites from low grade metamorphosed and unmetamorphosed deposits. In contrast however, in the highly metamorphosed deposits, cobalt was sharply concentrated in the margins of the pyrites and the content was uniformly low in the cores of grains. He concluded that under the higher grades of metamorphism cobalt atoms migrated to the margins of the recrystallising pyrite grains. In the Shirataki deposit (grade of metamorphism corresponding to epidote-amphibolite) carollite (Co_2 Cu S_4) was found. From its occurrence, it is inferred to have formed at the boundaries of pyrite and chalcopyrite by chalcopyrite reacting with cobalt rich zones in the pyrite.

The overall cobalt content of ores from cupriferous-pyrite deposits is in the range 0.03 to 0.5% Co.

5.1.2 Experimental Studies

Direct experimental work on trace elements in sulphides is limited to the work of Bethke and Barton (1971, 1959). They examined the distribution of cadmium, manganese and selenium between sphalerite and galena and manganese between wurtzite and galena over the temperature range 600-800°C and the distribution of selenium between galena and chalcopyrite between 390 and 595°C.

Hall *et al.* (1971) applied Bethke and Barton's data to the

Darwin silver-lead-zinc mine. Temperatures based on manganese

and cadmium distribution between sphalerite and galena, although

geologically reasonable, were consistently higher by about 60

and 90°C respectively compared with sulphur isotope temperatures

(Rye *et al.*, 1974). The fractionation of selenium gave

unreasonably high temperatures.

5.1.3 Theory

The following summary of the theory of trace element

partitioning is adopted from McIntire (1963).

(a) Equilibrium Partitioning Between Solid and Aqueous Phase

Consider the growth of a crystal in which a trace element (Tr)

occurs in dilute solution in a carrier Cr M, the trace and

carrier having the same valency. The situation is represented by

$$Cr\ M_{ss} + Tr_L^{m+} \quad \rightleftharpoons \quad Tr\ M_{ss} + Cr_L^{m+} \qquad (5.1)$$
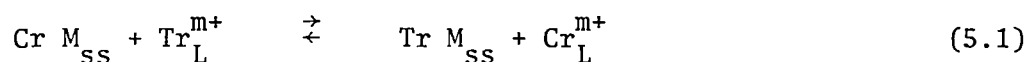
where Tr_L^{m+} and Cr_L^{m+} represent the trace and carrier ions in

solution and $Tr\ M_{ss}$ and $Cr\ M_{ss}$ represent the trace and carrier

components of the solid solution respectively. It follows that

$$K \quad = \quad \frac{(a\ Tr\ M_{ss})}{(a\ Cr\ M_{ss})} \quad \frac{(a\ Cr_L^{m+})}{(a\ Tr_L^{m+})} \qquad (5.2)$$

where K is the equilibrium constant and which can be evaluated

as follows.

The chemical potential of Tr M in aqueous solution is expressed

by

$$\mu^L Tr\ M \quad = \quad \mu Tr\ M + RT\ ln\ a\ ^L Tr\ M$$

where $\mu Tr\ M$ is the chemical potential of Tr M in the hypothetically

standard state of 1 mole in an infinitely dilute solution.

The chemical potential of Tr M in solid solution is expressed by

$$\mu^S_{Tr\ M} = \mu^o_{Tr\ M} + RT \ln a^S_{Tr\ M}$$

where $\mu^o_{Tr\ M}$ is the chemical potential of Tr M in the standard state which is pure crystalline Tr M.

At equilibrium

$$\mu^S_{Tr\ M} = \mu^L_{Tr\ M}$$

i.e.

$$\ln \frac{a^L_{Tr\ M}}{a^S_{Tr\ M}} = \frac{\mu^o_{TrM} - \mu_{Tr\ M}}{RT}$$

or

$$\frac{a^L_{Tr\ M}}{a^S_{Tr\ M}} = \exp \frac{\mu^o_{Tr\ M} - \mu_{Tr\ M}}{RT}$$

The right hand side of the equation is equal to the thermodynamic solubility product of pure Tr M,

i.e.

$$\frac{a^L_{Tr\ M}}{a^S_{Tr\ M}} = K_{Tr\ M} \tag{5.3}$$

Similarly

$$\frac{a^L_{Cr\ M}}{a^S_{Cr\ M}} = K_{Cr\ M} \tag{5.4}$$

Combining 5.3 and 5.4 and eliminating the common ion produces

$$\frac{a\ Tr\ M}{a\ Cr\ M} \bigg/ \frac{a\ Tr^{m+}_L}{a\ Cr^{m+}_L} = \frac{K_{Cr\ M}}{K_{Tr\ M}} = K_{5.5} \tag{5.5}$$

Substituting activity coefficients and rearranging gives,

$$D = \frac{X_{Tr\ M}}{X_{Cr\ M}} \bigg/ \frac{\Sigma^L_{Tr}}{\Sigma^L_{Cr}} = \frac{K_{Cr\ M}}{K_{Tr\ M}} \cdot \frac{\gamma_{Tr}^{m+}}{\gamma_{Cr}^{m+}} \cdot \frac{\gamma_{Cr\ M}}{\gamma_{Tr\ M}} \tag{5.6}$$

where $X_{Tr\ M}$, $X_{Cr\ M}$ are the mole fractions of trace and carrier

in solid solution;

Σ^L Tr, Σ^L Cr are the total molalities of trace and carrier

ions in aqueous solution;

γ Tr M, γ Cr M are the activity coefficients of trace and

carrier in solid solution and $\dot{\gamma}$ Tr $^{m+}$ and $\dot{\gamma}$ Cr $^{m+}$ are the

stoichiometric individual ion activity coefficients for

trace and carrier respectively (Helgeson, 1969).

For dilute solid solution γ Cr M = 1.

The partition coefficient, D, is dependent on three factors:

(i)   the ratio of the solubility products for the two end

members;

(ii)   the ratio of the aqueous solution activity coefficients;

(iii)   the departure of the solid solution from ideality.

The situation becomes more complex if altervalent

substitution occurs.

For trace partitioning between two phases, assuming sub-

stitution for the same element in both phases, it can be

readily shown that the partition coefficient is independent

of the solution composition.

(b) Logarithmic Distribution

As crystallisation proceeds in a closed system the trace

content of the liquid will vary continuously.   The instanteous

situation at the surface of the grain may be described by

$$\frac{(Tr)}{(Cr)} \text{ surface of crystal} = \lambda \frac{(Tr)}{(Cr)}_L \qquad (5.7)$$

where λ is a partition coefficient.

The interior of the grain may not equilibrate with the con-

tinuously changing $\frac{(Tr)}{(Cr)}$ ratio at the surface layer, hence growth

zoning will occur.   The diffusion of ions in solids is generally

a slow process relative to diffusion in liquids and the rate of crystal growth.

If at any instance N_{Tr}^S and N_{Cr}^S are the total number of moles of trace and carrier to have crystallised from initial N_{Tr}^I and N_{Cr}^I in solution then for the next infinitesmal layer crystallising it follows from 5.7 that

$$\frac{d\ N_{Tr}^S}{d\ N_{Cr}^S} = \lambda\ \frac{(N_{Tr}^I - N_{Tr}^S)}{(N_{Cr}^I - N_{Cr}^S)} \qquad (5.8)$$

Integration leads to

$$\ln \frac{N_{Tr}^I}{N_{Tr}^I - N_{Tr}^S} = \lambda\ \ln \frac{N_{Cr}^I}{N_{Cr}^I - N_{Cr}^S}$$

or

$$\ln \frac{N_{Tr}^I}{N_{Tr}^L} = \lambda\ \ln \frac{N_{Cr}^I}{N_{Cr}^L} \qquad (5.9)$$

where N_{Tr}^L and N_{Cr}^L are the instanteous concentrations in solution.

λ is known as the logarithmic partition coefficient. It will equal D if only infinitesmal supersaturation occurs. However in general,

$$D = \frac{N_{Tr}^I - N_{Tr}^L}{N_{Tr}^L} \Bigg/ \frac{N_{Cr}^I - N_{Cr}^L}{N_{Cr}^L}$$

will differ from λ and the true equilibrium value of D.

Springer *et al.* (1964) used similar theory to explain zonations observed in their experimentally produced bravoite. They observed both zoned and unzoned crystals.

The value of λ may vary with the degree of supersaturation or rate of crystallisation, the two being generally equivalent.

This has been explained by considering the difference in diffusion rates of trace and carrier through a thin boundary layer of liquid surrounding the growing crystal.

A relationship

$$\ln \frac{N_{Tr}^{I}}{N_{Tr}^{L}} = \frac{\lambda S \quad \delta Tr/\delta Cr}{\lambda(S - 1) + \delta Tr/\delta Cr} \quad \ln \frac{N_{Cr}^{I}}{N_{Cr}^{L}} \qquad (5.10)$$

(equation 37, McIntire, *op. cit.*)

may be derived such that, if an apparent partition coefficient λ' is defined, the relationship is of the same form as equation 5.9

$$\lambda' = \frac{\lambda S \cdot \delta Tr/\delta Cr}{\lambda(S - 1) + \delta Tr/\delta Cr}$$

where S is the degree of supersaturation and δTr and δCr are the diffusion coefficients. As S approaches 1, λ' approaches λ.

Whether the true equilibrium distribution law or the logarithmic law is followed depends upon the conditions of crystallisation. Generally if slow growth of crystals occur from a nonagitated solution in which supersaturation is gradually relieved or if rapidly precipitated crystals are allowed to recrystallise then the true equilibrium distribution law will be followed. Rapid precipitation with no recrystallisation, or slow growth at a constant degree of supersaturation, will produce a logarithmic distribution.

5.2 General Comments on Approach to the Mt. Lyell Problem

Loftus-Hills (1968) established the concentration ranges of cobalt and nickel in pyrite as 1 to 2400 ppm and 5 to 420 ppm respectively, and indicated an apparent enrichment of cobalt in pyrite associated with chalcopyrite mineralization. The current study is intended as a more extensive and intensive examination of

the distribution of cobalt and nickel in pyrite, particularly its

relationship to chalcopyrite mineralization and whether or not this

is of genetic significance.   The interpretative approach adopted

will follow the general pattern outlined by previous workers.   The

important factors and assumptions may be summarised as follows:

(a)   for true equilibrium distribution:

   (i)   Tr/Cr ratio in solution, which may be influenced by

           the initial ratio of the ore fluid, the value for the

           host rocks, and any changes during the depositional

           process,

   (ii)   temperature,

   (iii)   ionic strength of the solution which controls the

           complexing behaviour of trace and carrier ions in

           solution.

(b)   logarithmic distribution:

   (i), (ii) and (iii) as given above,

   (iv)   kinetic factors:- rate of precipitation or degree of

           supersaturation and the relative diffusion rates of

           trace and carrier in solution.

   If the true equilibrium distribution law is assumed to apply

then the behaviour of trace cobalt and nickel in pyrite may be

described by equation 5.6.

Hence for the reaction

$$Co^{2+} + FeS_2 \; \overset{\rightarrow}{\leftarrow} \; CoS_2 + Fe^{2+} \tag{5.11}$$

$$D = \frac{X \, CoS_2}{X \, FeS_2} \bigg/ \frac{\Sigma Co}{\Sigma Fe} = K \cdot \frac{\gamma Co^{2+}}{\gamma Fe^{2+}} \cdot \frac{\gamma FeS_2}{\gamma CoS_2} \tag{5.12}$$

Similar relationships may be written for

$$Ni^{2+} + FeS_2 \; \overset{\rightarrow}{\leftarrow} \; NiS_2 + Fe^{2+} \tag{5.13}$$

$$Co^{2+} + NiS_2 \; \overset{\rightarrow}{\leftarrow} \; CoS_2 + Ni^{2+} \tag{5.14}$$
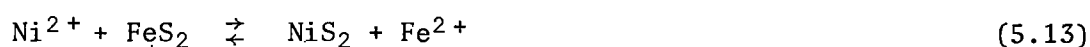
The three end members of the ternary system FeS_2 - CoS_2 - NiS_2 are similar in structure and radius of the cation and thus it is reasonable to assume ideal solid solution behaviour. Hence equation 5.12 becomes

$$D = \frac{X \; CoS_2}{X \; FeS_2} \Bigg/ \frac{\Sigma Co}{\Sigma Fe} = K \cdot \frac{\dot{\gamma}Co^{2+}}{\dot{\gamma}Fe^{2+}} \tag{5.15}$$

The equilibrium constants for equations 5.11, 5.13, 5.14 may be evaluated using data from table 4 and 5, Appendix A. The stoichiometric individual ion activity coefficients for Fe^{2+}, Ni^{2+} and Co^{2+} are given in table 8, Appendix A.

The variations of $\dfrac{X \; CoS_2}{X \; FeS_2}$, $\dfrac{X \; NiS_2}{X \; FeS_2}$ and $\dfrac{X \; CoS_2}{X \; NiS_2}$ with temperature from 100 to 300°C, for a ΣCl of 1 and 3, and given that $\dfrac{\Sigma Co}{\Sigma Fe} = \dfrac{\Sigma Ni}{\Sigma Fe} = 1$, are given in table 5.1. This data gives an indication of the likely variation of cobalt and nickel in pyrite in response to the changes in temperature and ionic strength. With decreasing temperature the nickel content of pyrite generally decreases over the temperature range 300 to 100°C. Cobalt in pyrite increases over the temperature range 300 to 200°C, particularly for ΣCl of 3, but decreases from 200 to 100°C. The lower cobalt in pyrite content at 200 to 300°C is due to the increase in stability of the Co Cl_3^{1-} complex (table 3, Appendix A). The Co/Ni ratio increases with decreasing temperature.

The $\Sigma Co/\Sigma Fe$ will be controlled either by the initial ratio of the fluid and/or the relative depletion of cobalt and iron as reaction proceeds. The background values of cobalt for the host rocks are too low to be of significance. Cobalt in the Mt. Read Volcanics ranges from 3 to 39 ppm (rhyolites to basalts, M. Solomon, pers. comm.) compared

to a bulk-rock cobalt content for Prince Lyell of 100 - 250 ppm.

However as bulk-rock nickel values are much lower, 10 - 50 ppm,

and as nickel contents of Mt. Read Volcanics vary from 1 - 27 for

rhyolites and up to 55 ppm for basalts (White, 1976; M. Solomon, pers.

comm.) it is possible that the host-rock nickel content, particularly

in the intermediate rocks, may influence the $\Sigma Ni/\Sigma Fe$ ratio.

Changes in the ΣFe may be related to fO_2, pH, aH_2S by

$$FeS_2 + 2H^+ + H_2O \; \rightleftarrows \; Fe^{2+} + 2H_2S + \tfrac{1}{2}O_2 \tag{5.16}$$
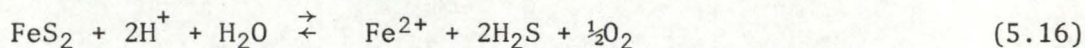
Hence, assuming constant ΣCo and ΣNi and combining 5.16 and 5.11, and

5.16 and 5.13, respectively, the relationships between $\Sigma Co/\Sigma Fe$,

$\Sigma Ni/\Sigma Fe$ and $X\, CoS_2/X\, FeS_2$, $X\, NiS_2/X\, FeS_2$ become a function of fO_2,

pH, aH_2S or fO_2, pH, ΣS.   That is, any change in the trace element

content of pyrite caused by a change in ΣFe, while $\Sigma Trace$ is constant,

may be represented on a log fO_2/pH diagram using the saturation

reaction for the trace-element end member.   For cobalt and nickel

in pyrite these are the saturation reactions for cattierite (CoS_2)

and vaesite (NiS_2) respectively.

$$CoS_2 + 2H^+ + 2H_2O \; \rightleftarrows \; Co^{2+} + 2H_2S + \tfrac{1}{2}O_2 \tag{5.17}$$

$$NiS_2 + 2H^+ + 2H_2O \; \rightleftarrows \; Ni^{2+} + 2H_2S + \tfrac{1}{2}O_2 \tag{5.18}$$
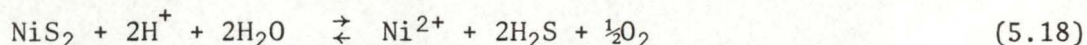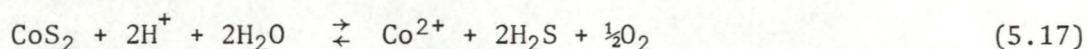
Contours of $X\, CoS_2$, given in ppm Co, are shown on figure 5.1.   It is

clear from this that changes in fO_2 and pH may lead to considerable

changes in cobalt and nickel concentration in pyrite at constant

ΣCo, ΣNi, ΣS and T.

The advantage of this style of presentation is that it readily

allows integration of the trace-element data with phase-data and sulphur-

isotope data.   The disadvantage of the diagram, a feature relevant to

all types of information represented on it, is the need to fix certain

solution parameters which in a real situation may not remain constant.
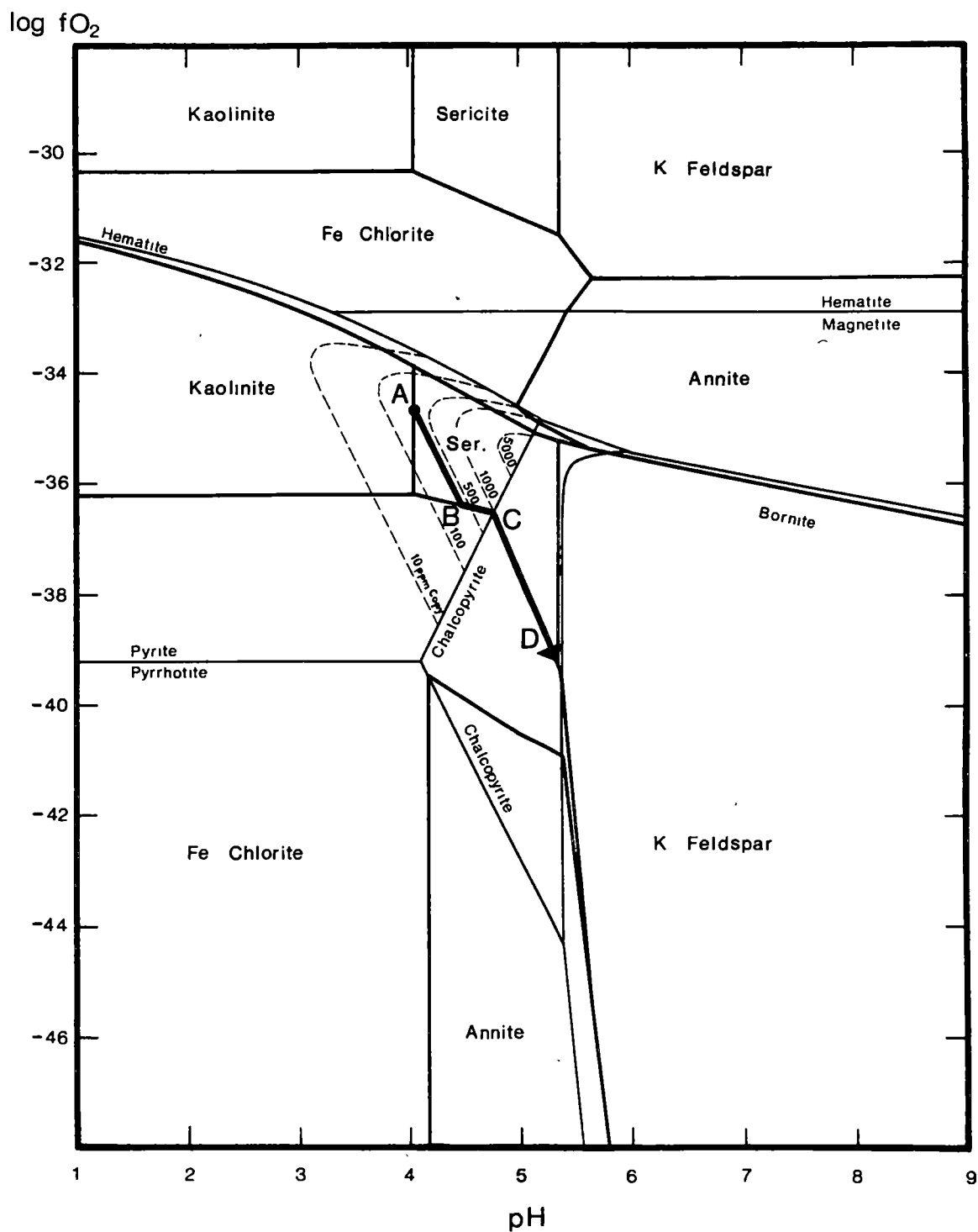
Fig. 5.1:   Log fO_2-pH diagram drawn for $250^{\circ}C$ and
1 atmos. Log $\Sigma S = -2$, log $\Sigma Cu = -4.7$, and log $\Sigma Co = -12.00$.
Ionic strength = 1. K/Na = 0.1. Activity of H_2O is taken
as unity. Quartz is present in excess.

In the above discussion it has been assumed that cobalt and nickel always remain at trace levels. The overall concentration of cobalt and nickel in pyrite give no reason to expect separate cobalt and nickel phases. According to Klemm (1962), pyrite at 400°C may contain up to 17 wt % cattierite and 13 wt % vaesite. The experimental work of Springer *et al.* (1964) over the temperature range 150-300°C suggests metastability over a much wider compositional range. However, Edwards (1939) has described probable linnaeite, occurring as minute blebs and rods in bornite and also in chalcopyrite, from a quartz vein containing bornite, chalcopyrite and tennantite (from the North Lyell mine). This suggests that it may be possible to generate a separate cobalt phase locally.

5.3 Cobalt and Nickel in Pyrite Data

Details of the sampling procedure, separation and analysis are given in Appendix C. Details of the cobalt, nickel, and manganese distributions in pyrite are also given in Appendix C. The data are given either on location plans (Maps C1 to C8) or, where not plotted, in table C1.

Although manganese concentrations in pyrite have been determined no attempt will be made to interpret the data. This is primarily because of possible manganese contamination from chlorite and siderite impurities. Probe analyses indicate MnO contents in chlorite and siderite of up to 0.8 and 10 wt % respectively. Hence only minor amounts of chlorite or siderite impurity would significantly affect the pyrite manganese determination. The data probably gives some guide to the overall levels of manganese in pyrite at Mt. Lyell.

Table 5.1 : COBALT AND NICKEL DISTRIBUTION IN PYRITE AS A FUNCTION
OF TEMPERATURE AND ΣCl

5.1.1 $\dfrac{X\ CoS_2}{X\ FeS_2}$ at $\dfrac{\Sigma Co}{\Sigma Fe}$ = 1

ΣCl		100	150	200	250	300	°C
1.0	$\dfrac{X\ CoS_2}{X\ FeS_2}$	1230	1258	1380	1175	1047	
3.0	$\dfrac{X\ CoS_2}{X\ FeS_2}$	1412	1548	1819	1122	562	

5.1.2 $\dfrac{X\ NiS_2}{X\ FeS_2}$ at $\dfrac{\Sigma Ni}{\Sigma Fe}$ = 1

ΣCl		100	150	200	250	300	°C
1.0	$\dfrac{X\ NiS_2}{X\ FeS_2}$	87	87	148	141	182	
3.0	$\dfrac{X\ NiS_2}{X\ FeS_2}$	60	74	158	166	209	

5.1.3 $\dfrac{X\ CoS_2}{X\ NiS_2}$ at $\dfrac{\Sigma Co}{\Sigma Ni}$ = 1

ΣCl		100	150	200	250	300	°C
1.0	$\dfrac{X\ CoS_2}{X\ NiS_2}$	14.1	11.5	9.3	8.3	5.8	
3.0	$\dfrac{X\ CoS_2}{X\ NiS_2}$	23.4	16.6	11.5	6.8	2.7	

5.3.1 . Prince Lyell

Cobalt in Pyrite

Cobalt in pyrite varies from 100 to 5000 ppm. Comparing C1 with figure 2.3. indicates that cobalt levels are highest over the orebody, with a plateau level of approximately 1500 ppm corresponding to the central core of Prince Lyell. The 1000 ppm cobalt contour approximates the limits of the mineralized zone. Values of greater than 2000 ppm are generally spasmodic except for two locations indicated on C1, one centred on 7-8 cross-cut and stope 8 and the other on the footwall of the 4-5 cross-cut.

The lowest cobalt values occur on the northern end of Prince Lyell; the decline section, WL 315, part of WL 352, and 1-2 cross-cut. Comparison with figure 2.3 indicates these low cobalt values coincide with the quartz-sericite-pyrite assemblage. This effect is observable over very short ranges. Sample 2-3/360 was taken across a quartz-sericite-pyrite/quartz-sericite-chlorite-pyrite assemblage boundary. The cobalt-in-pyrite values for the two assemblages were 300 and 1670 ppm respectively.

Samples of massive pyrite generally gave cobalt values consistent with the surrounding disseminated material; 5-6/100, 1270 ppm, 6-7/50, 750 ppm and 6-7/130, 1050 ppm.

Within the central-core, chloritic assemblage there is some indication that the spasmodic cobalt highs coincide with the higher grades of copper.

Nickel in Pyrite

Nickel values range from 14 to 625 ppm. The nickel distribution pattern is not dissimilar to the cobalt (C2) with an enrichment halo of greater than 100 ppm the boundaries of which approximate the limits of the mineralized zone. However it is

noticeable that the high cobalt zones (greater than 2000 ppm)
do not have corresponding high nickel zones. This is particularly
so for the 7-8 cross-cut. However two consistently high zones
of nickel show some correlation with the intermediate rocks
within the ore zone (fig.2.3).

5.3.2 Cape Horn

Cobalt in Pyrite

Cobalt in pyrite ranges from 150 to 2800 ppm. In a
similar manner to Prince Lyell the pyrite in the orebody (fig.
2.5) shows an enrichment in cobalt (C4). However, the enrich-
ment is not as great or as consistent as that observed for Prince
Lyell. The average cobalt value for Cape Horn orebody approximates
1050 ppm compared to an average for Prince Lyell of approximately
1600 ppm.

Nickel in Pyrite

Nickel in pyrite ranges from 13 to 2400 ppm. Like
cobalt the nickel is enriched in the orebody pyrite (C5). The
average orebody value is 770 ppm and this is considerably higher
than the corresponding Prince Lyell value.

Cobalt/Nickel in Pyrite

The variation in Co/Ni for Cape Horn pyrite is of
interest (C6). Pyrite in the hangingwall has Co/Ni ratios
varying from 6 to 30. All of the pyrite from the orebody has
Co/Ni ratios less than 6 and a considerable number are less than 1.
The overall orebody ratio is 2. The boundary separating the two
groups closely approximates the geological boundary shown on
figure 2.5.

5.3.3 Western Tharsis

Cobalt in Pyrite

Cobalt in pyrite ranges from 87 to 2080 ppm with an overall average value approximating 550 ppm. The cobalt levels taken overall are similar to those observed on the northern end of Prince Lyell and this is consistent with the similarity in the assemblages. However some local enrichments occur (C7) and these grossly relate to the concentrations of chalcopyrite. The average enrichment value, calculated using all the data over 1000 ppm, is approximately 1400 ppm which is not dissimilar to Prince Lyell enrichment zones although the consistently higher values (>2000 ppm) are not observed.

Nickel in Pyrite

Nickel in pyrite ranges from 20 to 600 ppm with an average of 160 ppm. Comparing this data with Prince Lyell and Cape Horn, indicates an overall similarity with Prince Lyell. However if the comparison with Prince Lyell data is made on the basis of similarity of assemblage and cobalt levels; that is comparison is made with the pyrite from the northern end of Prince Lyell (where most nickel values are less than 100 ppm) then Western Tharsis pyrite is slightly enriched in nickel. The Co/Ni ratios vary from 0.8 to 22 with a mean of 3.5.

5.3.4 Crown Lyell No. 3

Diamond drill holes NL 1044 and 1062 and the Crown open cut samples indicate the range of cobalt and nickel values for Crown Lyell No. 3 (table C1). NL 1044/150 - 240 and NL 1062 represent the chlorite rich sulphide assemblage on the foot-wall of Crown Lyell No. 3. Cobalt ranges from 130 to 820 ppm

for the Crown Lyell No. 3 ore and from 950 to 2500 ppm for
the footwall mineralization. Nickel ranges from 31 to
268 ppm for the Crown Lyell No. 3 ore and 107 to 1480 ppm for
the hanging wall mineralization.

5.3.5 Probe Information on Distribution of Cobalt in Pyrite

Only a limited amount of probe work on the trace dis-
tribution in pyrite has been carried out. What information
is available on cobalt indicates a heterogenous distribution.
Sample PL 4-5/70 (bulk pyrite assay 1540 ppm) contained
irregular cobalt rich zones of up to 4.6% Co with a background
reading of 100 - 300 ppm. Sample PL 2-3/280 (bulk pyrite
analysis 3700 ppm) also contained enriched zones of up to 4%
cobalt. Pyrite grains in this sample were zoned (etched with
$KMnO_4$ solution and conc. H_2SO_4) and the cobalt distribution
appeared to be related to the zonal pattern.

5.4 Cobalt and Nickel in Chalcopyrite

Chalcopyrites, co-existing with pyrite, were analysed for cobalt,
nickel, and manganese. The samples were from Western Tharsis and
Prince Lyell. The observed cobalt range in chalcopyrite was from
less than 5 ppm to 135 ppm with the majority of samples having less
than 50 ppm. Nickel ranged from less than 5 ppm to 15 ppm (table C2).
Because of the very low concentration of cobalt in chalcopyrite
relative to pyrite it requires almost 100% purity to be confident
of the data. After flotation, all samples were cleaned repeatedly
by magnetic separation. Purity of the samples was estimated by XRD
and was generally better than 98-99%.
However, because of the large uncertainties still involved, even

at this level of purity, no attempt has been made to interpret the data. The data gives a general impression of the trace levels in chalcopyrite co-existing with pyrite.

5.5 A Preliminary Interpretation

5.5.1 A Summary of the Salient Features of Cobalt and Nickel Distribution in Pyrite

(i)   All quartz-sericite-pyrite assemblages are low in cobalt and nickel.

(ii)   Cobalt and nickel both show enrichment in the chlorite-chalcopyrite assemblages of Prince Lyell and Cape Horn and the chlorite-oxide-sulphide assemblage on the footwall of Crown Lyell No. 3.

(iii)   Cobalt is enriched in the quartz-sericite-pyrite-chalcopyrite assemblage of Western Tharsis. Nickel does not show a similar enrichment.

(iv)   Cobalt ranges and averages appear to be similar for Prince Lyell and Western Tharsis. Cape Horn (orebody) values are lower.

(v)   Nickel ranges for Prince Lyell and Western Tharsis are similar but Cape Horn (orebody) is considerably enriched in nickel. A similar enrichment is shown for the Crown Lyell No. 3 hanging wall chlorite-oxide-sulphide assemblage.

(vi)   Cobalt shows a heterogenous distribution in pyrite.

5.5.2 Cobalt Variations due to "Local Enrichment"

An interpretation of the trace element data will be attempted on the basis of the approach adopted in 5.2 and consistent with the models of hydrothermal alteration, sulphide deposition and sulphur isotope distribution developed in Chapters 3 and 4.

A host-rock-controlled pH model has been suggested to account for the development of the quartz-sericite-pyrite ± chalcopyrite and the quartz-sericite-chlorite-pyrite-chalcopyrite assemblages. The reaction path A→B→C→D of figure 3.2 is reproduced on figure 5.1 with the cobalt-in-pyrite contours, constructed for a constant ΣCo in solution. For the given reaction path it is clear that pyrite precipitated along the quartz, sericite, pyrite segment (A→B) will be low in cobalt but that the cobalt-in-pyrite content will rapidly increase with the precipitation of chlorite and progress along B-C to C. In general this would suggest that the observed enrichments of cobalt in pyrite in quartz-sericite-chlorite-pyrite-chalcopyrite assemblages relative to quartz-sericite-pyrite assemblages is a result of the conditions of deposition rather than a difference in ΣCo/ΣFe of the initial solutions. Obviously the higher the pH at which pyrite forms, the greater will be the cobalt enrichment. Such a process would not only account for the gross distribution of cobalt in pyrite but will necessarily imply zoned or heterogenous distribution within pyrite grains.

The final distribution in any grain, or the final bulk value, will be the end product of an infinite number of solution increments reacting along A→C (D) or part thereof. Considering

this model only gives, in a qualitative manner, the result of
the reaction of one hypothetical increment of ore solution it
can only give in a general way the distribution of cobalt
within grains or for bulk samples.

The fact that cobalt is not substantially incorporated
into the chalcopyrite replacing pyrite at C leads to an
increase in the $\Sigma Co/\Sigma Fe$ ratio in solution. This will result
in an increase in the cobalt content of the remaining pyrite
and suggests the highest cobalt concentrations will occur in
chloritic assemblages rich in chalcopyrite relative to pyrite.
There is some evidence that this is the case, particularly
for Prince Lyell.

If chlorite is not saturated, continued reaction will produce
the assemblage quartz-sericite-pyrite-chalcopyrite. Replacement
of chalcopyrite by pyrite may lead to cobalt enrichment in
pyrite. This would account for the observed enrichment of
cobalt in pyrite associated with higher grades of copper in the
sericitic assemblages.

If pyrite is replaced by chlorite at any stage, at B or along
B-C, it will have a similar effect on the cobalt content of
pyrite as the replacement of pyrite by chalcopyrite, since
cobalt levels in chlorite are also low. Data on eight Prince
Lyell chlorite samples (Solomon and Green, pers. comm.) indicates
a range of cobalt in chlorite from 30 to 100 ppm.

5.5.3 Nickel Variations due to "Local Enrichment"

Local enrichment can be expected to be similar to cobalt
and an enrichment of nickel in pyrite with chloritic assemblages
is observed for Prince Lyell and Cape Horn. However as mentioned
above (5.2), because of the low bulk nickel contents, nickel may

be potentially influenced by the host rock composition and this
may have occurred to some extent at Prince Lyell.

Further, as nickel concentrations in chlorite are comparable
to nickel in pyrite then the nickel in pyrite will be influenced
by the precipitation of chlorite. Data on Prince Lyell chlorites
indicates a nickel in chlorite range of 33 to 108 ppm and an
average nickel distribution between pyrite/chlorite co-existing
pairs of 1.8 (Solomon and Green, pers. comm.).

5.5.4 The Cape Horn Values

The overall similarity between Western Tharsis and Prince
Lyell, and assuming similar temperatures of deposition, suggests
that it is possible to produce the trace distributions of both
sulphide zones from a solution with similar initial ratios of
$\Sigma Co/\Sigma Fe$ and $\Sigma Ni/\Sigma Fe$.

However the different trace characteristics of the Cape Horn
orebody, richer in nickel and lower in cobalt suggests either a
different temperature or a different solution composition.

To generate Cape Horn cobalt values from an ore solution of
trace characteristics similar to Prince Lyell would require an
increase in temperature. Assuming Prince Lyell and Western
Tharsis temperatures are around 250°C, it would require a less-than-
50°C temperature increase to produce the observed Cape Horn
cobalt values (Table 5.1). However this would not be sufficient
to account for the nickel increase and suggests a fluid of
different initial $\Sigma Co/\Sigma Fe$ and $\Sigma Ni/\Sigma Fe$ ratios.

An alternative explanation for the nickel enrichment in
the Cape Horn orebody is that the initial composition of the
solution was similar to the Prince Lyell solution but that nickel
was enriched in early-formed magnetite. Nickel-rich pyrite would

then be formed by replacement of the magnetite.   Minor magnetite/ hematite in the groundmass of some Cape Horn sections and the common occurrence of magnetite/hematite inclusions in the pyrite are consistent with this suggestion.   The high nickel-in-pyrite values for the Crown Lyell No.3 footwall chlorite-oxide-sulphide assemblage could have resulted from a similar mechanism. There is a marked change in Co/Ni ratio along the hanging wall-orebody contact.   The hanging wall sulphides are not dissimilar to the Western Tharsis and Prince Lyell zones but with higher Co/Ni and possibly lower nickel contents.   These characteristics could be accounted for by assuming a source fluid of similar trace characteristics to the Western Tharsis, Prince Lyell source fluid but with a lower temperature of formation, e.g. 100-150°C.

5.5.5   Metamorphism

The best definitive study on the effect of metamorphism on cobalt distribution is that by Itoh (1973) which was summarized in Section 5.1.2.   The heterogenous distribution of cobalt in pyrite grains, observed for the few Prince Lyell samples studied, is consistent with his observations for low grade metamorphic deposits, and indicates the grade was not high enough to cause a thorough redistribution of the cobalt.   This is also consistent with the disequilibrium present between minor inclusion assemblages in the pyrite, which has been taken as an indication that pyrite was not completely recrystallized during metamorphism.

5.5.6   Summary Comment

It is suggested that the distribution of cobalt and nickel in pyrite from Prince Lyell and Western Tharsis sulphide zones can be interpreted within the framework of the hydrothermal models

postulated to explain the phase data, assuming a source fluid

of unique $\Sigma Co/\Sigma Fe$ and $\Sigma Ni/\Sigma Fe$. The hangingwall sulphides of

Cape Horn are also consistent with this postulated source fluid,

but requires a lower temperature of formation. The trace

characteristics of the Cape Horn orebody pyrites suggest a

source fluid enriched in nickel, possibly by replacement of a

phase enriched in nickel, such as magnetite. The interpretations

(e.g. lower hangingwall temperatures) seem consistent with the

postulated geological framework.

6. MASS TRANSFER CALCULATIONS

6.1 Introduction

The geochemical evolution of the Mt. Lyell copper deposits has been dis-
cussed within the context of the fO_2/pH diagram. This type of static modelling
is useful in that it allows integration of phase, trace element and sulphur
isotope data.   However, at best the models must be qualitative, giving
an overall impression of the direction of reaction paths.   The mass
transfer modelling developed by Helgeson (1968, 1970) and Helgeson *et al.*
(1970) introduces the possibility of dynamic modelling of the reaction
path, calculating both the continuous changes in solution composition
and the quantities of various minerals produced and destroyed throughout
the reaction.

Interest in applying this technique to the Mt. Lyell interpretation
has centred on:-

(i)   The possibility of predicting the proportions of

       sulphides to silicates and using this as a further

       test of the models.

(ii)   Quantitative analysis of the pyrite-chalcopyrite

       sulphur-isotope partitioning data.

(iii) Further investigation of the trace element distribution

       in pyrite in order to develop a quantitative model

       predicting the levels of trace element concentration.

       This would permit effective comparison of the trace

       levels between the various deposits.

6.2 Theory

6.2.1 The Mass Transfer Equations

Details of the theory of mass transfer are given in the references cited and only a brief review will be given here.

Changes in the concentrations of species in solution and in the masses of minerals either produced or consumed are related to a progress variable (ε) via a reaction coefficient:-

$$\bar{n}_s = \frac{dm_s}{d\varepsilon} \tag{6.1}$$

and
$$\bar{n}_\phi = \frac{dm_\phi}{d\varepsilon} \tag{6.2}$$

where $\bar{n}_s$ is the reaction coefficient for a solution species (s) and $\bar{n}_\phi$ is the reaction coefficient for a mineral (ϕ), m_s and m_ϕ are respectively the concentration of a solution species and the mass of a mineral produced or destroyed, measured in moles/kg H_2O.

The reaction coefficients and the first differentials of the reaction coefficients may be evaluated by simultaneous solution of equations describing:-

(1) Conservation of mass

$$\Sigma_S V_{e,s} \bar{n}_s + \Sigma_\phi V_{e,\phi} \bar{n}_\phi = 0 \tag{6.3}$$

where $V_{e,s}$ and $V_{e,\phi}$ correspond to the number of moles of the eth element in the sth species and the ϕth phase respectively.

(2) Conservation of charge

$$\Sigma_s Z_s \bar{n}_s = 0 \tag{6.4}$$

where Z_s is the charge on the sth species.

(3) Equilibrium reactions

$$\Sigma_{s=2} \frac{\hat{n}_{s,j} \bar{n}_s}{m_s} + \Sigma_{s=2} \hat{n}_{s,j} (d \ln \gamma s/d\varepsilon) = 0 \tag{6.5}$$

Where $\hat{n}_{s,j}$ is coefficient of the sth species in the jth reversible reaction.

Evaluation of the reaction coefficients for a given set of conditions then allows evaluation of

$$m_s = \bar{n}_s \, \Delta \varepsilon \; + \; \frac{\bar{n}_s{}'(\Delta\varepsilon)^2}{2\,!} \tag{6.6}$$

$$m_\phi = \bar{n}_\phi \, \Delta \varepsilon \; + \; \frac{\bar{n}_\phi{}'(\Delta\varepsilon)^2}{2\,!} \tag{6.7}$$

This gives the changes in concentration of solution species and the changes in the masses of reactants and products per kg of solution for an increment of the progress variable. The reaction coefficients are then recalculated for the new solution composition and the process repeated until overall equilibrium is established.

Although theory is available for considering changes in the activity of water and activity coefficients, the calculations have been simplified by assuming both the activity of water and activity coefficients to be invariants.

6.2.2 Sulphur Isotopes

The sulphur isotope equations of Ohmoto (1972) have been included in the mass transfer calculations with some modification to allow for the effect of precipitating part of the sulfur in solution.

At any instance in the reaction sequence

$$m_{\Sigma S} \cdot \delta S^{34}_{\Sigma S} = m_{H_2S} \cdot \delta S^{34}_{H_2S} + m_{HS^-} \cdot \delta S^{34}_{HS^-} + m_{S^{2-}} \cdot \delta S^{34}_{S^{2-}}$$

$$+ \; m_{SO_4^{2-}} \cdot \delta S^{34}_{SO_4^{2-}} + m_{HSO_4^-} \cdot \delta S^{34}_{HSO_4^-}$$

$$+ \; m_{KSO_4^-} \cdot \delta S^{34}_{KSO_4^-} + m_{NaSO_4^-} \cdot \delta S^{34}_{NaSO_4^-} \tag{6.8}$$

and the isotopic equilibrium value of pyrite

$$\delta S^{34}_{py} = \delta S^{34}_{\Sigma S} + \Delta py - (\Delta HS^-.m_{HS^-} + \Delta S^{2-}.m_{S2-} + \Delta SO_4^{2-}.m_{SO_4{}^{2-}}$$

$$+ \Delta HSO_4^-.m_{HSO_4^-} + \Delta KSO_4^-.m_{KSO_4^-} + \Delta NaSO_4^-.m_{NaSO_4^-})$$

$$/m_{\Sigma S} \qquad (6.9)$$

(Δ values from Ohmoto, 1972)

If Δx moles of pyrite are then precipitated over a progress increment, $\Delta \varepsilon$, and assuming δS^{34}_{py} remains constant over this interval then

$$m_{\Sigma S'} \cdot \delta S^{34}_{\Sigma S'} = m_{\Sigma S} \cdot \delta S^{34}_{\Sigma S} - 2.\Delta x_{py}.\delta S^{34}_{py} \qquad (6.10)$$

where $m_{\Sigma S'}$ and $\delta S^{34}_{\Sigma S'}$ are the new total sulphur and isotopic value of the total sulphur in solution respectively. In practice the change in δS^{34}_{py} per increment is in the order of 0.01 per mil.

Reaction commences with initial values of ΣS and $\delta S^{34}_{\Sigma S}$ and the equilibrium value of δS^{34}_{py} is calculated from equation 6.9 (initial fO_2 and pH conditions also specified).

One iteration of the mass transfer calculations gives a value for Δx_{py} and new values for $m_{\Sigma S}$ and all the sulphur species in solution. The new value of $\delta S^{34}_{\Sigma S}$ is calculated from 6.10 and the δS^{34}_{py} equilibrium value updated (6.9).

If it is assumed there is no isotopic adjustment between the pyrite and solution then the mass transfer calculation allows an "average" isotopic value of the precipitated pyrite to be calculated, i.e.

$$\delta S^{34}_{py} \text{ (average)} = \frac{\Sigma \Delta x_{py} \cdot \delta S^{34}_{py}}{\Sigma \Delta x_{py}} \qquad (6.11)$$

The difference between δS^{34}_{py} av and δS^{34}_{ccp} av, the average isotopic value of chalcopyrite being calculated in a similar manner, is taken as the partitioning value that can best be related to the observed isotopic partitioning values (see chapter 4 for discussion).

If pyrite (or chalcopyrite) becomes unstable then it is assumed isotopic equilibrium is not maintained between the sulphide and solution. δS^{34}_{py} av is used in equation 6.10 rather than δS^{34}_{py}.

6.2.3 Trace Cobalt Distribution in Pyrite

Theory presented by Helgeson *et al.* (1970) includes provision for solid-solution reactions. From this, if the solid solution of the FeS_2 - $Co\ S_2$ system is described by

$$X\ Fe\ S_2 \quad = \quad \frac{x\ Fe\ S_2}{x\ Fe\ S_2 + x\ Co\ S_2}$$

$$X\ Co\ S_2 \quad = \quad \frac{x\ Co\ S_2}{x\ Fe\ S_2 + x\ Co\ S_2}$$

where $x\ Fe\ S_2$ and $x\ Co\ S_2$ refer to the total numbers of moles of $Fe\ S_2$ and $Co\ S_2$ that have been precipitated, two equations relating the change of mole fraction with reaction progress to the reaction coefficients of the two solid solution end members may be derived.

$$\frac{d\ \ln\ X\ Fe\ S_2}{d\ \varepsilon} \quad = \quad \frac{X\ CoS_2\ \bar{n}\ Fe\ S_2 - X\ Fe\ S_2\ \bar{n}\ Co\ S_2}{x\ Fe\ S_2} \quad (6.11)$$

$$\frac{d\ \ln\ X\ Co\ S_2}{d\ \varepsilon} \quad = \quad \frac{X\ Fe\ S_2\ \bar{n}\ Co\ S_2 - X\ Co\ S_2\ \bar{n}\ Fe\ S_2}{x\ Co\ S_2} \quad (6.12)$$

Equations 6.11 and 6.12 are then included into the appropriate statement of 6.5.

This approach has the limitation that the mole fraction
of CoS_2 maintained in equilibrium with the solution is always
the total mole fraction of CoS_2 precipitated.   A more
realistic approach would be to maintain the X CoS_2 of the last
reaction increment in equilibrium with the solution,

i.e.   X Co S_2 $= \dfrac{d\ x\ Co\ S_2}{d\ x\ Fe\ S_2\ +\ d\ x\ Co\ S_2}$

However such a definition leads to equations consisting of a
mixture of both reaction coefficient and first differential
reaction coefficient terms and is therefore not suitable.

An alternative is to use an approach similar to the
sulphur isotopes.

The X Co S_2 of a solution of known pH, fO_2, ΣS and ΣCo
can be calculated (equation 5.17) at any instance in the progress
reaction and the total or average mole fraction (assuming cobalt
in pyrite always remains at trace levels) will be

X Co S_2 average $= \dfrac{\Sigma \Delta x_{py}.X\ Co\ S_2}{\Sigma \Delta x_{py}}$

Difficulty arises in this second instance in that if pyrite
becomes unstable, e.g. by replacement by chalcopyrite, there is
no way of calculating the amount of Co S_2 which may continue to
precipitate, short of assigning an arbitrary reaction rate.

The solid-solution theory of Helgeson *et al.* (1970) has been
used in the calculations but the difficulties remain unresolved.
The instanteous value of X CoS_2 at any progress interval and the
total value of X CoS_2 will always be the same.

6.3 Results

Mass transfer calculations have been used to examine the reaction of an acid, chloride-rich solution with a felsic host rock, assumed for the purposes of calculation to approximate K-feldspar, at a constant temperature of 250°C. The initial pH was assumed to be at, or close to, the sericite/kaolinite boundary and quartz, sericite, and pyrite were assumed saturated. The use of solid-solution equations required some initial pyrite to be present.

Two sets of calculations were carried out. In the initial set (reactions 1 to 4),the pyrite solubility data of Helgeson (1969) and the δS^{34}_{py} - $\delta S^{34}_{H_2S}$ data of Ohmoto (1972) was used. New data on the solubility of pyrite (Crerar and Barnes, 1976) and the value of δS^{34}_{py} - $\delta S^{34}_{H_2S}$ (Ohmoto and Rye, in press) necessitated a second set of calculations (reactions 5 to 8). The new data has increased the solubility of pyrite and changed the value of δS^{34}_{py} - $\delta S^{34}_{H_2S}$ from -0.3 to +1.46 at 250°C.

The computer programme (G59) was written in ALGOL for use on an Elliott 503 and subsequently a Burroughs 6700.

6.3.1 Reactions 1 to 4

Calculations were carried out at 250°C with an ionic strength of 3 and K/Na ratio of 0.5. Log of initial ΣS and ΣCu were set at -3 and -3.5 respectively. Log of initial ΣCo was set such that cobalt-in-pyrite was equal to 270 ppm. $\delta S^{34}_{\Sigma S}$ was taken as zero.

Results of the four calculations are given in figures 6.1 to 6.8. Figure 6.1 describes the fO_2/pH paths of the reactions. The phase boundaries are drawn for the initial conditions of ΣS and ΣCu.

Figures 6.2 to 6.7 describe the changes in solution conditions and the masses of minerals produced or destroyed as a function of the progress variable.

Figure 6.8 gives the isotopic partitioning between pyrite and chalcopyrite as a function of the progress variable. If chalcopyrite is saturated this represents the difference between the average isotopic values of pyrite and chalcopyrite at any point in the reaction. If chalcopyrite is not saturated this represents the difference between the average isotopic value of pyrite and the isotopic value of the first precipitation of chalcopyrite, if the concentration of copper had been sufficient to saturate chalcopyrite at that instance.

The equilibrium partitioning value between pyrite and chalcopyrite at 250°C is taken as + 1.7.

Reaction 1.

Reaction 1 commenced at a log fO_2 value of -35.3 and a δS^{34} pyrite value of -0.31. Reaction proceeded to the lower chlorite boundary with only minor amounts of pyrite being precipitated (fig. 6.1 and 6.4). Chlorite saturated and reaction proceeded along the quartz-sericite-chlorite-pyrite boundary until chalcopyrite saturated. Chalcopyrite replaced pyrite and the reaction proceeded through to the K-feldspar boundary. ΣFe in solution was constant until chlorite saturated and then progressively decreased. The ΣCo decreased as chlorite precipitated, the $\Sigma Co/\Sigma Fe$ ratio remaining approximately constant. ΣCo and the cobalt content of the pyrite increased rapidly as chalcopyrite replaced pyrite. The sulphur isotope partitioning value did not deviate significantly from + 1.7 throughout the reaction (fig. 6.8).

Reaction 2.

Reaction 2 commenced at a log fO_2 value of -34.4 and a δS^{34} pyrite value of -0.8. Reaction initially produced a smaller fO_2 change relative to pH increase. ΣFe and ΣCo progressively decreased in solution and the cobalt-in-pyrite concentration dropped to a low of 50 ppm. A much higher proportion of pyrite was precipitated in comparison to Reaction 1 (fig. 6.1 and 6.4).

The different reaction path resulted in chalcopyrite rather than chlorite precipitating. Chalcopyrite precipitation resulted in a decline in ΣCu in solution and a slight fO_2 reversal. ΣCo and the concentration of cobalt in pyrite gradually increased as chalcopyrite replaced pyrite.

The isotopic partitioning value between pyrite and chalcopyrite varied from the initial value of +1.7 through to + 1.13 at K-feldspar saturation. The difference between the lightest pyrite, generated at the start of the reaction, and the heaviest chalcopyrite, generated at the K-feldspar boundary was + 0.7.

Reaction 3

Reaction 3 commenced at a log fO_2 value of -34.00 and a δS^{34} pyrite value of -3.19. Although only 0.4 units more oxidising than the starting point for reaction 2 the fO_2/pH path is significantly different (fig. 6.1). This change in reaction path relates to the starting point being above the reduced sulphur dominant field.[1] No chlorite or chalcopyrite were precipitated in this reaction.

Notably the different reaction path resulted in the reversal of the isotopic partitioning trend of reaction 2 (fig. 6.8). The isotope partitioning between pyrite and chalcopyrite ranged from +1.7 to +2.09.

[1] Reduced sulphur dominant field taken to mean $X H_2S > 0.9$.

Reaction 4.

Reaction 4 commenced at log fO_2 value of -33.40 with an initial δS^{34} pyrite value of -17.80. Reaction proceeded across the quartz-sericite-pyrite field to the upper chlorite boundary (fig. 6.1) and along the chlorite-sericite boundary to the K-feldspar boundary. This reaction path precipitated the greatest amounts of pyrite (fig. 6.7). Some pyrite dissolved after chlorite saturated and as a result cobalt-in-pyrite increased slightly. The isotopic difference between pyrite and chalcopyrite varied between + 1.7 and + 3.01. $\delta S^{34}_{\Sigma S}$ ranged from 0 to +4.22 throughout the reaction. Reaction 4 was the only reaction to show any significant departure of $\delta S^{34}_{\Sigma S}$ from zero.

6.3.2 Reactions 5 to 8

Calculations 5 to 8 were carried out at 250°C with an ionic strength of 1 and a K/Na ratio of 0.1. Log of initial ΣS and ΣCu were set at -2 and -4.5 respectively. Log of initial ΣCo was set such that cobalt-in-pyrite was equal to 10,000 ppm. $\delta S^{34}_{\Sigma S}$ was taken as zero.

Results of reactions 5 to 8 are given in figures 6.10 to 6.13. Figure 6.10 describes the fO_2/pH path of the reactions and figure 6.11 describes the changes in solution conditions and the masses of minerals produced for reaction 5 as a function of reaction progress. Figure 6.12 gives the isotopic composition of the solution and of pyrite as a function of reaction progress and figure 6.13 describes the isotopic partitioning between pyrite and chalcopyrite.

The initial oxidation conditions of reactions 5 to 8 were over a similar range to reactions 1 to 4 and in general they gave

similar fO_2/pH paths. However, the higher ΣFe in solution

permitted a much higher proportion of the sulphur in solution

to precipitate (fig. 6.11), in this case up to 50% compared to

10% for reactions 1 to 4. The increased proportion of sulphur

precipitated has a significant effect on the isotopic composition

of the fluid as reaction progresses (fig. 6.12). Reactions 6

to 8 produced variations in the isotopic composition of solution

ranging from +3.5 to +7.5. Hence, although the fO_2/pH paths of

reactions 5 to 8 are similar to reactions 1 to 4, the isotopic

partitioning between pyrite and chalcopyrite is significantly

different (fig. 6.13). The range of ΔS^{34} py-ccp values produced

shows good agreement with the range of Mt. Lyell values. Reaction

6 gave a maximum departure from equilibrium. Reaction 5, at

lower oxidation conditions, showed a smaller departure from

equilibrium and likewise reactions 7 and 8, at higher oxidation

conditions, showed progressively smaller departures from

equilibrium.

The calculations suggest reactions occurring in either the

reduced or oxidised sulphur fields will always give pyrite/

chalcopyrite partitioning approximating equilibrium partitioning.

In the transitional oxidation zone, increasing the initial

oxidation condition of reaction leads initially to smaller values

of ΔS^{34}py-ccp, apparently to a minimum of approximately -1.5.

Further oxidation leads to a progressive increase in the value of

ΔS^{34}py-ccp. Hence, given an approximate knowledge of the

temperature of deposition, this systematic variation in the value

of ΔS^{34}py-ccp may be a useful constraint on the oxidation

conditions of deposition.
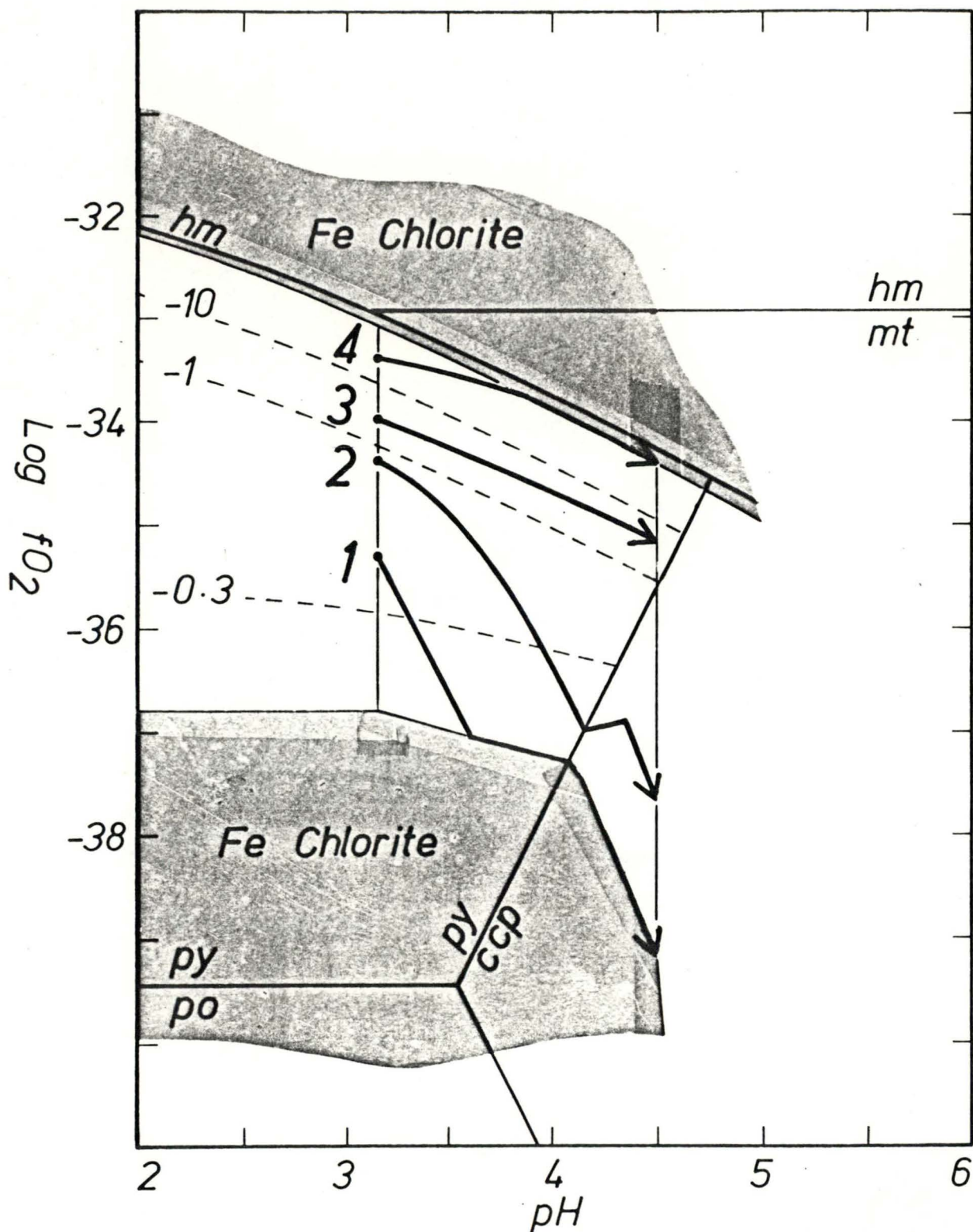
Fig. 6.1: Log fO_2/pH paths of reactions 1, 2, 3 and 4. Reactions commence at the kaolinite/sericite boundary and continue until K-Feldspar saturates. $T = 250°C$. Initial ΣS and ΣCu equal 0.001 and 0.0003 moles/kg H_2O respectively. $\delta S^{34}_{\Sigma S} = 0$. $I = 3$ and K/Na = 0.5.

Dashed lines are δS^{34}_{py} contours.
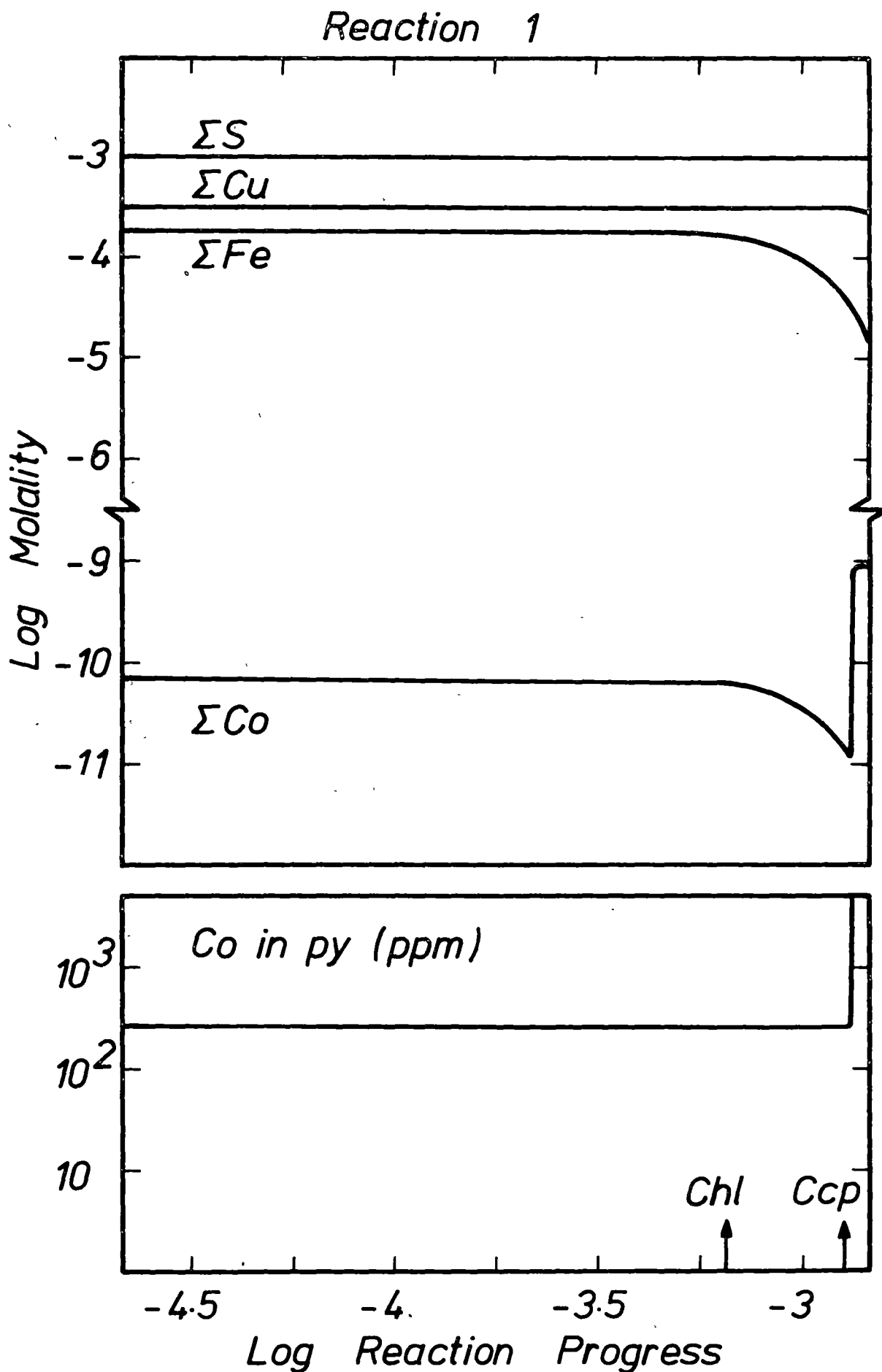
Fig. 6.2:   Log molalities of ΣS, ΣCu, ΣFe and ΣCo in solution and the concentration of Co in pyrite (ppm) as a function of reaction progress for reaction 1.
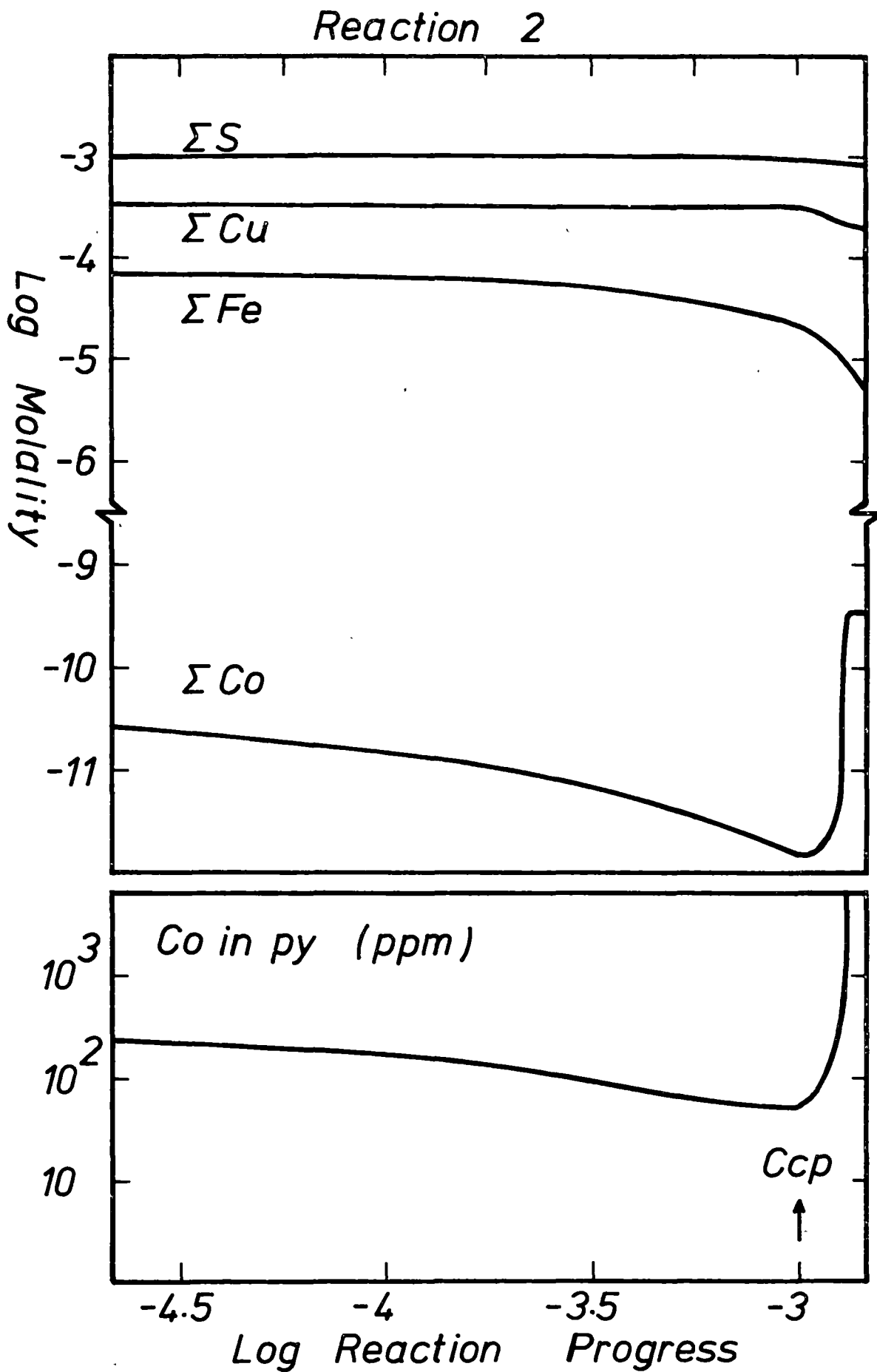
Fig. 6.3: Log molalities of ΣS, ΣCu, ΣFe and ΣCo in solution and the concentration of Co in pyrite (ppm) as a function of reaction progress for reaction 2.
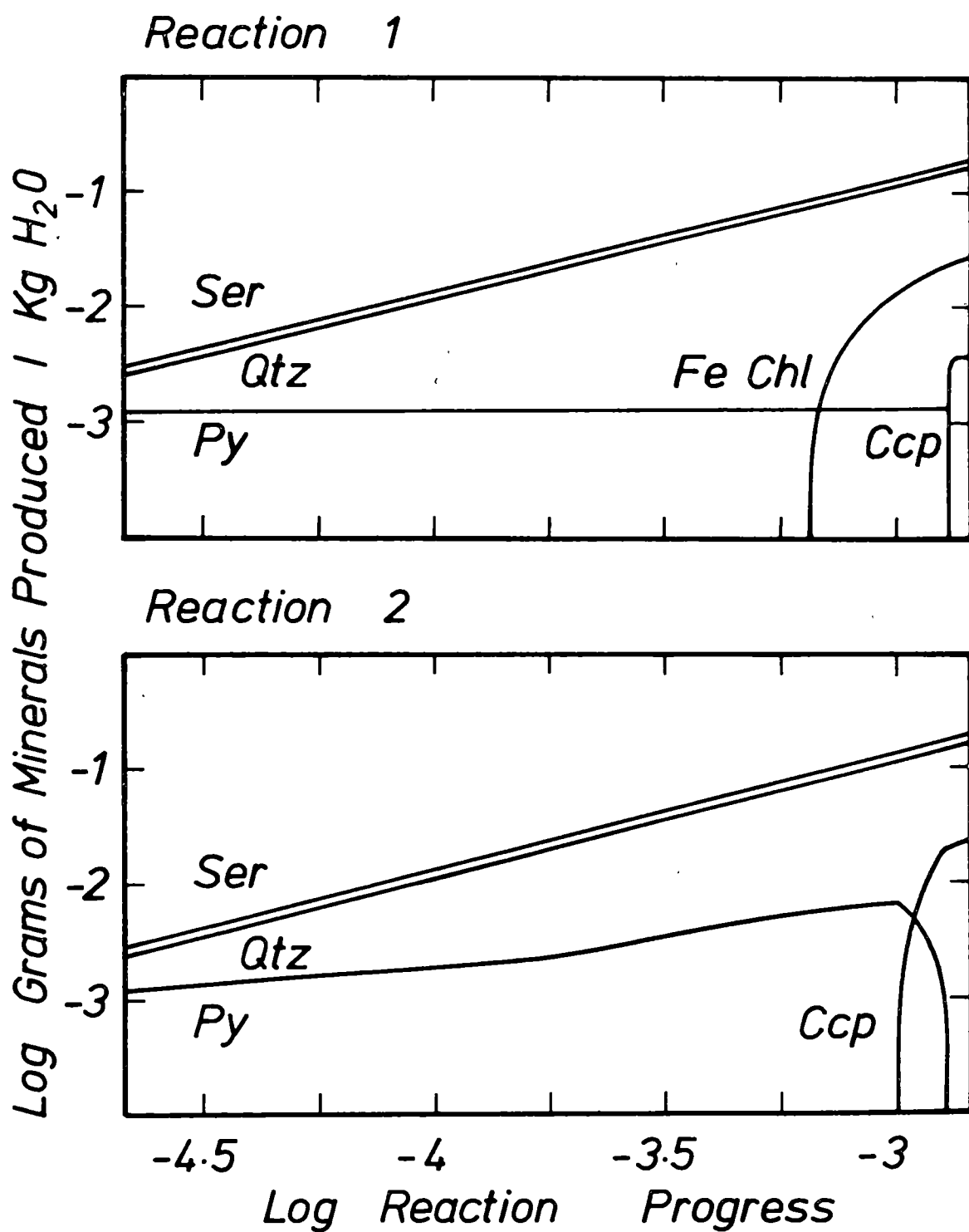
Fig. 6.4: Log grams of minerals produced or destroyed/kg H_2O as a function of reaction progress for reactions 1 and 2.
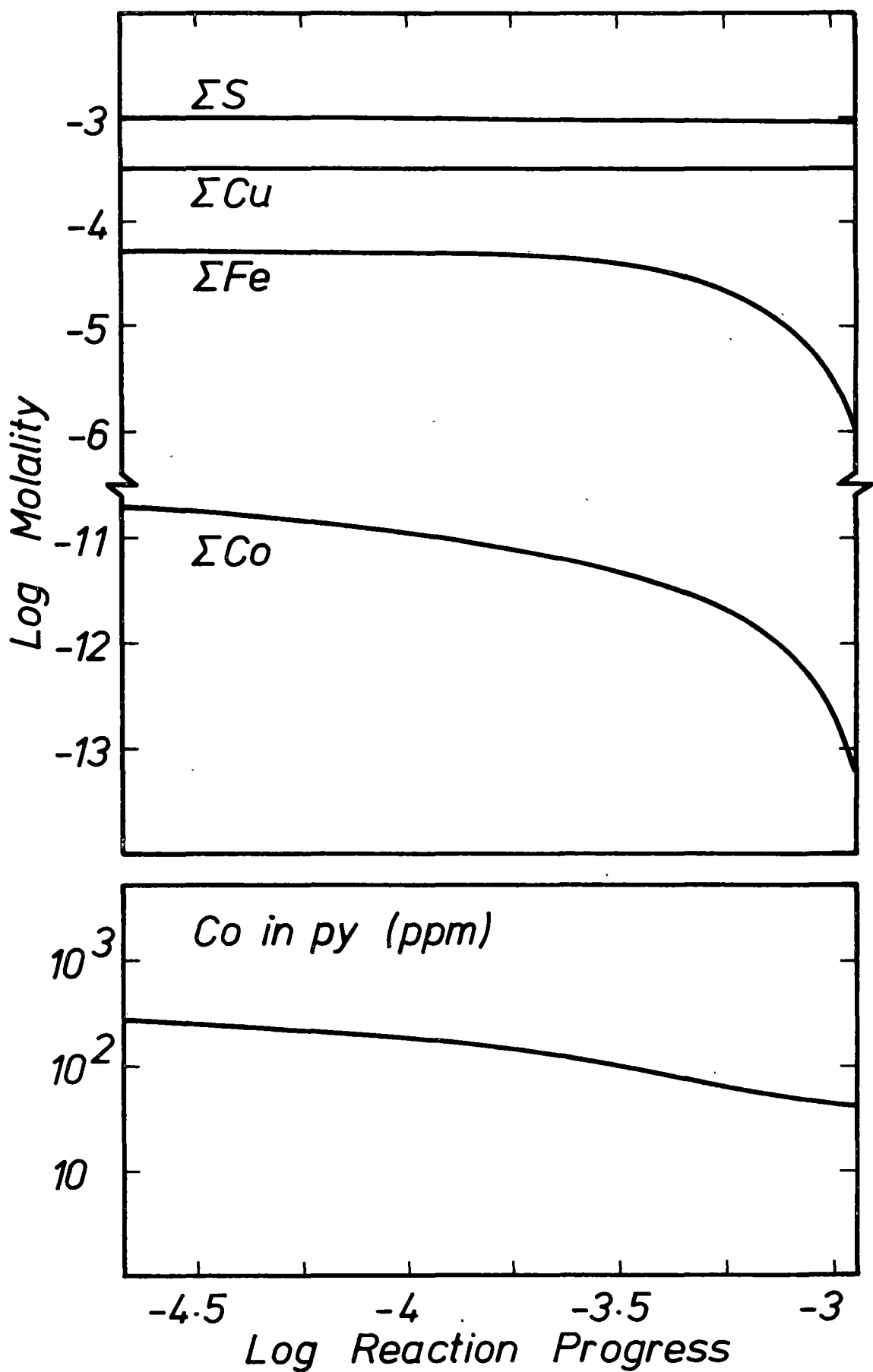
Fig. 6.5: Log molalities of ΣS, ΣCu, ΣFe and ΣCo in solution and the concentration of Co in pyrite (ppm) as a function of reaction progress for reaction 3.
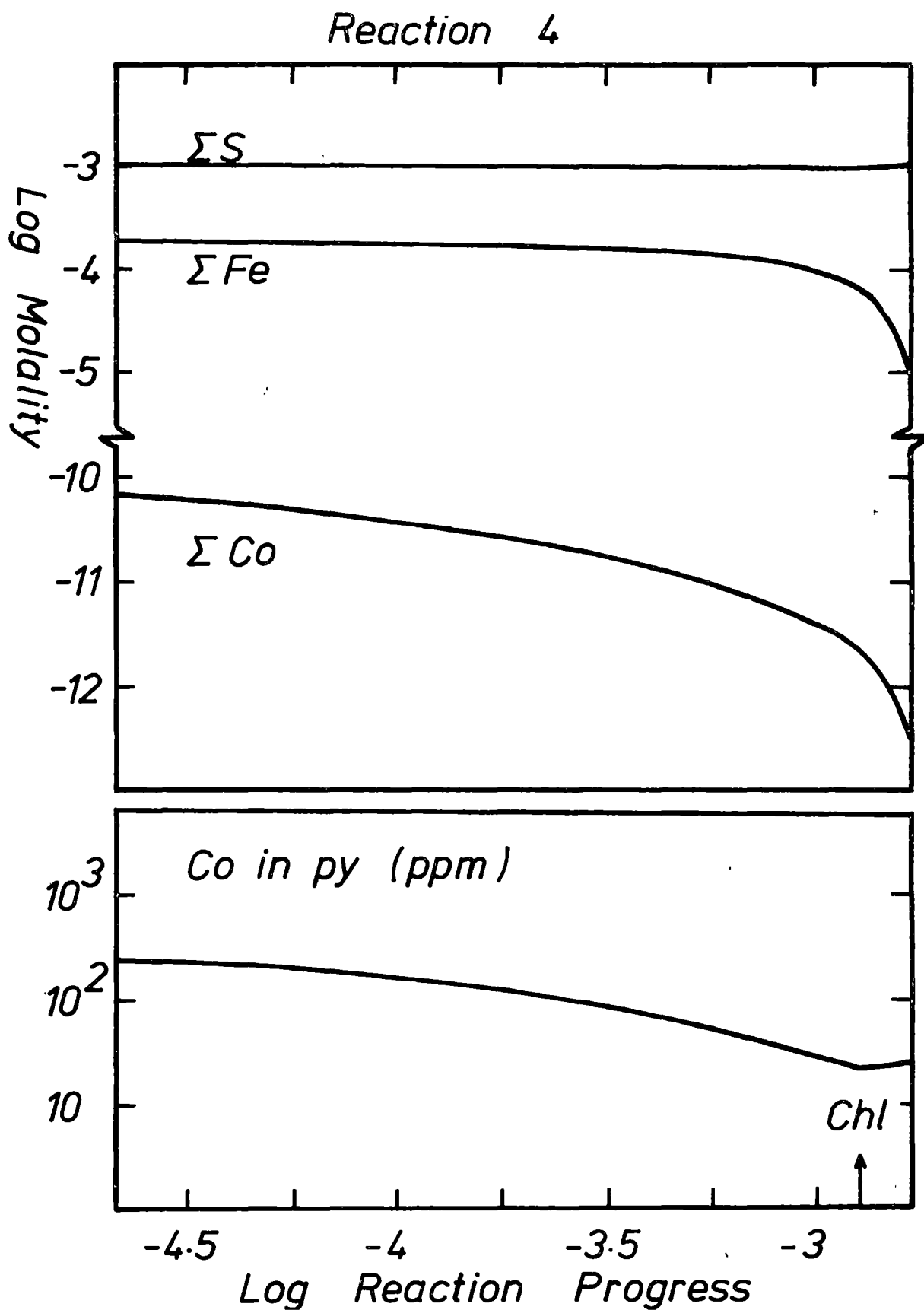
Fig. 6.6: Log molalities of ΣS, ΣFe and ΣCo in solution
and the concentration of Co in pyrite (ppm) as a function of
reaction progress for reaction 4.
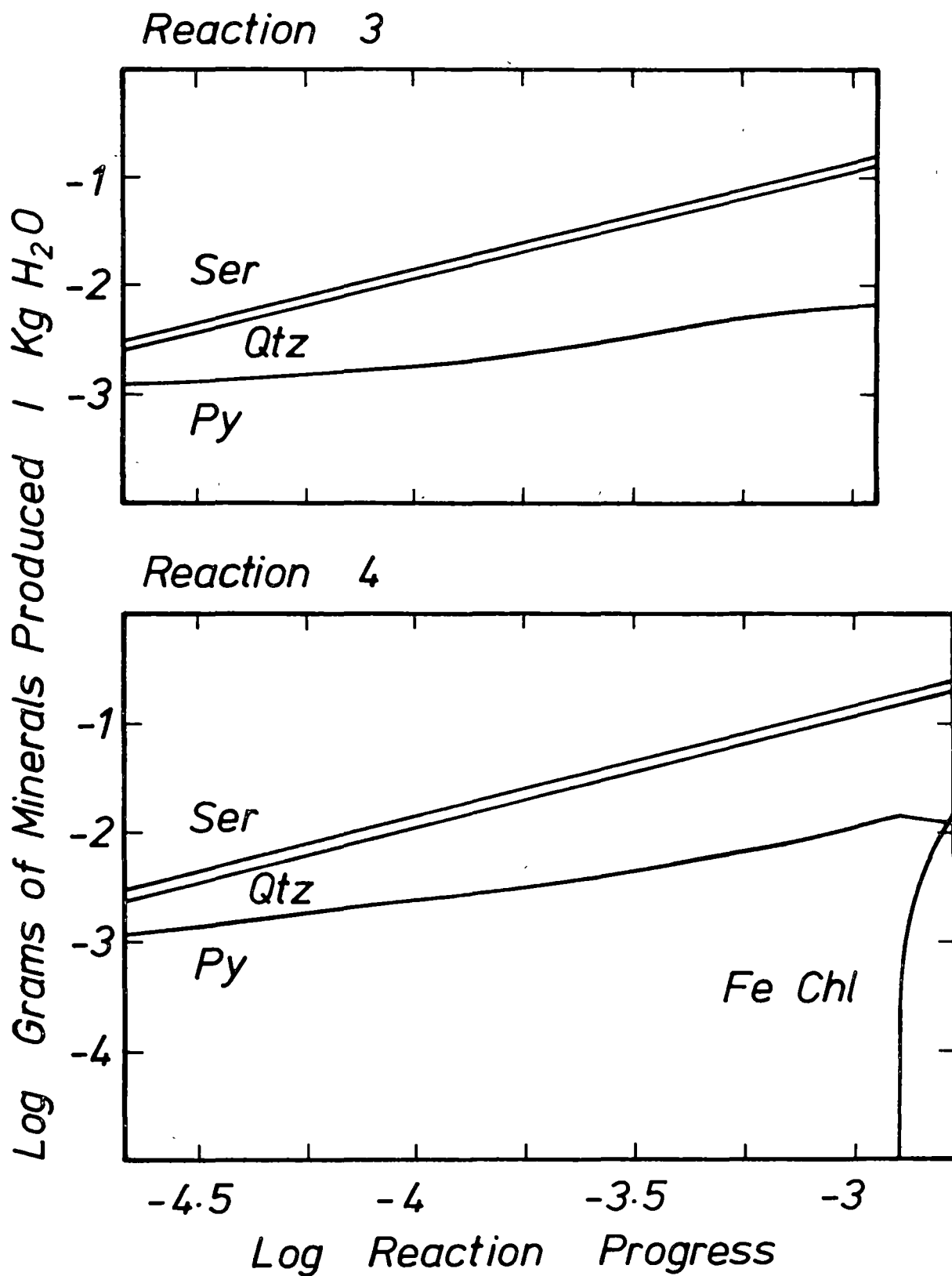
Fig. 6.7: Log grams of minerals produced or destroyed/kg
H_2O as a function of reaction progress for reactions 3 and 4.
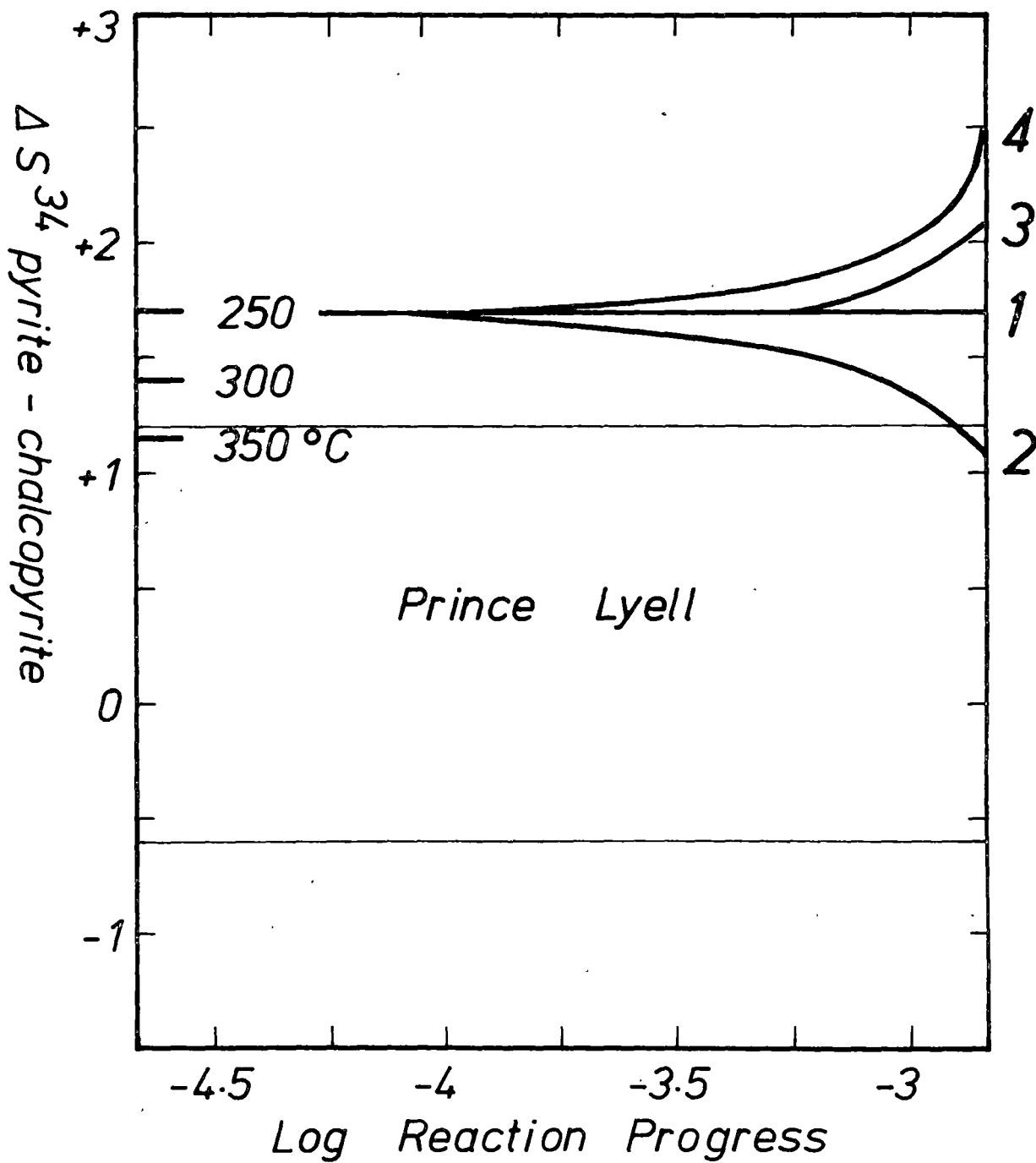
Fig. 6.8:   Sulphur isotope partitioning between pyrite
and chalcopyrite as a function of reaction progress for
reactions 1, 2, 3 and 4.
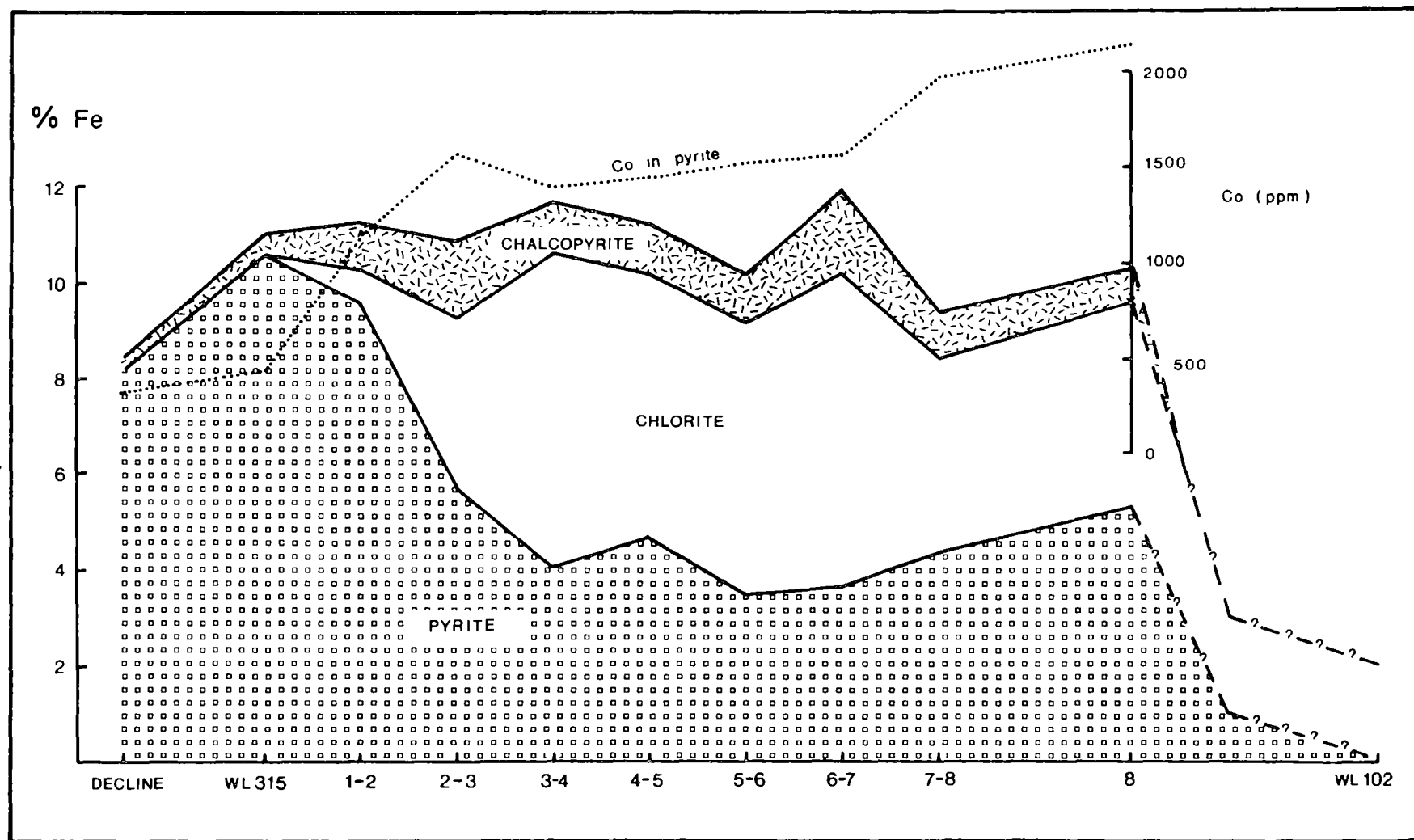
Fig. 6.9: Averaged proportions, given in percentage iron,
of pyrite, chlorite and chalcopyrite and the averaged variation
of cobalt in pyrite (ppm) for Prince Lyell.
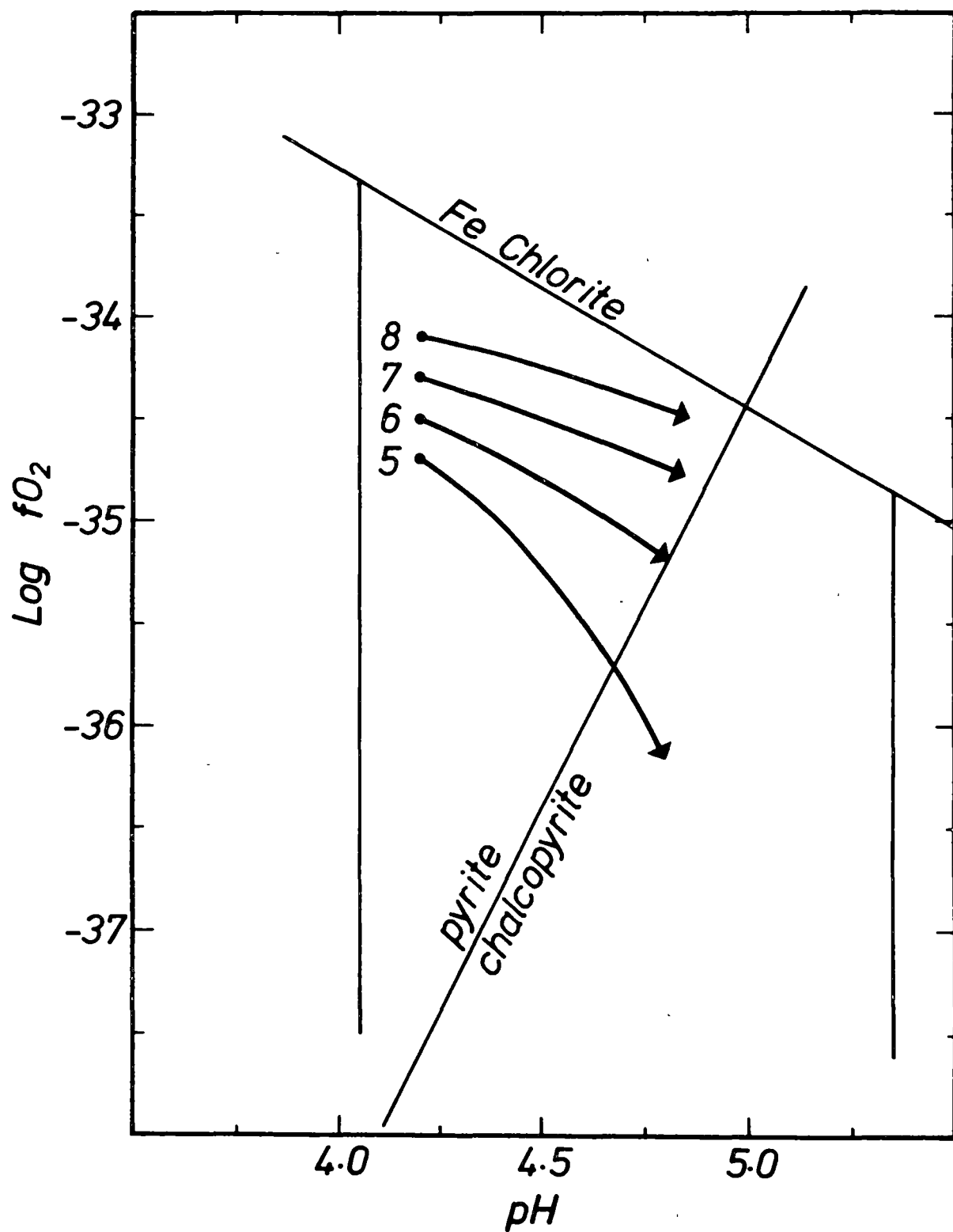
Fig. 6.10: Log fO_2/pH paths of reactions 5, 6, 7 and 8. Reactions commenced at a pH of 4.2. T = $250°C$. Initial log ΣS = -2 and ΣCu = -4.5. I = 1 and K/Na = 0.1. $\delta S^{34}_{\Sigma S}$ = 0.
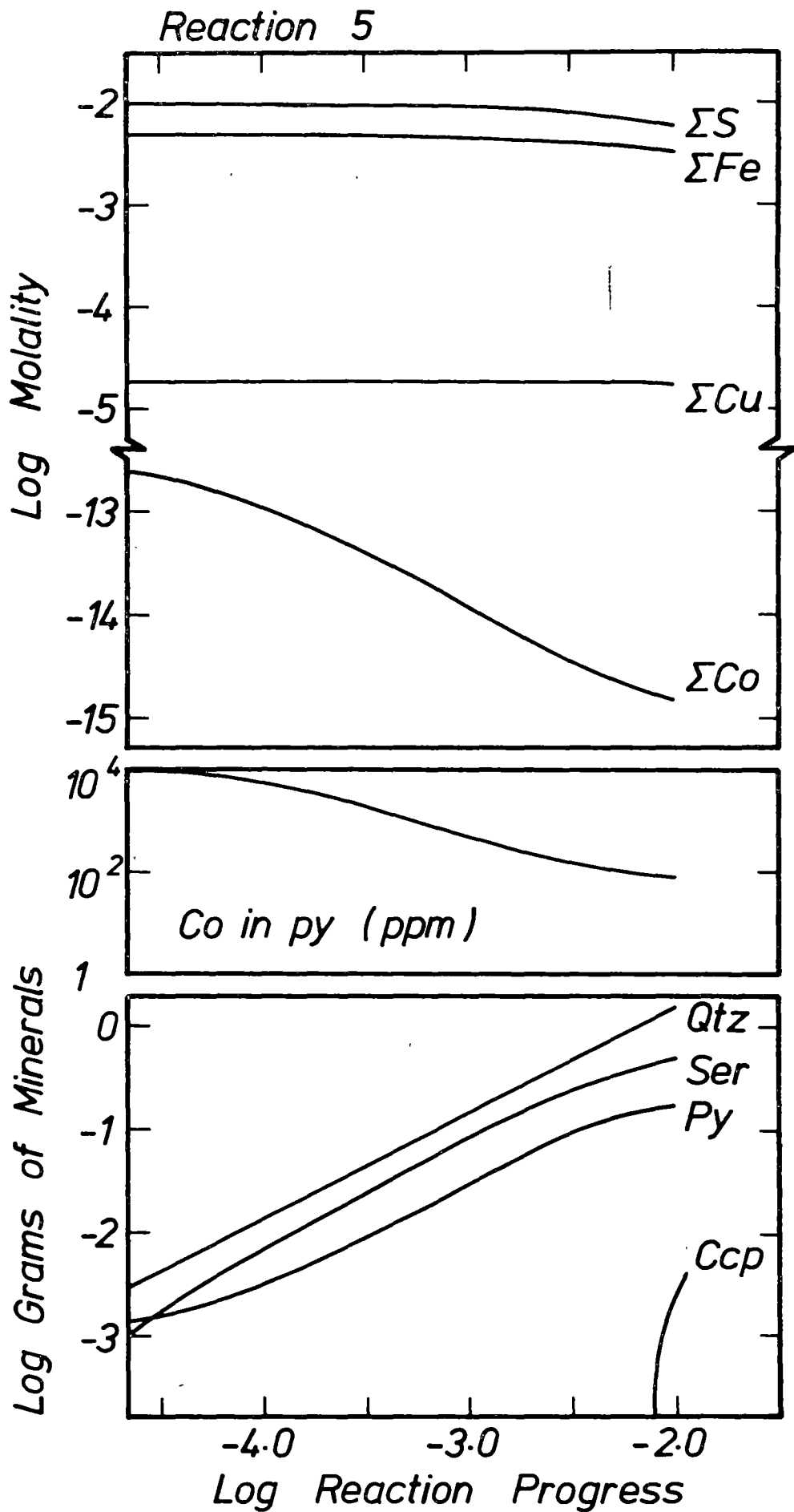
Reaction 5

Fig. 6.11:   Log molalities of ΣS, ΣCu, ΣFe and ΣCu in solution, the concentration of Co in py (ppm) and the log grams of minerals produced/kg H_2O as a function of reaction progress for reaction 5.
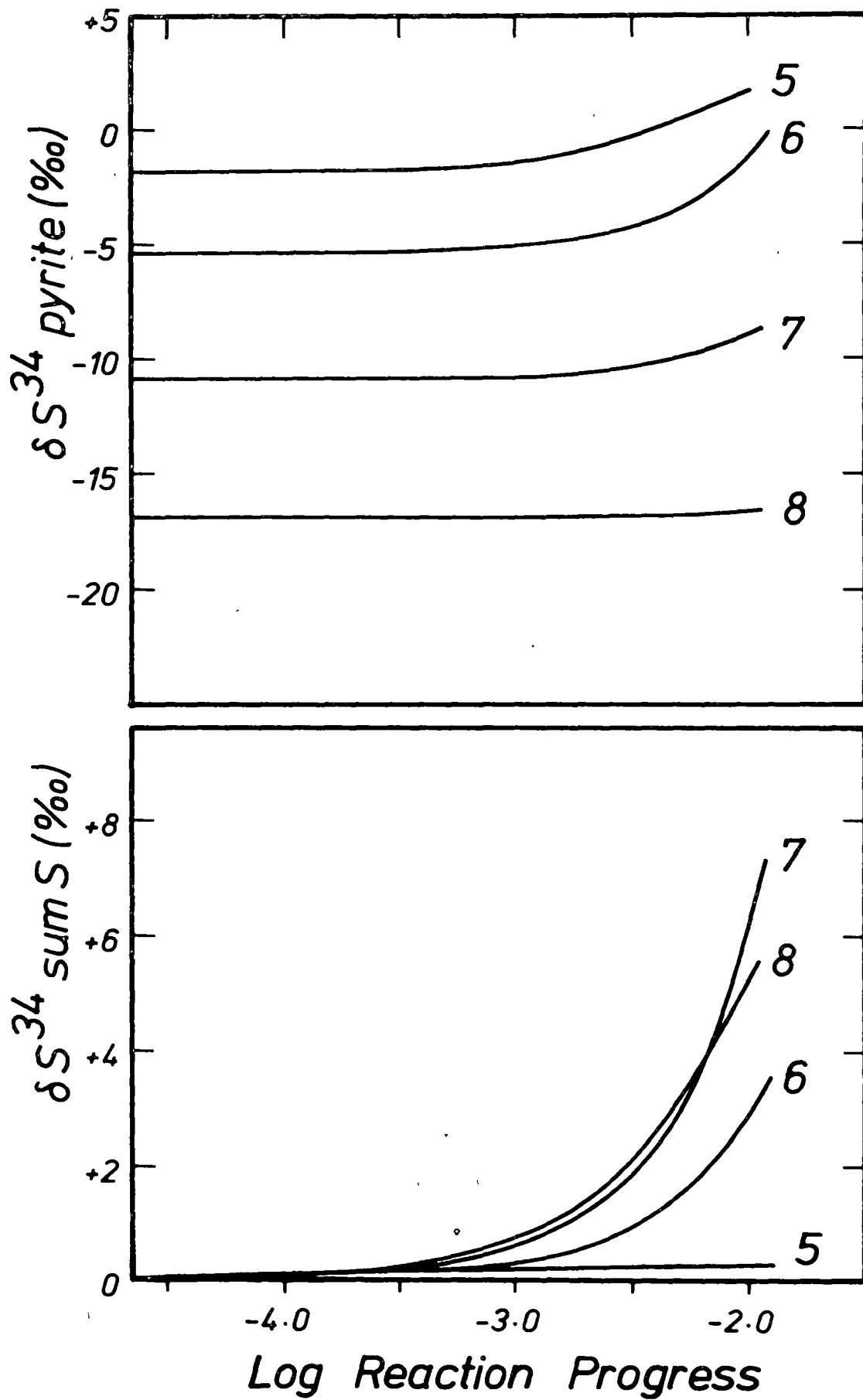
Fig. 6.12: The variation of $\delta S^{34}_{\Sigma S}$ and δS^{34}_{py} as a function of reaction progress for reactions 5, 6, 7 and 8.
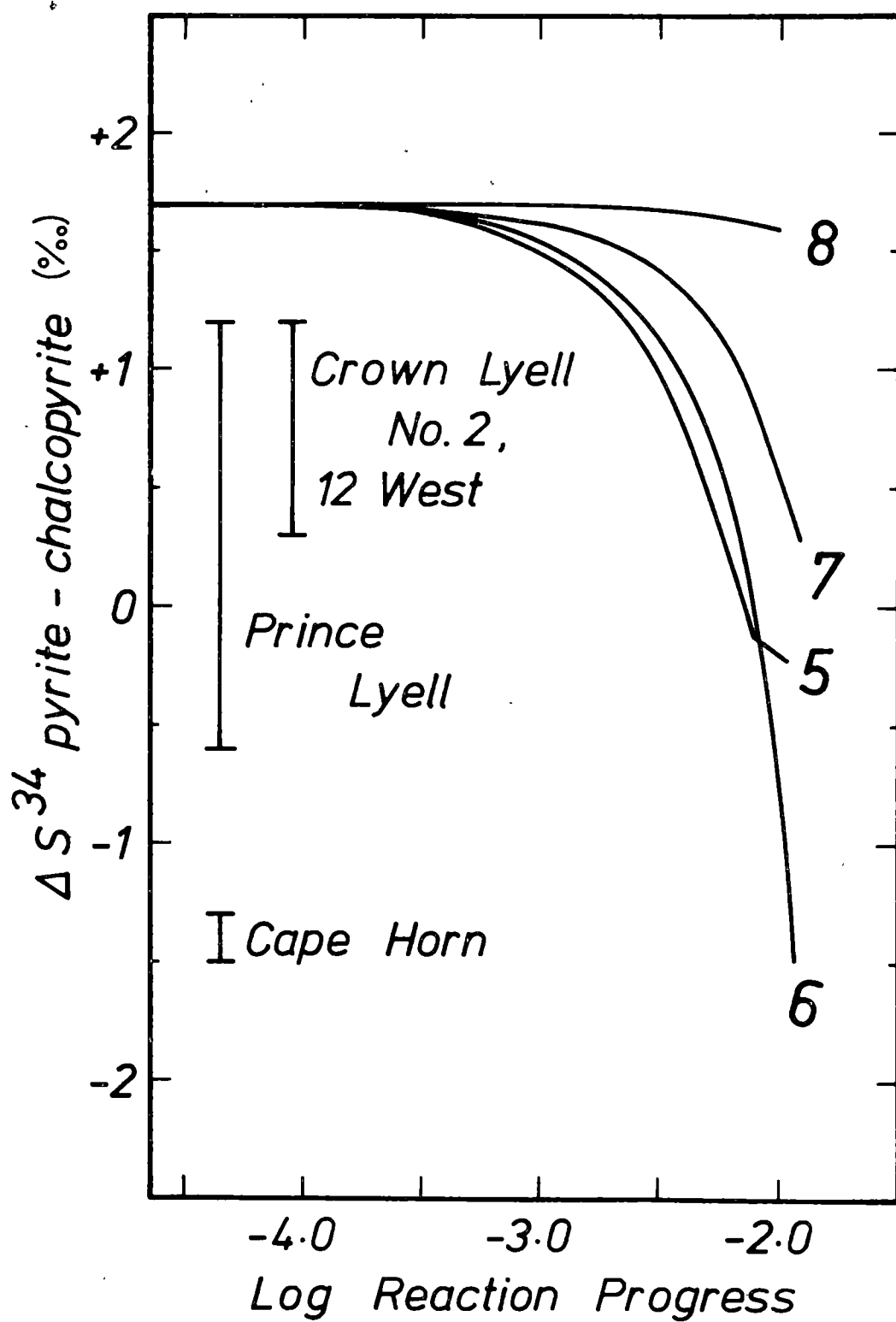
Fig. 6.13: The variation of ΔS^{34} py-ccp as a function of reaction progress for reactions 5, 6, 7 and 8.

6.4 Conclusions from the Mass Transfer Calculations

6.4.1 Sulphur Isotopes

The values of δS^{34}_{py} and $\Delta S^{34}py\text{-}ccp$ predicted by reactions 5 to 8 are consistent with the Mt. Lyell data. Reaction 5, assuming an initial value of $\delta S^{34}_{\Sigma S}$ of +7, would produce a range of δS^{34}_{py} values, from +5.3 to +8.6, which cover most of the Prince Lyell range. The $\Delta S^{34}py\text{-}ccp$ values predicted from reaction 5 are consistent with the Prince Lyell data which ranges from +1.2 to -0.6 (fig. 6.13). Reaction 6, again assuming an initial $\delta S^{34}_{\Sigma S}$ value of +7, would give δS^{34}_{py} values, ranging from +1.7 to +7, which account for most of the Cape Horn data. Reaction 6 gave the smallest values of $\Delta S^{34}py\text{-}ccp$ (fig. 6.13) and satisfactorily accounts for the Cape Horn $\Delta S^{34}py\text{-}ccp$ values. The higher oxidation conditions of reaction 7 gave results consistent with the Crown Lyell and North Lyell values of δS^{34}_{py} and $\Delta S^{34}py\text{-}ccp$.

It is therefore possible to account for the δS^{34}_{py} and $\Delta S^{34}py\text{-}ccp$ values of Prince Lyell, Cape Horn and Crown Lyell-North Lyell, given an initial $\delta S^{34}_{\Sigma S}$ value of +7. However, if the Western Tharsis $\Delta S^{34}py\text{-}ccp$ data approximates equilibrium partitioning and assuming the quartz-sericite-pyrite-chalcopyrite assemblage of Western Tharsis is formed at low oxidation conditions (see chapter 3), an initial $\delta S^{34}_{\Sigma S}$ value of +3.5 to +5 seems likely for Western Tharsis.

6.4.2 Sulphide to Silicate Ratios

The distribution of iron in the central core of Prince Lyell is given in figure 6.9 (details about the compilation of the figure are given at the end of the chapter). In general iron is equally distributed between sulphide and chlorite with an

overall whole rock content of 10-11%. Distribution of potassium
is not as well documented but available data indicates a range
from 0.5 to 4% with most data falling in the 1.5 to 2.5% range.

Reactions 1 to 4 gave sericite (as %K)/pyrite (as %Fe) ratios
varying from 1/0.05 to 1/0.2. The higher Fe content of
solutions in reactions 5-8 produced a much smaller sericite/
pyrite ratio of 1/2. This value is still greater than the 1/4
to 1/5 ratio of most quartz-sericite-pyrite assemblages. In a
trial reaction in which chlorite was saturated the sericite/pyrite/
chlorite ratio was 1/0.15/2.5 and suggests pyrite precipitation
will be limited once chlorite saturates. The much higher Fe
content of solutions considerably extended run times for reactions
involving chlorite and they have not been attempted in this study.

6.4.3 Trace Elements

Theory limitations have not permitted a detailed analysis
of the trace elements. However, reactions 1, 2 and 4 confirm the
suggestion of trace-element enrichment associated with chalco-
pyrite and chlorite precipitation, although the latter was not
particularly emphasised for the reaction paths considered. A
point noted in all calculations was that ΣCo in solution was
subject to considerable depletion as reaction progressed and this
would tend to negate the enrichment argument (see chapter 5) which
was based on the assumption of constant ΣCo.

6.5 Summary Comment

The mass transfer calculations give the likely isotope relationships between pyrite and chalcopyrite for the reaction of an acid, chloride-rich solution with a felsic host rock, assuming constant temperature. All ΔS^{34}py-ccp values are smaller than reasonable equilibrium values and this results from chalcopyrite precipitating in more reduced conditions and at higher pH relative to pyrite, and/or chalcopyrite precipitating from a solution enriched in S^{34} relative to its initial $\delta S^{34}_{\Sigma S}$ value. The value of ΔS^{34}py-ccp is strongly dependent on the oxidation conditions of the reactions and hence an oxidation dependent relationship exists between δS^{34}_{py} (or δS^{34}_{ccp}) and ΔS^{34}py-ccp. The δS^{34}_{py} and ΔS^{34}py-ccp data of Prince Lyell, Cape Horn, and Crown Lyell - North Lyell are consistent with this relationship and support the conclusion that the deposits formed from solutions with initial $\delta S^{34}_{\Sigma S}$ values of +7.

The present pyrite solubility data has not permitted a complete analysis of the sulphide/silicate ratios. The pyrite solubility data, together with theory limitations, has limited the analysis of the trace element variations.

6.6 Footnote to figure 6.9

Fig. 6.9 is a longitudinal section of Prince Lyell. The data is principally from samples collected on the 830 level (see Appendix C). Data points on the section represent mean values of the corresponding X-cut data. The analyses were carried out by the Mt. Lyell assay laboratory, copper and total sulphur analyses being done as part of the routine mine assay work. Iron as pyrite and chalcopyrite were calculated from this data. The percentage of iron as chlorite (and

minor siderite and oxides) was determined by digestion of the dilute
acid soluble fraction, using 1 N H Cl and digesting at 80°C for 10-12
hours.   Tests indicated a precision of better than 5% for 65% of
the data but 22% of the tested samples gave a precision of only
20-30%.   Continuous monitoring of copper in the acid digested
fraction indicated some dissolution of chalcopyrite and a minor
correction was generally necessary.

Checks on the calculated total iron content were made by total
digestion of a second series of samples and the potassium content
of these samples was determined.   Agreement was generally within 10%
although there were some notable discrepancies.

Copper, iron and potassium were determined by A A S.   Whole
rock standards from the Geology Department, University of Tasmania,
were used as accuracy tests for the whole rock digestion and the
Geology Department analyst, Mr. P. Robinson, analysed six Mt. Lyell
samples by XRF.   Total iron analyses were within 5% but potassium
determinations on some runs were shown to be 20-30% too high.

Analysis of the carbon dioxide content of samples, using the
technique of Shapiro and Brannock (1955), indicated a carbon dioxide
content of less than 0.5% for most samples, although occasional
samples gave 2-3%.

7.   SUMMARY AND CONCLUSIONS

The Mt. Lyell field consists of disseminated pyrite-chalcopyrite mineralization in altered felsic volcanics, disseminated bornite-chalcopyrite mineralization in cherts and silicified volcanics, and minor lenses of massive pyrite-chalcopyrite and sphalerite-galena-pyrite-chalcopyrite.

The alteration and mineralization of the felsic volcanic host rocks can be interpreted as having been largely controlled by the fO_2-T conditions of deposition and by H^+ exchange between the ore solution and the host rock.   Prince Lyell was formed under the most reducing conditions and probably at the highest temperature.   Main-stage sulphide deposition most likely commenced in the quartz-sericite-pyrite field with increasing pH and decreasing fO_2, as reaction proceeded, leading to chlorite formation and subsequently to chal____ite saturation. Minor magnetite, pyrrhotite and siderite were probably early phases, formed at a higher temperature and/or reduced conditions relative to main-stage mineralization and alteration.   A late-stage phase of quartz-sericite-pyrite-minor chalcopyrite mineralization and alteration occurred.

The Crown Lyell-North Lyell deposits consist of the following assemblages:

quartz-sericite-pyrite-chalcopyrite-minor barite,

quartz-bornite-chalcopyrite-minor sericite and pyrophyllite,

quartz-chlorite-minor sericite-pyrite-chalcopyrite-magnetite/

hematite-barite.

They were probably formed at lower temperatures and higher oxidation conditions relative to Prince Lyell.   The Cape Horn ore-body contains assemblages similar to both Prince Lyell and to Crown

Lyell-North Lyell and probably formed at intermediate fO_2-T

conditions relative to those deposits. The Western Tharsis quartz-

sericite-pyrite-minor chalcopyrite assemblage formed at a lower

temperature relative to Prince Lyell or the ore solutions contained

a higher initial total sulphur. Mainstage sulphide deposition at

Prince Lyell, Cape Horn and Western Tharsis appears to have been

preceded by an essentially non-sulphide quartz-sericite-minor

chlorite - hematite-barite-carbonate-possibly clay(?) alteration.

The variation in δS^{34}_{py} values from Prince Lyell to Cape Horn to Crown

Lyell-North Lyell is consistent with a progressive increase in the oxida-

tion conditions of deposition while having the same $\delta S^{34}_{\Sigma S}$ value. Mass

transfer calculations indicate the variation in ΔS^{34}py-ccp is consistent

with the oxidation trend with chalcopyrite precipitating at a higher pH

and lower oxidation conditions relative to pyrite, and/or precipitating

from a solution enriched in S^{34} by the precipitation of a significant amount

of sulphur as pyrite. The ΔS^{34}py-ccp values provide useful oxidation

constraints. The calculations indicate an initial $\delta S^{34}_{\Sigma S}$ value of +7

per mil for Prince Lyell, Cape Horn and Crown Lyell-North Lyell. If

the Western Tharsis ΔS^{34} py-ccp data approximates equilibrium

partitioning, the initial value of $\delta S^{34}_{\Sigma S}$ for the Western Tharsis

solutions will be less than +7 per mil.

Increasing Co/Fe and Ni/Fe ratios in solution, caused by the

precipitation of chlorite, and chalcopyrite replacing pyrite, are

the likely reasons for cobalt and nickel enrichment in pyrite from

chlorite-rich and chalcopyrite-rich assemblages. Mass transfer

calculations suggest that depletion of Co and Ni in solution is also an

important factor controlling the cobalt and nickel content of pyrite.

The precipitation of chalcopyrite and bornite relative to pyrite

is largely controlled by the total copper content of solution, the

pH and the temperature.   For a given copper content, rapid cooling

of the solution leads to bornite-chalcopyrite saturation and the

formation of deposits with a high Cu/Fe ratio (e.g. North Lyell).

At intermediate temperatures (200-300°C(?)) an increase in pH is

necessary to saturate chalcopyrite or bornite (depending on the

oxidation conditions of deposition) and this leads to deposits with

a low Cu/Fe ratio (e.g. Prince Lyell).   At higher temperatures the

pH increase will fail to saturate a copper phase probably giving rise

to   quartz-sericite-pyrite,

quartz-sericite-K-feldspar-pyrite, and

quartz-sericite-K-feldspar-chlorite-pyrite-magnetite

assemblages.

BIBLIOGRAPHY

BACHINSKI, D.J., 1976. Metamorphism of cupriferous iron sulphide deposits, Notre Dame Bay, Newfoundland. *Econ. Geol.*, v. 71, p. 443-452.

BARNES, H.L., and KULLERUD, G., 1961. Equilibria in sulphur - containing aqueous solutions, in the system Fe-S-O, and their correlation during ore deposition. *Econ. Geol.*, v. 56, p. 648-688.

BARTON, P.B., Jr., 1970. Sulphide petrology. *Mineral. Soc. Am. Spec. Pap.* 3, p. 187-198.

BARTON, P.B., Jr., BETHKE, P.M., and TOULMIN, P., III, 1963. Equilibrium in ore deposits. *Mineral. Soc. Am. Spec. Pap.* 1, p. 171-185.

BARTON, P.B., Jr., and SKINNER, B.J., 1967. Sulphide mineral stabilities. In *Geochemistry of Hydrothermal Ore Deposits* (ed. H.L. Barnes), New York, Holt, Rinehart, and Winston, p. 236-333.

BETHKE, P.M., and BARTON, P.B., Jr., 1959. Trace element distribution as an indicator of temperature and pressure of ore deposition (abs.). *Geol. Soc. America, Bull.*, v. 70, p. 1569-1570.

BETHKE, P.M., and BARTON, P.B., Jr., 1971. Distribution of some minor elements between coexisting sulphide minerals. *Econ. Geol.*, v. 66, p. 140-163.

BRADLEY, J., 1954. The geology of the West Coast Range of Tasmania. Part I. *Pap. Proc. Roy. Soc. Tas.*, v. 88, p. 193-243.

BRADLEY, J., 1956. The geology of the West Coast Range of Tasmania. Part II. *Pap. Roy. Soc. Tas.*, v. 90, p. 65-130.

BRADLEY, J., 1957. Geology of the West Coast of Tasmania,
Part III, Porphyroid Metasomatism. *Pap. Roy. Soc. Tas.*,
v. 91, p. 163-190.

BROWN, A.C., and BARTHOLOMÉ, P., 1972. Inhomogeneities in
cobaltiferous pyrite from the Chibuluma Cu-Co deposit,
Zambia. *Mineral. Deposita*, v. 7, p. 100-105.

BRYANT, C.J., 1976. The geology and mineralization of the
corridor area, Mt. Lyell, Tasmania. Unpubl. B.Sc. Hons.
thesis, Univ. of Tasm.

BURNHAM, C.W., 1959. Metallogenic provinces of south-western
United States and northern Mexico. *New Mexico, Bur. Mines
Mineral Resources*, Bull. 65.

CAREY, S.W., 1953. Geological structure of Tasmania in relation
to mineralization. *5th Emp. Min. Metall. Congr.*, 1,
p. 1108-1128.

CAREY, S.W. and BANKS, M.R., 1954. Lower Palaeozoic unconformities
in Tasmania. *Pap. Roy. Soc. Tas.*, v. 88, p. 295-269.

CONOLLY, H.J.C., 1947. Geology in exploration, Mt. Lyell example.
Proc. Australas. Inst. Min. and Metall., v. 146-7, p. 1-22.

CORBETT, K.D., REID, K.O., CORBETT, E.B., GREEN, G.R., WELLS, K.,
and SHEPPARD, N.W., 1974. The Mt. Read Volcanics and Cambrian-
Ordovician Relationships at Queenstown, Tasmania. *J. geol.
Soc. Aust.*, v. 21, p. 173-186.

CRERAR, D.A., 1974. Solvation and deposition of chalcopyrite and
chalcocite assemblages in hydrothermal solutions. Unpubl.
Ph.D. thesis, Pennsylvania State University.

CRERAR, D.A., and BARNES, H.L., 1976. Ore solution chemistry V.
Solubilities of chalcopyrite and chalcocite assemblages in
hydrothermal solution at 200° to 350°C. *Econ. Geol.*, v. 71,
p. 772-794.

CRISS, C.M., and COBBLE, J.W., 1964. The thermodynamic properties
     of high temperature aqueous solutions. V. The calculation of
     ionic heat capacities up to 200° : entropies and heat capacities
     above 200°. *Am. Chem. Soc. Jour.*, v. 86, p. 5390-5393.

DICKSON, F.W., and ELLIS, A.J., 1976. Rock/water interaction and
     the source of ore metals. *25th, Int. Geol. Congr., Abs.*, p. 821.

EDWARDS, A.B., 1939. Some observations on the Mineral Composition
     of the Mt. Lyell Copper Ores, Tasmania, and Their Modes of
     Occurrence. *Proc. Australas. Inst. Min. and Metall.*, v. 114,
     p. 67-109.

FOURNIER, R.O., 1967. The porphyry copper deposit exposed in the
     liberty open-pit mine near Ely, Nevada. Part II. The formation
     of hydrothermal alteration zones. *Econ. Geol.*, v. 62, p. 207-227.

FRENCH, B.M., 1971. Stability relations of siderite ($FeCO_3$) in the
     system Fe-C-O. *Am. Jour. Sci.*, v. 271, p. 37-78.

GHOSH-DASTIDAR, P., PARJARI, G.E., Jr., and TREMBATH, L.T., 1970.
     Factors affecting the trace element partition coefficients
     between coexisting sulphides. *Econ. Geol.*, v. 65, p. 815-837.

GREEN, G.R., 1971. Geology and mineralization of the Cape Horn -
     Lyell Comstock area, Mt. Lyell. Unpubl. B.Sc. Hons. thesis,
     Univ. of Tasm.

GREGORY, J.W., 1905. The Mt. Lyell Mining Field, Tasmania.
     Trans. Aust. Inst. Min. Engrs. 168 pp.

HALL, G., and SOLOMON, M., 1962. Metallic Mineral Deposits. In
     Geology of Tasmania (eds. Spry, A.H., and Banks, M.R.), J. geol.
     Soc. Aust., v. 9, p. 285-309.

HALL, W.E., ROSE, H.J., Jr., and SIMON, F., 1971. Fractionation of
     minor elements between galena and sphalerite, Darwin lead-silver-
     zinc mine, Inyo County, California and its significance in
     geothermometry. *Econ. Geol.*, v. 66, p. 602-606.

HELGESON, H.C., 1967. Solution chemistry and metamorphism.

In *Researches in Geochemistry*, v. II (ed. Abelson, P.H.),

New York, John Wiley and Sons Inc., p. 362-404.

HELGESON, H.C., 1968. Evaluation of irreversible reactions in

geochemical processes involving minerals and aqueous solutions:

I. Thermodynamic relations. *Geochim. et Cosmochim.* Acta,

v. 32, p. 853-877.

HELGESON, H.C., 1969. Thermodynamics of hydrothermal systems at

elevated temperatures and pressures. *Am. Jour. Sci.*,

v. 267, p. 729-804.

HELGESON, H.C., 1970. A chemical and thermodynamic model of ore

deposition in hydrothermal systems. *Mineral. Soc. Am. Spec.*

Pap. 3, p.155-186.

HELGESON, H.C., BROWN, T.H., NIGRINI, A., and JONES, T.A., 1970.

Calculation of mass transfer in geochemical processes

involving aqueous solutions. *Geochim. et Cosmochim. Acta*,

v. 34, p. 569-592.

HENDRY, D.A.F., 1972. The geochemistry of the Mt. Lyell copper

ores, Tasmania. Unpubl. Ph.D. thesis, Univ. of Cambridge.

HILLS, C.L., 1927. A synopsis of the geology of the Lyell district

of Tasmania. *Proc. Australas. Inst. Min. and Metall.*,

v. 66, p. 129-148.

HOLLAND, H.D., 1965. Some applications of thermochemical data to

problems of ore deposits, II. Mineral assemblages and the

composition of ore-forming fluids. *Econ. Geol.*, v. 60, p.1101-1166.

ITOH, S., 1973. Distribution of cobalt in pyrites from some cupriferous

pyrite deposits, with special reference to its relationship to

metamorphic grade. *Bull. Geol. Surv. Jap.*, v. 24, p. 285-310.

JAGO, J.B., REID, K.O., QUILTY, P.G., GREEN, G.R., and DALY, B., 1972. Fossiliferous Cambrian limestone from within the Mt. Read Volcanics, Mt. Lyell Mine Area, Tasmania. *J. geol. Soc. Aust.*, v. 19, p. 379-382.

KAJIWARA, Y., and KROUSE, H.R., 1971. Sulfur isotope partitioning in metallic sulphide systems. *Canadian Jour. Earth Sci.*, v. 8, p. 1397-1408.

KELLEY, K.K., 1960. Contributions to the data on theoretical metallurgy. XIII. High temperature heat content, heat capacity and entropy data for the elements and inorganic compounds. *U.S. Bur. Mines Bull.*, 584, 232p.

KIELLAND, J., 1937. Individual ion activity coefficients of ions in aqueous solutions. *Am. Chem. Soc. Jour.*, v. 59, p.1675-1678.

KLEMM, D.D., 1962. Untersuchungen über die Mischkristall bildung im Dreieck diagram FeS_2-CoS_2-NiS_2 und ihre Beziehungen zum Aufbau der naturlichen "Bravoite". *Neues Jahrb. Mineral. Monatsh.*, p. 76-91.

KLEVTSOV, P.V., and LEMMLEIN, G.G., 1959. Pressure corrections for the homogenization temperatures of aqueous NaCl solutions. *Akad. Nauk SSSR., Doklady*, v. 128, p. 1250-1253 (in Russian); translated in *Acad. Sci. USSR, Doklady*, v. 128, p. 995-997, 1960.

LOFTUS-HILLS, G., 1968. Cobalt, nickel and selenium in Tasmanian ore minerals. Unpubl. Ph.D. thesis, Univ. of Tasm.

LOFTUS-HILLS, G. and SOLOMON, M., 1967. Cobalt, nickel and selenium in sulphides as indicators of ore genesis. *Mineral. Deposita*, v. 2, p. 228-242.

MacDONALD, M.J., 1968. Progress report on the geology of the West Lyell orebodies at Mt. Lyell, Tasmania. Unpubl. report to Mt. Lyell Mining and Railway Co. Ltd.

MARKHAM, N.L., 1963. An interpretation of the Mount Lyell

(Tasmania) copper ore paragenesis. *Proc. Australas. Inst.*

Min. and Metall., v. 206, p. 123-141.

MARKHAM, N.L., 1968. Some genetic aspects of the Mt. Lyell

mineralization. *Mineral. Deposita*, v. 3, p. 199-221.

MARKHAM, N.L., and LAWRENCE, L.J., 1965. Mawsonite, a new copper-

iron-tin sulphide from Mt. Lyell, Tasmania and Tingha, New

South Wales. *Am. Mineral.*, v. 50, p. 900-908.

MARKHAM, N.L., and OTTEMAN, J., 1968. Betechtinite from Mt.

Lyell, Tasmania. *Mineral. Deposita*, v. 3, p. 171-173.

McINTIRE, W.L., 1963. Trace element partition coefficients - a review

of theory and applications to geology. *Geochim. et Cosmochim.*

Acta, v. 27, p. 1209-1264.

MIYASHIRO, A., 1973. Metamorphism and metamorphic belts. London,

George Allen and Unwin Ltd., 492 p.

MONTOYA, J.W., and HEMLEY, J.J., 1975. Activity relations and

stabilities in alkali feldspars and mica alteration reactions.

Econ. Geol., v. 70, p. 577-583.

NYE, P.B., BLAKE, F., and HENDERSON, Q.J., 1934. Report on the

Geology of the Mt. Lyell Mining Field. Unpublished Report

to Dept. Mines, Tasmania.

OHMOTO, Hiroshi, 1972. Systematics of sulfur and carbon isotopes

in hydrothermal ore deposits. *Econ. Geol.*, v. 67, p. 551-578.

OHMOTO, H., and RYE, R.O., in press. Isotopes of sulfur and carbon.

In 2nd edition *Geochemistry of Hydrothermal Ore Deposits* (ed. H.L.Barnes).

REID, K.O., 1976. The Geology of the Mount Lyell copper ore deposits.

In *Economic Geology of Australia and Papua-New Guinea*, Monogr. 5,

Metals (ed. C.L. Knight), Australas. Inst. Min. and Metall.,

Melbourne.

ROBIE, R.A., and WALDBAUM, D.R., 1968. Thermodynamic properties of minerals and related substances at 298.15°K (25°C) and one atmosphere (1.013 bars) pressure and at higher temperatures. *U.S. Geol. Survey Bull.* 1259, 256p.

ROSE, A.W., 1967. Trace elements in sulphide minerals from the Central district New Mexico and the Bingham district, Utah. *Geochim. et Cosmochim. Acta,* v. 31, p. 547-585.

ROSE, A.W., 1970. Origin of trace element distribution patterns in sulphides of the Central and Bingham districts, western U.S.A. *Mineral. Deposita,* v. 5, p. 157-163.

RYE, R.O., HALL, W.E., and OHMOTO, H., 1974. Carbon, hydrogen, oxygen and sulfur isotope study of the Darwin lead-silver-zinc deposit, southern California. *Econ. Geol.,* v. 69, p. 468-481.

RYE, R.O., and OHMOTO, H., 1974. Sulfur and carbon isotopes and ore genesis : a review. *Econ. Geol.,* v. 69, p. 826-842.

SALOMONS, W., 1971. Isotope fractionation between galena and pyrite and between pyrite and elemental sulfur. *Earth Planet. Sci. Letters,* v. 11, p.236-238.

SASAKI, A., 1974. Isotopic data of Kuroko deposits. In *Geology of Kuroko Deposits* (eds. Ishihara, S., Kanehira, K., Sasaki, A., Sato, T., and Shimazaki, Y.), Soc. Min. Geol. Jap., Spec. Issue, no. 6, p. 384-397.

SHAPIRO, L., and BRANNOCK, W.W., 1955. Rapid determination of carbon dioxide in silicate rocks. *Anal. Chemistry,* v. 27, p. 1796-1797.

SILLÉN, L.G., and MARTELL, A.E., 1964. Stability constants of metal-ion complexes. *London Chem. Soc.,* Special Publication no. 17, 754p.

SILLÉN, L.G., and MARTELL, A.E., 1971. Stability constants of metal-ion complexes. Supplement no. 1 *London Chem. Soc.,* Special Publication No. 25, 865p.

SOLOMON, M., 1962. The tectonic history of Tasmania. In *Geology of Tasmania* (eds. Spry, A.H. and Banks, M.R.), J. geol. Soc. Aust., v. 9, p. 311-354.

SOLOMON, M., 1964. The spilite-keratophyre association of West Tasmania and the ore deposits at Mt. Lyell, Rosebery and Hercules. Unpubl. Ph.D. thesis, Univ. of Tasm.

SOLOMON, M., 1967. Fossil Gossans (?) at Mt. Lyell, Tasmania. *Econ. Geol.* v. 62, p. 757-772.

SOLOMON, M., 1969. The copper-clay deposits at Mount Lyell, Tasmania. *Proc. Australas. Inst. Min. and Metall.*, v. 230, p. 39-47.

SOLOMON, M., 1972. Ore deposits associated with geosynclinal vulcanism in Tasmania and a genetic model for the Mt. Lyell pyrite-chalcopyrite ores. *Geol. Soc. Aust.*, Jnt. Spec. Gp. Mtg., Abs., p. C9-C10.

SOLOMON, M., 1976. "Volcanic" massive sulphide deposits and their host rocks - a review and explanation. In *Handbook of Strata-bound and Stratiform Ore Deposits* (ed. K. Wolf), v. 6, Elsevier, Amsterdam.

SOLOMON, M., and ELMS, R.G., 1965. Copper ore deposits of Mt. Lyell. 8th Comm. Min. and Metall. Congr., v. 1, p. 478-484.

SOLOMON, M., GREEN, G.R., and REID, K.O., 1976. Geological history of western Tasmania. In *Ore deposits of Western Tasmania* (eds. Solomon, M., and Green, G.R.), Excursion Guide No. 31AC, 25th Int. Geol. Congr., p. 1-12.

SOLOMON, M., and GRIFFITHS, J.R., 1974. Aspects of the early history of the southern part of the Tasman Orogenic Zone. In *The Tasman Geosyncline - a Symposium* (eds. Denmead, A.K., Tweedale, G.W., and Wilson, A.F.), Geol. Soc. Aust., Qd Div., p. 19-46.

SOLOMON, M., RAFTER, T.A., and JENSEN, M.L., 1969. Isotope studies on the Rosebery, Mount Farrell and Mount Lyell ores, Tasmania. *Mineral. Deposita*, v. 4, p. 172-199.

SPRINGER, G., SCHACHNER-KORN, O., and LONG, J.V.P., 1964. Metastable
solid solution relations in the system FeS_2-CoS_2-NiS_2.
Econ. Geol., v. 59, p. 475-491.

SPRY, A.H., 1962. Igneous activity. In *Geology of Tasmania*
(eds. Spry, A.H., and Banks, M.R.), J. geol. Soc. Aust.,
v. 9, p. 255-284.

TARDY, Y., and GARRELS, R.M., 1974. A method of estimating the
Gibbs energies of formation of layer silicates. *Geochim. et
Cosmochim. Acta*, v. 38, p. 1101-1116.

THOMPSON, A.B., 1970. A note on the kaolinite-pyrophyllite equilibrium.
Am. Jour. Sci., v. 268, p. 454-458.

TOKUNAGA, M., and HONMA, H., 1974. Fluid inclusions in the minerals
from some Kuroko deposits. In *Geology of Kuroko Deposits*
(eds. Ishihara, S., Kanehira, K., Sasaki, A., Sato, T. and
Shimazaki, Y.), Soc. Min. Geol. Jap., Spec. Issue, No. 6, p.385-388.

WADE, M.L., and SOLOMON, M., 1958. Geology of the Mt. Lyell Mines,
Tasmania. *Econ. Geol.*, v. 53, p. 367-416.

WALSHE, J.L., 1971. Geology of the southern Mt. Lyell field and
trace element studies of the pyrite mineralization. Unpubl.
B.Sc. Hons. thesis, Univ. of Tasm.

WEAST, R.C., (ed.), 1974. Handbook of Chemistry and Physics. 55th
edition, 1974-1975. CRC Press, Inc., Cleveland.

WHITE, D.E., 1968. Environments of generation of some base-metal
ore deposits. *Econ. Geol.*, v. 63, p. 301-335.

WHITE, N.C., 1976. Cambrian volcanism and mineralization in south-
west Tasmania. Unpubl. Ph.D. thesis, Univ. of Tasm.

WILLIAMS, E., SOLOMON, M., and GREEN, G.R., 1976. The geological
setting of metalliferous ore deposits in Tasmania. In
Economic Geology of Australia and Papua-NewGuinea, Monogr. 5,
Metals (ed. C.L. Knight), Australas. Inst. Min. and Metall.,
Melbourne.

Addendum:

ROBINSON, P., and WALSHE, J.L., in press.   Trace element analysis
        of pyrite - an interlaboratory survey.

Addendum:

APPENDIX A   THERMODYNAMIC DATA

Where possible the thermodynamic data compiled by Helgeson (1969) were used. However, several alterations and numerous additions have been necessary, hence comprehensive lists of data are given in Tables 1-8 in this appendix. Details of additional information are given in the footnotes for each table.

In the necessary estimate of entropies and heat capacities the procedures adopted by Helgeson (1969) have been followed. Estimation of the free energy of iron chlorite ($Fe_{4.5}^{2+}Al_{3.0}Si_{2.5}O_{10}(OH)_8$ was made using the technique of Tardy and Garrels (1974).

Where necessary, data for dissociation constants of aqueous species above 25°C were calculated using equation 16 from Helgeson (1969). If possible, experimental data were preferred.

Data for stoichiometric individual ion activity coefficients ($\hat{\gamma}_i$ such that $a_i = \hat{\gamma}_i m_{\Sigma i}$) where calculated using equation 49 Helgeson (1969). Only those species given in table 3 were used in the calculations. Necessary true individual ion activity coefficients for charged species were calculated from equation 43 using a° values at 25° from Kielland (1937). For neutral species the activity coefficient of CO_2 was used. For a discussion of assumptions and limitations in the estimation procedure for individual ion activity coefficients see Helgeson (1969).

TABLE I

THERMODYNAMIC DATA FOR MINERALS AND GASES [a].

	$\Delta H^\circ_{25^\circ C}$ (cal/mole)	$S^\circ_{25^\circ C}$ (cal/mole/deg)	Cp a'	$b \times 10^{-3}$	$c \times 10^{+5}$
SiO_2 quartz	-217,650	9.88	11.22	8.2	-2.7
$K\ Al_3Si_3O_{10}(OH)_2$ Sericite	-1,420,900	69.0	97.56	26.38	-25.44
$Al_2Si_2O_5(OH)_4$ Kaolinite	-979,465 [b]	48.53	67.93	19.22	-13.78
$K\ Al\ Si_3O_8$ K Feldspar	-946,000	52.47	63.83	12.90	-17.05
$Fe_{4.5}Al_3Si_{2.5}O_{10}(OH)_8$ Fe Chlorite	-1,752,180 [d]	151.03 [c]	157.8 [e]	36.43	-21.53
$K\ Fe_3Al\ Si_3O_{10}(OH)_2$ Annite	-1,233,750	100.0	100.4	36.4	-14.3
Fe_2O_3 Hematite	-197,300	20.89	23.49	18.6	-3.55
Fe_3O_4 Magnetite	-267,400	30.63	21.88	48.2	0.0
$Fe\ S_2$ Pyrite	-41,000	12.65	17.88	1.32	-3.05
$Fe\ S$ Pyrrhotite	-24,130	14.42	5.19	26.4	0.0
$Cu\ FeS_2$ Chalcopyrite	-44,550	31.2	15.6	21.6	0.6
Cu_5FeS_4 Bornite	-84,820	91.0	44.4	40.0	0.6
Cu_2S Chalcocite	-19,148	28.86	19.50	0.0	0.0

TABLE I (continued)

	$\Delta H^\circ_{25^\circ C}$	$S^\circ_{25^\circ C}$	Cp		
	(cal/mole)	(cal/mole/ deg)	a'	$b \times 10^{-3}$	$c \times 10^{+5}$
CuS Covellite	-11,610	15.93	10.60	2.64	0.0
Fe CO_3 Siderite	-	-	11.63	26.80	0.0
$S_2(g)$	30,680	54.51	8.72	0.16	-0.90
$O_2(g)$	0.0	48.996	7.16	1.0	-0.40
$CO_2(g)$	-94,050	51.06	10.57	2.10	-2.06

FOOTNOTES

a. All data from Helgeson (1969) except where noted.

b. Robie and Waldbaum (1968).

c. Estimated by summation of entropies of oxide components. Entropy of H_2O taken to be that of ice.

d. Calculated from relationship $\Delta H^\circ_{25} = \Delta G^\circ_{25} + T\Delta S^\circ_{25}$

The value of ΔG°_{25} (-1,610,350 cals/mole) estimated by the summation of free energies of oxide components in layered silicates given by Tardy and Garrels (1974).

e. Estimated by summation of heat capacity power functions of oxide components. Ice (Cp = 9.0) was used for H_2O. The power function for FeO (Cp = $11.67 + 2.6 \times 10^{-3}T - 0.49 \times 10^{+5}T^{-2}$) calculated from the enthaplies between 400° and 1000°K given by Robie and Waldbaum (after Kelley, 1960).

TABLE 2

THERMODYNAMIC DATA [a] FOR AQEOUS SPECIES

Species	$\Delta H°25$ (cals/ mole)	S°25 (cals/deg/ mole)	Average Heat Capacity 100°	150°	200°	250°	300°C
H_4SiO_4	-348,060	45.84	49	46	46	46	45
H_2S (aqu.)	-9,030	30.9	39	35	32	33	35.5
H_2O (liq.)	-68,315	16.71	18	18	18	18	18
H^+	0.0	0.0	31	33	35	37	39
Cu^{1+}	16,930	9.4	44	43	47	50	53
Cu^{2+}	15,390	-23.6	65	66	71	75	79
Fe^{2+}	-21,000	-27.1	66	68	73	78	82
Fe^{3+}	-11,400	-70.1	93	96	105	109	115
Co^{2+}	-16,100[b]	-37.1[b]	72[c]	74[c]	80[c]	84[c]	89[c]
Ni^{2+}	-15,300[b]	-38.1[b]	72[c]	74[c]	80[c]	85[c]	89[c]
K^+	-60,040	24.5	35	35	39	41	43
Al^{3+}	-127,000	-76.9	95	99	108	114	120

Difference in Average Heat Capacity	300°	350°	400°	450°	550°C
$\Delta\bar{C}p\ K^+ - H^+$	+3.76[d]	+1.34[d]	-0.14[d]	-1.35[e]	-3.63[d]

a.   All data from Helgeson (1969) except where noted.

b.   Weast (1974).

c.   Calculated using procedure of Criss and Cobble (1964).

d.   Calculated from the K-feldspar/muscovite reaction using the log $\frac{aK^+}{aH^+}$ ration given by Montoya and Hemley (1975, fig. 1), corrected to 1 atmos. ΔV for K^+ and H^+, 3.4cc/mole and 5.7cc/mole respectively.

e.   Interpolated.

TABLE 3

THERMODYNAMIC DATA [a] FOR DISSOCIATION EQUILIBRIA IN AQUEOUS SOLUTION

	ΔH^o_{25} (cals/ mole)	S^o_{25} (cals/ mole/ deg.)	100°	150°	200°	250°	300°C
$H_2O_{liq.} \rightleftarrows H^+ + OH^-$	13,335	-19.31	-12.26	-11.64	-11.27	-11.13	-11.39
$H_2S \rightleftarrows H^+ + HS^-$	4,800	-15.90	- 6.63	- 6.72	- 6.96	- 7.35	- 8.06
$HS^- \rightleftarrows H^+ + S^=$	13,300	-19.0	-11.78	-10.62	- 9.57	- 8.61	- 7.72
$HSO_4^- \rightleftarrows H^+ + SO_4^=$	- 3,850	-22.0	- 2.99	- 3.74	- 4.49	- 5.41	- 7.06
$KSO_4^- \rightleftarrows K^+ + SO_4^=$	- 2,635	-12.7	- 1.30	- 1.60	- 1.94	- 2.4[b]	- 3.0[b]
$NaCl \rightleftarrows Na + Cl^-$				0.97	0.42	0.15	- 0.82
$KCl \rightleftarrows K^+ + Cl^-$					0.9	0.3	- 0.6
$HCl \rightleftarrows H^+ + Cl^-$	-18,630	-34.4	2.9	1.23	0.06	- 0.67	- 1.24
$FeCl^{1+} \rightleftarrows Fe^{2+} + Cl^-$			0.25[d]	-0.15[d]	- 0.67[c]	- 1.0[c]	- 1.2[c]
$CoCl^{1+} \rightleftarrows Co^{2+} + Cl^-$	- 2,900[e]	- 6.0[e]	0.33[f]	0.04[f]	- 0.25[f]	- 0.57[d]	- 0.9[d]
$CoCl_2 \rightleftarrows Co^{2+} + 2Cl^-$	- 5,000[e]	0.0[e]	2.92[f]	2.58[f]	2.31[f]	2.11[d]	1.95[d]
$CoCl_3^{1-} \rightleftarrows Co^{2+} + 3Cl$	-16,300[e]	-26.0[e]	3.63[f]	2.12[f]	0.64[f]	- 0.74[d]	- 2.05[d]
$NiCl^{1+} \rightleftarrows Ni^{2+} + Cl^-$	- 500[g]	- 0.87[g]	0.1[f]	0.05[f]	0.0[f]	- 0.05[d]	- 0.06[d]
$NiCl_2 \rightleftarrows Ni^{2+} + 2Cl^-$	- 1,120[h]	- 3.87[h]	- 0.22[f]	- 0.36[f]	- 0.51[f]	- 0.65[d]	- 0.76[d]

a. All data from Helgeson (1969) except where noted.

b. Extropolated, from Ohmoto (1972).

c. Crerar (1974).

d. Extrapolated.

e. Sillén and Martell (1971, p. 171, ref. 68Z).

f. Calculated as in Helgeson (1967, 1969).

g. Sillén and Martell (1971, p. 173, ref. 66 Kd + 60 La).

h. Entropy estimated for $NiCl_2 \rightleftarrows NiCl^{1+} + Cl^-$ by procedure from Helgeson (1969). Log K from Sillén and Martell (1964, p.282, ref. 57 Ka).

TABLE 4

EQUILIBRIUM CONSTANTS [a] FOR HYDROTHERMAL REACTIONS

OXIDATION - REDUCTION REACTIONS

	Log K(T)				
	100	150	200	250	300
$2H_2S_{aq} + O_{2(g)} \rightleftarrows S_{2(g)} + 2H_2O_\ell$	46.27	39.99	35.05	30.88[b]	27.21
$H_2S_{aq} + 2O_{2(g)} \rightleftarrows 2H^+ + SO_4^=$	94.45[b]	79.4[b]	67.24[b]	57.24[b]	48.82[b]
$S^= + 2O_{2(g)} \rightleftarrows SO_4^=$	112.70	96.68	83.74	73.22[b]	64.26
$Fe^{3+} + \frac{1}{2}H_2O_\ell \rightleftarrows Fe^{2+} + \frac{1}{4}O_{2(g)} + H^+$	- 4.16	- 2.48	- 1.15	- 0.05[b]	0.84
$Cu^{2+} + \frac{1}{2}H_2O_\ell \rightleftarrows Cu^{1+} + \frac{1}{4}O_{2(g)} + H^+$	- 12.83	-10.34	- 8.35	- 6.71[b]	- 5.33
$Cu^{1+} + Fe^{3+} \rightleftarrows Cu^{2+} + Fe^{2+}$	8.67	7.86	7.20	6.66[b]	6.17
$Co^{2+} + H_2O_\ell \rightleftarrows Co + \frac{1}{2}O_2 + 2H^+$	- 38.13[c]	-32.41[c]	-27.96[c]	-24.39[c]	-21.51[c]
$Ni^{2+} + H_2O_\ell \rightleftarrows Ni + \frac{1}{2}O_2 + 2H^+$	- 37.45[c]	-31.78[c]	-27.37[c]	-23.86[c]	-20.97[c]
$H_2CO_3 (ap) \rightleftarrows H^+ + HCO_3^-$	- 6.45	- 6.73	- 7.08	- 7.63	- 8.86
$H CO_3^- \rightleftarrows H^+ + CO_3^=$	- 10.16	-10.29	-10.68	-11.43	-13.38
$CH_4(aq) + 2O_2 \rightleftarrows H_2CO_3(ap) + H_2O_\ell$		98.34[d]	86.87[d]	77.52[d]	69.74[d]
$C + O_2 + H_2O_\ell \rightleftarrows H_2CO_3(ap)$		46.62[d]	41.49[d]	37.41[d]	34.13[d]
$CO_{2(g)} + H_2O_\ell \rightleftarrows H_2CO_3(ap)$		- 2.07[d]	- 2.06[d]	- 1.98[d]	- 1.83[d]

a. All data from Helgeson (1969) except where noted.

b. Minor correction to make compatible with ΔS°_{25}, ΔH°_{25} and heat capacity data.

c. Calculated using data from Table 1, Table 2, Robie and Waldbaum (1968) and Kelley (1960).

d. Ohmoto (1972).

TABLE 5

EQUILIBRIUM CONSTANTS [a] FOR HYDROTHERMAL OXIDE AND SULPHIDE REACTIONS

	log K(T)				
	100°	150°	200°	250°	300°C
$Cu_5FeS_4 + 4FeS_2 \rightleftarrows 5CuFeS_2 + S_{2(g)}$	- 18.2	- 14.2	- 11.1	- 8.5	- 6.4
$4FeS_2 + 4H_2O \rightleftarrows 4Fe^{2+} + 7S^=$ $+ SO_4^= + 8H^+$	-171.89	-158.96	-149.17	-141.49	-136.04
$3Fe_2O_3 \rightleftarrows 2Fe_3O_4 + \frac{1}{2}O_{2(g)}$	- 26.02	- 22.07	- 18.95	- 16.44	- 14.35
$FeS_2 \rightleftarrows FeS + \frac{1}{2}S_{2(g)}$	- 12.5	- 10.25	- 8.48	- 7.03	- 5.81
$2FeS_2 + \frac{3}{2}O_{2(g)} \rightleftarrows Fe_2O_3 + 2S_{2(g)}$	38.39	34.66	31.72	29.35	27.41[b]
$3FeS_2 + 2O_{2(g)} \rightleftarrows Fe_3O_4 + 3S_{2(g)}$	44.57	40.95	38.11	35.81	33.93
$Co + S_{2(g)} \rightleftarrows CoS_2$	29.25[c]	24.69[c]	21.09[c]	18.18[c]	15.78[c]
$Ni + S_{2(g)} \rightleftarrows NiS_2$	27.50[c]	23.07[c]	19.57[c]	16.74[c]	14.41[c]
$Cu_2S + \frac{1}{2}S_{2(g)} \rightleftarrows 2 CuS$	6.06	4.72	3.66	2.77	2.09
$Cu_5FeS_4 \rightleftarrows 4Cu^{1+} + Cu^{2+} + Fe^{2+}$ $+ 4S^=$	-133.4	-120.8	-110.6	-102.3	- 95.6
$CuFeS_2 \rightleftarrows Cu^{2+} + Fe^{2+} + 2S^=$	- 53.1	- 49.2	- 46.2	- 43.7	- 41.9
$FeS \rightleftarrows Fe^{2+} + S^=$	- 17.12	- 16.33	- 15.71	- 15.22	- 14.94
$BaSO_4 \rightleftarrows Ba^{2+} + SO_4^=$	- 9.22	- 9.34	- 9.76	- 10.34	- 11.05
$CaCO_3 \rightleftarrows Ca^{2+} + CO_3^=$	- 9.39	- 10.25	- 11.37	- 12.72	- 14.10
$3FeCO_3 + \frac{1}{2}O_2 \rightleftarrows Fe_3O_4 + 3CO_2$	19.82[d]	20.36[d]	20.78[d]	21.12[d]	21.39[d]

a. All data from Helgeson (1969) except where noted.
b. Minor correction to make compatible with $\Delta S°_{25}$, $\Delta H°_{25}$ and heat capacity data.
c. Calculated from ΔG values given by Barton and Skinner (1967). For NiS the free energy temperature function was extrapolated below the given temperature interval.
d. $\Delta H°_{25}$ and $\Delta S°_{25}$ for the reaction of +7.6 kcal/mole and +111.1 cal/mole/deg respectively (French 1971).

TABLE 6

EQUILIBRIUM CONSTANTS [a] FOR HYDROTHERMAL SILICATE REACTIONS

	Log K(T)				
	100°	150°	200°	250°	300°C
$SiO_2 + 2H_2O \rightleftharpoons H_4SiO_4$	- 3.08	- 2.67	- 2.35	- 2.11	- 1.94
$KAlSi_3O_8 + 4H^+ + 4H_2O$ $\rightleftharpoons K^+ + Al^{3+} + 3H_4SiO_4$	- 0.32	- 1.14	- 1.57	- 1.96	- 2.38
$KAl_3Si_3O_{10}(OH)_2 + 10H^+$ $\rightleftharpoons K^+ + 3Al^{3+} + 3H_4SiO_4$	7.97	3.80	0.93	- 1.38	- 3.31
$Al_2Si_2O_5(OH)_4 + 6H^+$ $\rightleftharpoons 2Al^{3+} + H_2O + 2H_4SiO_4$	2.59	0.15	- 1.48	- 2.76	- 3.82
$Fe_{4.5}Al_{3.0}Si_{2.5}O_{10}(OH)_8 + 18H^+$ $\rightleftharpoons 4.5Fe^{2+} + 3Al^{3+} + 2.5H_4SiO_4$ $+ 8H_2O$	26.78	17.89	11.39	6.41	2.32
$KFe_3AlSi_3O_{10}(OH)_2 + 10H^+$ $\rightleftharpoons K^+ + 3Fe^{2+} + Al^{3+} + 3H_4SiO_4$	14.7	10.8	8.0	5.8	3.9
$3KAlSi_3O_8 + 2H^+ \rightleftharpoons KAl_3Si_3O_{10}(OH)_2$ $+ 2K^+ + 6SiO_2$	9.55	8.91	8.49	8.12	7.82
$2KAl_3Si_3O_{10}(OH)_2 + 2H^+ + 3H_2O$ $\rightleftharpoons 3Al_2Si_2O_5(OH)_4 + 2K^+$	8.18	7.15	6.29	5.52	4.84
$Fe_{4.5}Al_{3.0}Si_{2.5}O_{10}(OH)_8 + K^+ +$ $0.5SiO_2 + 8H^+ \rightleftharpoons 4.5Fe^{2+}$ $KAl_3Si_3O_{10}(OH)_2 + 7H_2O$	17.27	12.76	9.29	6.74	4.66

a.   Data either from Helgeson (1969) or derived from data in
     Tables 1 and 2.

TABLE 7

LOG OF THE INDIVIDUAL ION ACTIVITY COEFFICIENTS

	M_T NaCl	100	150	200	250	300°C
H^+	1	-0.10	-0.12	-0.14	-0.19	-0.27
	3	-0.03	-0.05	-0.08	-0.16	-0.30
K^+	1	-0.25	-0.29	-0.34	-0.42	-0.54
	3	-0.24	-0.28	-0.35	-0.47	-0.68
HS^-	1	-0.23	-0.26	-0.31	-0.38	-0.50
	3	-0.20	-0.24	-0.30	-0.42	-0.61
HSO_4^-, HCO_3^-	1	-0.21	-0.24	-0.28	-0.35	-0.47
KSO_4^-, $NaSO_4^-$	3	-0.17	-0.21	-0.27	-0.38	-0.56
H_2S, CH_4	1	+0.08	+0.08	+0.09	+0.13	+0.18
H_2CO_3 (ap)	3	+0.24	+0.23	+0.24	+0.27	+0.36
$SO_4^=$	1	-0.97	-1.09	-1.26	-1.50	-1.86
	3	-1.10	-1.24	-1.44	-1.74	-2.24
$S^=$	1	-0.84	-0.95	-1.09	-1.30	-1.63
	3	-0.91	-1.04	-1.21	-1.47	-1.91
$CO_3^=$	1	-0.90	-1.02	-1.17	-1.39	-1.74
	3	-1.00	-1.13	-1.31	-1.60	-2.06

TABLE 8

STOICHIOMETRIC INDIVIDUAL ION ACTIVITY COEFFICIENTS [a]

	M_T NaCl	100	150	200	250	300°C
log $\dot{\gamma}$ Fe^{2+}	1	-0.8	-0.9	-1.1	-1.3	-1.6
	3	-0.9	-1.1	-1.3	-1.6	-1.9
log $\dot{\gamma}$ Co^{2+}	1	-0.8	-0.9	-1.0	-1.2	-1.5
	3	-0.8	-0.9	-1.1	-1.4	-2.1
log $\dot{\gamma}$ Ni^{2+}	1	-0.8	-0.9	-1.0	-1.2	-1.5
	3	-1.1	-1.1	-1.2	-1.4	-1.7
log $\dot{\gamma}$ Cu^{1+}	1	-4.9[b]	-5.0[b]	-5.4[b]	-6.0[b]	-6.6[b]
	3	-5.9[b]	-6.0[b]	-6.3[b]	-6.8[b]	-7.5[b]

a.   Calculated using equilibrium constants given in Table 3.   Individual

ion activity coefficients estimated following procedures by

Helgeson (1969).   Stoichiometric mean activity coefficient of NaCl

from Helgeson (1969).

b.   Helgeson (1969).

APPENDIX B

Discussion of Phase Diagrams

B 1. General Comments

To facilitate discussion of the alteration assemblages it is

desirable to represent all the common phases on a single diagram.

The diagrams most commonly used are

(i)   Log fS_2/log fO_2 diagrams   Holland (1965)

(ii)   Activity diagrams

e.g. $\log \dfrac{aFe^{2+}}{(aH^+)^2}$/ $\log \dfrac{aCu^{1+}}{aH^+}$ at

constant T and aH_2S (Helgeson 1970)

(iii)   Log fO_2/pH diagrams at constant ΣS and T

Barnes and Kullerud (1961), Ohmoto (1972)

The latter two diagrams are potentially the most useful. As

noted by Helgeson the advantage of the activity diagram is the

convenient solution parameters. However, difficulty arises in

many instances with the fixed aH_2S, as moving from low oxidation

conditions to high oxidation conditions would necessarily imply

an increase in ΣS. Attempts to reconstruct the

$\log \dfrac{aFe^{2+}}{(aH^+)^2}$/ $\log \dfrac{aCu^{1+}}{aH^+}$ diagram by fixing the aCu^{1+} and rearranging

to produce a $\log \dfrac{aFe^{2+}}{(aH^+)^2}$ / pH at constant ΣS and T were unsuccessful

as many log fO_2/pH conditions did not appear on the diagram (fig. B 1).

Clearly the log fO_2/pH diagram is the best general purpose diagram

and this will be discussed in some detail.

B 2. The Relationship between ΣS and Sulphur Species

The important sulphur species in aqueous solution are assumed

to be H_2S, HS^-, $S^=$, $SO_4^=$, HSO_4^-, KSO_4^- and $NaSO_4^-$ (Ohmoto 1972).

Hence $\Sigma S = mH_2S + mHS^- + mS^= + mSO_4^= + mHSO_4^- + mKSO_4^-$ (1)

log $a_{Fe^{2+}}/a_{H^+}^2$

6

Magnetite ——————————————— 48

5 46
46

Pyrite 44

4 42

44 40

38

3 36

Magnetite ——— 34
42
Hematite
32

2 ——————————————— 30

Hematite

—log fO_2 28

1

0

-1

0   1   2   3   4   5   6   7   8

pH
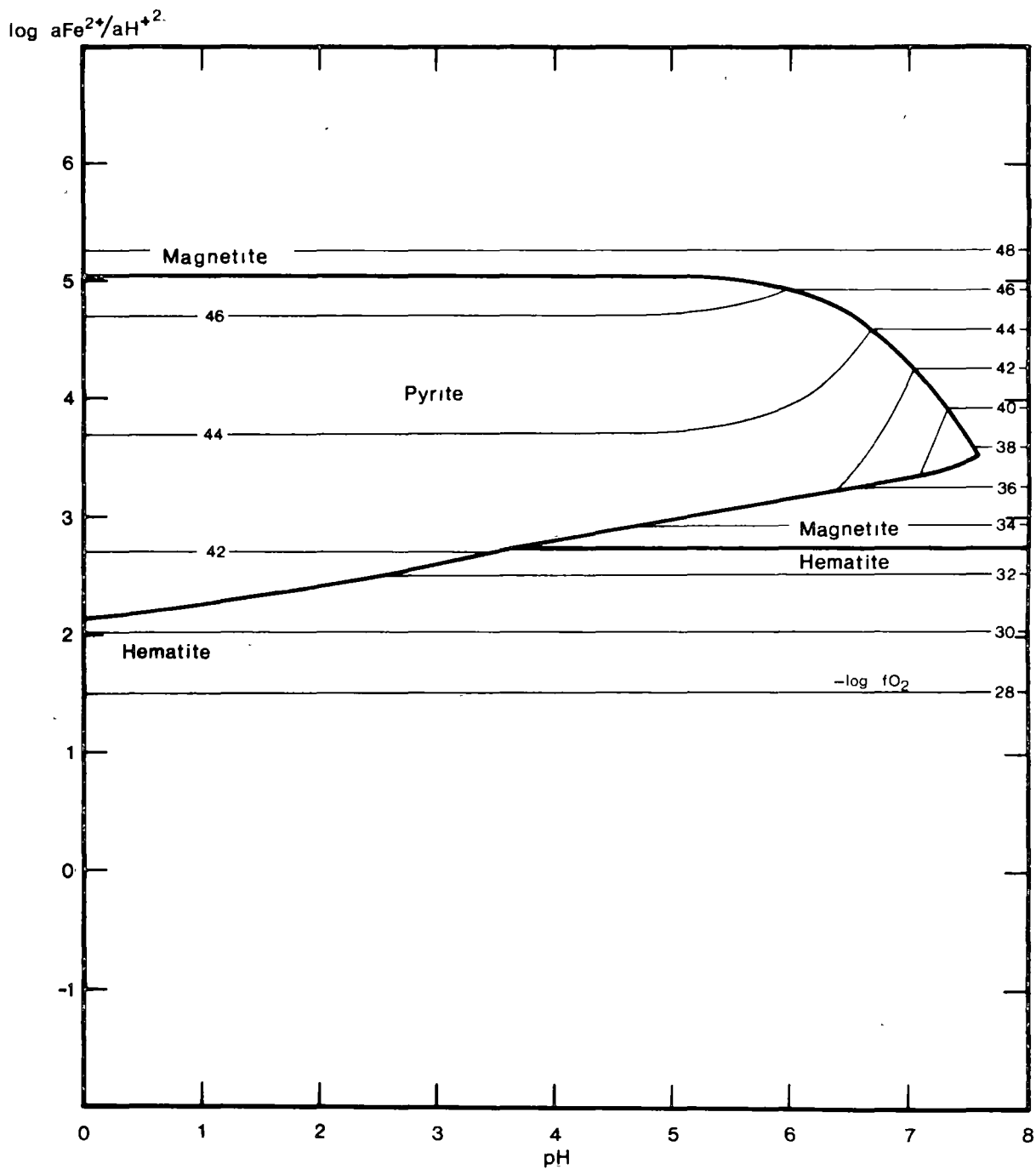
Fig. B1: Log $a_{Fe^{2+}}/a_{H^+}^2$ - pH diagram.drawn for 250°C and
1 atmos. ΣS = 0.01 moles/kg of H_2O. Ionic strength = 3. Activity
of H_2O is taken as unity.

The $NaSO_4^-$ species is treated as being equivalent to the KSO_4^-

species (Ohmoto op. cit.).

It follows that

$$\Sigma S = \frac{aH_2S}{\gamma H_2S} + \frac{aHS^-}{\gamma HS^-} + \frac{aS^=}{\gamma S^=} + \frac{aSO_4^=}{\gamma SO_4^=} + \frac{aHSO_4^-}{\gamma HSO_4^-} + \frac{aKSO_4^-}{\gamma KSO_4^-} \qquad (2)$$

Substituting the following equilibrium reactions

$$H_2S \rightleftharpoons H^+ + HS^- \qquad K_{H_2S} \qquad (3)$$

$$HS^- \rightleftharpoons H^+ + S^= \qquad K_{HS^-} \qquad (4)$$

$$2H^+ + SO_4^= \rightleftharpoons H_2S + 2O_2 \quad K_{SO_4^=} \qquad (5)$$

$$HSO_4^- \rightleftharpoons H^+ + SO_4^= \qquad K_{HSO_4^-} \qquad (6)$$
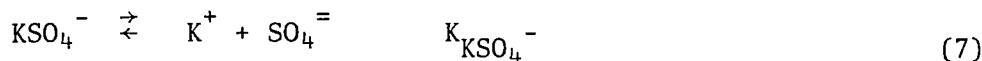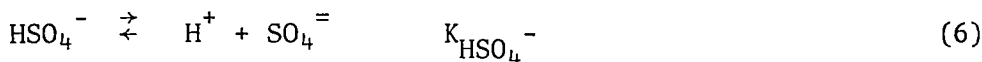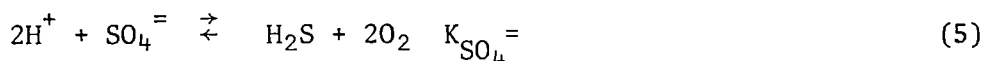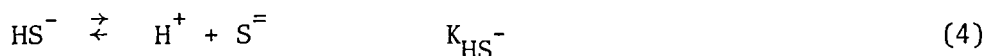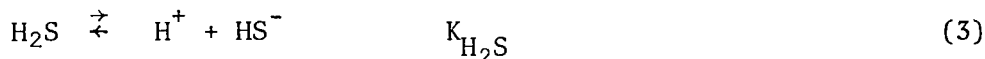
$$KSO_4^- \rightleftharpoons K^+ + SO_4^= \qquad K_{KSO_4^-} \qquad (7)$$

into equation 2 leads to

$$\Sigma S = \frac{aH_2S}{\gamma H_2S} + \frac{K_{H_2S}\,aH_2S}{\gamma HS^-\,(aH^+)} + \frac{K_{HS^-}\,K_{H_2S}\,aH_2S}{(aH^+)^2\,\gamma S^=} + \frac{(fO_2)^2 aH_2S}{\gamma SO_4^=\,K_{SO_4^=}(aH^+)^2}$$

$$+ \frac{(fO_2)^2\,aH_2S}{\gamma HSO_4^-\,K_{SO_4^=}\,K_{HSO_4^-}\,(aH^+)} + \frac{fO_2^2\,aH_2S}{\gamma KSO_4^-\,K_{SO_4^=}\,K_{KSO_4^-}\,(aH^+)^2}\,\frac{\gamma K^+\,mK^+}{}$$

where mK^+ is made equal to $mK^+ + mNa^+$. Rearranging leads to

$$\frac{\Sigma S\,\gamma H_2S}{aH_2S} = 1 + \frac{1}{aH^+}(A_1 + A_2\,fO_2^2) + \frac{1}{(aH^+)^2}(A_3 + A_4\,fO_2^2) \qquad (8)$$

where $\qquad A_1 = \dfrac{\gamma H_2S\;K_{H_2S}}{\gamma HS^-}$

$$A_2 = \frac{\gamma H_2S}{\gamma SO_4^-\;K_{SO_4^=}\;K_{HSO_4^-}}$$

$$A_3 = \frac{\gamma_{H_2S}\;K_{HS^-}\;K_{H_2S}}{\gamma S^=}$$

$$A_4 = \frac{\gamma H_2S}{K_{SO_4^=}}\left(\frac{1}{\gamma SO_4^=} + \frac{\gamma K^+\,mK^+}{\gamma KSO_4^-\,K_{KSO_4^-}}\right)$$

Values of the constants over the temperature range 100 - 300°C and for ΣCl^- of 1 and 3 and K/Na atomic ratio of 0.1 are given in table B1.

Equation (8) expresses the relationship between the activity of the reduced species H_2S and the fO_2, pH and ΣS for given T and ΣCl^-. It would clearly be possible to write similar expressions for the other sulphur species.

B 3. Sulphide/Oxide Phase Relationships

Reactions between the common iron oxides and iron and copper sulphides can be grouped as follows:

(a) Reactions dependent on aH_2S and fO_2 py/hm, py/mt, py/po, and mt/po

$$e.g. \quad 2FeS_2 + 4H_2O \underset{\leftarrow}{\rightarrow} Fe_2O_3 + 4H_2S + \tfrac{1}{2}O_2 \qquad (9)$$

(b) Reactions dependent on fO_2, pH and aCu^{1+}

$$CuFeS_2 + H^+ + \tfrac{1}{4}O_2 \overset{ccp/py}{\underset{\leftarrow}{\rightarrow}} FeS_2 + Cu^{1+} + \tfrac{1}{2}H_2O \qquad (10)$$
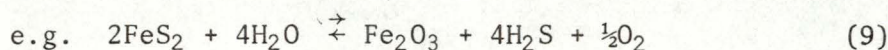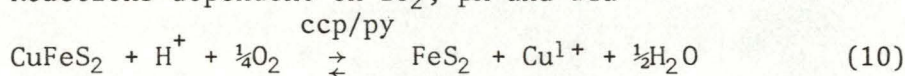
(c) Reactions dependent on pH, aH_2S and aCu^{1+}

$$Cu_5FeS_4 + 4H^+ \overset{bn/ccp}{\underset{\leftarrow}{\rightarrow}} 2H_2S + CuFeS_2 + 4Cu^{1+} \qquad (11)$$
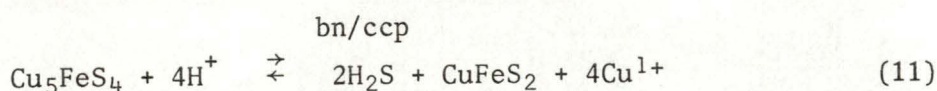
(d) Reactions dependent on fO_2, pH, aH_2S and aCu^{1+}

ccp/mt	ccp/hm	bn/mt

$$e.g. \ 3\,Cu_5FeS_4 + 4.5H_2O + 15H^+ \underset{\leftarrow}{\rightarrow} 15Cu^{1+} + Fe_3O_4 + 12H_2S + \tfrac{1}{4}O_2 \qquad (12)$$
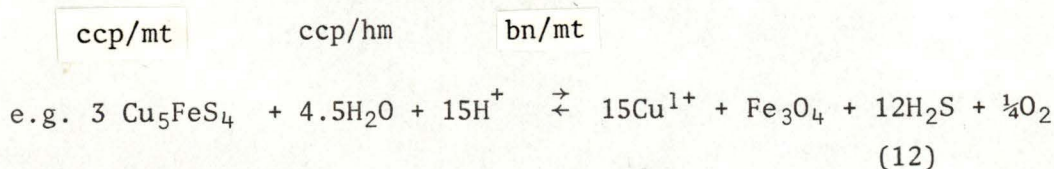
For the py/hm reaction

$$K_{(9)} = (aH_2S)^4\,(fO_2)^{\tfrac{1}{2}}$$

(The activity of water is set equal to one)

$$or \quad \frac{1}{aH_2S} = \frac{(fO_2)^{\tfrac{1}{8}}}{K_9^{\tfrac{1}{4}}} \qquad (13)$$

Combining equation 13 and 8

$$\frac{\Sigma S \ \gamma H_2S\,(fO_2)^{\tfrac{1}{8}}}{K_9^{\tfrac{1}{4}}} = 1 + \frac{1}{aH^+}(A_1 + A_2\,fO_2{}^2) + \frac{1}{aH^+2}(A_3 + A_4\,fO_2{}^2)$$

Table B 1:

°C	m_T[a]	A1	A2	A3	A4[b]
100	1	4.777×10^{-7}	5.360×10^{97}	3.230×10^{-18}	9.311×10^{95}
	3	6.465×10^{-7}	7.088×10^{97}	5.502×10^{-18}	3.116×10^{96}
150	1	4.126×10^{-7}	2.855×10^{83}	4.848×10^{-17}	1.428×10^{81}
	3	5.629×10^{-7}	3.806×10^{83}	8.520×10^{-17}	5.083×10^{81}
200	1	2.754×10^{-7}	1.259×10^{72}	4.466×10^{-16}	1.913×10^{69}
	3	3.807×10^{-7}	1.740×10^{72}	8.328×10^{-16}	6.703×10^{69}
250	1	1.436×10^{-7}	1.340×10^{63}	2.932×10^{-15}	5.118×10^{59}
	3	2.185×10^{-7}	1.993×10^{63}	6.019×10^{-15}	1.775×10^{60}
300	1	4.131×10^{-8}	3.358×10^{56}	1.062×10^{-14}	6.876×10^{51}
	3	8.125×10^{-8}	6.307×10^{56}	3.089×10^{-14}	2.604×10^{52}

[a] $m_T = m_{NaCl} + m_{KCl}$ in moles/Kg H_2O.

[b] $m_K{}^+ + m_{Na}{}^+$ evaluated for $m_T = 1$ and 3 and K/Na atomic ratio of 0.1 using KCl dissociation constants and degree of dissociation constant for NaCl given by Helgeson (1969). Complete dissociation assumed for 100 and 150°C.

Rearranging gives the quadratic form:

$$\frac{1}{aH^+{}^2}(A_3 + A_4\ fO_2{}^2) + \frac{1}{aH^+}(A_1 + A_2 fO_2{}^2) + (1 - A_5 fO_2{}^{\frac{1}{8}}) = 0 \quad (14)$$

where $\quad A_5 \quad = \quad \dfrac{\Sigma S\ \gamma H_2 S}{K_9{}^{\frac{1}{4}}}$

For a given fO_2 equation 14 may be solved for the corresponding pH.

Clearly all reactions in group (a) will be of similar form.

Group (b) type reactions, providing aCu^{1+} is constant, are simply

linear log fO_2/pH relationships. For a constant temperature, ΣCl^-,

and ΣCu, the aCu^{1+} will be constant.

For the bornite/ccp reaction (group c)

$$K_{11} \quad = \quad \frac{(aH_2S)^2(aCu^{1+})^4}{(aH^+)^4}$$

or $\quad \dfrac{1}{aH_2S} \quad = \quad \dfrac{(aCu^{1+})^2}{(aH^+)^2} \quad \dfrac{1}{K_{11}{}^{\frac{1}{2}}} \quad\quad (15)$

or for equation 8

$$\frac{\Sigma S\gamma H_2 S}{aH_2 S} \quad = \quad \frac{\Sigma S\gamma H_2 S\ (aCu^{1+})^2}{K_{11}{}^{\frac{1}{2}}} \quad \frac{1}{(aH^+)^2}$$

$$= \quad A_5 \quad \frac{1}{aH^+{}^2}$$

where $\quad A_5 \quad = \quad \dfrac{\Sigma S\ \gamma H_2 S\ (aCu^{1+})^2}{K_{11}{}^{\frac{1}{2}}}$

If, as in this instance, the power of the $A_5/_{(aH^+)}n$ term is either

1 or 2, then equation 8 reduces to the form of equation 14 and

can be solved in like manner. Otherwise equation group c reactions

may be evaluated rearranging 8 to solve for fO_2 at a given pH.

The bornite to magnetite reaction is used as an example of

group d reactions

$$K_{12} \quad = \quad \frac{(aH_2S)^{12}(aCu^{1+})^{15}(fO_2)^{\frac{1}{4}}}{(aH^+)^{15}}$$

Fig. B2: Log fO_2-pH diagram drawn for 250°C and 1 atmos.
ΣS = 0.01 moles/kg of H_2O. Log aCu^{1+} = -10. Ionic strength = 1.
Activity of H_2O is taken as unity.

or $\quad \dfrac{1}{aH_2S} = \dfrac{(a\ Cu^{1+})^{1.25}}{(aH^+)^{1.25}} \dfrac{(fO_2)^{\frac{1}{48}}}{K_{12}^{\frac{1}{12}}}$

or for equation 8 $\quad \dfrac{\Sigma S\ \gamma H_2S}{aH_2S} = \dfrac{\Sigma S\ \gamma H_2S\ (aCu^{1+})^{1.25}(fO_2)^{\frac{1}{48}}}{(aH^+)^{1.25}\ K_{12}^{\frac{1}{12}}}$

$$= \dfrac{A_5(fO_2)^{\frac{1}{48}}}{(aH^+)^{1.25}}$$

where $A_5 = \dfrac{\Sigma S\ \gamma H_2S\ (aCu^{1+})^{1.25}}{K_{12}^{\frac{1}{12}}}$

Rearranging equation 8 leads to

$$\dfrac{A_5\ (fO_2)^{\frac{1}{48}}}{(aH^+)^{1.25}} - \dfrac{A_1 + A_2(fO_2)^2}{aH^+} - \dfrac{A_3 + A_4(fO_2)^2}{(aH^+)^2} = 1 \qquad (16)$$

Equation 16 may be indirectly solved by holding either pH or fO_2 constant and iterating for the other.

Equations 14 and 16, or equations of similar form have readily been solved using a programmable calculator. This permits log fO_2/pH diagrams of the type shown in fig. B2 to be directly and easily plotted.

The positions of the copper sulphide phase boundaries will clearly be strongly controlled by the aCu^{1+} as well as by ΣS and T. Increasing the aCu^{1+} will shift the py/ccp boundary to higher fO_2 and lower pH positions. Fig. B2 has been drawn so that py/ccp/bn coexist. A lowering of the aCu^{1+} at constant ΣS and T may preclude that possibility.

B 4. Oxide/Silicate Phase Relationships

The phase relationships between kaolinite/sericite and sericite/ K feldspar are readily represented on a log fO_2/pH diagram by fixing the activity of potassium in solution.

The phase relationships between the iron silicates (annite and Fe

chlorite) and the K-silicates and Kaolinite may be represented if

iron is conserved in the reaction by the presence of an oxide.

For example combining the reaction

$$\overset{(1)}{Fe_{4.5}} Al_{3.0} Si_{2.5} O_{10} (OH)_8 + \overset{(2)}{K^+} + 0.5SiO_2 + 8H^+$$

$$\rightleftharpoons \quad 4.5\ Fe^{2+} + KAl_3Si_3O_{10}(OH)_2 + 7H_2O \qquad (17)$$
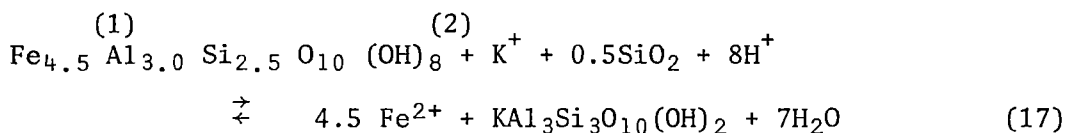
with the hematite saturation reaction

$$4.5\ Fe^{2+} + 1.1250_2 + 4.5H_2O \rightleftharpoons 2.25Fe_2O_3 + 9H^+ \qquad (18)$$

gives the reaction

$$Fe_{4.5} Al_{3.0} Si_{2.5} O_{10}(OH)_8 + K^+ + 0.5SiO_2 + 1.1250_2$$

$$\rightleftharpoons \quad KAl_3Si_3O_{10}(OH)_2 + 2.5H_2O + 2.25\ Fe_2O_3 + H^+ \qquad (19)$$
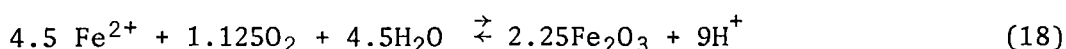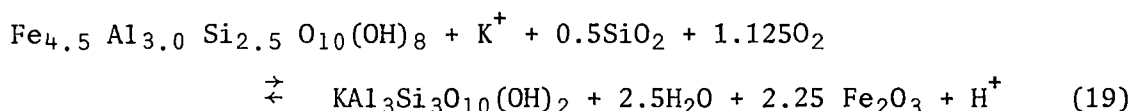
Similar reactions may be written for kaolinite/Fechlorite, K-feldspar/

Fechlorite, K-feldspar/annite and annite/Fechlorite. The relationships

are illustrated in figure B3.

For convenience the activities of all phases in fig. B 3 have

been set at unity.

The exact location of phase boundaries however will depend upon

the mole fractions of Fechlorite in chlorite, annite in biotite and

sericite in phengite-sericite solid solution together with the

respective activity coefficients. The mixing properties of the

chlorite and the phengite-sericite solid solution are not known; hence

it is not possible to locate precisely the reaction of most interest,

the Fechl/ser + hem. reaction. If ideal solid solution was assumed

and given the mole fraction of Fechlorite in chlorite of 0.68 (Prince

Lyell chlorite) and the mole fraction of pure sericite in phengite solid

solution of 0.52 i.e. a log aFechl/aSer ratio of 0.12, then little change

(1) Taken as Fe^{2+}

(2) The thermodynamic data for FeChlorite has been estimated.
   For details see appendix 1.
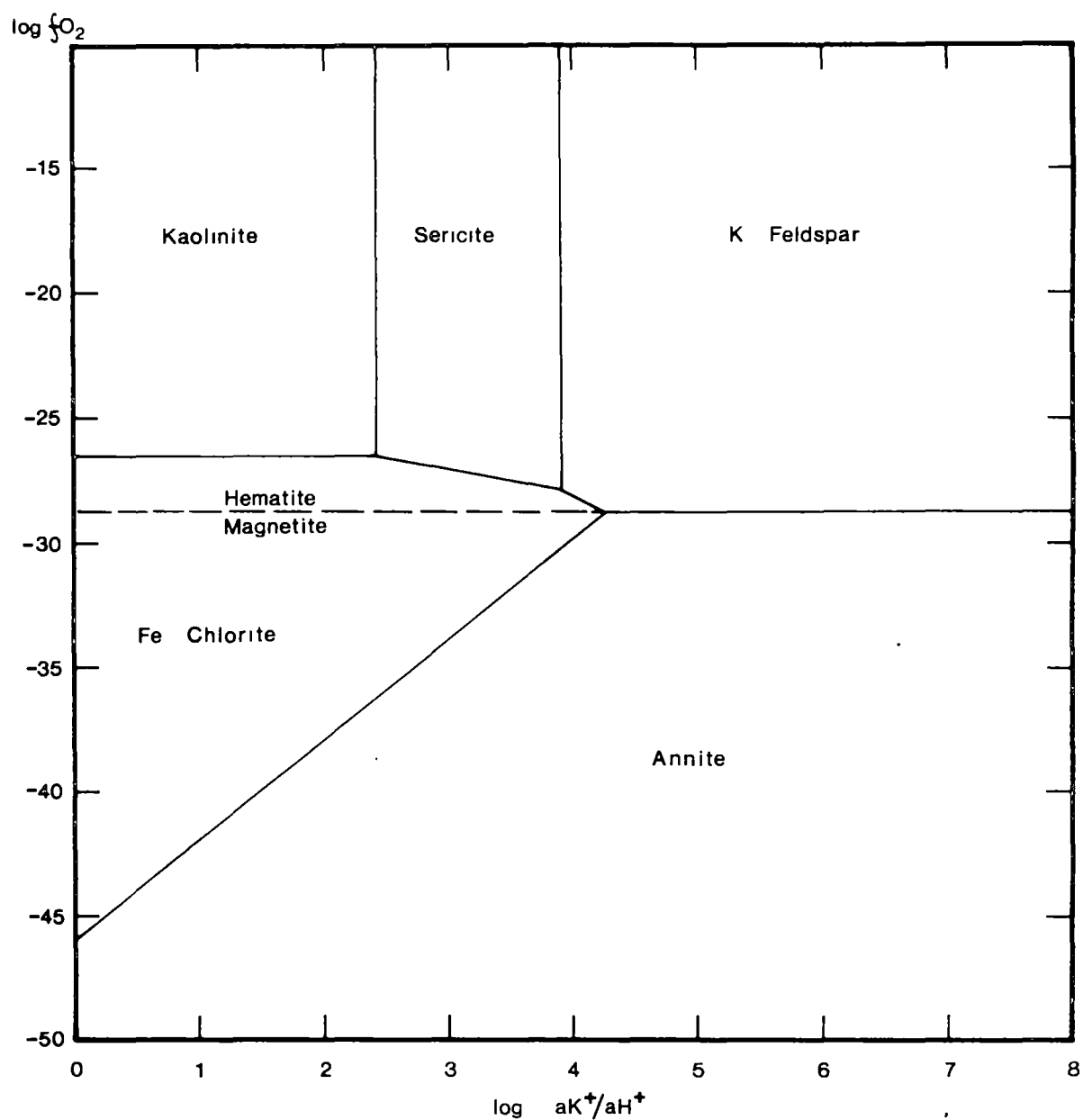
Fig. B3: Log fO_2-log aK^+/aH^+ diagram for 300°C and 1 atmos. Activity of H_2O is taken as unity. Quartz is present in excess.
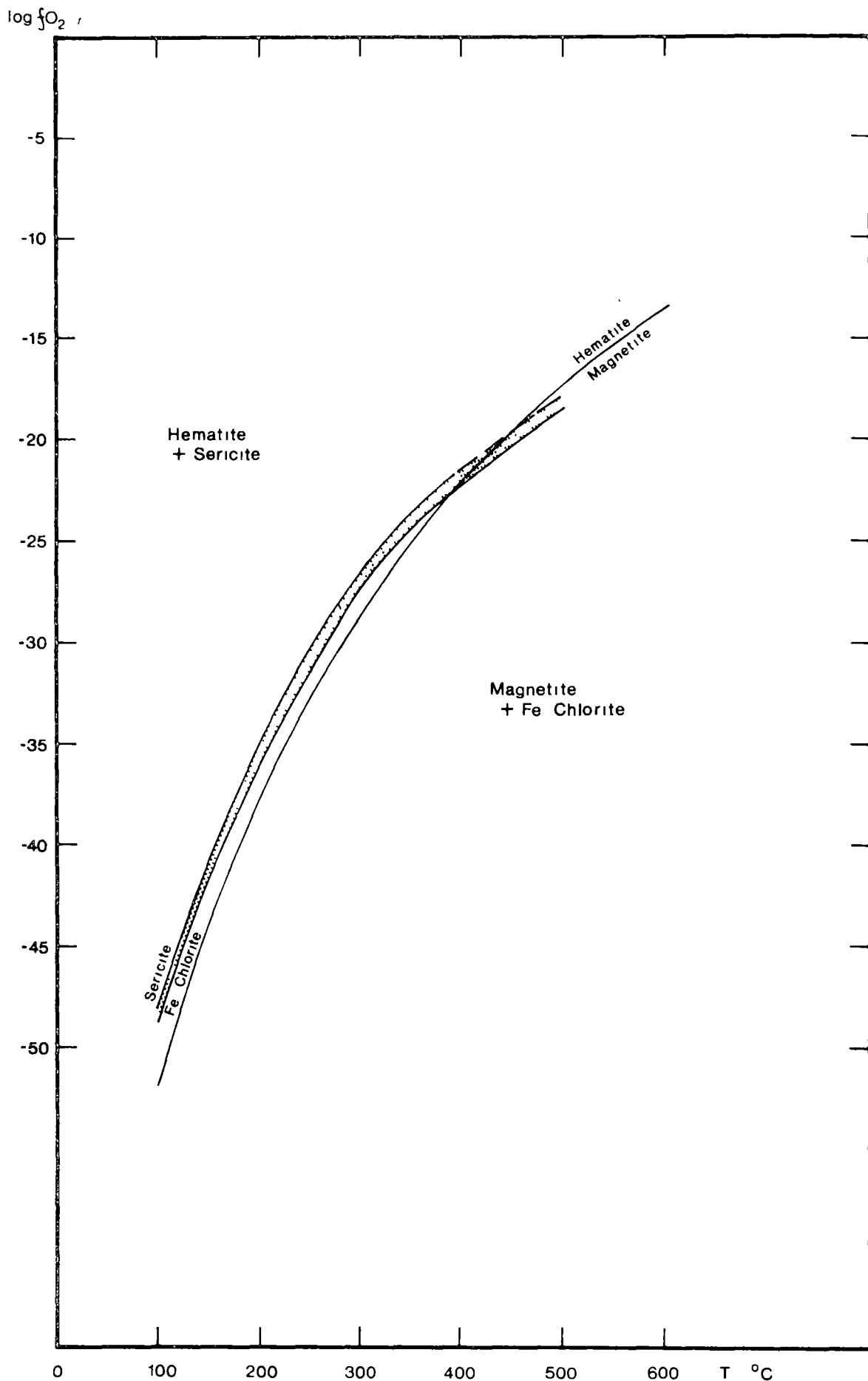
Fig. B4: Log fO_2-T diagram at 1 atmos. Kaol./Ser.<
log aK^+/aH^+ < Ser./K Feld. Activity of H_2O is unity. Quartz is
present in excess.

in the Fechl/ser + hem boundary from the position as given would
be expected.

Because of the uncertainties with activity coefficients and
also with the estimated thermodynamic data of Fe chlorite, in all
following discussion the activity of Fe chlorite and sericite, and
also annite, will be taken as unity. Although this doesn't strictly
represent the real situation it is probably not significantly different
from it.

The temperature effect on the reaction sericite + Fe oxide/Fe
chlorite has been evaluated over the temperature range 100° to 500°C
at 1 atmos. (fig. B4). It would seem, bearing in mind the uncer-
tainties noted above, that an iron-rich chlorite will not coexist
with sericite and magnetite under 400°C at 1 atmosphere pressure.

B 5. Sulphide/Silicate Phase Relationships

Reactions between the iron silicates and the K silicates and
kaolinite using pyrite or pyrrhotite to conserve iron will be
dependent on the activity of H_2S in solution and also the a Cu^{1+}
if chalcopyrite or bornite is used.

The reactions may be grouped as follows:

(a) Reaction dependent on pH and aH_2S

kaolinite + pyrite/Fe chlorite

(b) Reactions dependent on pH, fO_2 and aH_2S

e.g. ser + py/Fechl, K feld + py/Fe chl, ann/Fe chl + py

(c) Reactions dependent on pH, fO_2, aH_2S and aCu^{1+}

e.g. ser + ccp/Fe chl, ser + bn/Fe chl, K feld + bn/Fe chl.

The kaolinite + py/Fe chl reaction is derived by combining the
saturation reactions for kaolinite, Fe chlorite and pyrite,
conserving aluminium and iron.

$\frac{3}{2}Al_2Si_2O_5(OH)_4 + 4.5\ FeS_2 + 10H_2O$

$$\rightleftarrows\ Fe_{4.5}Al_{3.0}Si_{2.5}O_{10}(OH)_8 + 0.5SiO_2 + 2.25O_2 + 9H_2S \qquad (20)$$

$K_{20} = (fO_2)^{2.25}(aH_2S)^9$
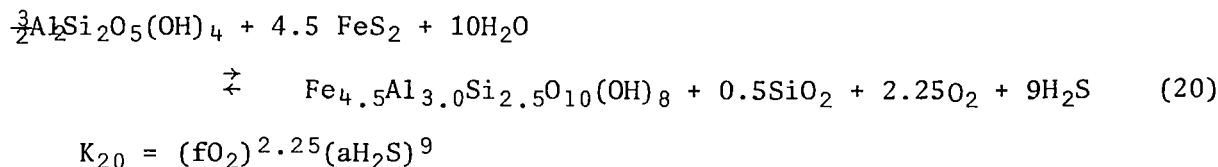
Rearranging and combining with 8 leads to

$$\frac{1}{aH^+\,^2}(A_3 + A_4fO_2{}^2) + \frac{1}{aH^+}(A_1 + A_2fO_2{}^2) + (1 - A_5fO_2{}^{\frac{1}{4}}) = 0 \qquad (21)$$

$$\text{where}\ A_5 = \frac{\Sigma S\ \gamma H_2S}{K_{20}{}^{\frac{1}{9}}}$$

Equation 21 is of the same form as equation 14 and may be similarly

solved.

The ser + py / Fechl reaction (group 6) is derived by combining

reaction 17 with the saturation reaction for pyrite.

$KAl_3Si_3O_{10}(OH)_2 + 4.5\ FeS_2 + H^+ + 11.5\ H_2O$

$$\rightleftarrows\ Fe_{4.5}Al_{3.0}Si_{2.5}O_{10}(OH)_8 + 0.5SiO_2 + K^+ + 9H_2S + 2.25O_2 \qquad (22)$$

$$K_{22} = \frac{aK^+}{aH^+}\ (fO_2)^{2.25}(aH_2S)^9$$
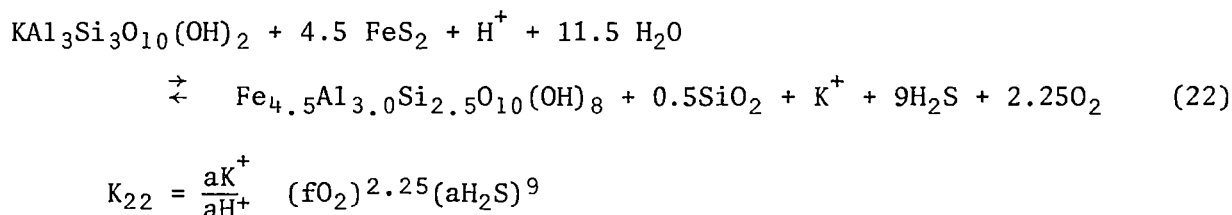
Combining with 8 and rearranging leads to

$$\frac{A_5fO_2{}^{\frac{1}{4}}}{(aH^+)^{\frac{1}{9}}} - \frac{A_1 + A_2(fO_2)^2}{(aH^+)} - \frac{A_3 + A_4(fO_2)^2}{(aH^+)^2} = 1 \qquad (23)$$

$$\text{where}\qquad A_5 = \frac{\Sigma S\ \gamma H_2S(aK^+)^{\frac{1}{9}}}{(K_{22})^{\frac{1}{9}}}$$

Equation 23 is similar to equation 16 and is solved in the same way.

Equations for group c reactions will be of the same form as equation 23

except that A_5 will have an activity of Cu term.

The silicate reactions are shown superimposed on the sulphides and

oxides in figure B5. Heavy lines represent silicate reactions and the

light lines represent sulphide and oxide boundaries. Two Fe chlorite

fields occur, such that the qtz/ser/py field is bounded at high oxidation
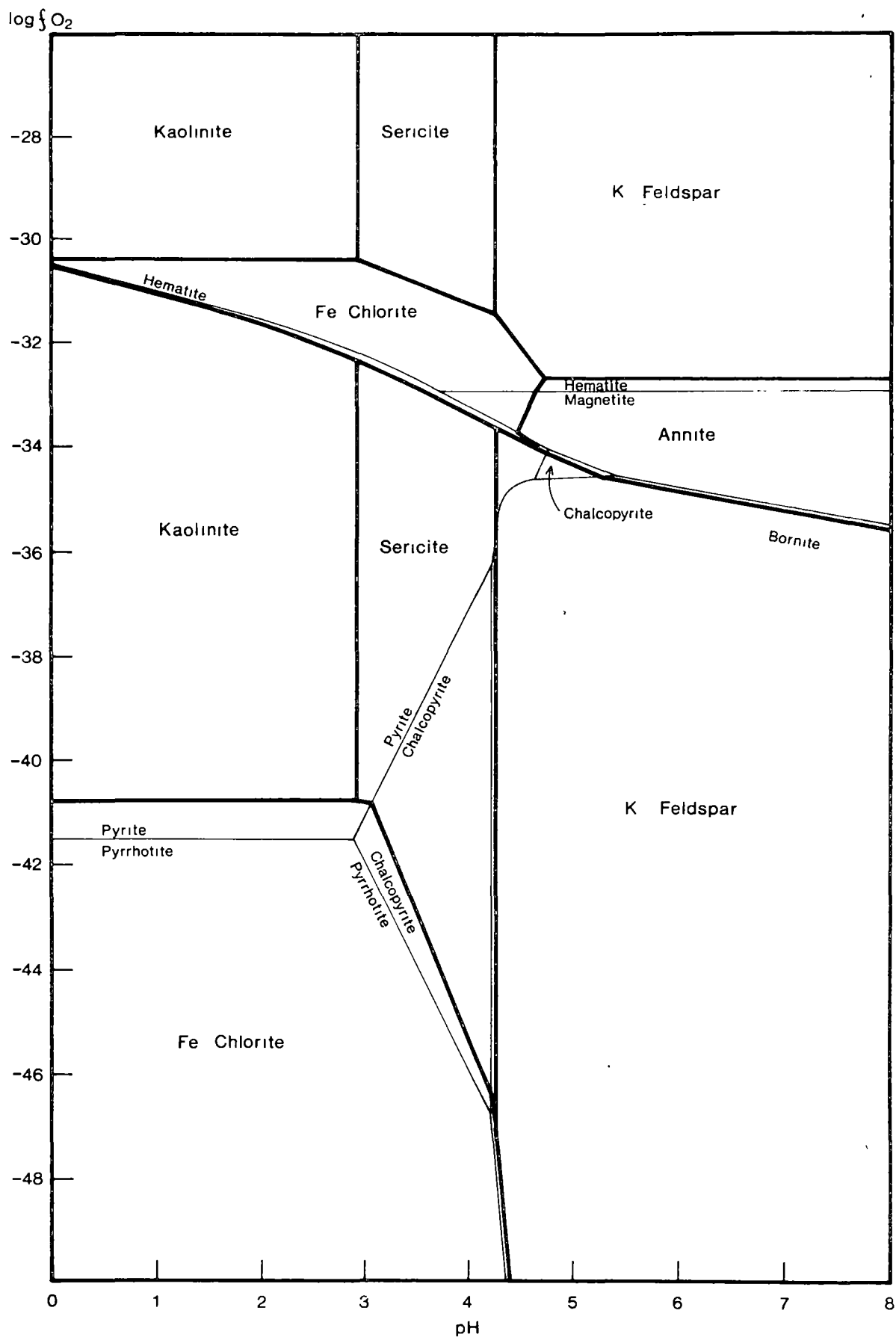
Fig. B5: Log fO_2-pH diagram drawn for 250°C and 1 atmos. ΣS = 0.01 moles/ kgm of H_2O. Ionic strength = 3. mK^+/mNa^+ = 2. Log a Cu^+ = -10. Activity of H_2O is taken as unity. Quartz is present in excess.
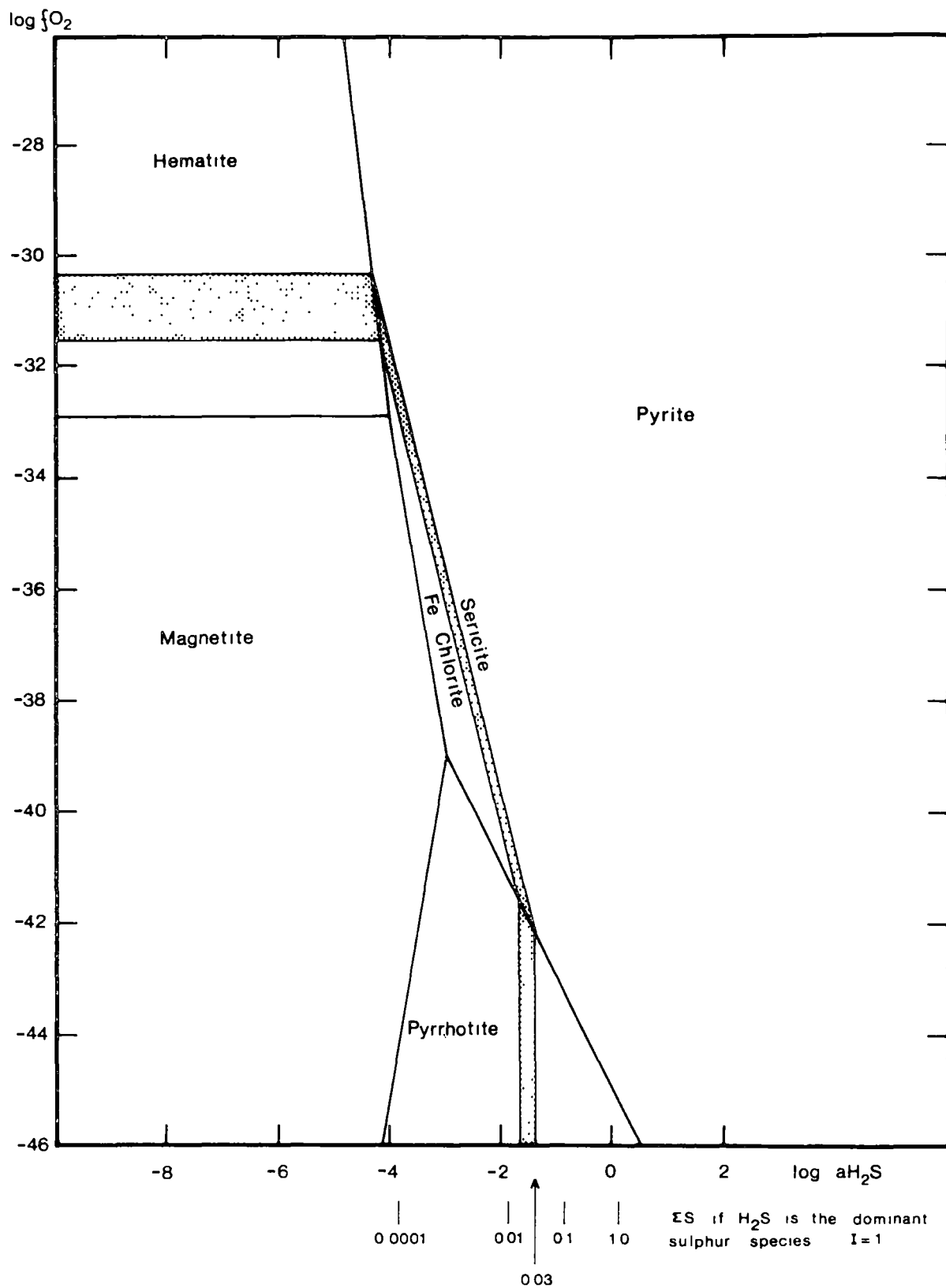
Fig. B6: Log fO_2-log aH_2S diagram for $250^\circ C$ and 1 atmos.
Kaol./Ser. $<$ log aK^+/aH^+ $<$ Ser./K Feld. Activity of H_2O is taken
as unity. Quartz is present in excess.

conditions and low oxidation conditions by an Fe chlorite field.

Because the silicate reactions, in the presence of sulphides,

are dependent on aH_2S their location on the $logfO_2$/pH diagram

will also depend on ΣS. The relationship between $logfO_2$ and aH_2S

(ΣS where appropriate) for the ser/Fe chl reaction is given in fig B6.

Decreasing ΣS by an order will shift the reduced ser/Fe chl boundary

in the pyrite field (fig. B5) 4 log fO_2 units to higher oxidation

conditions.

For figure B5 the relative positioning of the kaolinite/ser/K feldspar

fields to the pyrite/chalcopyrite/bornite fields is dependent on the

relative values of aK^+ and aCu^{1+}.

B 6. Graphite and Carbonate Relationships

a) Relations between aqueous species

Following Ohmoto (1972)

$$m\Sigma C = mH_2CO_3(ap) + mHCO_3^- + mCO_3^= + mCH_4(aq) \qquad (24)$$

where $mH_2CO_3(ap) = mCO_2(aqu) + mH_2CO_3$

It follows that

$$m\Sigma C = \frac{aH_2CO_3(ap)}{\gamma H_2CO_3} + \frac{aHCO_3^-}{\gamma HCO_3^-} + \frac{aCO_3^=}{\gamma CO_3^=} + \frac{aCH_4(ap)}{\gamma CH_4} \qquad (25)$$

Substituting the following equilibrium reactions

$$H_2CO_3(ap) \rightleftharpoons H^+ + HCO_3^- \quad K_{H_2CO_3(ap)}$$

$$HCO_3^- \rightleftharpoons H^+ + CO_3^= \quad K_{HCO_3^-}$$

$$CH_4(aq) + 2O_2 \rightleftharpoons H_2CO_3(ap) + H_2O_\ell \quad K_{CH_4}$$
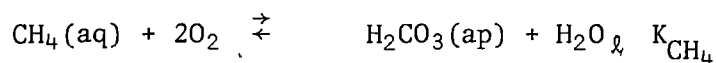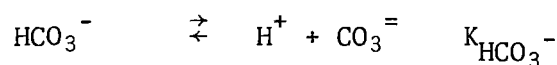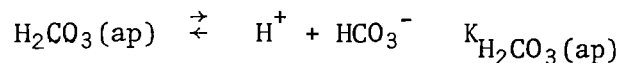
into equation 25 leads to

$$m\Sigma C = \frac{aH_2CO_3(ap)}{\gamma H_2CO_3(ap)} + \frac{K_{H_2CO_3(ap)}}{\gamma HCO_3^-} \frac{aH_2CO_3(ap)}{aH^+}$$

$$+ \frac{K_{H_2CO_3(ap)}\ K_{HCO_3^-}}{\gamma CO_3^=} \frac{aH_2CO_3(ap)}{(aH^+)^2}$$

$$+ \frac{aH_2CO_3(ap)}{K_{CH_4}(fO_2)^2\ \gamma CH_4} \qquad (26)$$

or

$$\frac{\gamma H_2CO_3(ap)\ m\Sigma C}{aH_2CO_3(ap)} = 1 + \frac{B_1}{aH^+} + \frac{B_2}{(aH^+)^2} + \frac{B_3}{fO_2^2} \qquad (27)$$

where

$$B_1 = \frac{\gamma H_2CO_3(ap)\ K_{H_2CO_3(ap)}}{\gamma HCO_3^-}$$

$$B_2 = \frac{H_2CO_3(ap)\ K_{H_2CO_3(ap)}\ K_{HCO_3^-}}{\gamma CO_3^=}$$

$$B_3 = \frac{\gamma H_2CO_3(ap)}{K_{CH_4}\ \gamma CH_4}$$

Values of B_1, B_2 and B_3 are given in table B2 for 250°C.

Table B 2.

Constants for equation   at 250°C.

	I = 1	I = 3
B_1	7.031 x 10^{-8}	1.047 x 10^{-7}
B_2	2.864 x 10^{-18}	6.457 x 10^{-18}
B_3	3.02 x 10^{-78}	3.02 x 10^{-78}

b) The graphite boundary.

Ohmoto (op. cit.) expresses the graphite saturation equation as

$$C + O_2 + H_2O \;\rightleftharpoons\; H_2CO_3 \text{ (ap)} \tag{28}$$
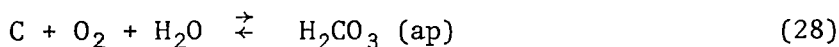
for which

$$K_{28} = \frac{aH_2CO_3 \text{(ap)}}{fO_2} \quad (aH_2O = 1) \tag{29}$$

Combining equation 28 and 29 leads to

$$\frac{B_3}{(fO_2)^2} - \frac{\gamma H_2CO_3 \text{(ap)}^m \Sigma C}{K_{28} fO_2} + 1 + \frac{B_1}{aH^+} + \frac{B_2}{(aH^+)2} = 0 \tag{30}$$

which is readily evaluated.

c) Calcite saturation line.

$$CaCO_3 + 2H^+ \;\rightleftharpoons\; Ca^{2+} + H_2CO_3 \tag{31}$$
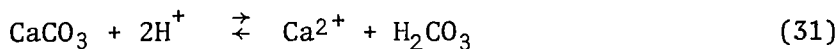
for which

$$K_{31} = \frac{aCa^{2+} \; aH_2CO_3 \text{(ap)}}{(aH^+)2} \tag{32}$$

Combining equation 27 and 32 leads to

$$\frac{B_4}{(aH^+)2} = 1 + \frac{B_1}{aH^+} + \frac{B_2}{(aH^+)2} + \frac{B_3}{fO_2{}^2} \tag{33}$$

where $B_4 \quad = \quad \dfrac{\gamma H_2CO_3 \text{(ap)}^m \Sigma C \; aCa^{2+}}{K_{31}}$

or

$$fO_2{}^2 = \frac{B_3}{\frac{1}{(aH^+)2}(B_4 - B_2) - \frac{B_1}{aH^+} - 1} \tag{34}$$

(d) Oxide/Siderite Relationships

The magnetite/siderite reaction,

$$Fe_3O_4 + 3H_2CO_3 \;\rightleftharpoons\; 3FeCO_3 + \tfrac{1}{2}O_2 + 3H_2O \tag{35}$$
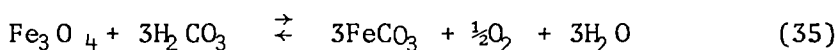
$$K_{35} = \frac{(fO_2)^{\frac{1}{2}}}{(aH_2CO_3)^3} \qquad aH_2O = 1 \tag{36}$$

Combining equation 27 and 36 leads to

$$\frac{\gamma H_2CO_3(ap) \; m\Sigma C \; K^{\frac{1}{3}}}{(fO_2)^{\frac{1}{6}}} \quad - \; C_1 \quad - \; \frac{B_3}{fO_2{}^2} \quad = \quad 1 \qquad (37)$$

where $\quad C_1 \quad = \quad \dfrac{B_1}{aH^+} \quad + \quad \dfrac{B_2}{(aH^+)^2}$

Equation 37 may be solved indirectly by iterating for fO_2 at a fixed pH value. A similar expression may be derived for the hematite/ siderite reaction.

e) Sulphide/Siderite Relationships.

The pyrite/siderite reaction is dependent on both the aH_2S and aH_2CO_3

$$FeS_2 + H_2O + H_2CO_3 \quad \overset{\rightarrow}{\leftarrow} \quad FeCO_3 + 2H_2S + \tfrac{1}{2}O_2 \qquad (38)$$
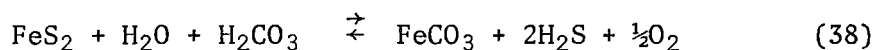
$$K \quad = \quad \frac{(aH_2S)^2 (fO_2)^{\frac{1}{2}}}{aH_2CO_3} \qquad (39)$$

Combining equations 8, 27 and 39 leads to

$$\frac{1 + C_1 + \dfrac{B_3}{fO_2}}{\left(1 + C_2 + (fO_2)^2 C_3\right)^2} \quad - \quad \frac{C_4}{(fO_2)^{\frac{1}{2}}} \quad = \quad 0 \qquad (40)$$

where

$$C_1 \quad = \quad \frac{B_1}{aH^+} \quad + \quad \frac{B_2}{(aH^+)^2}$$

$$C_2 \quad = \quad \frac{A_1}{aH^+} \quad + \quad \frac{A_3}{(aH^+)^2}$$

$$C_3 \quad = \quad \frac{A_2}{aH^+} \quad + \quad \frac{A_4}{(aH^+)^2}$$

$$C_4 \quad = \quad \frac{\gamma H_2CO_3}{(\gamma H_2S)^2} \quad \frac{m\Sigma C \; K}{(m\Sigma S)^2}$$

Equation 40 may be evaluated by iterating for fO_2 at constant pH.
A similar expression may be derived for the pyrrhotite/siderite reaction.

The phase relationships given above are illustrated in figure B7 for $\Sigma S = 0.001$, ΣC of 0.1 and 1.0, at $250^{\circ}C$.
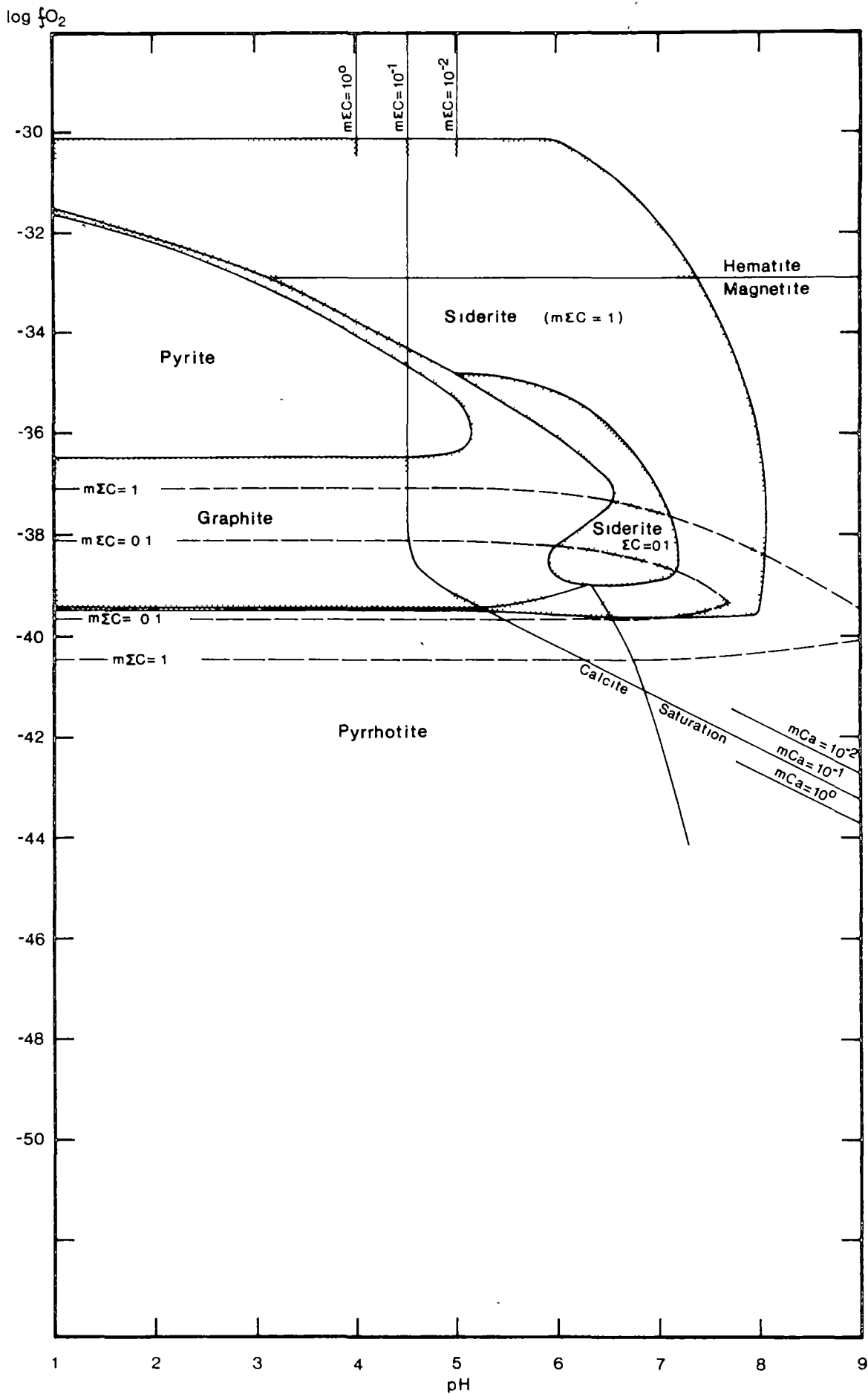
Fig. B7: Log fO_2-pH diagram drawn for 250°C and 1 atmos.
$\Sigma S = 0.001$ moles/kg of H_2O. Ionic strength = 3. Activity of
H_2O is taken as unity.

APPENDIX C

Trace Element Analysis of Pyrite and Chalcopyrite

C1 Sampling

Prince Lyell orebody was sampled on the 830' level on X-Cuts 1-2 through to 7-8, at intervals of 10'. (all sampling was carried out prior to metrification). A section on 7-8 X-Cut was sampled on a slightly smaller interval and Stope 8, the Decline, and D.D.H.s WL315, 352, 360, 368 and 369 were less intensively sampled. The programme was designed to test the spatial variation of trace elements in the sulphides within the ore zone. To minimise variations on the hand specimen scale, bulk ore samples (5-10 kg) were taken. Obvious remobilised material was avoided and samples restricted to uniform rock types. Massive banded pyrite was sampled separately. The use of drill core (previously split for copper and sulphur analysis) restricted the sample weight to 500-1000 gms. The samples were taken by spot sampling over intervals which corresponded with the mine assay sample intervals.

Cape Horn (255m level) was sampled in a similar manner to Prince Lyell (830' level). Some Cape Horn samples were from drill core (D.D.H.s CH 71 and 76). Western Tharsis sampling was entirely from drill core.

C2 Separation

Flotation was used to separate the pyrite and chalcopyrite. Where necessary magnetic separation and heavy liquids were used to further clean the samples, particularly the chalcopyrite. However, two flotations and a washing were generally sufficient to give better than 95% purity.

Samples were crushed to less than 10 mesh using a jaw crusher
and roller mills.   The sample size was then reduced to approximately
2000 gms by splitting.   A second split of 200 gms was set aside
for analysis.   The 2000gm split was ground in a ball mill for 15
minutes with 1800cc of water and 10,000 gms of balls (314-1¼").
3gms of lime were added to each grind to set the initial pH.

A bench-size Denver cell of 500 to 2000cc capacity was used
for the flotation.   For the chalcopyrite float, the pH was set at
11.5 to 12.   1.3cc of a 1% solution of potassium amyl zanthate was
added as collector and 10 drops of methyl isobutyl carbonyl (MIBC)
as frother.   For the pyrite float the pH was dropped to 9 to 10
using dilute sulphuric acid and an additional 10cc of potassium amyl
zanthate added.   Both the pyrite and chalcopyrite were refloated
in smaller capacity cells and washed using a panning dish.

C3 Analytical Method, Accuracy and Precision

The samples were analysed using atomic absorption spectrophotometry
following the method of Loftus-Hills (1968).   1gm samples were roasted,
dissolved in conc. HCl, and the iron in solution removed with di-
isopropyl ether.   An interlaboratory survey was made to determine the
accuracy and precision of the trace element analytical work (Robinson
and Walshe, 1977), using two Mt. Lyell samples as standards.

A summary of the results is given in the following table.

	PYRITE 1		PYRITE 2	
	$\bar{X}$	C	$\bar{X}$	C
Co	1309	3.4	366	6.3
Ni	190	4.7	32	15.6
Mn	64	3.1	5.6	9.3
Cu	1896	3.0	2377	2.4
Se	82	12.3	64	20.5

where $\bar{X}$ is the mean value (ppm)

C is the per cent coefficient of variation

$$C = \frac{100\sigma}{\bar{X}}$$

The per cent coefficient for metal values above 50 ppm is less than 5. 5% of the total pyrite samples analysed in the Mt. Lyell study were analysed in triplicate to test the homogeneity of the samples. The per cent coefficient of variation was less than 5 for 90% of the samples tested and less than 3 for 75% of the samples.

C4 Data

Trace cobalt, nickel and manganese in pyrite data for Prince Lyell, Cape Horn and Western Tharsis are given on plans C1 to C8. Data not plotted on the plans are given in table C1. The trace cobalt, nickel and manganese contents of coexisting pyrite and chalcopyrite are given in table C2.

TABLE C1:   COBALT, NICKEL AND MANGANESE CONTENTS OF PYRITE (ppm)

	Co	Ni	Mn
WL231/300	950	415	50
330	2270	505	114
370	2150	330	290
WL258/290	500	108	24
370	920	71	53
450	370	67	265
WL352/ 24	770	141	0
40	522	84	6
50	520	70	7
62	590	60	8
70	530	36	4
86	3460	120	12
90	2330	160	56
110	2620	123	47
120	1880	255	30
130	1400	241	70
140	2980	160	126
170	873	176	152
190	4150	225	130
208	4590	163	250
220	3800	251	276
268	1920	233	70
WL360/ 6	3300	230	518
18	2560	75	335
30	2090	240	530
46	2900	31	45
62	926	21	15
80	700	52	74
94	770	154	53
100	680	48	17
130	675	27	124
150	1051	77	37
170	1670	237	20
174	581	62	10
190	880	208	15

	<u>Co</u>	<u>Ni</u>	<u>Mn</u>
WL368/ 6	490	620	40
16	990	123	10
42	1340	94	190
70	420	18	0
96	1800	109	336
102	2050	235	710
180	4700	154	62
186	1533	112	128
178	5170	201	167
216	476	39	42
WL369/ 36	312	40	87
66	482	14	0
86	2060	92	84
100	1740	125	591
124	653	121	80
164	720	208	110
170	2100	272	5344
186	791	140	263
192	1200	235	109
Cape Horn			
CH 71/560	2706	1490	228
580	680	887	176
590	1658	1330	43
600	1076	745	56
740	616	187	6
765	852	343	13
CH 76/ 70	2806	1843	64
80	2614	2399	160
95	1202	845	126
105	1566	527	90
115	616	697	63
125	1571	1107	44
255A	245	157	38
255B	245	161	0
255C	245	161	0
280	484	422	11

Crown Lyell No.3	Co	Ni	Mn
NL1044/ 15	255	84	26
25	350	60	22
35	330	31	24
50	220	124	21
75	130	32	11
150	820	107	18
165	1690	182	517
220	1660	1330	94
240	2500	900	31
NL1062/ 45	950	220	3470
105	2010	1480	250
120	2430	1340	400
160	1510	123	44
195	2020	460	13
Crown Open-Cut			
1	790	70	45
2	390	268	30
Massive Sulphides			
Blow			
1	200	56	25
2	370	78	23
3	100	38	-
Comstock			
1	28	31	35
2	37	29	77
Lake Selina			
SL 4 /415	400	62	-
445	430	50	-
480	570	45	-
510	600	30	-
540	1200	25	-
570	730	20	-
600	2530	25	-
630	380	20	-
660	950	15	-
690	2250	30	-
720	540	20	-
750	710	20	-

Lake Selina (contd.)	Co	Ni	Mn
SL 4/ 780	1220	78	-
810	2620	48	-
840	1690	48	-
870	1700	40	-
900	3700	78	-
930	515	23	-
960	2530	91	-
990	570	32	-
1020	400	32	-
1045	400	16	-
SL 5/ 210	2130	260	53
245	2100	36	77
275	1080	35	36
310	1750	45	37
445	2520	65	100
470	2000	61	134
500	1050	61	59
530	1220	100	181
720	1470	32	73
750	2130	32	71
780	600	16	37
810	670	114	0
840	1610	166	200
SL 6/ 215	1340	95	11
285	1670	270	172
310	336	270	88
340	2250	156	35
630	1400	160	80
740	1620	80	63
770	2150	232	0
800	1350	95	49
830	1550	162	0
860	1200	95	0
900	1470	127	117
930	1400	112	0

Lake Selina (contd.)	Co	Ni	Mn
SL 7/1200	623	42	0
1210	670	38	0
1220	4360	54	0
1230	1843	42	0
1240	741	42	0
1250	1030	46	0
Surface Samples			
A	720	240	13
B	720	56	9
C	2250	50	20
D1	1610	150	37
D2	1900	140	48
E	5000	170	0
F	720	61	0

TABLE C2: COBALT, NICKEL and MANGANESE CONTENTS of CO-EXISTING
PYRITE and CHALCOPYRITE

	Pyrite				Chalcopyrite		
	Co	Ni	Mn		Co	Ni	Mn
Western Tharsis							
257/ 950	1135	75	9		22	<5	10
1030	1597	265	35		27	<5	15
1050	1297	310	10		15	<5	<5
317/ 550	326	245	7		13	<5	5
760	1627	250	<5		54	15	5
910	430	98	<5		26	<5	5
950	1020	160	8		19	<5	20
1310	87	72	47		7	<5	50
332/ 790	140	50	-		25	5	<5
820	580	223	-		21	<5	5
880	540	205	-		21	<5	5
371/ 150	1027	174	8		24	<5	5
212	1329	603	6		25	5	<5
272	183	152	4		12	<5	<5
374/ 224	1283	214	5		31	<5	5
232	2081	360	10		19	<5	5
298	1439	262	12		51	15	10
356	382	141	4		21	<5	25
Prince Lyell							
315/ 30	670	66	-		15	10	<5
40	465	46	-		10	10	<5
100	280	42	-		<5	10	5
150	258	66	-		<5	15	5
1-2/ 100	580	72	5		5	15	<5
130	1720	138	5		30	10	<5
160	2420	215	9		5	10	<5
180	1580	225	60		20	20	20
192	1340	71	76		45	10	10
198	1580	126	17		10	15	10
200	1020	78	14		15	10	10
220	1940	82	16		20	10	10

Prince Lyell (contd.)	Pyrite			Chalcopyrite		
	Co	Ni	Mn	Co	Ni	Mn
2-3/ 230	1250	160	10	45	<5	<5
240	700	82	5	62	<5	<5
310	810	100	50	100	5	40
3-4/ 35	327	40	600	20	<5	110
40	1679	191	235	60	5	170
130	1755	134	96	95	<5	90
4-5/ 220	2550	180	60	45	5	15
7/ 25	2540	120	-	100	10	15
80	1880	50	-	35	5	30
7-8/ 38	3438	50	-	100	5	20
116	1320	60	-	15	5	20
8/ 10A	1553	235	-	70	10	25
220	3594	15	-	45	5	28
250	1600	55	-	30	<5	10
250E	1960	121	-	40	10	20
350	1140	82	-	35	5	30
Cape Horn						
4-5/ 80	575	400	806	20	5	100
71/ 600	1076	745	56	25	<5	20

APPENDIX D

Lake Selina D.D.H.s Nos. 4, 5 and 6

D1 Introduction

Several copper prospects occur in the Lake Selina area (fig. 1.2),

20 kilometres north of Queenstown. A number of exploration holes

have been drilled by the Mt. Lyell Company to test related geophysical

anomalies. Three of the holes, D.D.H. Nos. 4, 5 and 6, have been

examined as a comparative study with the Mt. Lyell mineralization.

A brief description of the geology, petrography and mineragraphy is

given below. Regional geological mapping by the Mt. Lyell Company

and the Mines Department has shown that the Lake Selina prospects

occur within the central lava belt (fig. 1.2, Corbett *et al.*, 1974).

D2 Geology

D2.1 Description of DDH No.4

D.D.H. No.4 consists, in the upper nonmineralized part of

the hole, of a massive pink rhyolite with quartz and altered feldspar

and ferro-magnesian phenocrysts (45848). Alteration is to sericite

and iron-rich chlorite respectively. The groundmass consists of

fine-grained quartz and feldspar with sericite and chlorite. From

445' to 680' the rhyolite is altered to a grey or pink-grey quartz-

potassium feldspar-sericite-pyrite assemblage. The potassium

feldspar appears to be a mixture of microcline and adularia. It is

pink or creamy pink and occurs predominately in small discontinuous

veinlets, 2-3 mm. in width. Pyrite occurs as massive bands 1-2 cm.

wide or as disseminations. Thin section textures vary from coarse

siliceous fragmental to fine integrowths of quartz and sericite.

Minor chlorite is present (45849, 45850, 45852). From 680' through

to the end of the hole the sulphide zone is chloritised. The assemblage is quartz-chlorite-sericite-potassium feldspar-pyrite (45853). Thin sections show the typical siliceous fragmental texture with a chlorite, sericite, pyrite matrix. Minor chalcopyrite and magnetite are present (45854, 45855). Magnetite is only slightly altered to hematite. Magnetite, pyrrhotite and pyrrhotite/chalcopyrite inclusions are present in the pyrite.

D2.2 Description of D.D.H. No.5

D.D.H. consists essentially of chloritised rhyolites. An altered quartz-feldspar-hornblende(?) porphyry intrusive(?) occurs in the bottom of the hole.

The nonmineralized volcanics in the first 200' are more chloritised than their counterparts in D.D.H. No. 4 (45856). Hematite is more abundant (45857). The alteration in the sulphide zones is quartz, chlorite, potassium feldspar, sericite and pyrite. Pyrite and chlorite are disseminated through the siliceous volcanic and commonly associated (45862, 45861, 45863). Potassium feldspar occurs as irregular microveins (45860) or as a dispersed component within the siliceous fragments. Minor magnetite veins occur (45858, 45859). Pyrite and chlorite occur with the magnetite veins. There is little alteration of the magnetite to hematite. Accessory minerals include sphalerite, galena, molybdenite and rutile. Pyrrhotite and pyrrhotite/chalcopyrite inclusions occur in the pyrite. Two types of chlorite are present. One has the "normal" grey-blue interference colour, the second has colours ranging up to second order yellow and green.

In thin section the feldspar porphyry consists of quartz phenocrysts, some partially resorbed, altered feldspar and ferromagnesian

(hornblende ?) phenocrysts in an equigranular groundmass of quartz and feldspar with interstitial sericite. Some megacrysts of feldspar occur and minor zircon and sphene (45864).

D2.3 Description of D.D.H. No.6

D.D.H. No. 6 is similar to D.D.H. No.5 in texture and mineralogy. However the sulphide zone is less continuous and magnetite more abundant.

The magnetite commonly occurs as massive bands usually rimmed or veined by pyrite (45867, 45868, 45869, 45870). Some alteration of magnetite to hematite occurs (45865). Pyrite commonly contains magnetite inclusions and more rarely pyrrhotite and pyrrhotite/ chalcopyrite inclusions (45866). Minor chalcopyrite, sphalerite and galena are present and secondary digenite(?) after chalcopyrite.

The feldspar-hornblende(?) porphyry occurs again in the bottom of D.D.H. No.6.

D3 Trace Cobalt and Nickel in Pyrite

Trace cobalt values range from 400 to 5000 ppm (table C1). Selina No. 4 tends to have the lowest cobalt values with about 60% of the data points having less than 1000 ppm cobalt. A substantial zone of high cobalt, greater than 1500 ppm, occurs from 800 to 950 feet. All except two sample points from Selina Nos. 5 and 6 have greater than 1000 ppm cobalt. The average value for these two holes is 1640 ppm.

Nickel values range from 15 to 270 ppm. In a similar pattern to cobalt, most low nickel values occur in Selina 4.

Overall ranges in cobalt and nickel values are similar to Prince Lyell.

D4   Comparison of the Selina Sulphide Zone with the Mt. Lyell Deposits

The Selina mineralization occurs within a correlate of the host sequence for Mt. Lyell.

The alteration assemblages present may be summarised as:-

(a)   quartz-sericite-K-feldspar-pyrite.

(b)   quartz-chlorite-sericite-K-feldspar-pyrite.

(c)   quartz-chlorite-sericite-K-feldspar-pyrite-magnetite.

There is some alteration of magnetite to hematite. Only minor chalcopyrite occurs. Pyrrhotite occurs as inclusions in the pyrite. In comparing these assemblages to Mt. Lyell three points are noteworthy:-

(i)   Only minor chalcopyrite is present.

(ii)   K-feldspar occurs in the Selina assemblages but not at Mt. Lyell.

(iii) Given the differences in (i) and (ii) the assemblages (b) and

(c) above are most comparable to the quartz-sericite-chlorite-pyrite assemblage of Prince Lyell and the quartz-sericite-chlorite-pyrite-oxide assemblage of the Prince Lyell footwall rather than the quartz-chlorite-sericite-oxide-barite assemblages of North Lyell-Crown Lyell or Cape Horn. The presence of pyrrhotite inclusions in the pyrite is consistent with this.

The presence of K-feldspar implies a higher mKCl/mHCl ratio and/or a higher temperature of formation relative to the Mt. Lyell mineralization. If the former situation held this would imply the solutions contained a lower copper content relative to the ore fluids of Mt. Lyell. The alternative suggestion of a higher temperature of formation implies a grossly similar solution to the Mt. Lyell solutions and that the depositional temperature was above the chalcopyrite or bornite stability fields.

APPENDIX E

PROBE ANALYSES OF SERICITE, CHLORITE AND CARBONATE FROM PRINCE LYELL

E1 Sericite Analyses

	1-2/190	1-2/190	1-2/190	2-3/360	4-5/210	4-5/260	5-6/120
			OXIDE PERCENTAGES				
SiO_2	47.80	47.71	46.65	44.93	45.20	47.23	45.00
TiO_2	0.0	0.0	0.0	0.25	0.22	0.61	0.27
Al_2O_3	36.61	36.55	36.25	32.36	31.85	30.53	32.36
FeO	0.70	0.58	0.53	2.40	2.48	2.95	4.35
MgO	0.58	0.42	0.50	1.11	1.25	1.79	1.49
Na_2O	0.35	0.36	0.30	0.0	0.0	0.0	0.0
K_2O	10.23	10.39	10.07	10.02	10.23	10.22	9.89
Total	96.28	96.01	94.29	91.08	91.23	93.33	93.36
			NUMBERS OF IONS				
Si 4+	6.236	6.243	6.199	6.276	6.313	6.454	6.196
Ti 4+	0.0	0.0	0.0	0.026	0.023	0.063	0.028
Al 3+	5.629	5.637	5.677	5.328	5.244	4.917	5.252
Fe 2+	0.077	0.064	0.059	0.280	0.290	0.337	0.501
Mg 2+	0.114	0.082	0.099	0.231	0.261	0.364	0.305
Na 1+	0.087	0.092	0.077	0.0	0.0	0.0	0.0
K 1+	1.703	1.734	1.707	1.786	1.822	1.781	1.737
Total	13.845	13.851	13.816	13.927	13.953	13.915	14.019

	5-6/142	5-6/192	5-6/200	5-6/210	6-7/170	8/350	8/350
SiO_2	47.41	46.90	45.39	47.48	47.07	47.30	47.26
TiO_2	0.40	0.41	0.51	0.46	0.58	0.31	0.49
Al_2O_3	32.16	32.74	31.74	32.03	31.65	30.34	30.89
FeO	3.37	3.14	3.79	3.57	3.45	3.55	3.74
MgO	1.41	1.23	1.15	1.48	1.33	1.91	1.85
K_2O	10.59	10.61	10.39	10.74	10.66	10.64	10.67
Total	95.34	95.03	92.98	95.77	94.74	94.05	95.05

NUMBERS OF IONS

	5-6/142	5-6/192	5-6/200	5-6/210	6-7/170	8/350	8/350
Si 4+	6.362	6.310	6.273	6.357	6.367	6.452	6.391
Ti 4+	0.041	0.042	0.053	0.047	0.059	0.031	0.050
Al 3+	5.086	5.191	5.170	5.053	5.046	4.877	4.923
Fe 2+	0.378	0.353	0.438	0.400	0.391	0.405	0.423
Mg 2+	0.282	0.246	0.238	0.296	0.269	0.388	0.373
K 1+	1.812	1.821	1.831	1.835	1.840	1.851	1.841
Total	13.960	13.963	14.004	13.987	13.970	14.004	14.018

E2 Chlorite Analyses

	2-3/270	2-3/280	2-3/280	3-4/60	4-5/190	4-5/190	4-5/260
				OXIDE PERCENTAGES			
SiO_2	21.72	24.16	22.40	22.66	22.69	22.97	24.75
TiO_2	0.0	0.0	0.0	0.00	0.15	0.00	0.00
Al_2O_3	23.17	22.13	23.32	22.53	22.67	22.58	21.67
FeO	35.89	33.97	36.32	37.57	38.29	38.18	32.24
MnO	0.0	0.43	0.37	0.51	0.56	0.55	0.19
MgO	7.59	9.30	8.27	7.85	6.93	7.05	12.54
Na_2O	0.24	0.40	0.25	0.83	0.30	0.25	0.20
Total	88.62	90.39	90.93	91.95	91.73	91.58	91.59
				NUMBER OF IONS			
Si 4+	4.829	5.173	4.852	4.899	4.926	4.985	5.179
Ti 4+	0.0	0.0	0.0	0.0	0.024	0.0	0.0
Al 3+	6.069	5.584	5.953	5.740	5.800	5.775	5.344
Fe 2+	6.672	6.083	6.578	6.794	6.952	6.930	5.641
Mn 2+	0.0	0.078	0.068	0.093	0.102	0.101	0.033
Mg 2+	2.516	2.967	2.669	2.531	2.242	2.282	3.911
Na +	0.104	0.167	0.105	0.349	0.127	0.105	0.082
Total	20.188	20.091	20.224	20.405	20.199	20.179	20.189
Mg/Mg+Fe	27.40	32.80	28.90	27.10	24.40	24.80	40.90

	4-5/290	5-6/120	5-6/142	5-6/192	5-6/200	6-7/170	8/350
			OXIDE	PERCENTAGES			
SiO_2	22.08	22.34	22.73	23.57	21.87	23.24	24.09
TiO_2	0.0	0.0	0.0	0.0	0.0	0.11	0.0
Al_2O_3	20.94	22.31	22.58	23.15	22.53	21.13	21.53
FeO	33.92	37.38	36.58	35.50	38.84	32.88	31.00
MnO	0.0	0.16	0.30	0.30	0.0	0.54	0.23
MgO	8.57	7.38	8.18	9.18	6.77	10.04	11.74
Na_2O	0.27	0.19	0.27	0.24	0.22	0.19	0.21
Total	85.77	89.76	90.63	91.64	90.22	88.13	88.81
			NUMBERS	OF IONS			
Si 4+	5.044	4.936	4.946	5.002	4.846	5.114	5.186
Ti 4+	0.0	0.0	0.0	0.0	0.0	0.012	0.0
Al 3+	5.638	5.811	5.790	5.792	5.884	5.481	5.462
Fe 2+	6.480	6.909	6.656	6.301	7.199	6.050	5.581
Mn 2+	0.0	0.030	0.055	0.053	0.0	0.100	0.042
Mg 2+	2.916	2.433	2.653	2.904	2.235	3.293	3.767
Na 1+	0.117	0.079	0.114	0.099	0.095	0.081	0.089
Total	20.196	20.198	20.215	20.151	20.259	20.169	20.127
Mg/Mg+Fe	31.0	26.0	28.5	31.6	23.7	35.2	40.3

E3 <u>Carbonate Analyses</u>

	2-3/120	3-4/60	4-5/260	4-5/290	5-6/142	5-6/142	5-6/200
			OXIDE	PERCENTAGES			
SiO_2	0.20	0.84	0.53	0.0	0.0	0.0	0.0
Al_2O_3	0.35	0.18	0.15	0.15	0.17	0.15	0.14
FeO	47.56	44.50	56.63	46.33	47.83	50.60	52.04
MnO	3.48	9.54	5.04	3.24	1.63	4.89	3.20
MgO	9.22	7.88	1.03	8.12	6.87	8.04	6.91
CaO	0.41	0.65	1.52	0.34	0.0	0.29	0.53
Total	61.22	63.58	64.90	58.19	56.49	63.96	62.82
			NUMBER	OF IONS			
Si 4+	0.007	0.028	0.019	0.0	0.0	0.0	0.0
Al 3+	0.014	0.007	0.006	0.007	0.008	0.006	0.006
Fe 2+	1.373	1.246	1.688	1.429	1.541	1.434	1.518
Mn 2+	0.102	0.271	0.152	0.101	0.053	0.140	0.094
Mg 2+	0.475	0.393	0.055	0.446	0.395	0.406	0.359
Ca 2+	0.015	0.023	0.058	0.014	0.0	0.010	0.020
Total	1.986	1.968	1.978	1.997	1.996	1.997	1.997

APPENDIX F

SAMPLE LOCATION AND DESCRIPTION

Specimen locations are referenced by

    (1) D.D.H. No. and distance from the D.D.H. collar.

          Distances are given in feet if the D.D.H.s were drilled

          prior to metrification otherwise they are given in metres.

    (2) Mine Level No., Cross-Cut or Stope No., and the distance

          from the hanging wall of the orebody (in feet).

Locality maps for Prince Lyell and Cape Horn Mine samples and

Western Tharsis D.D.H. samples are given in appendix C. The

location of the North Lyell holes, NL1044 and NL1062, are given

on Crown Lyell level plans 7 and 9 respectively, in C. Bryant's

Honours thesis, "The Corridor Area - Mt. Lyell". Locations of

the Lake Selina D.D.H.s are given in the Mt. Lyell Mining and

Railway Co. Ltd. reports on the prospect.

Prince Lyell

Catalogue No.	Field No.	Description	Code	Locality
				8013-827421
45721	1-2/110	Quartz-sericite-pyrite altered felsic volcanic	R, PS	830' level 1-2 X-CUT
45722	1-2/170	" " "	R, PT	" "
45723	1-2/190	Qtz-ser-altered felsic volcanic. Massive pyrite band.	R, PT	" "
45724	1-2/192	Fragmental felsic volcanic. Ser-minor chl-py-ccp.	R	" "
45725	1-2/270	Massive pyrite	R, PS	" "
45726	1-2/280	Qtz-ser-py altered felsic volcanic.	R, PT	" "
45727	2-3/120	Fine grained, qtz-ser-chl-py altered volcanic	R, PT	830' level 2-3 X-CUT
45728	2-3/270	Coarse fragmental felsic volcanic. Qtz-ser-chl-py-ccp alteration	R	" "
45729	2-3/280	" "	R, PT	" "

Prince Lyell (contd.)

Catalogue No.	Field No.	Description	Code	Locality
45730	2-3/310	graded tuff	R	830' level 2-3 X-CUT
45731	3/70	Fine grained, chlorite flecked, intermediate	R, T	830' level Stope 3
45732	3/110	Fine grained, chlorite flecked, intermediate volcanic	R, T	" "
45733	3/120	Fine grained, chloritic volcanic, pyrite banding	R	" "
45734	3/140	Fine grained, chlorite flecked intermediate	R, T	" "
45735	3-4/35	Pyrite banding	R	830' level 3-4 X-CUT
45736	3-4/70	Fine grained, chloritic volcanic, pyrite banding	R, PT	" "
45737	3-4/190	Fine grained, chlorite flecked, intermediate.	R, T	" "
45738	3-4/240	Fine grained, chlorite flecked, intermediate	R	" "
45739	3-4/250	Qtz-ser-chl-py-ccp altered, coarse fragmental.	R, PT	" "
45740	3-4/260	Fine grained, chlorite flecked, intermediate.	R, T	" "
45741	4/40	Coarse fragmental, qtz-ser-chl-py altered.	R	830' level Stope 4
45742	4/50	" " "	R	" "
45743	4/90	Fine grained, chloritic fragmental, pyrite banding	R	" "
45744	4-5/10	Fine grained intermediate	R,PT,T	830' level 4-5 X-CUT
45745	4-5/70	Chlorite altered, coarse siliceous fragmental.	R	" "
45746	4-5/90	" "	R, PT	" "
45747	4-5/210	Qtz-ser-chl-py-ccp altered, siliceous, fragmental.	R, PT	" "
45748	4-5/220	" "	R	" "
45749	4-5/228	Siliceous fragmental, with massive ccp.	R	" "
45750	5-6/3	Fine grained intermediate.	R,T	830' level 5-6 X-CUT
45751	5-6/150	Siliceous fragmental with chloritic matrix	R, PT	" "
45752	5-6/192	Qtz-ser-chl-py-ccp altered, siliceous fragmental.	R, PT	" "

Prince Lyell (contd.)

Catalogue No.	Field No.	Description	Code	Locality
45753	5-6/210	Qtz-ser-chl-py-ccp altered, siliceous fragmental	R	830' level 5-6 X-CUT
45754	5-6/220	Fine grained, chloritic fragmental.	R, T	" "
45755	5-6/230	Tuffaceous lens in a fine grained, chloritic, siliceous fragmental	R, T	" "
45756	5-6/250	Massive magnetite	R, PT	" "
45757	5-6/302	Massive pink felsic volcanic	R	" "
45758	5-6/310	Pink felsic volcanic, diss py, minor chl.	R, PT	" "
45759	6-7/20	Fine grained, chlorite pyrite altered, fragmental	R	830' level 6-7 X-CUT
45760	6-7/50	Fine grained, siliceous fragmental with chloritic clots.	R	" "
45761	6-7/55a	Fine grained, chloritic fragmental.	R, T	" "
45762	6-7/80	Qtz-ser-chl-py-ccp altered fragmental	R, PT	" "
45763	6-7/90	" "	R, PT	" "
45764	6-7/170	Fine grained, chloritic fragmental	R, PT	" "
45765	6-7/180	Qtz-ccp remobilisation	R	" "
45766	7/90	Qtz-ser-chl-py-ccp altered fragmental	R, PT	830' level Stope 7
45767	7-8/38	" "	R, T	830' level 7-8 X-CUT
45768	7-8/58	" "	R, T	" "
45769	7-8/160	Fine grained, chlorite flecked, intermediate	R. PT	" "
45770	8/0	Qtz-ser-chl-py-ccp altered fragmental	R, T	830' level Stope 8
45771	8/110	Chlorite/magnetite flecked, intermediate	R, T	" "
45772	8/280	Chlorite flecked intermediate	R, PT	" "
45773	8 S/127	" "	R, T	" "
45774	140/425	Fine grained, chlorite flecked, fragmentals	R	DDH WL140, /425'
45775	141/320	" "	R	DDH WL141 /320'
45776	207/647	Mafic intrusive	R	DDH WL207 /647'

Prince Lyell (contd.)

Catalogue	Field No.	Description	Code	Locality
45777	214/800	Magnetite/pyrite veining	R, PS	DDH WL214 /800'
45778	214/809	Felsic volcanic, mt-chl-sid alteration	R, PT	DDH WL214 /809'
45779	214/830	" " "	R, PT	DDH WL214 /830'
45780	214/847	" " "	R	DDH WL214 /847'
45781	221/1110	" " "	R, PT	DDH WL221 /1110'
45782	227/520	Massive magnetite with apatite	R, PT	DDH WL227 /520'
45783	236/505	Mafic intrusive	R	DDH WL236 /505'
45784	236/832	Pyritic, chlorite fragmental	R	DDH WL236 /832'
45785	268/874	Felsic volcanic, mt-chl-py alteration	R, PS	DDH WL268 /874'
45786	274/517	" " "	R, PT	DDH WL274 /517'
45787	337/308	Massive pink felsic volcanic. Py-hem alteration	R, PT	DDH WL337 /308'
45788	338/114	" " "	R, PT	DDH WL338 /114'
45789	360/6	Felsic volcanic, mt-chl-ccp alteration	R	DDH WL360 /6m
45790	360/17	" " "	R, PT	DDH WL360 /17m
45791	360/66.5	Pink felsic volcanic, hem. alteration.	R, PT	DDH WL360 /66.5m
45792	360/87	" " "	PT	DDH WL360 /87m
45793	360/97	" " "	R, PT	DDH WL360 /97m
45794	360/98	" " "	R	DDH WL360 /98m
45795	360/174	Hem. veining	R	DDH WL360 /174m
45796	368/40	Barite veining	R	DDH WL368 /40m
45797	150m	Felsic volcanic, mt-chl-py-ccp alteration	R, PT	150m level footwall driv
45798	150mB	Barite/pyrite banding	R, PT	150m level footwall driv

Prince Lyell (contd.)

Catalogue No.	Field No.	Description	Code	Locality
45799	2-3/S2	Massive magnetite, sid/hem veining	R	2-3 X-CUT /310'
45800	2-3/S3	Massive magnetite with apatite and pyrite veining	R	2-3 X-CUT /310'

Cape Horn

				8013-823440
45801	1-2/0	Fine grained pink Felsic volcanic, chl/ser blebs	R	255m level 1-2 X-CUT
45802	1-2/90	Fine grained chlorite flecked intermediate	R	" "
45803	1-2/130	Qtz-ser-py-ccp, coarse fragmental.	R, PT	" "
45804	2-3/14m	Pink felsic pyroclastic, chl/hem blebs.	R, PT	255m level 2-3 X-CUT
45805	2-3/20m	" "	R	" "
45806	2-3/70	Qtz-ser-chl-py-ccp altered felsic volcanic	PT	" "
45807	4/0	" " "	R, PT	255m level Stope 4
45808	4/90	" " "	R, PT	" "
45809	4-5/20	" " "	R, PT	225m level 4-5 X-CUT
45810	4-5/100	" " "	R, PT	" "
45811	76/95	As above with oxide	R, PT	DDH CH76 /95m
45812	76/105	As above with barite	R	DDH CH76 /105m
45813	71/765	Siliceous fragmental, py-ccp-bn	R, PS	DDH CH71 /765m

Western Tharsis

				8013-824432
45814	257/1030	Qtz-ser-py-ccp-minor bn altered	R, PT	DDH WL 257
45815	257/1080	felsic volcanic	PS	" "
45816	257/1105	" "	R	" "
45817	257/1165	" "	PS	" "
45818	317/220	Qtz-ser-py-ccp altered felsic volcanic	R	DDH WL 317

Western Tharsis (contd.)

Catalogue No.	Field No.	Description	Code	Locality
45819	317/505	Qtz-ser-py-ccp altered felsic volcanic	R, PS	DDH WL 317
45820	317/685	" " "	R, PS	" "
45821	317/880	" " "	R	" "
45822	317/950	" " "	R, PT	" "
45823	332/701	" " "	R	DDH WL 332
45824	332/1128	pyrite/hematite banding	R	" "
45825	332/1130	" "	PS	" "
45826	371/150	Qtz-ser-py-ccp altered felsic volcanic	R, PS	DDH WL 371
45827	371/229	Qtz-ccp-fluorite vein	R, F	" "
45828	374/225	Qtz-ser-py-ccp minor chl altered felsic volcanics	R	DDH WL 374
45829	374/235	" " "	R, PT	" "

North Lyell

Catalogue No.	Field No.	Description	Code	Locality
				8013-831434
45830	1044/15	Siliceous or chert fragmental with py-ccp-bn-minor sericite and pyrophyllite	R	DDH NL 1044
45831	1044/27	" " "	R, PS	" "
45832	1044/37	" " "	R	" "
45833	1044/40	" " "	R, PS	" "
45834	1044/50	" " "	R	" "
45835	1044/63	Qtz-chl-hm/mt-py-ccp-barite altered felsic fragmental.	R	" "
45836	1044/65	" "	R	" "
45837	1044/168	" "	R	" "
45838	1044/220	" "	R	" "
45839	1044/240	" "	R, PT	" "
45840	1044/242	" "	R, PT	" "
45841	1062/45	" "	R, PT	DDH NL 1062
45842	1062/48	" "	R, PT	" "
45843	1062/105	" "	R, PS	" "
45844	1062/120	" "	R	" "
45845	1062/177	" "	R, PS	" "
45846	1062/193	" "	R, PS	" "
45847	1062/195	" "	R, PT	" "

Lake Selina

Catalogue No.	Field No.	Description	Code	Locality 8014-850630
45848	4/390	Massive pink feldspar porphyry	R, T	DDH Selina No. 4
45849	4/445	Qtz-K-feldspar-ser-py altered felsic volcanic	R, PT	" "
45850	4/510	" " " "	R, PT	" "
45851	4/595	" " " "	R	" "
45852	4/610	" " " "	R, PT	" "
45853	4/830	Qtz-K-feldspar-ser-chl-py-minor mt altered felsic volcanic	R	" "
45854	4/970	" " "	R, PT	" "
45855	4/1025	" " "	R, PT	" "
45856	5/112	Chloritised rhyolite	R	DDH Selina No. 5
45857	5/196	Hematite veining	R, PS	" "
45858	5/212	Diss. hematite with pyrite	R, PS	" "
45859	5/244	Qtz-ser-chl-K-feldspar-py-mt altered felsic volcanic	R, PS	" "
45860	5/470	" " "	R, PT	" "
45861	5/575	" " "	R	" "
45862	5/732	" " "	R	" "
45863	5/807	" " "	R, PS	" "
45864	5/865	Quartz, feldspar, hornblende porphyry	R, T	" "
45865	6/230	Qtz-chl-ser-Kfeldspar-mt-py altered felsic volcanics	R, PS	DDH Selina No. 6
45866	6/387	" "	R, PS	" "
45867	6/650	" "	R, PS	" "
45868	6/655	Magnetite/pyrite veins and banding	R	" "
45869	6/675	" "	R, PS	" "
45870	6/770	" "	R, PS	" "